THÈSE DE DOCTORAT

NNT : 2025UPASP067

université PARIS-SACLAY

TECHNISCHE UNIVERSITÄT WIEN
Vienna University of Technology

Detection of nuclear recoils at the 100 eV scale : Characterization of the response of bolometers and application to coherent scattering of reactor neutrinos with the nucleus experiment

Détection de reculs nucléaires à l'échelle de 100 eV : Caractérisation de la réponse des bolomètres et application à la diffusion cohérente des neutrinos de réacteur avec l'expérience NUCLEUS

Thèse de doctorat de l'université Paris-Saclay et l'université technique de Vienne (TU Wien)

École doctorale n° 576 : particules hadrons énergie et noyau : instrumentation, imagerie, cosmos et simulation (PHENIICS)
Spécialité de doctorat: Physique des Particules
Graduate School : Physique. Référent : Faculté des sciences d'Orsay

Thèse préparée dans les unités de recherche **Département de Physique Nucléaire (Université Paris-Saclay, CEA)** et **Atominstitut (TU Wien)**, sous la direction de **David LHUILLIER**, directeur de recherche, le co-encadrement de **Hartmut Abele**, professeur et **Erwin JERICHA**, professeur assistant

Thèse soutenue à Paris-Saclay, le 19 Septembre 2025, par

Romain MARTIN

Composition du jury

Membres du jury avec voix délibérative

Andrea Giuliani Directeur de Recherche, Université Paris-Saclay	Président
Corinne Goy Directrice de Recherche, HDR, CNRS	Rapporteur & Examinatrice
Jules Gascon Professeur des Universités, Université Claude Bernard Lyon 1	Rapporteur & Examinateur
Florian Reindl Assistant Professor, TUWien	Examinateur
Jaime Dawson Chargée de Recherche, CNRS, APC	Examinatrice
Erwin Jericha Assistant Professor TUWien	Examinateur

université PARIS-SACLAY

ÉCOLE DOCTORALE
Particules, hadrons, énergie et noyau : instrumentation, imagerie, cosmos et simulation (PHENIICS)

Titre: Détection de reculs nucléaires à l'échelle de 100 eV : Caractérisation de la réponse des bolomètres et application à la diffusion cohérente des neutrinos de réacteur avec l'expérience NUCLEUS

Mots clés: Neutrino, Réacteur, Diffusion cohérente, Bolomètre, Calibration

Résumé: Cette thèse s'articule autour de deux axes principaux : d'une part, ma contribution à l'expérience NUCLEUS, qui vise à détecter les reculs nucléaires (NR) induits par la diffusion cohérente des neutrinos de réacteur sur les noyaux (CEνNS); d'autre part, le développement de la méthode CRAB (Calibrated Recoil for Accurate Bolometry) pour la calibration en énergie des NR dans les cryodétecteurs. L'expérience NUCLEUS sera prochainement installée à proximité de la centrale nucléaire de Chooz (Ardennes, France). Sur ce site, les principales sources de bruit de fond proviennent des γ ambiants, des neutrons atmosphériques et des muons cosmiques. La réduction du bruit de fond constitue un enjeu central pour NUCLEUS, condition indispensable à l'observation du signal CEνNS. Pour y répondre, l'expérience repose sur un cryodétecteur cible, des blindages passifs, ainsi que deux systèmes de veto destinés à identifier et rejeter les différentes contributions au bruit de fond. Avant son installation à Chooz, l'expérience a été déployée dans un laboratoire souterrain à Munich pour une phase de préparation, comprenant un montage à blanc suivi d'un First Commissioning Run (FCR). Dans cette thèse, je présente la mise en service du veto muon. La réponse de l'ensemble des modules du système ainsi que leurs performances ont pu être validées. J'aborde également l'analyse des données du FCR, qui a permis de confirmer le bon fonctionnement de l'ensemble des détecteurs de l'expérience NUCLEUS. Un effort particulier a été consacré à la synchronisation des différents systèmes d'acquisition, afin de valider l'efficacité des systèmes de veto dans le rejet du bruit de fond. En particulier, l'efficacité du veto muon à rejeter le bruit de fond induit par les muons cosmiques a été clairement démontrée.
Dans le second volet de cette thèse, je présente mes contributions dans le développement et la validation de la méthode CRAB. Cette méthode permet de calibrer des NR dans la région sub-keV, ce qui constitue un progrès déterminant pour les futures expériences de physique des neutrinos et de matière noire. Cette méthode repose sur la capture radiative de neutrons par un noyau cible. Lors de la désexcitation du noyau par émission d'un γ, celui-ci subit un recul d'énergie fixée par la cinématique à deux corps, générant ainsi un pic de calibration dans la région d'intérêt. J'ai conduit des simulations permettant de valider cette approche pour plusieurs matériaux cibles ($CaWO_4$, Al_2O_3, Ge, Si), en analysant notamment l'impact de la coïncidence γ-NR sur le rapport signal/bruit. J'ai également participé à la validation expérimentale de la méthode sur une cible en Al_2O_3. Dans le cadre de ma cotutelle avec l'Université technique de Vienne (Autriche), j'ai séjourné un an sur place afin de contribuer au développement instrumental de la phase II du projet CRAB, mené auprès du réacteur de recherche TRIGA-Mark II de l'Atominstitut, qui fournit un faisceau de neutrons purement thermiques. Cette thèse présente cette installation ainsi que la mise en service des détecteurs γ. Enfin, l'analyse des premières données collectées à Vienne a permis d'obtenir des résultats prometteurs, en bon accord avec les simulations, confirmant la coïncidence γ-NR.

Title: Detection of nuclear recoils at the 100 eV scale : Characterization of the response of bolometers and application to coherent scattering of reactor neutrinos with the NUCLEUS experiment

Keywords: Neutrino, Reactor, Coherent scattering, Bolometer, Calibration

Abstract: This thesis is structured around two main axes: on the one hand, my contribution to the NUCLEUS experiment, which aims to detect nuclear recoils (NR) induced by the coherent elastic scattering of reactor neutrinos off nuclei (CEνNS); on the other hand, the development of the CRAB method (Calibrated Recoil for Accurate Bolometry) for the energy calibration of NR in cryogenic detectors. The NUCLEUS experiment will soon be installed near the Chooz nuclear power plant (Ardennes, France). At this site, the main sources of background are ambient γ radiation, atmospheric neutrons, and cosmic muons. Background reduction is a central challenge for NUCLEUS, and a prerequisite for the observation of the CEνNS signal. To address this, the experiment relies on a cryogenic target detector, passive shielding, and two veto systems, designed to identify and reject various background contributions. Prior to its installation at Chooz, the experiment was deployed in an underground laboratory in Munich for a preparatory phase, including a blank assembly followed by a First Commissioning Run (FCR). In this thesis, I present the commissioning of the muon veto system. The response and performance of all modules were successfully validated. I also discuss the analysis of FCR data, which confirmed the proper functioning of all NUCLEUS detectors. Particular effort was devoted to the synchronization of the different data acquisition systems to validate the efficiency of the veto systems in rejecting background signals. In particular, the muon veto was shown to be highly effective in rejecting cosmic muon-induced background.
The second part of this thesis presents my contributions to the development and validation of the CRAB method. This method enables the calibration of nuclear recoils in the sub-keV energy range, representing a key advancement for future neutrino and dark matter experiments. The method is based on the radiative neutron capture by a target nucleus. During the de-excitation of the nucleus via γ emission, it undergoes a recoil with energy determined by two-body kinematics, thereby generating a calibration peak in the region of interest. I conducted simulations to validate this approach for several target materials ($CaWO_4$, Al_2O_3, Ge, Si), focusing in particular on the impact of the γ-NR coincidence on the signal-to-background ratio. I also took part in the experimental validation of the method on an Al_2O_3 target. As part of my joint PhD program with the Technical University of Vienna (Austria), I spent one year on site contributing to the instrumental development of Phase II of the CRAB project, carried out at the TRIGA-Mark II research reactor at the Atominstitut, which provides a purely thermal neutron beam. This thesis presents the setup and commissioning of the γ detectors at this facility. Finally, the analysis of the first data collected in Vienna yielded promising results, in good agreement with simulations, and confirmed the γ-NR coincidence.

Acknowledgments

Une thèse n'est pas un long fleuve tranquille. C'est une aventure intellectuelle et humaine, exigeante, passionnante, et profondément enrichissante qui demande beaucoup d'investissement personnel. Si j'ai pu mener ce travail à bien, c'est grâce à toutes celles et ceux qui m'ont accompagné, soutenu et inspiré, tant dans ma vie professionnelle que personnelle, et que je souhaite remercier ici sincèrement.

Tout d'abord, je souhaite remercier très chaleureusement l'ensemble des membres de mon jury de thèse: Andrea Giuliani, Corinne Goy, Jules Gascon, Jaime Dawson, Florian Reindl, Erwin Jericha et Hartmut Abele, pour le temps qu'ils ont consacré à l'évaluation de mon travail et pour l'intérêt qu'ils ont porté à cette recherche.

J'aimerais adresser mes plus sincères remerciements à mon directeur de thèse, David Lhuillier. David, je mesure la chance que j'ai eue de t'avoir comme directeur de thèse. Ton encadrement et ta façon de manager ont été particulièrement bénéfiques pour moi : ils correspondaient parfaitement à ce dont j'avais besoin pour progresser, apprendre et m'épanouir dans ce travail de recherche. Ta rigueur et ta capacité à toujours ramener les discussions vers l'essentiel comptent pour beaucoup dans la qualité du travail présenté dans ce manuscrit. Mais au-delà de l'aspect scientifique, j'ai surtout apprécié la dimension humaine de notre collaboration. Ton humour, ton calme et ta bienveillance ont grandement contribué à rendre ces trois années à la fois stimulantes et agréables. Je garde d'excellents souvenirs de nos shifts à Munich, Vienne et Chooz. Certains moments resteront gravés dans ma mémoire, des parties de billard improvisées à un currywurst beaucoup trop épicé, en passant par une carte bleue malencontreusement coincée en vitrine...

I would also like to express my sincere gratitude to my co-supervisor, Erwin Jericha, who guided me during my second year at the Atominstitut in Vienna. Erwin, thank you for being there for me, your support was invaluable, especially in navigating all the necessary procedures in Vienna. Your presence became a real anchor for me during my year in a foreign country, and I am deeply grateful for the guidance and reassurance you provided.

Il m'est absolument impossible de ne pas remercier chaleureusement les chercheurs, doctorants et post-doctorants avec qui j'ai eu le plaisir de travailler pendant ces trois années.

Au CEA, un grand merci à Chloé pour son soutien au début de ma thèse. Je garde un excellent souvenir de nos shifts à Munich, à coder chacun dans notre coin entre une chaise et une table pour débugguer NUCLEUS. Ta bonne humeur était contagieuse et j'espère sincèrement que nous aurons encore de nombreuses occasions de nous revoir !

Je souhaite également exprimer ma gratitude à Corentin, qui nous a rejoints sur CRAB l'an dernier. Je ne regrette absolument pas d'avoir squatté ton bureau pendant ces six derniers mois, car cela m'a permis d'avoir d'excellentes discussions sur la physique. Bien sûr, je n'oublierai pas nos règlements de compte quotidiens après le déjeuner, au sous-sol du laboratoire, autour du baby-foot. J'en profite aussi pour adresser un petit clin d'œil à Éric, compagnon de baby-foot et désormais redoutable (ou presque...) adversaire aux échecs !

Un grand merci à Gabrielle pour ton extrême bienveillance et tout le soutien que tu m'as apporté tout au long de ma thèse. Merci également d'avoir traversé, juste avant moi, le parcours administratif et les procédures de fin de thèse, ce qui m'a permis de suivre tes pas sans encombre!

Je tiens aussi à souligner l'aide précieuse de Loïc, que je considère comme un co-encadrant tant il m'a guidé dans mes simulations CRAB et dans de nombreux autres domaines. Ton expertise m'a été essentielle et j'ai beaucoup appris à tes côtés.

Acknowledgments

Enfin, je souhaite remercier Matthieu et Fabien du DPhP, avec qui j'ai eu le plaisir de collaborer et de réaliser des missions pour NUCLEUS.

I would also like to sincerely thank Elisabetta, with whom I analyzed NUCLEUS data. I learned a lot from you in terms of data analysis methods and techniques. I would also like to thank Andy. I am amazed by your dedication to NUCLEUS and CRAB collaborations, and thanks to you, I learned a lot about cryogenics and gained hands-on experience with the CRAB cryostat!

On the Vienna side, I want to deeply thank Sebastian and his family for helping me, especially during my move to Vienna, and for renting me a flat in the city! A special thought goes to Alberto and Johannes, my former office mates, with whom I shared discussions, exchanges, and great moments.

Finally, I would like to thank all the members of the NUCLEUS and CRAB collaborations for the fruitful discussions, collaborative work, and enjoyable moments during our meetings. A special thought goes to the young physicists: Andy, Nicole, Mattia, Matteo, Marco, Giorgio, Margarita, Liliane, Lily, and Alex!

Je remercie les membres de mon comité de soutien individuel, Luca et Emmeric pour avoir suivi et veillé au bon déroulement de la thèse.

Cette thèse a été financée par l'Université Paris-Saclay et l'Université technique de Vienne, que je remercie sincèrement. Ce programme de cotutelle m'a offert l'opportunité de passer une année à Vienne et de contribuer de manière significative au développement de la phase II du projet CRAB. Je tiens également à remercier les laboratoires du DPhN et de l'Atominstitut ainsi que l'ensemble de leurs équipes, pour m'avoir accueilli dans d'excellentes conditions.

Bien sûr, je n'oublie pas certains professeurs qui, je crois, m'ont aidé à arriver jusqu'à la thèse. Tout d'abord Monsieur Seban, professeur de physique-chimie en terminale au lycée Stendhal de Grenoble, pour m'avoir transmis sa passion pour la physique par la rigueur avec laquelle il expliquait les phénomènes physiques. Mon parcours doit également beaucoup aux méthodes de travail et à l'exigence de la classe préparatoire. À ce titre, je pense très chaleureusement aux professeurs de la CPGE du lycée Paul Valéry à Paris : Chloé Sabban, Gaël Benabou et Youssef Ezzine, qui m'ont permis de donner le meilleur de moi-même pendant ces deux années fondatrices de mon parcours scientifique.

Je souhaite également exprimer ma profonde gratitude à ma famille et à mes amis, pour leur soutien indéfectible tout au long de ces années. À mes parents, pour leur encouragement constant et à mes proches, pour leur présence, leurs conseils et les moments de joie partagés, qui m'ont permis de garder un équilibre.

Enfin, mon pilier, le véritable mur porteur de mon quotidien, a été ma compagne tout au long de ces années. Merci Roxane pour ton amour, ta patience, ton soutien sans faille et pour avoir partagé mes joies. J'espère que tu me supporteras pendant encore plusieurs années!

Contents

List of Figures

List of Tables

Introduction

The existence of neutrinos was first proposed by Pauli in 1930 [1] to explain the continuous energy spectrum of electrons observed in the β-decay process [2]. Due to their extremely weak interaction with matter, it was not until 1956 that neutrinos were first detected by Reines and Cowan at the Savannah River nuclear reactor via the inverse beta decay (IBD) process [3]. This reaction later enabled the detection of neutrinos including the solar, atmospheric and reactor neutrinos. There are three neutrino flavors: electron (ν_e), muon (ν_μ), and tau (ν_τ). Neutrino experiments have revealed the phenomenon of oscillations between these flavor states during propagation, providing evidence for physics beyond the Standard Model.

While the IBD process requires an energy threshold for neutrino detection, an alternative interaction—Coherent Elastic Neutrino-Nucleus Scattering (CEνNS)—was proposed by Freedman in 1974 [4]. CEνNS has no intrinsic energy threshold and features a relatively large cross-section, especially for heavy nuclear targets. Its experimental signature is a low-energy nuclear recoil, which poses a significant detection challenge. Thanks to technological advances in low-threshold detectors, the first observation of CEνNS was achieved in 2018 by the COHERENT collaboration, using accelerator neutrinos at the Spallation Neutron Source (SNS) in Oak Ridge National Laboratory, with a CsI target [5, 6]. Since the coherence condition requires low momentum transfer, the CEνNS process is favored for low-energy neutrinos. (below 10 MeV). Thus, nuclear reactors are promising sources for CEνNS detection, despite the extremely low nuclear recoil energies involved (sub-keV range). Recently, the CONUS+ collaboration reported the first detection of CEνNS from reactor neutrinos [7].

The NUCLEUS experiment aims to observe CEνNS at the Chooz nuclear power plant in France and addresses the challenges associated with detecting such low-energy recoils in the high-background surface environment [8]. The site is located 72 m and 102 m from two 4.25 GW_{th} reactors. The detector consists of arrays of 10 g $CaWO_4$ and Al_2O_3 crystals, which have demonstrated excellent low-energy thresholds. Operated at $\sim$ 10 mK, nuclear recoils deposit heat in the crystals, which is measured using Transition-Edge Sensors (TES). Given the extremely low expected CEνNS event rate—on the order of a few events per week—background suppression is of critical importance for the NUCLEUS experiment. The dominant background sources arise primarily from cosmogenic particles, such as neutrons and muons. To mitigate these backgrounds, a combination of passive and active shielding is employed, including dedicated veto systems.

This thesis presents the NUCLEUS experiment, with a focus on the development and commissioning of its detector systems—particularly the target cryogenic detector and the Muon Veto designed to suppress muon-induced backgrounds. It also introduces a novel and promising method for low-energy nuclear recoil calibration in cryogenic detectors: CRAB (Calibrated Recoil for Accurate Bolometry) [9].

Accurate calibration of nuclear recoils is essential for a precise determination of the recoil energy spectrum induced by CEvNS, which is a key requirement for probing new physics. To achieve this, a detailed understanding of the cryodetector response to sub-keV nuclear recoils is necessary. Standard calibration techniques typically rely on electronic recoils, which do not accurately mimic the CEνNS signal. CRAB addresses this limitation by inducing low-energy nuclear recoils of fixed energy, thus allowing for a direct characterization of the cryodetector response to CEνNS-like events.

Chapter 1 provides an introduction to the history of neutrino physics and details the theoretical foundation of CEνNS. It discusses various neutrino sources, with particular emphasis on nuclear reactors as promising sources for CEνNS detection. The chapter concludes with an overview of current reactor-based CEνNS experiments. Chapter 2 describes the NUCLEUS experiment in detail. It includes a presentation of the experimental site and the different sources of background identified. The design and strategies for background mitigation are outlined. The principles of the cryogenic detectors readout by TES are also discussed. Finally, the chapter provides a perspective on the current status and future goals of NUCLEUS, along with the remaining challenges. Chapter 3

focuses on my work on the NUCLEUS Muon Veto. It begins with the preparation and testing of all veto modules before their blank assembly at the Underground Laboratory (UGL) in Munich. Each module was validated and demonstrated good performance and stability during the First Commissioning Run (FCR) of NUCLEUS. Chapter 4 focuses on this FCR, which lasted nine weeks. During this period, the experiment achieved excellent time stability and low-energy resolution. The main goals included the simultaneous operation of the cryogenic detectors and veto systems, as well as initial background rejection studies. The chapter presents the cryodetector data analysis framework for energy calibration and background rate estimation. First coincidence measurements with the Muon Veto validated the mitigation of muon-induced background. Several analyses have been conducted by the collaboration; the results presented here come from an analysis in which I was directly involved.

The second part of the thesis is dedicated to low-energy nuclear recoil calibration in cryogenic detectors using the CRAB method. This approach is based on radiative thermal neutron capture, which is associated with a well-defined nuclear recoil (NR) via momentum conservation. Chapter 5 explains this principle in detail, along with the simulation framework developed to validate the method. I present simulation results for various target materials including $CaWO_4$, Al_2O_3, Ge, and Si. Chapter 6 presents two experimental validations of the CRAB method using two different targets: $CaWO_4$ and Al_2O_3. I was highly involved in the validation with the Al_2O_3 target. These tests employed a portable neutron source but were limited by high background levels, originating from fast neutrons of the source, preventing precise measurements. Chapter 7 introduces CRAB phase II, which aims to overcome the background limitations by operating near the TRIGA MARK-II research reactor at the Atominstitut in Vienna, thus benefiting from its pure, collimated thermal neutron beam. As part of my work, I performed simulations that highlight the benefit of using γ–NR coincidences to enhance the signal-to-background ratio. The chapter concludes with a description of the phase II experimental setup. The final chapter details the preparation, installation, and commissioning of CRAB Phase II in Vienna. I played a major role in most of the steps described, particularly in the commissioning of the gamma detector and in all aspects of data analysis. Results from the initial commissioning data validated the simulation predictions and confirmed our understanding of both signal and background components. First γ-NR coincidences were also observed. The thesis concludes with a discussion on the future prospects of CRAB, including its potential application to other target materials such as germanium.

1

Scientific context and motivations

This chapter is dedicated to the scientific context of this thesis. It begins with a historical overview of the neutrino (Section 1.1), followed by a presentation of a special interaction between neutrinos and matter known as coherent elastic neutrino-nucleus scattering (CEνNS) (Section 1.2). The CEνNS process opens the door to probing both neutrino properties and Standard Model (SM) physics (Sections 1.3 and 1.4). Various neutrino sources relevant for CEνNS detection are then introduced (Section 1.5). The first observation of CEνNS by the COHERENT collaboration using accelerator neutrinos (Section 1.6) paved the way for the more challenging detection of CEνNS from reactor neutrinos (Section 1.7).

1.1 Historical context

1.1.1 Neutrino discovery

At the beginning of the 20th century, extensive research on radioactivity was underway. Three types of radiation were identified: alpha and beta by Rutherford [10], and gamma by Villard [11]. In particular, beta radiation was recognized as consisting of electrons emitted during neutron decay. At the time, it was assumed that beta decay was a two-body process, which would imply that the emitted electrons should have a discrete, fixed energy. However, in 1902, James Chadwick demonstrated that the energy spectrum of beta electrons was continuous [2]. This unexpected result ruled out the two-body decay hypothesis. In 1930, Wolfgang Pauli proposed the existence of a light and neutral third particle in the final state to explain the continuous spectrum [1]. In 1934, Enrico Fermi developed the first theory of beta decay, incorporating Pauli's hypothetical particle, which he named the "neutrino," meaning "little neutron" in Italian. The beta decay processes are:

$$n \rightarrow p + e^- + \bar{\nu_e} \tag{1.1}$$

$$p \rightarrow n + e^+ + \nu_e \tag{1.2}$$

Fermi's theory laid the foundation for the understanding of weak interactions. Because of their extremely weak interaction with matter neutrinos are almost unaffected by the surrounding environment. As an example, they can easily pass through the Earth without being stopped. This makes neutrino detection extremely challenging. Bethe and Bacher identified one possible process for detecting neutrinos: Inverse Beta Decay (IBD), in which

neutrinos or antineutrinos are captured by a nucleus, resulting in the emission of electrons or positrons [12]:

$$\bar{\nu_e} + p \rightarrow n + e^+ \tag{1.3}$$

$$\nu_e + n \rightarrow p + e^- \tag{1.4}$$

Given the extremely low cross section of IBD on the order of 10^{-44} cm^2 ,the first detection of a neutrino (in fact, an antineutrino) had to wait until the 1950s. In 1956, Clyde Cowan and Frederick Reines successfully detected antineutrinos emitted from a nuclear reactor at the Savannah River power plant [3]. They observed IBD by detecting a prompt signal from the emitted positron, followed by a delayed gamma signal resulting from neutron capture on Cadnium atoms. From the conservation of electric charge and angular momentum, it can be deduced that the neutrino has no electric charge and a spin 1/2. It is worth noting that IBD interaction has a well-defined energy threshold for the incoming antineutrino. This threshold arises from the mass difference between the initial and final states of the reaction. For energy conservation, the antineutrino should have an energy more than 1.8 MeV.

1.1.2 Brief description of the neutrino

In the Standard Model, neutrinos are massless fermions belonging to the lepton sector and interact exclusively via the weak interaction. Lee and Yang suggested that parity may not be conserved by weak interaction [13]. In 1956, Chien-Shiung Wu provided experimental evidence of parity violation in weak interaction studying the β-decay of ^{60}Co [14]. The electrons in the final state were found to have exclusively left-handed helicity. In 1958, Goldhaber, using gamma resonance from the electron capture of ^{152}Eu, ultimately demonstrated that only left-handed neutrinos interact via the weak interaction [15]. In 1970, Palathingal proved that only right-handed antineutrinos interact [16]. In 1962, a new neutrino flavor was discovered: the muon neutrino (ν_μ). An experiment at the Brookhaven Alternating Gradient Synchrotron used a proton beam directed onto a beryllium target to produce pions [17]. These pions decayed into antimuons and muon neutrinos. The discovery of the τ lepton in 1975 motivated the search for a tau neutrino, which was eventually observed for the first time by the DONUT experiment in 2000 [18]. Earlier, in 1987, after a competitive race between the LEP accelerator at CERN and SLC at SLAC, the invisible decay width of the Z boson via $Z_0 \rightarrow \nu\bar{\nu}$ was measured. The more neutrino families exist, the fewer Z bosons decay into visible (hadronic) channels. This led to the conclusion that the number of weakly interacting neutrinos with masses below 91/2 GeV is: $N_\nu = 2.984 \pm 0.0082$ [19]. Therefore, within the Standard Model, there are three families of neutrinos associated with the electron, muon, and tau flavors: ν_e, ν_μ and ν_τ.

1.1.3 Neutrino oscillations

The question of whether neutrinos have mass was challenged by the observation of neutrino oscillations. In particular, at Brookhaven National Laboratory (BNL), the Homestake experiment observed a deficit in the solar neutrino flux, detecting only about one-third of the predicted number of neutrinos using a chlorine-based detector. Other experiments using radiochemical and water Cherenkov detectors, such as GALLEX [20], SAGE [21] and Kamiokande [22], also reported similar deficits. In the 1980s, another anomaly was observed in atmospheric neutrinos by the Kamiokande experiment that measured a different number of electron and muon neutrinos than expected from theoretical predictions [23]. A possible explanation for these deficits is neutrino flavor oscillation, a phenomenon first proposed by Bruno Pontecorvo in 1957 [24]. This hypothesis assumes that the flavor (interaction) eigenstates of neutrinos are not identical to their mass (propagation) eigenstates. The

flavor eigenstates are related to the mass eigenstates through a unitary mixing matrix, commonly referred to as the PMNS (Pontecorvo–Maki–Nakagawa–Sakata) matrix, which involves three mixing angles θ_{ij}, with $i, j \in \{1, 2, 3\}$. As a result, the flavor states are quantum superpositions of mass states, leading to oscillations between different neutrino flavors as they propagate through space. In this formalism the appearance and disappearance probabilities of specific neutrino flavors depend on the squared mass differences $|\Delta m^2_{ij}|$, the mixing angles: θ_{ij}, the neutrino energy: E_ν and the propagation distance: L. The required existence of neutrino mass points to physics beyond the Standard Model. The SuperKamiokande and the Sudbury Neutrino Observatory reported first evidences for solar neutrino oscillations, confirming that neutrinos have non-zero mass [25, 26].

1.1.4 Open questions

There are several open questions in neutrino physics, particularly regarding their mass. While neutrino oscillation experiments have successfully measured mixing angles and mass-squared differences, an ambiguity remains: only the absolute value of $|\Delta m^2_{32}|$ has been determined. This leaves two possible mass orderings: the normal hierarchy ($m_1 < m_2 < m_3$) and the inverted hierarchy ($m_3 < m_1 < m_2$). Oscillation experiments are sensitive only to differences in mass, not to the absolute neutrino mass scale. This absolute scale is constrained from cosmological observations; the PLANCK mission set a bound on the sum of neutrino masses at 0.12 eV [27]. On the other hand, the KATRIN experiment aims to directly measure the neutrino mass by measuring the endpoint of the tritium β-decay spectrum. KATRIN currently places an upper limit of 0.45 eV at 90% confidence level, with the goal of pushing this sensitivity further in future [28]. Another fundamental question is the nature of the neutrino: is it a Dirac or a Majorana particle? If the neutrino is of Majorana type, it would be its own antiparticle. This would allow for processes that violate lepton number conservation, such as neutrinoless double beta decay ($\beta\beta0\nu$). Several experiments including CUORE [29], GERDA [30] and CUPID-Mo [31] are currently searching for this rare decay. Beyond these foundational questions, neutrinos also offer a unique probe for testing the Standard Model, by measuring key parameters. A recently observed process, coherent elastic neutrino–nucleus scattering (CEνNS), opens a new window to explore neutrino properties and probe physics beyond the Standard Model, particularly at low energies. This process allows the study of a new neutrino–matter coupling via the weak nuclear charge.

1.2 The CEνNS scattering

The elastic scattering of neutrinos on a nucleus was first suggested by D. Freedman in 1974 [4] after the discovery of the existence of neutral currents by the Gargamelle experiment at CERN. Neutrino-nucleus scattering relies on a momentum transfer q between the neutrino and the components of the nucleus, such as nucleons. This results in a nuclear recoil (left of Figure 1.1). The cross-section of CEνNS is enhanced by $\sim N^2$ where N is the number of neutron of the target. The only experimental signature of this process is a low-energy nuclear recoil of energy:

$$E_R = \frac{q^2}{2M} \tag{1.5}$$

where M is the target nucleus mass. One of the main challenges in CEνNS detection, beyond background reduction, is the measurement of extremely low-energy nuclear recoils in the sub-keV range. The recoil energy depends both on the mass of the target nucleus and on the energy of the interacting neutrino. The two-body kinematics gives the maximum energy for the nuclear recoil:

$$E_R^{\max} = \frac{2E_\nu^2}{M + 2E_\nu} \approx \frac{2E_\nu^2}{M} \tag{1.6}$$

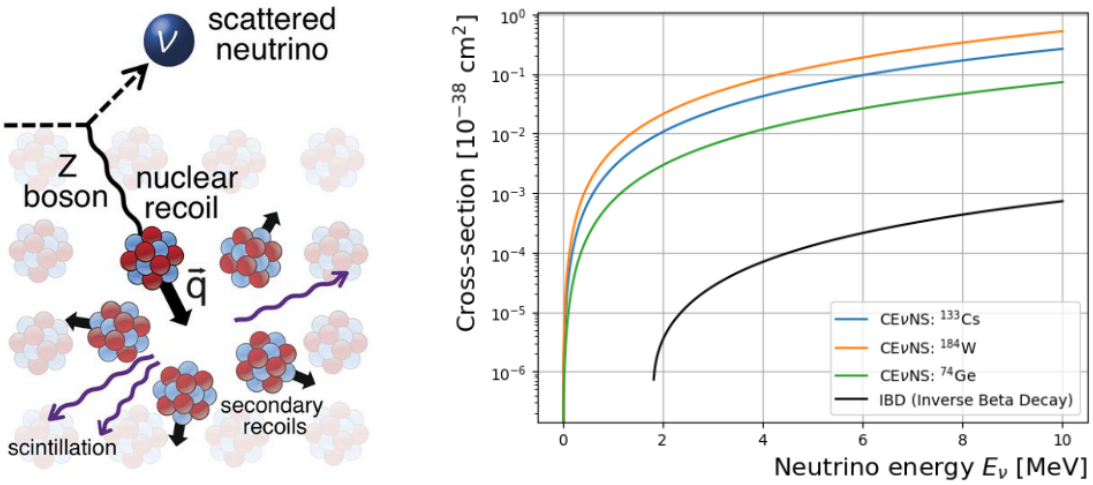

Figure 1.1. Left: Schematic of a CEνNS process showing a Z boson exchange between a neutrino and a nucleus inducing a nuclear recoil. Right: Comparison of various process cross sections as a function of neutrino energy. The CEνNS cross section is more than two orders of magnitude larger than that of the IBD process.

The challenge of detecting low-energy nuclear recoils led to a delay of over 40 years between the prediction and the first experimental detection of CEνNS in 2017 by the COHERENT collaboration.

In the coherent regime, the neutrino interacts with the entire nucleus rather than with individual nucleons. This condition is satisfied for low momentum transfer ($qR \ll h$). Targets commonly used in cryogenic experiments, such as germanium or tungsten, have nuclear radii on the order of $R \sim 10$ fm, which implies $q \ll 50$ MeV/c, resulting in nuclear recoils below tens of keV according to Equation 1.5. From Equation 1.6, such small recoils can only be induced by neutrinos with energies below a few tens of MeV. Therefore, the coherent regime is guaranteed for low-energy neutrinos, typically below 10 MeV. To study this process, the measurable observable is the scattering rate related to the cross section $\sigma_{CE\nu NS}$.

1.3 Cross section

In this section is presented the differential cross-section of the CEνNS process. In the Standard Model this is expressed as follows [32]:

$$\frac{d\sigma}{dE_R} = \frac{G_F^2 M}{2\pi}\left[G_V^2 + G_V^2(1 - \frac{E_R}{E_\nu})^2 - (G_V^2 - G_A^2)\frac{ME_R}{E_\nu^2}\right] \tag{1.7}$$

where $G_F = 1.17 \times 10^{-5}$ GeV^2 is the Fermi constant, M is the mass of the nucleus, E_ν the neutrino energy and E_R is the nuclear recoil energy. $G_{V,A}$ are respectively the vector and axial nuclear weak charges.

We have [6]:

$$G_V = \left(g_V^p Z + g_V^n N \right) F_V(q^2) \tag{1.8}$$

$$G_A = \left(g_A^p (Z_+ - Z_-) + g_A^n (N_+ - N_-) \right) F_A(q^2) \tag{1.9}$$

where $F_{V/A}(q^2)$ are the vector/axial nuclear form factor, which depend on the squared momentum transfer. The nuclear weak charge, denoted as $G_{V/A}$, receives two different contributions from protons and neutrons, namely $g_{V/A}^p$ and $g_{V/A}^n$. These are referred to as the weak vector/axial neutrino-nucleon couplings. $Z_\pm$ and $N_\pm$ represent the number of spin up/down of protons/neutrons in the nucleus. In even-even nuclei, the numbers of spin-up and spin-down nucleons are equal, leading to $(Z_- - Z_+) = (N_+ - N_-) = 0$. As a result, the axial term G_A vanishes in the cross section expression of these nuclei. In heavy nuclei, the relative imbalance between spin-up and spin-down nucleons remains small, leading to a negligeable axial contribution. Therefore, Equation 1.7 can be simplified to:

$$\frac{d\sigma}{dE_R} = \frac{G_F^2 G_V^2 M}{2\pi} \left[1 + (1 - \frac{E_R}{E_\nu})^2 - \frac{M E_R}{E_\nu^2} \right] \tag{1.10}$$

In the coherent regime, the form factor $F_V(q^2 \to 0) \sim 1$. When the momentum transfer q increases, the coherence is lost and the probability of an elastic scattering, encoded in F_V, drops rapidely. The coherence condition requires the neutrino energy to be below 10 MeV, allowing the approximation $E_\nu \ll M$, where M is the mass of the target nucleus. Then the Equation 1.10 simplifies in:

$$\frac{d\sigma}{dE_R} = \frac{G_F^2 G_V^2 M}{\pi} \left[1 - \frac{M E_R}{2E_\nu^2} \right] = \frac{G_F^2 G_V^2 M}{\pi} \left[1 - \frac{E_R}{E_R^{max}} \right] \tag{1.11}$$

The Standard Model expressions of the weak vector neutrino-nucleon couplings are [33]:

$$g_V^p = \frac{1}{2}(1 - 4\sin^2\theta_W)$$
$$g_V^n = -\frac{1}{2}$$

where θ_W is the Weinberg angle. Inserting in Equation 1.8 we find:

$$G_V = F_V(q^2) \left[\frac{Z}{2}(1 - 4sin^2\theta_W) - \frac{N}{2} \right] \tag{1.12}$$

leading to the differential cross section formula:

$$\frac{d\sigma}{dE_R} = \frac{G_F^2 M}{4\pi} F_V^2(q^2) Q_W^2 \left[1 - \frac{E_R}{E_R^{max}} \right] \tag{1.13}$$

where $Q_W = N - Z(1 - 4sin^2\theta_W)$ is the nuclear weak charge. Since $sin^2\theta_W \approx \frac{1}{4}$, we have $Q_W \approx N$. So the CEνNS process on proton is strongly supressed and the cross section is approximately proportional to N^2. Thus, using high N materials enhances the cross section of CEνNS. However, the higher the target mass, the fainter the nuclear recoil, making detection very challenging. The CEνNS cross section on tungsten and germanium is plotted in the right panel of Figure 1.1 showing the dependance $\sigma \propto N^2$. For heavy targets, the CEνNS process dominates other neutrino interactions, such as IBD. Moreover, the kinematic of this scattering does not require an energy threshold for the neutrino unlike the IBD process. It open a possibility to explore and test the standard model at low energy.

1.4 Physics with CEνNS

The measurement of the CEνNS cross section offers valuable insights into neutrino properties and can serve as a way to test the standard model. In this section, I discuss a non-exhaustive list of physics sensitivities.

1.4.1 Weak mixing angle

In the Standard Model, the weak mixing angle θ_W arises from electroweak unification [34]. While $SU(2)_L$ is the symmetry group associated with weak isospin (describing the weak interaction), and $U(1)_Y$ corresponds to weak hypercharge, the unified electroweak interaction is described by the enlarged gauge group $SU(2)_L \times U(1)_Y$. Let us denote by g_w and g the coupling constants associated with the $SU(2)_L$ gauge bosons (W^3_μ) and the $U(1)_Y$ gauge boson ($B\mu$), respectively. Within this formalism, the weak mixing angle θ_W characterizes the mixing of the neutral gauge bosons W^3_μ and B_μ into the physical fields: the photon field A_μ and the Z boson field Z_μ. It is related to the coupling constants via: $tan(\theta_W) = \frac{g_w}{g}$.

Because Equation 1.13 depends on the weak mixing angle through the coupling to the proton (which is strongly suppressed), the measurement of the CEνNS cross section (more precisely, the suppression of the proton contribution) is a probe of θ_W at low momentum transfer.
The neutrino-nucleon coupling given in Section 1.3 is true at the tree level. When including radiative corrections, a flavor dependence arises for the CEνNS process. In this case, the Weinberg angle is running over the value of momentum transfer q. The correction terms involve loops containing all possible particles. Thus, a deviation of the CEνNS event rate from SM prediction could be explained by the existence of new particles and Beyond Standard Model (BSM) physics. Due to its limited sensitivity mainly due to uncertainties in the normalization of the neutrino flux, CEνNS is less precise than parity-violation experiments performed at accelerators or with atoms. Nevertheless, it offers a valuable opportunity to probe the weak mixing angle at low momentum transfer, providing a unique test of the Standard Model in the low-q regime through low-energy nuclear recoils.

1.4.2 Neutrino properties

Although neutrinos are neutral particles, they can still have electromagnetic properties such as a nonzero charge radius and a magnetic moment. A charge radius can be defined for the neutrino through loop corrections involving charged bosons ($W^\pm$) and leptons, and can be interpreted as the length scale of the distribution of virtual charges around the bare neutrino field. The charge radius is related to the first moment of the charge form factor [35]; which can be seen as the Fourier transform of the spatial charge distribution:

$$< r^2_\nu >= 6\frac{df_Q(q^2)}{dq^2}\Big|_{q=0} \tag{1.14}$$

A calculation yields to [35]:

$$< r^2_{\nu X} >= \frac{G_F}{4\pi^2\sqrt{2}}\left[3 - 2ln(\frac{m^2_X}{m^2_W})\right] \tag{1.15}$$

where G_F is the Fermi constant, m_W the mass of the W boson, X the flavor of the neutrino and m_X is the mass of the associated charged lepton. Therefore, a contribution of this term would bring a flavour dependence to the CEνNS cross section. This charge radius leads to correct θ_W according to [36]:

$$sin^2(\theta_W) \rightarrow sin^2(\theta_W)(1 + \frac{1}{3}m^2_W < r^2_{\nu X} >) \tag{1.16}$$

Another electromagnetic property is the existence of a neutrino magnetic moment μ_ν, leading to an additional term in the expression of the cross section. For a spin-zero nucleus, this correction can be written as [37]:

$$\frac{d\sigma}{dE_R} = \frac{\pi\alpha^2\mu^2_\nu}{m^2_e}\left[\frac{1 - E_R/E_\nu}{E_R} + \frac{E_R}{4E^2_\nu}\right] \tag{1.17}$$

where α is the fine structure constant.
The neutrino magnetic moment is related to the Dirac neutrino mass by the relation [38]:

$$\mu_v = 3.2 \times 10^{-19}\mu_B\frac{m_\nu}{1eV} \tag{1.18}$$

where $\mu_B = 9.2 \times 10^{-24}J.T^{-1}$ is the Bohr magneton. Such a magnetic moment is very low and below experimental limits. In certain extensions of the Standard Model, the neutrino magnetic moment could be significantly enhanced, particularly if neutrinos are Majorana particles. Spectral distortions in the CEνNS cross-section could reveal an anomalously large magnetic moment, which would provide strong evidence for new physics or support the hypothesis of a Majorana nature of neutrinos.

1.4.3 Nuclear form factor

The weak nuclear form factor $F_V(q^2)$ in Equation 1.13 as two contributions from neutron and protons form factor ($F_n(q^2)$ and $F_p(q^2)$). Those form factor are defined as the Fourier transform of the density distribution of protons and neutrons in the nucleus. The CEνNS scaterring is strongly suppressed on proton, so it's mainly sensitive to the neutron distribution.

While proton density distributions have been extensively probed by elastic electron scattering experiments [39], measurements of the neutron distribution are poorly known experimentaly. Best available data are from parity-violating electron scattering experiments like PREX [40] for lead and CREX [41] for calcium. Since the differential cross section in Equation 1.13 is directly proportionnal to F_V, CEνNS process offers a unique possibility to investigate the nuclear neutron distribution. There are many neutron distribution parametrizations summarized in [42]. A famous parametrization was done by Helm [43]. In this approach, the neutron distribution is a uniform spherical density with radius r_n convoluted by a Gaussian profile with width s (surface thickness). In

such parametrization, we have $r_n^2 = c^2 + \frac{7\pi^2 a^2}{3} - 5s^2$, where s =0.9 fm, a = 0.52 fm and $c = 1.23A^{1/3} - 0.6$ fm [42]. Within this parametrization we obtain:

$$F_{Helm}(qr_n) = 3\frac{j_1(qr_n)}{qr_n} e^{-\frac{q^2 s^2}{2}} \tag{1.19}$$

where j_1 is the first spherical Bessel function. Figure 1.2 illustrates the evolution of the form factor, which starts at 1 for zero momentum transfer and decreases rapidly as q increases, marking the transition from the coherent regime to a domain dominated by inelastic processes.

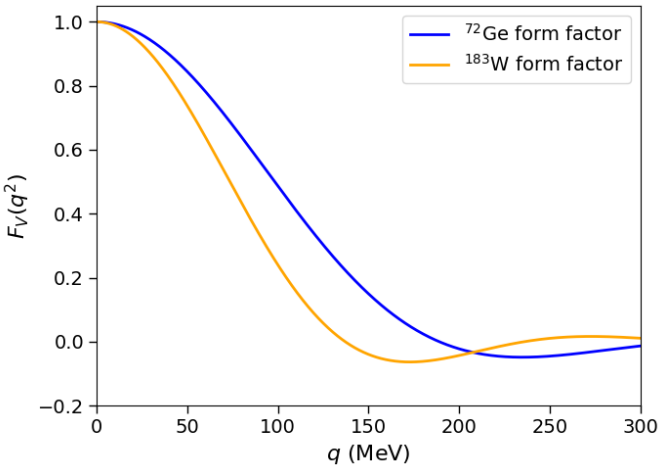

Figure 1.2. Roll-off of the Helm form factor when q increases. We see the loss of coherence with increasing nuclear recoil energy (high q-value).

In the Helm parametrization, the neutron radius R_n is related to r_n by $R_n^2 = \frac{3}{5}r_n^2 + 3s^2$ [44]. Hence, the measurement of the cross section should constrain the value of the neutron radius and the neutron skin $R_{skin} = R_n - R_p$. Such a measurement has strong implications on the evolution of neutron stars because the equation of state gets a term taking into account the symmetry breaking between neutron and proton [45].

1.4.4 Beyond Standard Model interactions

The CEνNS cross section is well defined within the SM, thus, inconsistent measure with the SM prediction could point to BSM physics. A common BSM theory is the non standard interaction (NSI) of the neutrino with other particles. Such interaction would arise flavour dependence in CEνNS and may change the value of the weak charge. It also disturbs long baseline neutrino oscillation experiment such as DUNE because it impacts the neutrino propagation in matter [46, 47]. The SM Lagrangien at quark level can be written as:

$$\mathcal{L} = -\sqrt{2}G_F \sum_q g_V^q \bar{\nu} P_L \nu \bar{q}\gamma_\mu q + g_A^q \bar{\nu} P_L \nu \bar{q}\gamma_\mu \gamma_5 q \tag{1.20}$$

NSI would arise from an additionnal term in the previous lagrangian [48]:

$$\mathcal{L}_{NSI} = -2\sqrt{2}G_F \sum_{\alpha,\beta} \sum_{q,P} \epsilon^{qP}_{\alpha\beta} \bar{\nu_\alpha} P_L \nu_\beta \bar{q} \gamma_\mu P q \tag{1.21}$$

where α, β are respectively the incoming and outcoming neutrino flavour, $q \in [u, d]$, $P = P_{L,R} = \frac{1\pm\gamma_5}{2}$ and $\epsilon^{qP}_{\alpha\beta}$ is the new coupling strength compared to SM interaction. This terms adds a flavour dependance in CEνNS. Developping Equation 1.20 gives:

$$\mathcal{L}_{NSI} = -\sqrt{2}G_F \sum_{\alpha,\beta} \sum_{q} \epsilon^{qV}_{\alpha\beta} \bar{\nu_\alpha} \gamma^\mu P_L \nu_\beta \bar{q} \gamma_\mu q - \epsilon^{qA}_{\alpha\beta} \bar{\nu_\alpha} \gamma^\mu P_L \nu_\beta \bar{q} \gamma_\mu \gamma_5 q \tag{1.22}$$

where we define $\epsilon^{qV}_{\alpha\beta} = \epsilon^{qL}_{\alpha\beta} + \epsilon^{qR}_{\alpha\beta}$ and $\epsilon^{qA}_{\alpha\beta} = \epsilon^{qL}_{\alpha\beta} - \epsilon^{qR}_{\alpha\beta}$. Thus, comparing Equations 1.20 and 1.22 shows that NSI can easily be interpreted as a modification of the vector coupling $g^q_{V,A}$:

$$g^q_V \to g^q_V + \epsilon^{qV}_{\alpha\beta} \tag{1.23}$$

$$g^q_A \to g^q_A - \epsilon^{qA}_{\alpha\beta} \tag{1.24}$$

Applying this on the previous expression of G_V and G_A for an electronic antineutrino:

$$G_V = \Big((g^p_V + 2\epsilon^{uV}_{ee} + \epsilon^{dV}_{ee})Z + (g^n_V + \epsilon^{uV}_{ee} + 2\epsilon^{dV}_{ee})N \Big) F_V(q^2) \tag{1.25}$$

$$G_A = \Big((g^p_A + 2\epsilon^{uA}_{ee} + \epsilon^{dA}_{ee})(Z_+ - Z_-) + (g^n_A + \epsilon^{uA}_{ee} + 2\epsilon^{dA}_{ee})(N_+ - N_-) \Big) F_A(q^2) \tag{1.26}$$

Neglecting the axial contribution (even-even or heavy target), this lead to the new cross section formula [32]:

$$\left(\frac{d\sigma}{dE_R}\right)_{\nu_\alpha} = \frac{G_F^2 M}{\pi} F_V^2(q^2) \left[1 - \frac{ME_R}{2E_\nu^2}\right] \left[\left((g^p_V + 2\epsilon^{uV}_{\alpha\alpha} + \epsilon^{dV}_{\alpha\alpha})Z + (g^n_V + \epsilon^{uV}_{\alpha\alpha} + 2\epsilon^{dV}_{\alpha\alpha})N \right)^2 + \sum_{\alpha\neq\beta} \Big(Z(2\epsilon^{uV}_{\alpha\beta} + \epsilon^{dV}_{\alpha\beta}) + N(\epsilon^{uV}_{\alpha\beta} + 2\epsilon^{dV}_{\alpha\beta}) \Big)^2 \right] \tag{1.27}$$

The $\epsilon^{qV}_{\alpha\beta}$ coupling describes both the flavor-conserving (non-universal) of the NSI within $\alpha = \beta$ and the flavor-changing $\alpha \neq \beta$. CEνNS experiment are then sensitive to vector couplings $\epsilon^{qV}_{\alpha\beta}$ and could constrain the strength of non-standard interactions through deviations in the normalization of the cross section from the Standard Model prediction. Recent measurements from the COHERENT collaboration have led to constraints on these coefficients [49].

1.4.5 Neutrino floor

The "neutrino floor" is a term used to describe an experimental limit in the sensitivity of next-generation dark matter experiments due to the contribution of CEνNS. Weakly Interacting Massive Particles (WIMPs) are one of the leading candidates for the identity of dark matter, and direct detection experiments have been designed to detect the low-energy nuclear recoils that are expected from WIMP-nucleus interactions. However, these experiments are limited by an irreducible background signal from CEνNS due to solar and atmospheric neutrinos, which produce an identical signal to those expected from WIMPs.
The dark matter signal could be overwhelmed by statistical fluctuations of the CEνNS rate. It results in the existence of a neutrino floor below which dark matter researches are compromised. Such neutrino floor can be predicted by the Standard Model as it depends on the CEνNS cross section [50]. Precise measurement of the cross section would provide a precise location of the neutrino floor in the WIMP parameter space. A status of dark matter research in WIMP parameter space is shown on the Figure 1.3. We can see that for dark matter masses above 1 GeV, dark matter experiments exclude cross sections down to levels close to the neutrino floor, indicated by the orange dashed line.

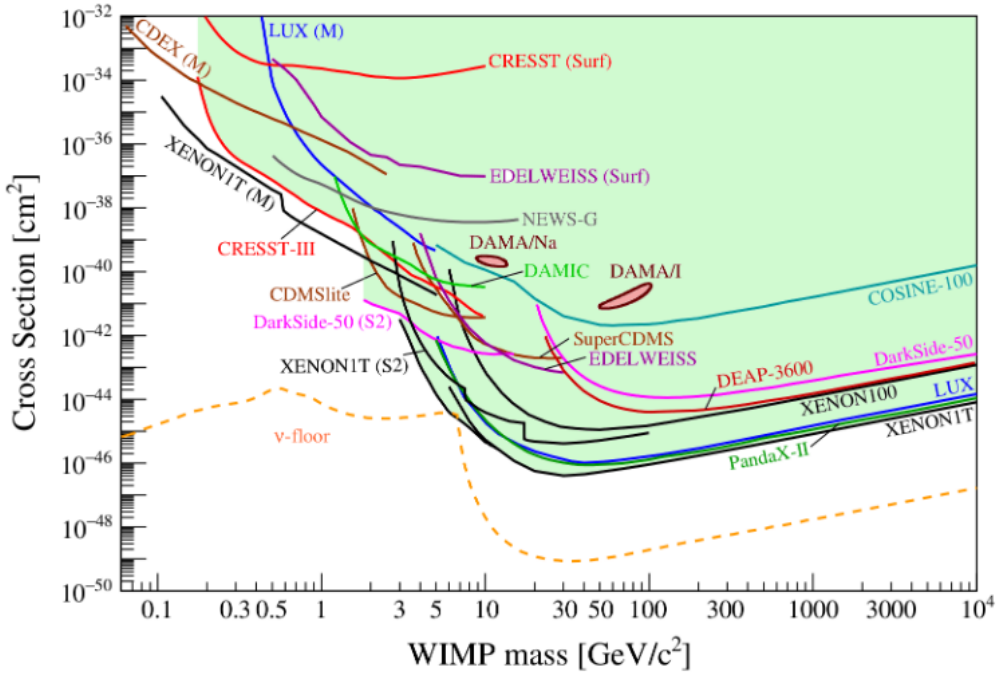

Figure 1.3. WIMP parameter space for spin-independant WIMP-nucleon interactions. We can see the exclusion curves of some dark matter experiment and the neutrino floor in dashed orange line. While solar neutrino affect the research of low mass dark matter, energetic atmospheric neutrino affect research of heavy dark matter. Figure from [50].

1.5 Neutrino sources for CEνNS

While astrophysical sources such as solar, atmospheric, and supernova neutrinos may also be used for CEνNS detection, terrestrial sources provide a larger flux, allowing for more statistics.

When deploying a neutrino source for CEνNS, the requirements presented in Section 1.2 must be kept in mind to ensure that we are in the coherent regime ($E_\nu < 50\,\text{MeV}$). In addition, precise measurement of the cross-section requires accurate knowledge of the neutrino flux. Hence, this section will focus on both the description of the neutrino source and the derivation of the neutrino spectra for each of them. Figure 1.4 shows typical neutrino fluxes from nuclear reactors and accelerators. Neutrinos from reactors are in the fully coherent regime and can be used to probe neutrino properties, while neutrinos from accelerators can be used to probe nuclear properties. Therefore, both sources are complementary for the study of CEνNS scattering.

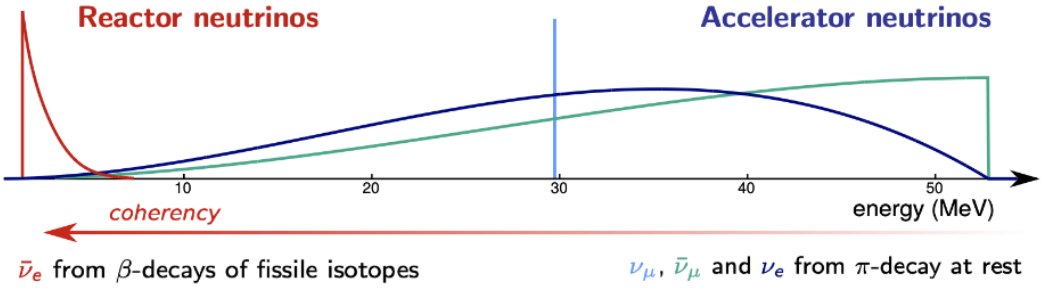

Figure 1.4. Neutrino spectra from nuclear reactor and accelerator sources. Figure from [51].

1.5.1 Stopped pion source

Neutrinos from stopped pion sources rely on a suite of byproducts from an energetic proton beam interacting with a target. For example, the Spallation Neutron Source (SNS) at Oak Ridge National Laboratory (ORNL) is the most intense source of neutrons and charged mesons. The SNS LINAC, which is 300 m long, accelerates H^- ions to 1 GeV, and a foil strips the electrons from H^- to produce a proton beam. These protons are stored and merged into bunches that are ejected onto a Hg target at a frequency of 60 Hz and with a nominal power of 1.4 MW. The protons can undergo spallation on the mercury target, producing a large number of neutrons and byproduct mesons such as π^+ and π^-. This pulsed beam is very useful because the majority of neutrinos are produced within 10 μs after the nuclear spallation, allowing for a narrow time window of the expected neutrino signal. While π^- are captured by the Hg nuclei without producing neutrinos, the π^+ come to rest and decay:

$$\pi^+ \rightarrow \mu^+ + \nu_\mu \tag{1.28}$$

The emitted muon stops within the target and decays contributing to a delayed emission (muon lifetime is about 2.2 μs) of electron neutrino and muon antineutrino through:

$$\mu^+ \rightarrow e^+ + \nu_e + \bar{\nu_\mu} \tag{1.29}$$

Neutrino energy can be deduced using kinematics. The 2-body pion decay leads to a mono-energetic muon neutrino:

$$E_\mu = \frac{m_\pi^2 - m_\mu^2 + m_\nu^2}{2m_\pi} c^2 = 29.8\ MeV \tag{1.30}$$

The three-body decay of the muon leads to a continuous spectra of ν_e and $\bar{\nu}_\mu$ in the allowed region:

$$0 < E_\nu < \frac{m_\mu c^2}{2} = 52.8 \text{ MeV}$$

The fluxes distribution of ν_μ, ν_e and $\bar{\nu}_\mu$ normalized to one are [52]:

$$\phi_{\nu_\mu}(E_{\nu_\mu}) = \frac{2m_\pi}{m_\pi^2 - m_\mu^2}\delta\left(1 - \frac{2E_{\nu_\mu}m_\pi}{m_\pi^2 - m_\mu^2 + m_\nu^2}\right) \tag{1.31}$$

$$\phi_{\bar{\nu}_\mu}(E_{\bar{\nu}_\mu}) = \frac{64E_{\bar{\nu}_\mu}^2}{m_\pi^3}\left(\frac{3}{4} - \frac{E_{\bar{\nu}_\mu}}{m_\mu}\right) \tag{1.32}$$

$$\phi_{\nu_e}(E_{\nu_e}) = \frac{192E_{\nu_e}^2}{m_\pi^3}\left(\frac{1}{2} - \frac{E_{\nu_e}}{m_\mu}\right) \tag{1.33}$$

Such neutrino sources offer a well-predicted energy spectrum of the neutrino flux, as illustrated in the left panel of Figure 1.5. Looking at the timing spectrum of neutrinos, we expect a prompt and delayed neutrino signal after a proton-on-target (POT) trigger as shown in the right panel of the same figure. We can see that the bunch length is about 10 μs while the pulsed beam at 60 Hz gives a bunch separation of 16.7 ms. Therefore, we have a bunch length much smaller than the bunch separation, which strongly suppresses the steady-state background (60 Hz $\times 10\ \mu s \sim 10^{-3}$).

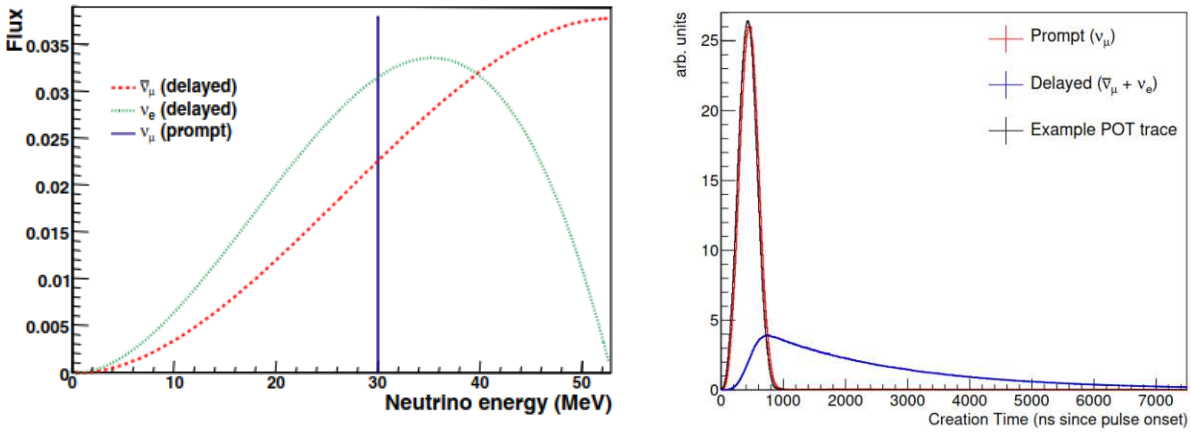

Figure 1.5. Left: Neutrino flux spectra from pion decay. We can see the mono-energetic peak of ν_μ at 30 MeV from the pion decay and the continuous spectra of ν_e and $\bar{\nu_\mu}$ from the muon decay. Figure from [53]. Right: timing spectrum of emitted neutrino, we see a prompt and delayed emission. Figure from [6].

At the SNS, with a proton beam power of 1.4 MW, approximately 2.36×10^{15} neutrinos are produced per second, resulting in a neutrino flux of $\phi = 4.7 \times 10^7 \nu.cm^{-2}.s^{-1}$ at a distance of 20 meters from the target. Stopped pion sources allow for coherent scattering and provide access to study the flavor dependence of the CEνNS process due to the presence of muon and electron neutrinos. However, a major disadvantage of such a source is the high neutron flux, which can result in a dangerous background for CEνNS. This requires the detector to be placed in an experimental site that is well-shielded from the source.

1.5.2 Nuclear reactors

Nuclear reactors have proven to be a very interesting source of antineutrinos for many experiments. As with stopped pion sources, our aim is to determine the neutrino flux from nuclear reactors. Many isotopes contribute to the neutrino emission in nuclear reactors. To better understand the challenges associated with determining the neutrino spectrum, let's briefly review how nuclear reactors operate. In a commercial Pressurized Water Reactor (PWR), the fuel used is primarily enriched uranium, with a significant proportion of ^{235}U, a fissile isotope (which can undergo fission with thermal neutrons), and a majority of ^{238}U, which is fertile but not fissile under the reactor's thermal conditions (it requires fast neutrons to undergo fission). The fuel is regularly replaced, and the period between two refueling operations is called a cycle. A typical cycle duration for a commercial reactor is one year. At the beginning of the cycle, most of the fissions are provided by ^{235}U, which is the main source of nuclear energy at this stage. However, as the reactor operates, neutrons are captured by ^{238}U nuclei, initiating a chain of nuclear reactions described in Figure 1.6.

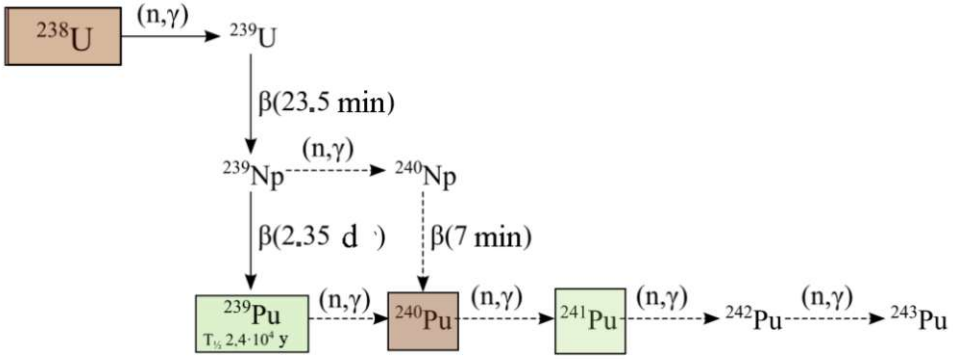

Figure 1.6. Production of isotopes heavier than ^{238}U via neutron capture and beta-decay chains. Brown isotopes have small cross section for fast neutron fission while green are fissile isotope for thermal neutron.

This chain begins with the capture of a neutron by ^{238}U, forming ^{239}U, which rapidly decays via β^- emission into ^{239}Np. The latter then transforms into ^{239}Pu, a fissile isotope that plays an increasingly important role as ^{235}U is gradually depleted. As a result, while the contribution of ^{235}U to the fission rate decreases over time, the contribution from ^{239}Pu increases, reaching a significant fraction by the middle and end of the cycle. Through successive neutron captures, ^{239}Pu can be converted into ^{240}Pu, which is not fissile with thermal neutrons, but can nonetheless capture another neutron to form ^{241}Pu. This isotope is also fissile, and its contribution becomes noticeable toward the end of the cycle. Throughout the cycle, the isotopic composition of the fuel evolves—this is referred to as "burn-up": the role of ^{235}U diminishes, while that of plutonium, particularly ^{239}Pu and ^{241}Pu, increases. The contributions to the fission rate over a cycle are shown in Figure 1.7. Consequently, the nuclear fuel composition changes over time, resulting in a mixture of ^{235}U, ^{238}U, ^{239}Pu, and ^{241}Pu all contributing to the total fission rate. The fission fraction for each isotope averaged over the course of a cycle is provided in Table 1.1.

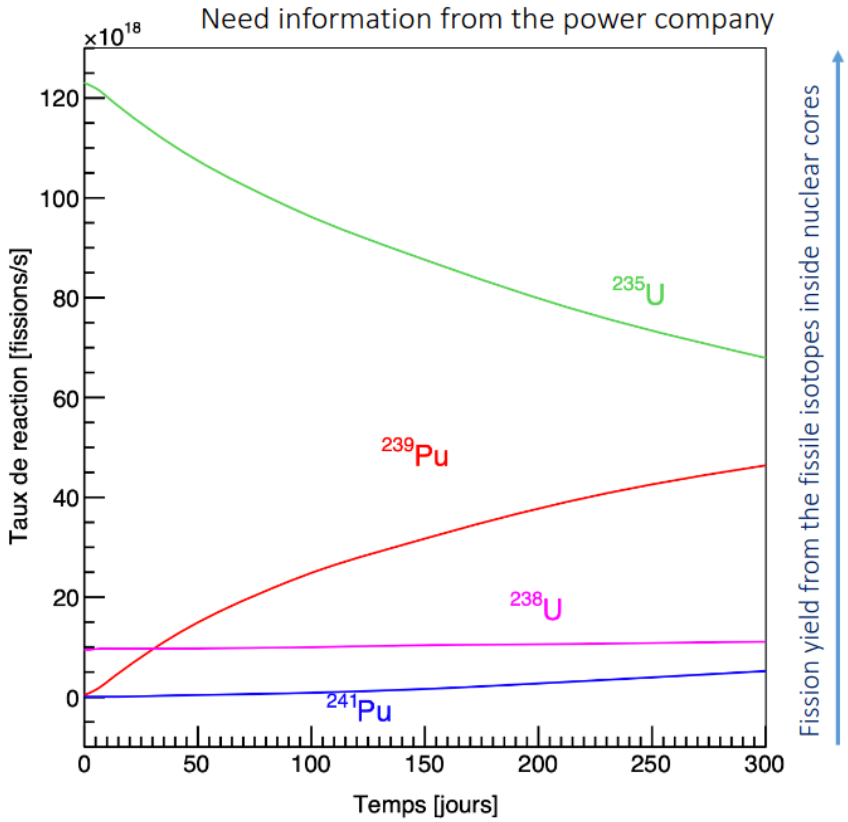

Figure 1.7. Time evolution of isotope content in the fuel mixture over a cycle of 300 days starting with fresh fuel (No Plutonium from previous cycles). Figure from [54].

Isotope	fission fraction
^{235}U	54%
^{239}Pu	33%
^{238}U	9%
^{241}Pu	6%
Others	$< 0.1\%$

Table 1.1. Average fission fraction for different isotopes in the mixture fuel.

The fission products are all neutron-rich and therefore undergo β-decay, producing electron antineutrinos:

$$n \rightarrow p + e^- + \bar{\nu_e} \tag{1.34}$$

with a continuous energy spectrum of neutrino due to 3-body kinematics. Thus the neutrino energy spectrum depends on the fission rate as well as on the composition of the fuel as the distribution of fission products differs from one fissioning isotope to another. The beta decay of fission products produce a high flux of anti-neutrinos with an average of about six $\bar{\nu_e}$ per fission.

Now that the evolution of reactor fuel and the origin of neutrinos have been qualitatively described, let us focus on the prediction of the neutrino energy spectra. There are two main approaches to determining the neutrino spectrum. The first, known as the summation method (or ab initio), involves summing the neutrino spectra from all the β-decays of the fission products. It relies on theoretical models and nuclear databases [55, 56].

This method has the advantage to describe all β-branches contribution to the total fission spectrum and to predict the energy spectrum even below the IBD threshold (1.8 MeV). However, it suffers from uncertainties and the incompleteness of nuclear databases. The second approach is the conversion method [57], which is based on experimental measurements of the β-electron spectra emitted by fission products. Despite the missing information of all elementary β-branches, the antineutrino spectra are derived from the measured electron spectra. This method compensates for the lack of detailed nuclear data in the summation approach. However, the conversion process may introduce systematic biases.

A hybrid approach combining both methods was introduced in 2011 and led to new predictions of the reactor antineutrino spectra [58, 59]. This development had significant implications for short-baseline neutrino oscillation experiments and contributed to explaining the so-called reactor antineutrino anomaly observed in several experiments at nuclear reactors [60–62]. A reference prediction of the antineutrino spectrum obtained using the summation method is shown in Figure 1.8 and leads to a good compatibility with IBD measurements [61]. Notably, this approach provides predictions below the IBD threshold, which can be useful for studies involving CEνNS signal inference.

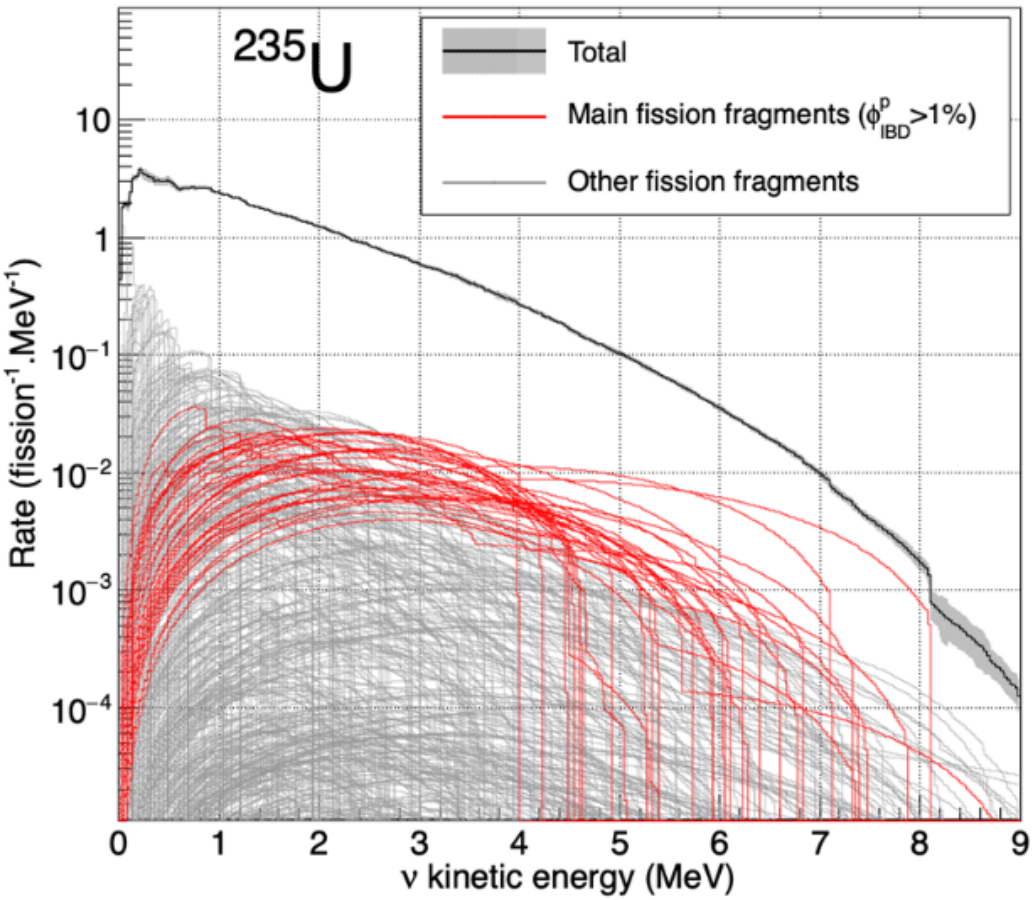

Figure 1.8. Antineutrino energy spectrum from ^{235}U using sommation calculation. Figure from [61].

1.6 COHERENT experiment: CEνNS discovery

The COHERENT collaboration was formed in 2013 and is located at the Spallation Neutron Source (SNS) at Oak Ridge National Lab (ORNL). Its primary goal was to carry out the first measurement of CEνNS using neutrinos from SNS (as described in Section 1.5.1). The first observation of CEνNS was achieved in 2017 with a significance of 6.7 σ. This section describes the experimental setup and reports on the first observation of CEνNS. More details about the background and detector device can be found in [6].

1.6.1 Experimental setup

The COHERENT experiment operates close to the mercury (Hg) spallation target, which provides a neutrino flux of about $\phi \sim 10^7 \nu/cm^2/s$. The advantage of the SNS source is the production of an intense pulsed neutrino flux. The pulsed flux leads to a beam-related signal, allowing CEνNS events to be searched for in coincidence with a neutrino pulse. Backgrounds can be estimated with beam-off measurements and then subtracted from the beam-on data. The experimental setup is presented in Figure 1.9. One can see the target hall and the neutrino alley where several target detectors are located. The neutrino alley must be well-shielded from beam-related neutrons and cosmic rays. Concrete and gravel are used against spallation neutrons, and an 8 m.w.e shields reduces the flux of cosmic rays. The neutrino alley hosts 6 detectors located between 19 and 28 meters from the mercury target. COHERENT uses various target materials to test the $\sigma_{CEvNS} \propto N^2$ prediction. The MARS and NIN cubes are devices used to measure backgrounds such as neutrino-induced neutrons (NINs). Other devices are used for CEνNS detection, and their characteristics can be seen in Table 1.2.

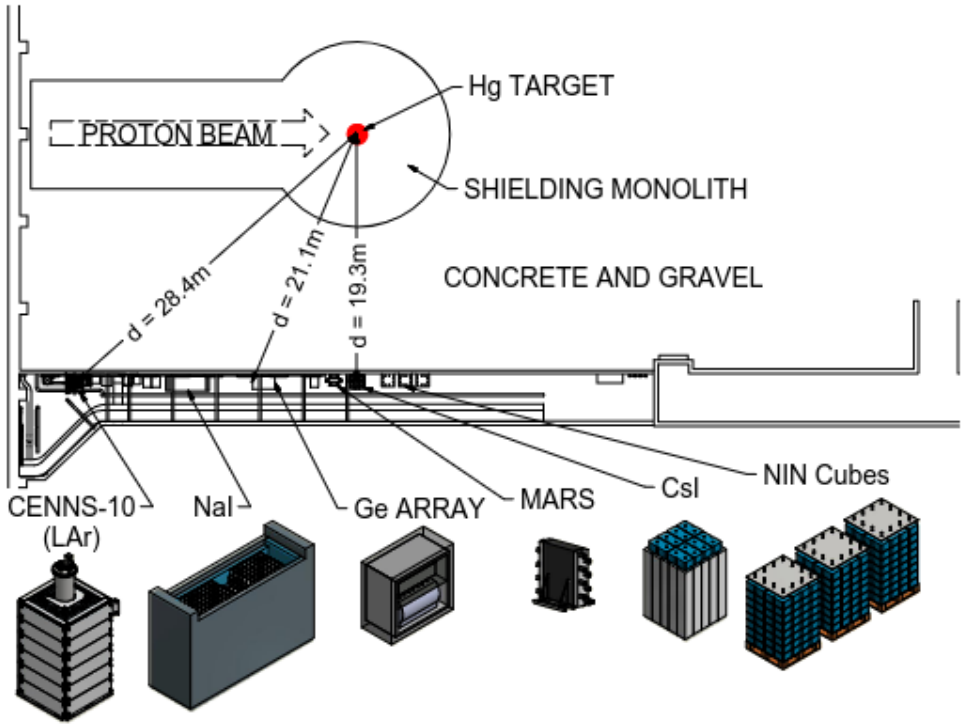

Figure 1.9. COHERENT experimental setup at SNS with the proton beam on the Hg target and the neutrino alley. The neutrino alley contains 6 detectors with different material used for CEνNS detection or background studies. Figure from [6].

Target Isotope	Technoloy	Mass (kg)	Distance from source (m)	Recoil threshold (keV_{nr})	Maximum recoil energy (keV_{nr})
CsI[Na]	Scintillating crystal	14.6	19.3	6.5	40
Ge	HPGE PPC	10	22	5	75
LAr	Single phase	22	29	20	135
NaI[Tl]	Scintillating crystal	2000	28	13	40

Table 1.2. Characteristics of the four CEνNS detectors of COHERENT. The maximum CEνNS recoil energy has been calculated using the Equation 1.6. Adapted table from [6].

1.6.2 First observation of CEνNS

The CsI[Na] crystals benefits from a high light yield of 64 photons/keV_{ee}, allowing the low nuclear recoil from CEνNS to produce a measurable scintillation signal. The analysis leading to the first observation of CEνNS used data from June 2016 to May 2017 and included beam-on (153.5 days) and beam-off (308.1 days) measurements [5]. The results from the beam-off dataset can be seen on the left of Figure 1.10, while the results from the beam-on dataset are on the right. The y-axis shows the residuals differences between signals in the 12 μs following proton on target triggers and those in a 12 μs window before as a function of event energy in PE (A) and arrival time (B). We clearly see an event excess in time with the beam pulses. Null hypothesis can be excluded at 6.7 σ. They observe 134 $\pm$ 22 counts consistent with the standard model prediction of 174$\pm$49 counts.

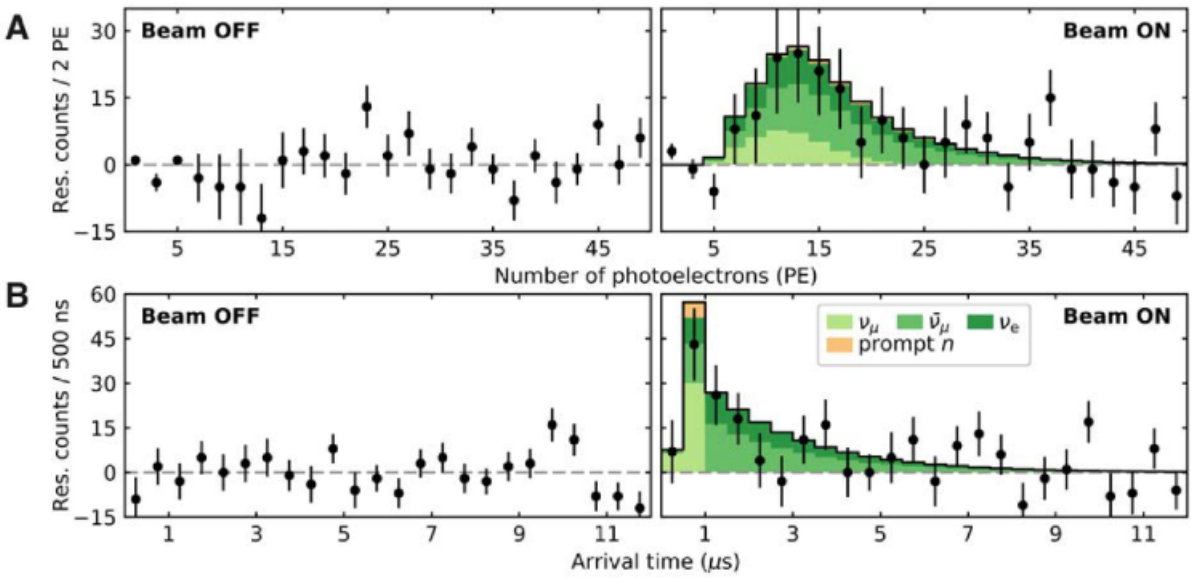

Figure 1.10. Residual differences between signals in the 12 μs following POT, and those in a 12 μs window before as a function of event energy (A) and arrival time (B). We clearly see a beam-related signal due to CEνNS. Figure from [5].

1.6.3 Physical implications from COHERENT

The first measurements of CEνNS by the COHERENT collaboration paved the way to probing the underlying physics of CEνNS, as discussed in Section 1.4. Left of Figure 1.11 shows the CEνNS cross section measurements using CsI and LAr targets. Future deployments in the "neutrino alley" will include Na and Ge targets. The

observed deviation from the expected behavior $\sigma \propto N^2$ highlights the transition out of the coherent regime. Using CsI data, the neutron RMS radius was extracted as $R_n = 5.62^{+0.41}_{-0.40}$ fm [49]. A combined fit of the CsI and LAr data also yielded a value for the weak mixing angle (see right of Figure 1.11), as reported in [49]:

$$sin^2\theta_W = 0.237 \pm 0.029. \tag{1.35}$$

in good agreement with SM prediction.

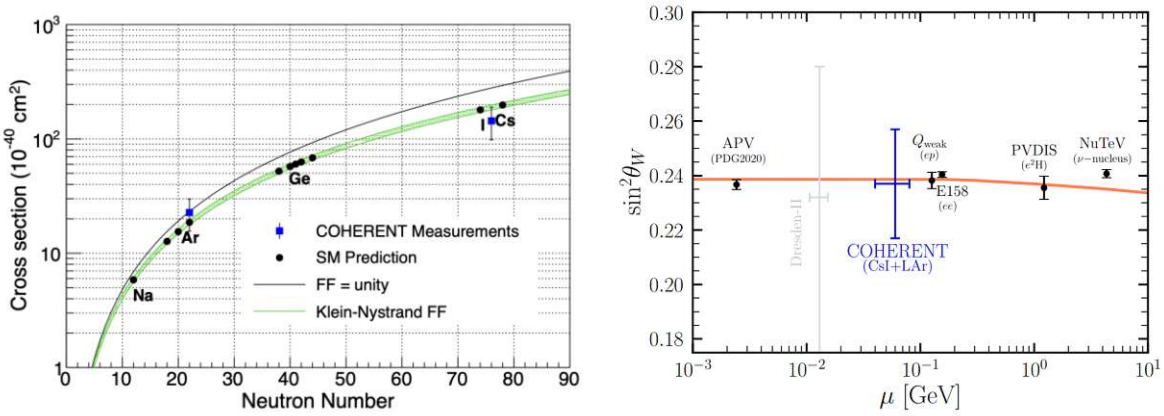

Figure 1.11. Left: Measured CEνNS cross section by COHERENT on CsI and LAr target. Black line assumes the N^2 dependance along with a form factor $F(q^2) = 1$. Green curve shows the expected deviation from the coherent regime from the Klein-Nystrand parameterized form factor. Figure from [6]. Right: Weak mixing angle measurement from CsI + LAr data. Figure from [49].

1.7 Measuring CEνNS at a reactor power plant

In Section 1.5.2, we saw that nuclear reactors are strong sources of neutrinos. Several reactor-based neutrino experiments are currently ongoing. From the CEνNS cross section, it is possible to probe new physics; however, this requires an accurate knowledge of the neutrino flux. I will first derive the relation between the CEνNS cross section and the measured antineutrino event rate in the detector. Then, I will present the applications, the detector requirements for a CEνNS measurement at a nuclear reactor and provide an overview of the ongoing experiments.

1.7.1 Probing the CEνNS cross section

The CEνNS cross section $\sigma_{CEvNS}(E)$, can be inferred from the observed neutrino interaction rate in a detector. The expected number of neutrino interactions in the detector per unit of time and volume n_ν can be expressed as follows [54]:

$$n_\nu = \int \frac{\epsilon N_p \sigma_{CEvNS}(E)\phi(E)}{4\pi D^2} dE \tag{1.36}$$

where ϵ is the detection efficiency of the detector, N_p is the number of target atoms, D is the distance between the reactor core and the detector and $\phi(E)$ the neutrino flux emitted by the reactor. It then requires a very precise knowledge of the neutrino flux.

This flux can be written as [63]:

$$\phi(E) = \frac{P_{th}}{1.6.10^{-13} \sum_i \alpha_i Q_i} \sum_{isotope,i} \alpha_i S_i(E) \tag{1.37}$$

where the sum runs over all fissile isotopes i, each contributing a neutrino spectrum $S_i(E)$, weighted by their respective fission rate α_i averaged over a fuel cycle to account for the evolution of the fuel composition, P_{th} the thermal power of the reactor in GW and Q_i the energy released by the fission of the isotope i in MeV. The factor $1.6.10^{-13}$ stands for the conversion GW to MeV.s^{-1}. By reinserting this into Equation 1.36, we find that:

$$n_\nu = \frac{N_p \epsilon P_{th}}{1.6.10^{-13} 4\pi D^2 \bar{Q}} \sum_i \alpha_i < \sigma_i > \tag{1.38}$$

with $< \sigma_i >= \int S_i(E) \sigma_{CEvNS}(E) dE$ being the contribution to the total cross section from neutrinos produced by the fission of isotope i and $\bar{Q} = \sum_i \alpha_i Q_i$ is the mean energy released per fission. We can also re-write Equation 1.38 in a more compact form as:

$$n_\nu = \frac{N_p \epsilon P_{th} \bar{\sigma}}{1.6.10^{-13} 4\pi D^2 \bar{Q}} \tag{1.39}$$

where $\bar{\sigma} = \sum_i \alpha_i < \sigma_i >$ is the mean cross section per fission.

1.7.2 Applications

From Equation 1.39, we see that the CEνNS process is directly sensitive to nuclear reactor activity. Therefore, detecting reactor neutrinos through CEνNS opens the possibility of monitoring reactor parameters such as thermal power and fuel composition evolution [64]. The advantage of CEνNS over IBD lies in its enhanced cross section, which allows for the use of smaller detectors. In principle, CEνNS also enables the measurement of the reactor antineutrino spectrum, as illustrated in Figure 1.8. Until now, IBD-based detection has only been sensitive to the antineutrino spectrum above the IBD energy threshold of 1.8 MeV. The three β branches from successive neutron captures on ^{238}U (see Figure 1.6), lie below this threshold. Thus, the absence of a reaction threshold allows to detect these β transitions, providing a direct probe of plutonium accumulation in the reactor core. Moreover, in this energy range, one expects a spectrum with characteristic intense peaks. As highlighted in Section 1.5.2, the predicted antineutrino flux depends on nuclear models. While these models are largely indistinguishable above the IBD threshold, probing the sub-IBD threshold region with CEνNS would provide valuable insights and could help discriminate between the different models.

1.7.3 Detector requirements

Based on the elements presented in this chapter, let's summarize all the requirements and specifications necessary to build an experiment for CEνNS detection.
On one hand, neutrinos have an extremely low interaction probability, so the first challenge is to maintain a reasonable signal-to-background ratio. Nuclear reactors are a strong source of neutrinos, and placing an experimental site close to a reactor can increase the signal strength. However, this comes with the downside of significant ambient background from reactor-induced radiation and shallow overburden. Therefore, CEνNS

experiments, especially those at nuclear power plants, must effectively manage their background sources by adopting a good shielding strategy.

On the other hand, the experimental signature of CEνNS is a low-energy nuclear recoil, which requires a detection threshold below around 100 eV- a true technological challenge. This explains the 40-year gap between the theoretical prediction and the first measurement by COHERENT in 2017. The choice of the target detector is crucial, as it influences both the neutrino interaction probability and the energy of the nuclear recoil. To achieve very low energy threshold, various methods and detectors are employed: ionization, scintillation, and calorimeter detectors. An overview of experiments located at nuclear power plants is presented in Section 1.7.4.

Finally, any interpretation of the detected recoils require a precise calibration. No satisfactory method is available for sub-keV nuclear recoils. A promising new technique, CRAB (Calibrated Recoil for Accurate Bolometry), is presented in a second part of this thesis.

1.7.4 Overview

Several experiments have emerged in recent years to detect CEνNS. These may include experiments with a stopped-pion source like COHERENT or dark matter detectors such as XENON or DarkSide, which will soon be sensitive to CEνNS from sources like supernova, solar or atmospheric neutrinos. In this section, we will give a non exhaustive list of experiments located at nuclear power plant, as it provides high neutrino fluxes allowing for large statistics to study CEνNS.
We can classify the experiments into three categories based on the detection method used: those that use ionization detectors, such as CONUS, CONUS+, CONNIE, NuGEN, RICOCHET and TEXONO; those that use scintillation detectors, such as NeON and SBC. All these detectors are subject to low quenching factors at low recoil energies for both ionization and scintillation detectors, making the detection of low-energy recoils very challenging. Finally, there are calorimetric detectors used by collaborations like NUCLEUS, MINER, and RICOCHET. This technology is presented in Section 2.4.1 and allows for very low energy thresholds. However, these detectors are very sensitive to ambient noise and are limited by the so-called low-energy excess (see Section 2.6). Finally, the choice of experimental site between a research reactor or a commercial reactor presents both advantages and disadvantages. A research reactor has lower power and requires positioning close to the reactor core to achieve a sufficient neutrino flux, implying subsequent reactor-induced background. However, unlike a commercial reactor, there is the possibility of having more reactor OFF time for precise measurements of the onsite background, which can strongly increase the significance of a potential CEνNS observation.

CONUS:

The CONUS (Coherent Elastic Neutrino Nucleus Scattering) experiment is located 17.1 meters from a 3.9 GW commercial reactor in Brokdorf, Germany [65], providing a neutrino flux of $2.3 \times 10^{13} \nu/(s \cdot cm^2)$. The target detector consists of four 1 kg high-purity point-contact doped germanium spectrometers (HPGe), with electrodes used to read the ionization signal induced by nuclear recoils. These detectors have a low energy threshold (300 eV_{ee}, equivalent to 1.5 keV_{nr} assuming a quenching factor of 0.16). The uncertainty in the quenching factor is a significant limitation for precise measurements, and efforts have been made to measure it [66]. Thanks to passive shielding and a muon veto, a background rate of 10 c/kg/d below 1 keV has been achieved [67], reaching a sensitivity close to the expected CEνNS signal strength, only a factor of two away [68].

CONUS+:

CONUS+ is the next phase of CONUS [69]. After the Brokdorf nuclear power plant stopped its operation at the end of 2021, the experiment moved to Switzerland, 21 meters from the Leibstadt power plant (3.6 GW

thermal), providing a high neutrino flux of $1.45 \times 10^{13} \nu/(s \cdot cm^2)$. The HPGe detectors were upgraded, and their threshold is now below 200 eV_{ee}. With such a low energy threshold, CONUS+ became sensitive to the high-energy tail of the CEνNS spectrum, despite the low expected event rate. For this reason, nearly 4 kg of target mass were deployed. A precise background model, derived from reactor-off data, allows for effective background subtraction. In early 2025, the collaboration reported the first observation of CEνNS from reactor antineutrinos with a significance of 3.7 σ [7]. The dataset includes 119 days of reactor-on operation, during which (395 $\pm$ 106) neutrino events were detected, in good agreement with the (347 $\pm$ 59) events predicted. The next step will focus on a more precise measurement of the CEνNS cross section, by increasing the target mass, lowering the detector energy threshold, and extending the data-taking period.

NuGEN:

The NuGEN experiment is located in Russia, 11 meters from one of the reactors at the Kalinin Nuclear Power Plant (3.1 GW thermal), providing a neutrino flux of $4.0 \times 10^{13} \nu/(s \cdot cm^2)$. NuGEN uses four 400 g high purity germanium with an energy threshold of 300 eV_{ee} [70]. These detectors are surrounded by passive shielding and a muon veto to reduce the background rate to 2.5 /(keV.kg.day). Installed in 2019, NuGEN presented its first results in [71], with no CEνNS signal observed.

TEXONO:

The TEXONO detector uses 1.43 kg of electro-cooled (EC) point-contact germanium detectors (PCGe) with an energy threshold of 200 eV_{ee}. It is located at the Kuo-Sheng Reactor Neutrino Laboratory (KSNL) in Taiwan, 28 meters from a 2.9 GW reactor [72], providing a neutrino flux of $6.35 \times 10^{12} \nu/(s \cdot cm^2)$. No CE$\nu$NS signal has been detected at KSNL. TEXONO is currently looking for a new site as the Kuo-Sheng Reactor is being phased out.

CONNIE:

CONNIE aims to detect CEνNS at the Almirante Alvaro Alberto Nuclear Power Plant in Brazil. The target detector is placed 30 meters from the Angra 2 nuclear reactor, providing a neutrino flux of $7.8 \times 10^{12} \nu/(s \cdot cm^2)$. The CONNIE collaboration uses fully depleted charge-coupled devices (CCDs) that form 2D arrays of silicon pixels [73]. The nuclear recoil of silicon nuclei produces an ionization signal sensitive to the quenching factor of silicon. Measurements of the quenching factor for Si have been conducted in [74]. In 2016, 8 CCDs of 36.2 g with an exposure of 2.2 kg $\cdot$ days reached a sensitivity 40 times higher than the CEνNS rate prediction [75]. The collaboration is working on scaling the detector mass up to 100 g and exploring a new technology: skipper CCDs, which allow for a lower detection threshold, reduced readout noise, and increased efficiency [76].

NEON:

The Neutrino Elastic-scattering Observation on NaI(Tl) (NEON) experiment is based on the technology of COSINE-100 and uses a scintillation detector with NaI(Tl) crystals featuring high light yield [77]. The main challenge for scintillation detectors is to achieve a low energy threshold, which requires operating with a high light yield [78]. The experiment is located 24 meters from the Hanbit nuclear reactor in Korea, with a thermal power of 2.5 GW, providing a neutrino flux of $7.1 \times 10^{12} \nu/(s \cdot cm^2)$. Phase I consists of a 3×2 array of 6 detectors with a total mass of 15 kg and aims to reach an energy threshold of 300 eV. The next phase will scale up the mass to 100 kg.

SBC:

The SBC (Scintillating Bubble Chamber) aims to use a liquid argon (LAr) bubble chamber to detect CEνNS. It is currently under construction at Fermilab for a commissioning phase [79, 80]. The target mass is 10 kg, and

the nuclear recoil energy threshold is 100 eV. The collaboration is actively looking for a site to measure CEνNS and has considered the TRIGA Mark III research reactor located at the National Institute for Nuclear Research (ININ) near Mexico. The reactor power is only 1 MW, but the site is just 3 meters from the core! Moreover, research reactors can offer more reactor OFF days for background measurements.

MINER:

The Mitchell Institute Neutrino Experiment at Reactor (MINER) experiment inherits technology from the CDMS dark matter experiment and utilizes Germanium and Silicon semiconductors equipped with Tungsten-Transition-Edge-Sensors (W-TES, see Section 2.4). Thus, the MINER detector serves as both an ionization and calorimeter detector, allowing it to achieve a very low energy threshold of approximately 100 eV_{nr} in the heat channel [81]. This ionization readout allows for rejecting heat-only background events, especially those from low energy excess (see Section 2.6), and helps discriminate between electron recoils (ER) and nuclear recoils (NR). MINER is installed 2 meters from the 1 MW research reactor at Texas A&M University. This reactor has a movable core, so the distance to the core can vary from 1 to 10 meters.

RICOCHET:

The RICOCHET experiment [82] uses a cryocube consisting of an array of 27 (3×3×3) HPGe detectors, each with a mass of 42 g, reaching a total target mass of around 1 kg. The heat produced by nuclear recoil is read out by a Germanium Neutron Transmutation Doped (NTD) sensors attached to each HPGe [83]. The targeted energy threshold for the heat channel is 50 eV_{nr}. Particle discrimination can be performed using the ionization signal as a second readout channel, thanks to aluminum electrodes on the surface. This also offers a promising tool to reject low-energy excess, assuming the ability to reach low thresholds for the ionization channel as well. The experimental setup is installed at the research reactor at the Institut Laue-Langevin (ILL) in Grenoble, 8 meters away from the 58.3 MW reactor core. The neutrino flux at this location is $1.2 \times 10^{12} \nu/(s \cdot cm^2)$. Currently, 9 detectors are already deployed on-site, with 9 additional units in the process of being installed, leading to a total payload of 18×42 g. The achieved energy resolutions are 40 eV_{ee} for the ionization channel and 50–80 eV_{ph} for the phonon channel. With these performances, RICOCHET is approaching the sensitivity required for a CEνNS measurement. Data-taking is expected to begin in the summer of 2025.

2

The NUCLEUS experiment

The NUCLEUS collaboration has been established in 2018 and consists of about fifty people from several institutes across 4 European countries: Commissariat à l'Energie Atomique et aux Energies Alternatives de Saclay (CEA Saclay, France), Technische Universität München (TUM, Germany), Max-Planck-Institut für Physik (MPP, Germany), Istituto Nazionale di Fisica Nucleare (INFN, Italy), Sapienza Università di Roma (Italy), Institute of High Energy Physics (HEPHY, Austria) and Technische Universität Wien (TUWien, Austria).

NUCLEUS aims to detect CEνNS at the Chooz nuclear power plant, France. The NUCLEUS detector will stand at the Very Near Site close to the two reactor cores. The neutrinos produced by nuclear reactors have an energy below 10 MeV, ensuring the coherent regime. In this chapter, I present the cryogenic detectors with a sub-keV threshold used by NUCLEUS to detect the low-energy nuclear recoils induced by CEνNS events. After listing the various background sources at the Very Near Site, I present the design of NUCLEUS and its shielding strategy. Then the operation of the cryogenic detectors are explained. Simulation benchmarks provide the expected background levels in the detectors. The low-energy excess is presented along with the Inner Veto system designed to mitigate it. Finally, the NUCLEUS timeline is outlined, including its current status and future.

2.1 The NUCLEUS cryogenic detector as target for CEνNS

As discussed in the first chapter, the signature of CEνNS is a sub-keV nuclear recoil. The detection of phonons induced by such a nuclear recoil allows for better sensitivity to low energies than what can be achieved with scintillation and ionization channels. The use of cryogenic detectors provides good resolution and a low energy threshold. NUCLEUS inherits from the technology of the CRESST experiment, which aims to perform a direct dark matter detection. Indeed, the signatures of Weakly Interacting Massive Particles (WIMPs) and CEνNS are similar (low-energy nuclear recoil). Furthermore, since the "neutrino floor" will impact the sensitivity of dark matter detection experiments, efforts have been made within these same experiments to detect CEνNS, fostering strong interactions between the scientific communities working on dark matter and CEνNS research. NUCLEUS thus benefits from the R&D work carried out by CRESST, which validated the stable use of cryogenic detectors with a low energy threshold [84], with the phonon channel being read by Transition Edge Sensors (TES). A 0.5 g Al_2O_3 prototype detector reached a threshold of (19.7 ± 0.9) eV in 2017 [85–87], paving the way for the launch of the NUCLEUS collaboration in 2018. These cryogenic detectors are operated at temperature of the order of 10 mK to maintain the TES at their normal to superconducting transition. The principles of these cryogenic detectors and the operation of the TES will be detailed in Section 2.4.

The choice of the target is based on physical criteria. On one hand, the coherent cross-section scales with the square of the number of nucleons, so a heavy target maximizes the CEνNS rate. On the other hand, the signature, i.e., the nuclear recoil, is suppressed in energy by the nucleus mass. The target choice is a trade-off.

Figure 2.1 shows the CEνNS rate in dru (events per keV per day per kg) for different targets. Below 100 eV, the N^2 scaling is evident, with the counting rate in $CaWO_4$ being nearly 100 times higher than in Al_2O_3. This is why NUCLEUS uses $CaWO_4$ crystals for CEνNS detection. Beyond 100 eV, the event rate from low-energy reactor neutrino scattering decreases, with a faster suppression observed for heavier target nuclei. The region of interest (ROI) is below 100 eV, where CEνNS rate is expected above the background level of 100 dru targeted by the NUCLEUS experiment (gray band). Hence, an energy threshold of O(10 eV) is needed to explore the CEνNS signal with heavy targets.

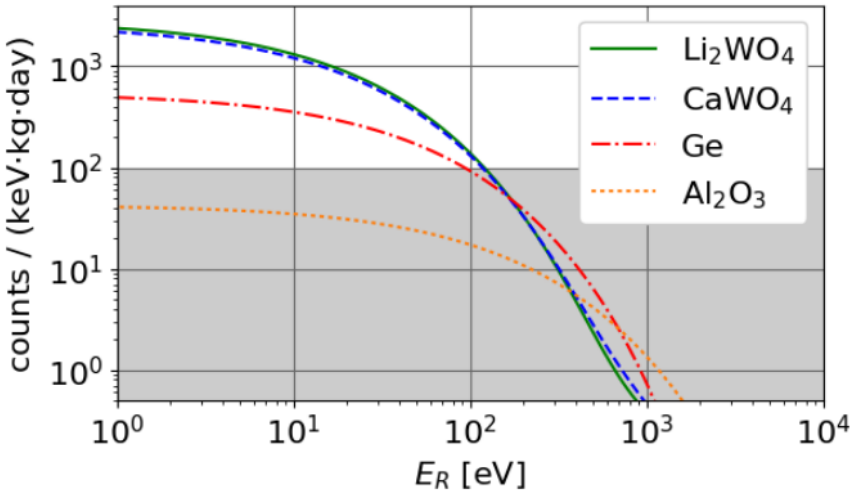

Figure 2.1. Differential CEνNS count rate in different target materials at the Very Near Site at Chooz. The gray band shows the target background level of 100 dru. We see the importance of having a low energy threshold to be sensitive to CEνNS. Tungsten target nuclei maximize the cross section due to their high number of nucleon. Figure from [8].

.

2.2 NUCLEUS at the Chooz Nuclear Power Plant

The NUCLEUS collaboration turned to the Chooz Nuclear Power Plant in the Ardennes, France. Indeed, this plant has already hosted neutrino experiments such as Chooz [88] and Double Chooz [89] for studying neutrino oscillations. The Chooz plant is operated by the French company Electricité de France (EDF). It contains two commercial nuclear reactors of type N4, labeled B-1 and B-2, each providing a power output of 4.25 GWth. Each reactor is shut down for approximately one month per year for maintenance and refueling. Unfortunately (for physicists), the shutdowns are not scheduled to occur simultaneously, ensuring that one of the two reactors is always operational to provide a continuous electricity supply. This may prevent us from performing a measurement of an OFF-OFF background with sufficient statistics. However, the configurations ON-ON, ON-OFF, and OFF-ON provides some lever arm to measure a neutrino signal with intensity correlated to the total thermal power of the two cores.
The NUCLEUS experiment will be installed at an experimental site, referred to as the Very Near Site (VNS), located between the two reactor cores, thus benefiting from a high neutrino flux of 3×10^{12} $\nu_e/(\mathrm{s} \cdot \mathrm{cm}^2)$. Figure 2.2 presents a 3D schematic of the Chooz nuclear power plant along with the location of the VNS. Facing the experiment room, is the compressor room, which host the compressor and water cooling systems required to cool the cryostat.

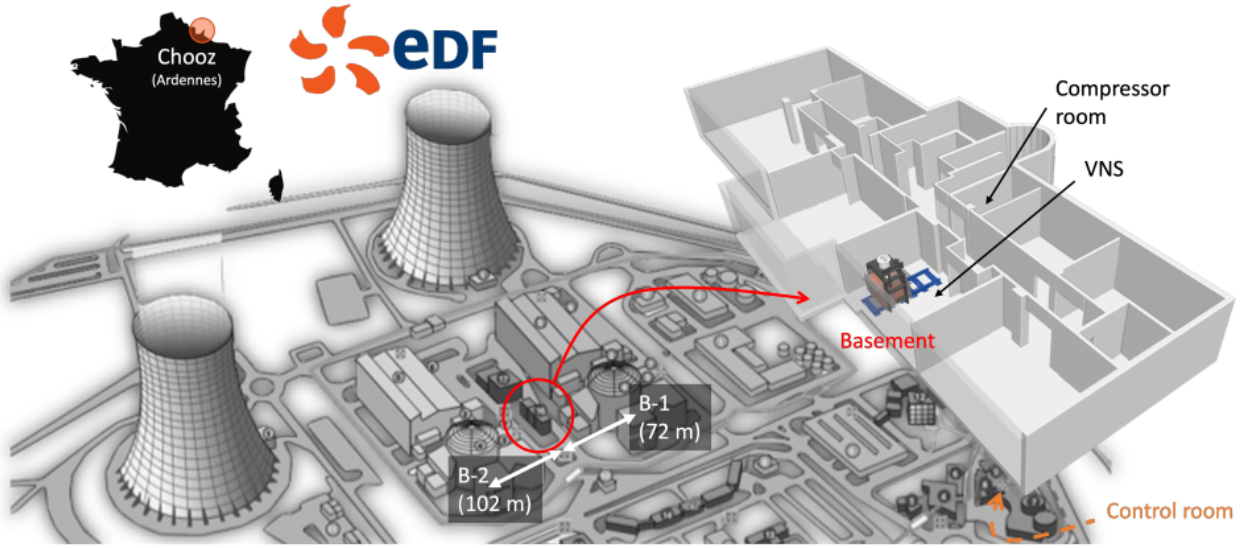

Figure 2.2. 3D view of the Chooz Nuclear Power plant and of the VNS. The VNS is located at 72 m from B-1 and 102 m from B-2 in the basement of an administrative building. Figure from EDF, CNPE de Chooz (2019).

2.2.1 Description of the Very Near Site

The VNS is a 24 m^2 room located 72 m and 102 m away from reactor cores B-1 and B-2, respectively. It is situated in the basement of a six-storey administrative building. The space constraints of the room impose a compact design for the NUCLEUS experiment, which occupies no more than a few square meters. A 3D drawing of NUCLEUS at the VNS is shown in Figure 2.3.

The background at the site can be classified into three categories: reactor-induced background, cosmic-ray induced background, and external and internal radiogenic background. Thanks to the distance between the VNS and the two reactor cores the reactor-induced background sources are negligible. An attenuation factor of $6.38^{+2.65}_{-1.45}$ for the atmospheric neutron flux with energies above 10 MeV [90], and (1.41 ± 0.02) for the atmospheric muon flux have been measured at the VNS. It corresponds to an overburden of (2.9 ± 0.1) meters water equivalent (m.w.e.) [8]. These cosmic-rays induced particles are the main source of background.

2.2.2 On-site backgrounds

As in any physics experiment searching for rare events, background mitigation is a key aspect of the NUCLEUS experiment. Here, I provide a brief presentation of the two main sources of external background: cosmogenics and radiogenics. A more detailed study can be found in [90]. An other class of background, inherent to the cooling and holding of the target crystals is treated in Section 2.6.

2.2.2.1 Cosmogenic background

The Earth is continuously exposed to cosmic rays, mainly composed of protons, which interact in the atmosphere to produce secondary particles. These, in turn, decay, leading to a shower of particle hitting the ground, consisting of muons, neutrons, electrons, γ-rays, protons, and pions. Electrons, protons, and pions are efficiently

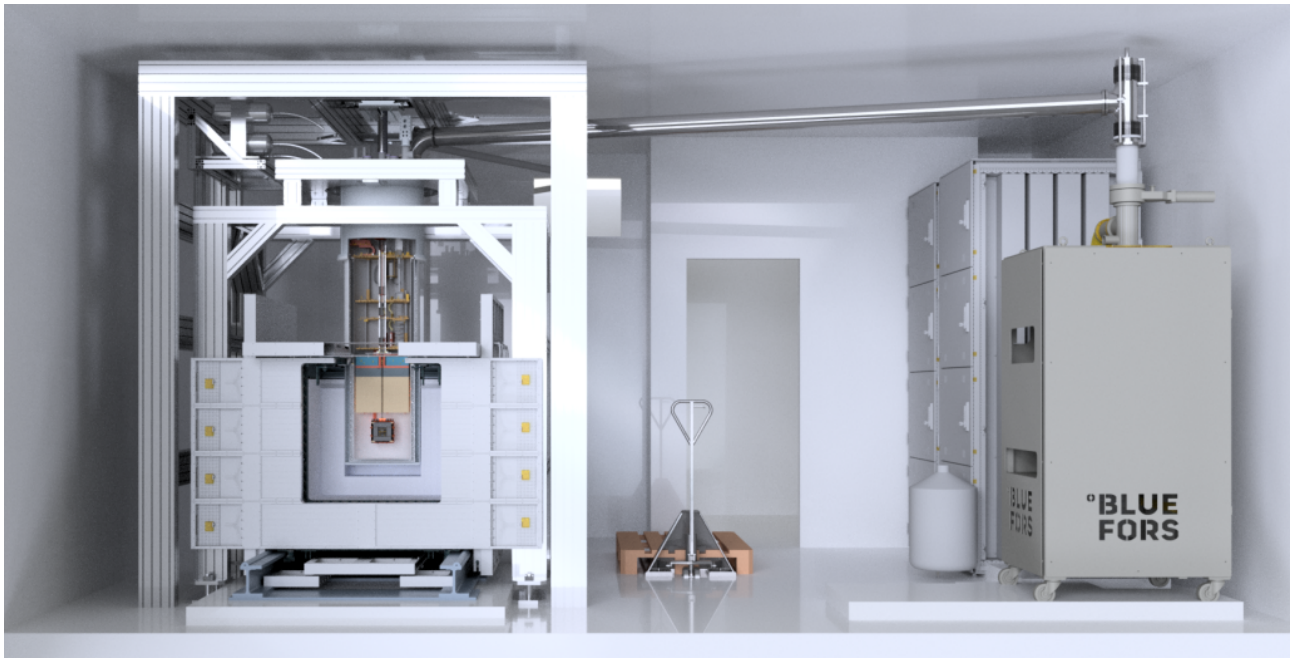

Figure 2.3. 3D view of the Nucleus experiment in the VNS with the cryostat inside a multi-layer of active and passive shielding on the left (see Section 2.3) and the Helium gas handling system of the cryostat on the right.

stopped by lead shielding and the VNS overburden. Only muons and neutrons remain: they are the main source of background for NUCLEUS.

Atmospheric neutrons constitute a dangerous background source for NUCLEUS since the signature of their elastic scattering in $CaWO_4$ is a nuclear recoil. The maximum nuclear recoil is given by the two-body kinematic:

$$E_R^{max} \approx \frac{4 m_n T_n}{M_W} \tag{2.1}$$

where m_n is the neutron mass, T_n the neutron kinetic energy and M_W the tungsten mass. From this simple formula we deduce that neutrons below 35 keV can produce a nuclear recoil of O(100 eV) in the same kinematic domain than the CEνNS signal (see Figure 2.4). The energy distribution of atmospheric neutrons is well described by the measured spectra from Gordon [91], which predicts a neutron flux of 0.0134 $n/(s.cm^2)$. Low-energy atmospheric neutrons are largely suppressed by polyethylene shielding. However, such shielding also thermalizes high-energy neutrons (in the MeV range), resulting in a population of neutrons with energies of a few keV. These neutrons can undergo elastic scattering on tungsten nuclei, making them the main background source for the NUCLEUS experiment.

The other penetrating particles of the cosmic showers that can reach the NUCLEUS detectors are the muons. They can interact through various processes: ionization, pair production, Bremsstrahlung, and nuclear reactions such as spallation reactions in high-Z materials. The latter can generate neutrons with energies of a few keV in the lead shielding used by the NUCLEUS experiment to mitigate ambient gamma background. These neutrons can subsequently scatter off the $CaWO_4$ crystal. To suppress this component, NUCLEUS opted for an active Muon Veto surrounding the detector.

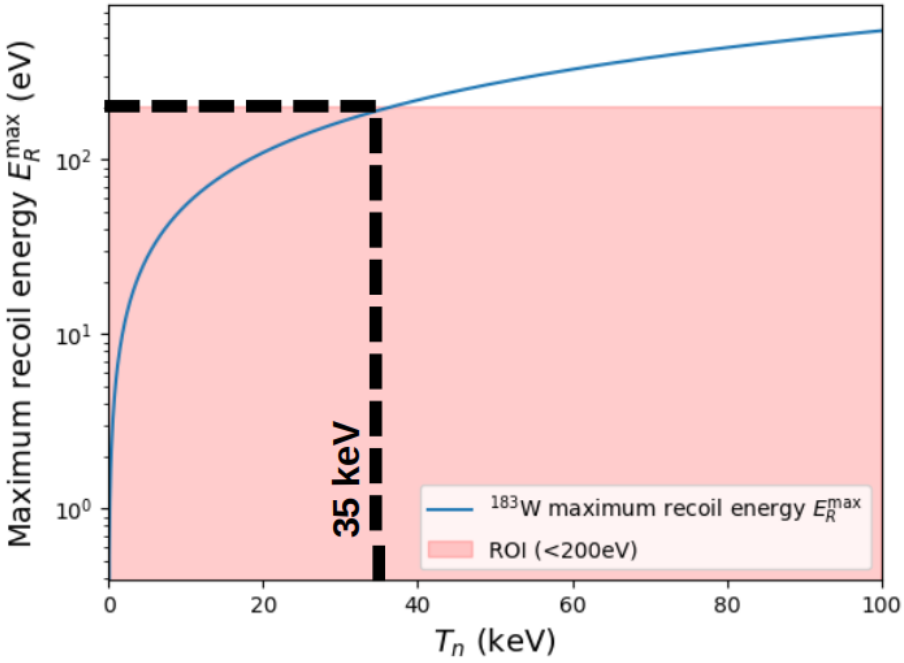

Figure 2.4. This figure shows the maximum nuclear recoil energy vs incident neutron kinetic energy for an elastic scattering on a Tungsten target. The neutrons inducing recoils in the ROI are those with energies below 35 keV.

Muons are produced in the upper atmosphere as a result of pion decay:

$$\pi^- \rightarrow \mu^- + \bar{\nu_\mu} \tag{2.2}$$

The energy spectrum of muons at the Earth surface is driven by muon interactions in the atmosphere, in which they lose about 2 GeV per ionization and can also decay. The angular distribution of muons at the surface is expected to follow a $cos^2(\theta)$ dependence [33], as muons arriving at large zenith angles traverse a larger thickness of atmosphere and have a higher probability of being stopped and decay before reaching the surface. The Gaisser parametrization provides the muon angular and energy distribution [92]:

$$\frac{dN_\mu}{dE_\mu d\Omega} = \frac{0.14 E_\mu^{-2.7}}{cm^2.s.sr.GeV}\left[\frac{1}{1+\frac{1.1E_\mu cos\theta}{115GeV}} + \frac{0.054}{1+\frac{1.1E_\mu cos\theta}{850GeV}}\right] \tag{2.3}$$

Such parametrization leads to an integrated muon flux of $\phi_0 = 0.019\ \mu.cm^{-2} \cdot s^{-1}$. At the surface, most muons have an energy below 10 GeV, as shown in the muon energy spectrum in Figure 2.5. We can see that this spectrum drops above 10 GeV because high energy muons come from very energetic pions, which are more likely to interact in the atmosphere before decaying. The muon attenuation factor was measured at VNS with the cosmic wheel developed by the Centre de Physique des Particules de Marseille (CPPM) for the "Science à l'école" project [93]. The setup comprises three scintillator modules operated in coincidence to identify cosmic muon events. These modules are mounted on a motorized rotating frame, allowing adjustment of the detection angle up to 70°. The acquired data confirmed the anticipated $cos^2\theta$ behavior of the muon flux and measured an attenuation factor of 1.41 ± 0.02 from the VNS building [8].

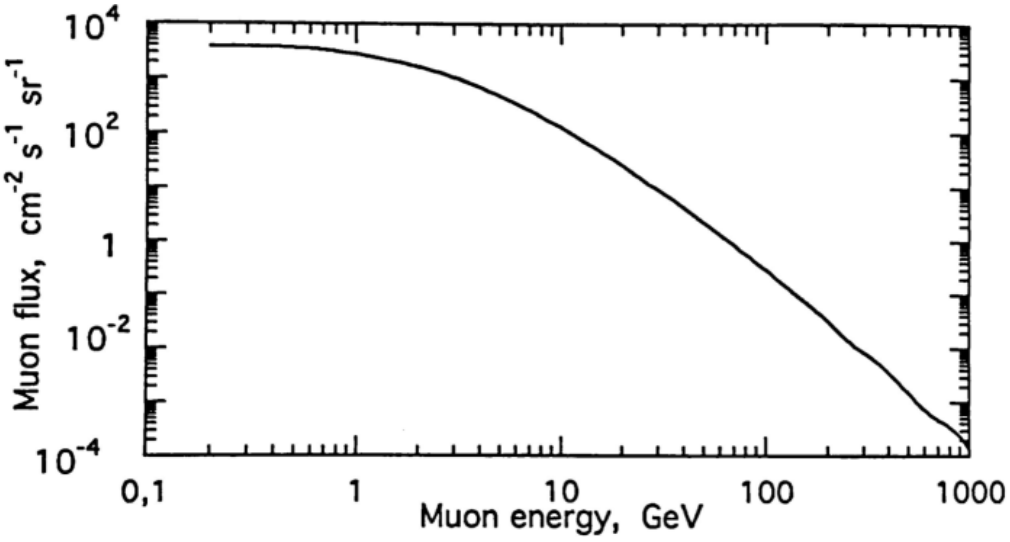

Figure 2.5. Energy spectrum of muons at sea level. Figure from [94].

2.2.2.2 Radiogenic

Radiogenic backgrounds mainly originate from the intrinsic radioactivity of radionuclides contained in various materials. These radionuclides can be present either in the materials surrounding the detector or within the detector itself. The external radioactivity of the environmental materials at VNS consists of α, β, and γ radiations from the main radionuclides: ^{232}Th, ^{238}U, ^{235}U, ^{40}K. Potassium is the most abundant in rocks and soils. We have γ radiations up to 2.6 MeV (from ^{208}Tl) which can interact via Compton scattering and deposit energy in the ROI. Regarding alpha and beta radiations, their penetration depth is very low (a few μm to a few mm), and they are only dangerous in the case of surface contamination of the materials surrounding the detector itself. In particular, radon present in the decay chains of ^{232}Th, ^{238}U and ^{235}U is a source of airborne radioactivity. Through deposition on the detector surface, radon and its daughters constitute the main source of surface backgrounds. External radiogenic background can be easily shielded by high-Z materials such as lead, while internal surface backgrounds would require a specific veto system (see Section 2.7).

2.3 Design of NUCLEUS

The background level targeted for NUCLEUS is 100 d.r.u (events per kg, per keV, and per day). For a single 0.75 g $CaWO_4$ cube, this corresponds to 5 events per year in the ROI (<200 eV). This background level is very challenging on surface, therefore it's crucial that NUCLEUS adopts an efficient strategy of background strategy!

Figure 2.6 presents a cut view of the NUCLEUS setup. The NUCLEUS design contains several elements nested within each other, like Russian dolls. First, there is the Muon Veto, which serves to reject muon induced background, followed by the passive shielding containing lead to attenuate ambient gamma rays and polyethylene to reduce the component related to atmospheric neutrons. These passive and active shields enclose the cryostat, which contains the inner shielding (a simple extension of the external shielding within the cryostat) and the cryogenic outer veto, which serves to reject the residual gamma and neutron components passing through the passive shields. Finally, the shields rest on rails and have been designed such that it is possible to open the setup in two parts and access the cryostat. In this section, I will present each of those elements in more detail.

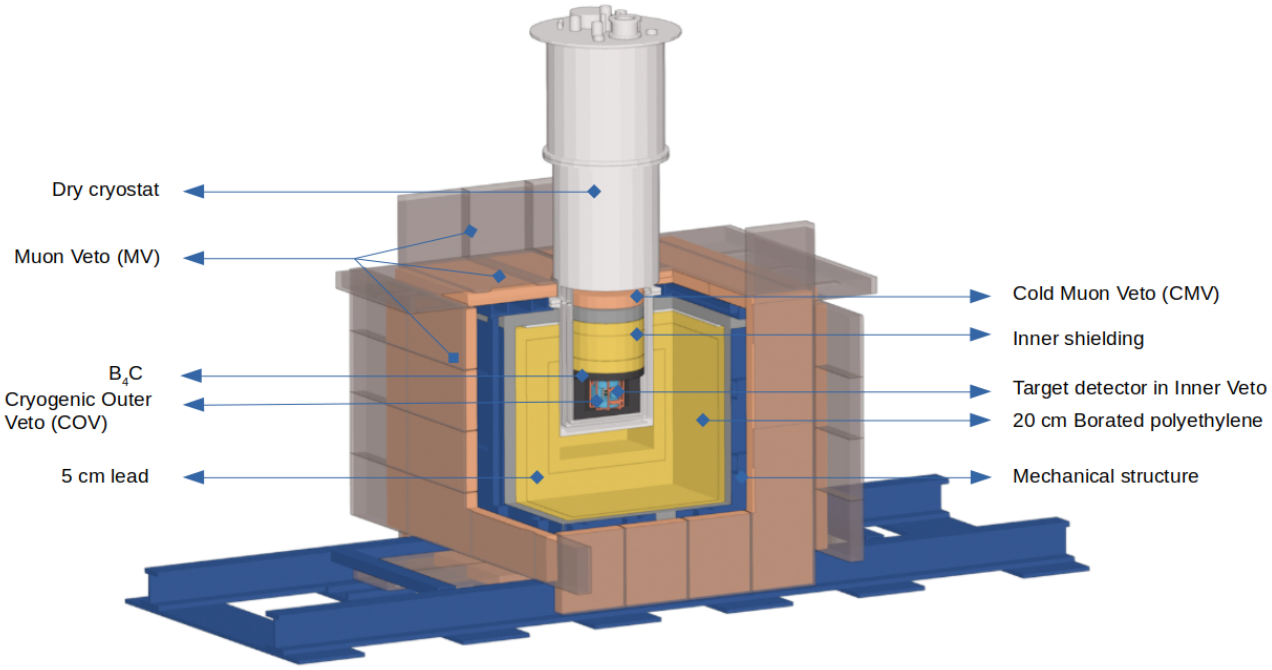

Figure 2.6. Cut view of the Nucleus experimental setup. Credits: C.Goupy.

2.3.1 Muon Veto

The Muon Veto (MV) consists in a cube assembly of plastic scintillators to tag the passage of muons in the vicinity of the cryodetectors. Events coincident with the Muon Veto are rejected in the analysis. The Muon Veto must meet certain criteria. First, the trigger rate must be low so that the dead time remains reasonable, which implies a compact Muon Veto. It must also have nearly 4π coverage to achieve the best geometrical efficiency. Thus, the Muon Veto contains 28 scintillator blocks from St-Gobain [95], forming a cube around the passive shielding. Each scintillator contains WLS fibers that capture the blue-peaked scintillation light, shift it to green, and guide it to one or two Silicon Photomultiplier (SiPM) modules (PE3325-WB-TIA-SP) from KETEK [96]. This design was validated during the characterization and performance study of a prototype panel [97]. The design and assembly of each individual panel is presented in [90]. A sketch of the Muon Veto is shown on the Figure 2.7. This compact configuration is designed to ensure a geometrical efficiency of 99.7% . The expected muon rate at the VNS is 325 Hz. Assuming a 240 μs veto window, we end up with an acceptable dead time of 7.8%. This veto window was chosen based on the time response of the cryodetector. The first part of my thesis was devoted to the commissioning of the Muon Veto, including calibration, analysis, and monitoring. This is covered in Chapter 3 where the Muon Veto is presented in more detail. The study of the cryodetectors events in anticoincidence with the Muon Veto is discussed in Chapter 4.

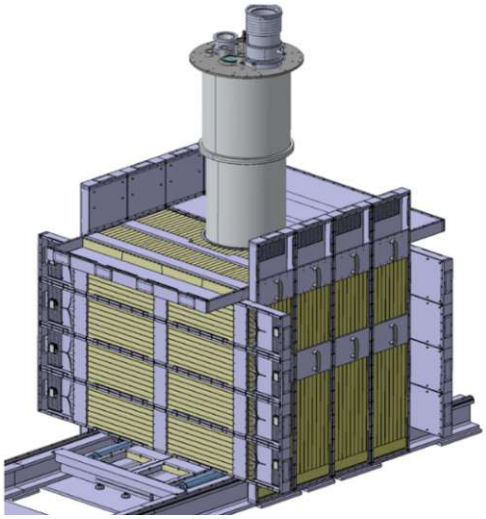

Figure 2.7. 3D drawing of the Muon Veto.

2.3.2 External passive shielding

The external passive shielding is located inside the Muon Veto, following the same cubic geometry. It surrounds closely the cryostat. As shown in the Figure 2.8, a first external layer of 5 cm thick attenuates ambient gamma rays, followed by an inner layer of 20 cm thick 5% borated polyethylene to reduce the neutron background. Its shape is a parallelepiped with dimensions of $(93 \times 93 \times 86)$ cm^3, with a cylindrical hole of 430 mm diameter on the top, in which the cryostat is placed. Just like the Muon Veto, the external passive shielding is cut into two parts, allowing the opening of the shielding and access to the cryostat.

2.3.3 The NUCLEUS Cryostat

The operation of cryogenic detectors for low-energy nuclear recoil detection requires cooling down to temperatures on the order of 10 mK (see Section 2.4.1). NUCLEUS therefore uses a BlueFors LD400 dry cryostat [98], which, through the condensation of a ^{3}He/^{4}He mixture, provides a strong cooling power of approximately 0.5 mW when operated at 100 mK. The cooling principle is described in more detail in appendix A. Figure 2.9 shows the different temperature stages inside the cryostat. The advantage of using a dry cryostat is the ability to perform automatic cool downs remotely without use of cryogenics liquid difficult to manage on the nuclear power plant site. However, dry dilution refrigerators use a pulse tube to cool down to 1 K, which generates mechanical vibration noise, problematic for the cryodetector resolution.
Therefore, a vibration decoupling system has been developed illustrated on the left of Figure 2.9. This system is suspended on an XY table standing on a rack independent of the cryostat and has several stages: a hydroformed bellow, a steel spring, a copper wire, and a kevlar wire connected to the detector box. The detector holder is hanging without contact with the cryostat, except for loose copper braids that ensure the thermal coupling between the mixing chamber and the detector box for thermalization. The vibration decoupling system has a resonance frequency of 1 Hz, and its transmissibility beyond this frequency becomes negligible, effectively decoupling the detector from vibrations. Residual vibrations are transmitted through the thermal links and readout cables. This system has demonstrated good noise performance with the pulse tube running. Several cool downs of this system have been successfully carried out, and it has been possible to operate the detector continuously and stably with an energy resolution of O(10 eV), demonstrating the independence of detector operation from pulse tube vibrations [99, 100].

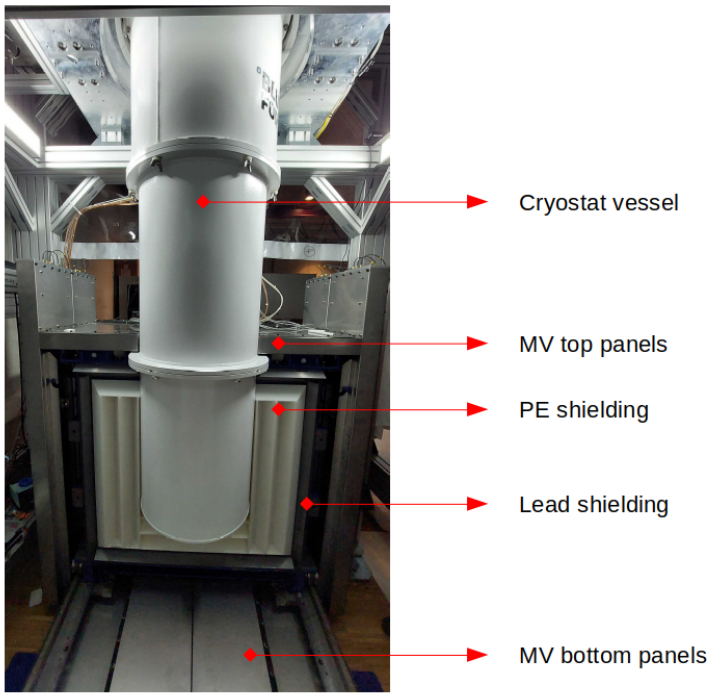

Figure 2.8. Picture of the NUCLEUS shielding. The outer layer is the Muon Veto. Next, there is a 5 cm layer of lead, followed by the white block of borated polyethylene that surrounds the cryostat. Credits: A. Wex.

2.3.4 Inner shielding

The inner shielding, located inside the cryostat, is an extension of the external shielding layer structure. It ensures a 4π-coverage essential to achieve a low background rate. The inner shielding is a cylinder with a diameter of 297 mm, containing several layers, as shown in the picture on the right of Figure 2.9. The top layer is the Cold Muon Veto (CMV), with readout and design similar to the external Muon Veto. The CMV is cooled down to 800 mK, while the SiPMs are located at the 300 K stage. The ability to cool down and operate a plastic scintillator at sub-Kelvin temperatures has been demonstrated in [101]. Below the CMV, there is a lead layer, followed by four layers of borated polyethylene. Finally, the inner shielding is identical to the external shielding, with careful alignment of each shielding layer. To thermalize the inner shielding to 800 mK, each layer is separated by copper foils connected to copper cold fingers going through the entire inner shielding pile. Weighing 68 kg, the inner shielding adds thermal inertia. However, it was successfully thermalized to 800 mK after 11 days of cooling, and the mixing chamber temperature remained at its nominal temperature of O(10 mK). Additionally, a 4 cm-thick layer of boron carbide (B_4C) will be added in the cryostat around the cryogenic outer veto. Its purpose is to capture the residual epithermal and fast neutrons inside the polyethylene shielding. Indeed, simulations have shown that fast atmospheric neutrons can be thermalized in the polyethylene, resulting in neutrons of a few keV near the detector [102, 103]. This additional B_4C layer is necessary to mitigate this neutron background.

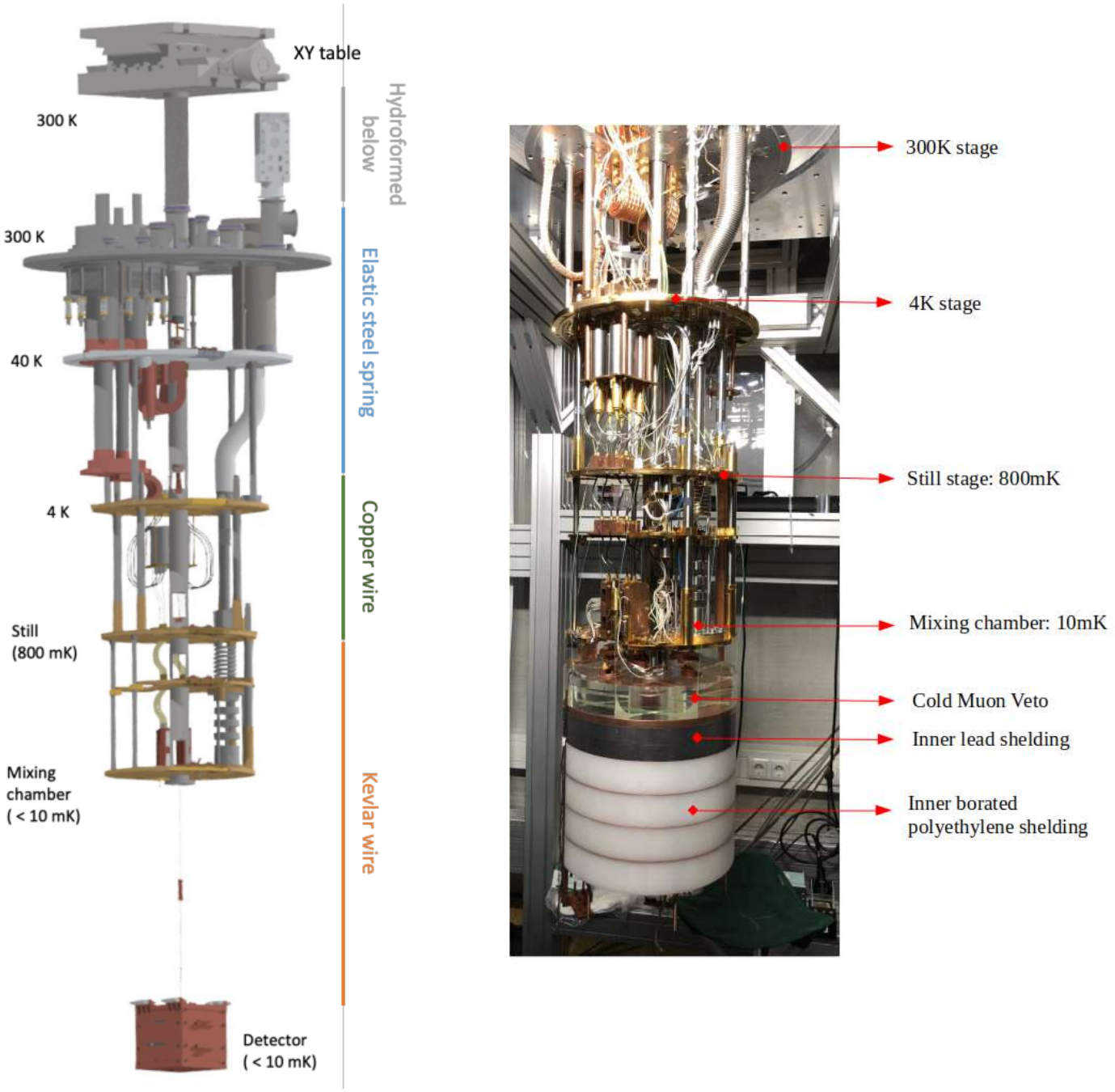

Figure 2.9. Left: Diagram of the NUCLEUS vibration decoupling system. The temperature stages and the four stages of the decoupling system are visible: a hydroformed bellow, a steel spring, a copper wire, and a kevlar wire that decouple the detector box from cryostat vibrations. Right: Picture of the NUCLEUS cryostat. The temperature stages, Cold Muon Veto, and inner shielding layers can be seen. Credits: A. Wex.

2.3.5 Cryogenic outer veto

To mitigate the residual gamma rays and neutrons in the vicinity of the detector, a Cryogenic Outer Veto (COV) covers a solid angle of 4π around the target detectors inside the cryostat. It consists of 6 high-purity germanium crystals on which electrodes have been evaporated to read the ionization signal produced when a gamma ray or neutron interacts. The geometry of the COV is as follows: two cylindrical crystals with a 100 mm diameter and 25 mm height at the top and bottom, and four parallelepiped crystals $(50 \times 74.5 \times 25)$ mm^3 on the sides, forming the cage of the COV. This cage encloses a volume of $(50 \times 50 \times 50)$ mm^3, in which the target detectors are located (see left of Figure 2.10). The COV specifications are an energy threshold below 10 keV and a time resolution better than 10 μs to maintain a reasonable dead time. This is why we use Germanium detectors, known for their fast time response and good energy resolution, resulting in a low energy threshold [104].
The complete assembly of the COV cage was finished at the end of 2024 (see right of Figure 2.10). Informations regarding the preparation, characterization, and commissioning of the COV can be found in [90, 105].

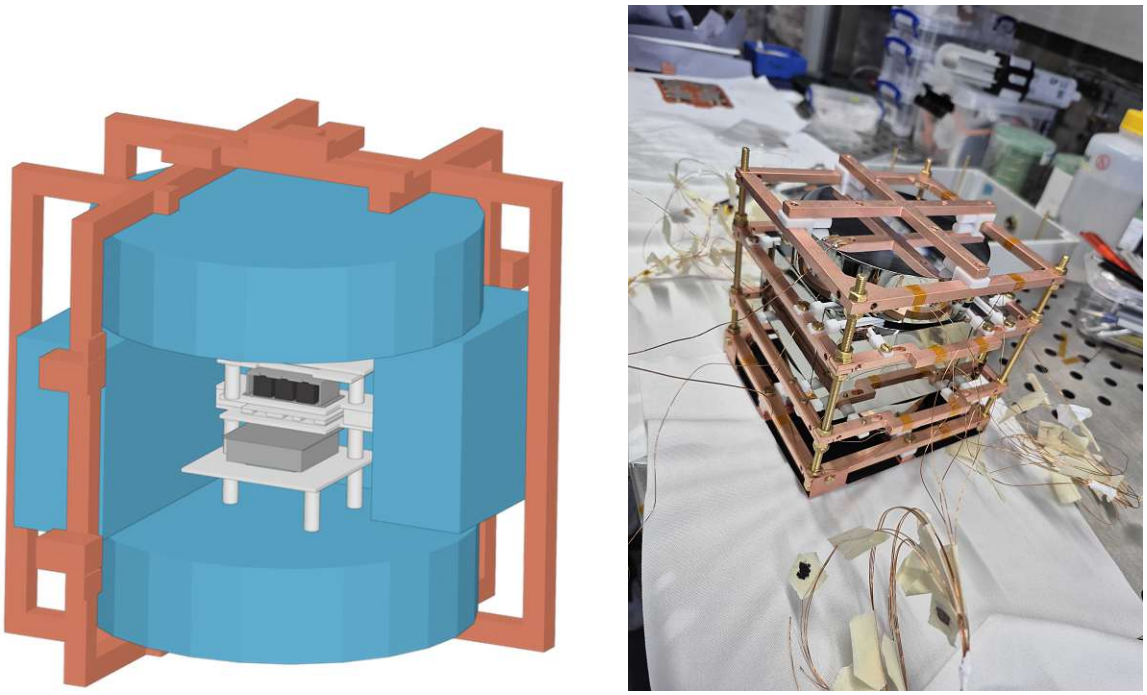

Figure 2.10. Left: 3D drawing of the COV Germanium cage (in blue) which houses the target detectors. Right: Picture of the COV crystals. Credits: A.Wex.

2.4 The NUCLEUS cryogenic calorimetric detectors

A nuclear recoil in the cryodetector target can deposit its energy through different channels: heat, ionization, and scintillation. In $CaWO_4$, being a dielectric material, only heat and scintillation are relevant. In the region of interest (ROI), at recoil energies of a few hundred eV, the scintillation light yield is negligible. Therefore, the readout channel for NUCLEUS is the phonon signal induced by the nuclear recoil, which provides a direct measurement of the recoil energy. The phonon channel enables excellent energy resolution and extremely low detection thresholds. The full detection chain is as follows:

$$\textbf{Energy} \xrightarrow{\text{NR produces phonons}} \textbf{Phonons} \xrightarrow{\text{TES temperature rise}} \textbf{Temperature} \xrightarrow{\text{TES resistance change}} \textbf{Resistance} \xrightarrow{\text{SQUID}} \textbf{Voltage}$$

In this section, I will describe the calorimeters, the corresponding thermal sensors (TES), and their settings. Finally, I will present the different calibration methods.

2.4.1 Cryogenic calorimeters

In a calorimeter, the deposited energy induces a temperature change according to the relation:

$$\Delta T = \frac{\Delta E}{C} \tag{2.4}$$

where C is the heat capacity of the absorber. In dielectrics like $CaWO_4$ and Al_2O_3, the thermal capacity is described by the Debye model [106]:

$$C = \frac{12 m \pi^4}{5M} . N_a k_B \left(\frac{T}{T_D} \right)^3 \tag{2.5}$$

where T_D is the Debye temperature, m is the mass of the crystal, M is its molar mass, and k_B is the Boltzmann constant. It is worth noting that the thermal capacity vanishes at zero temperature. This is an important property because it enables cryogenic calorimetry: at very low temperatures, a small energy deposition can lead to a measurable temperature variation. For example, a 1 g Al_2O_3 crystal with a heat capacity $C = 5.6 \times 10^{-14}$ J/K induces a temperature rise of 2.8 mK/keV. Furthermore, cooling the calorimeter allows for a larger relative temperature variation $\frac{\Delta T}{T}$. Thus, to be sensitive to small energy deposits, a low heat capacity is required, which, as shown in Equation 2.5, scales with the absorber mass. This leads to an anti-correlation between the temperature rise and the size of the crystal. Hence, to achieve the required low energy thresholds on the order of a few eV, the NUCLEUS experiment employs gram-scale crystals with millimeter-scale dimensions. Since the CEνNS cross-section scales with the target mass, the experimental strategy is to operate several crystals simultaneously. Figure 2.11 shows a $5 \times 5 \times 5$ mm^3 Al_2O_3 crystal used by the NUCLEUS collaboration, alongside a 3×3 matrix of $CaWO_4$ before cutting.

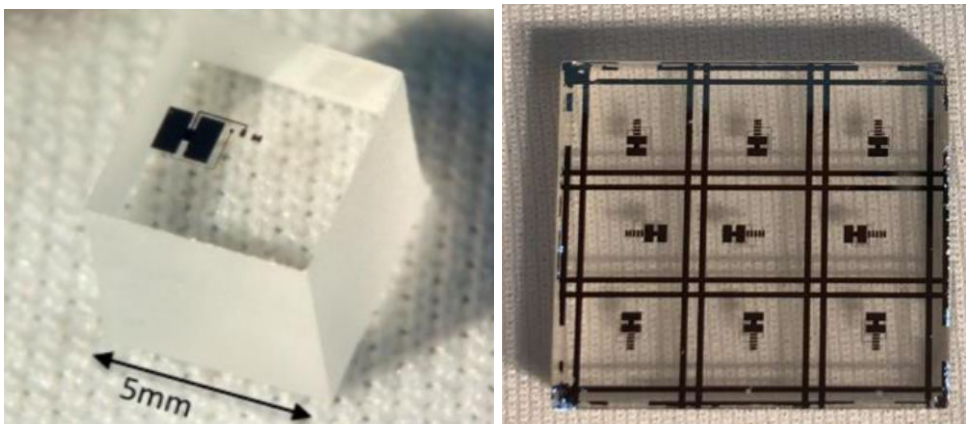

Figure 2.11. Left: A saphire (Al_2O_3) cube of $5 \times 5 \times 5, \mathrm{mm}^3$ with an evaporated tungsten TES on his surface (Picture from [107]). Right: Large $CaWO_4$ crystal. Cutting lines to produce 9 NUCLEUS detectors are visible (picture from [108]).

As depicted on the left of Figure 2.12, a cryogenic calorimeter can be modeled as an absorber with heat capacity C, in which the particle deposits its energy, a thermal sensor, and a weak thermal link with thermal conductivity G, between the absorber and a thermal bath, enabling the temperature relaxation of the absorber [107]. In this model, the response of a cryogenic calorimeter to a prompt energy deposition is is a pulse with amplitude $\frac{\Delta E}{C}$. Thus, the pulse amplitude allows for a direct measurement of the deposited energy. The decay time of the pulse is $\tau = \frac{C}{G}$. For a $CaWO_4$ crystal with a mass of 0.75 g (M = 288 g/mol, $T_D = 90\,K$, mass scaled from [109]), the heat capacity is $C = 2.3 \times 10^{-11}$ J/K. If we take a 0.7 nW/K thermal conductivity [110], we end up with a decay time of $\tau = 33$ ms, which is compatible with the pulse from real data shown in Figure 2.12.
These cryogenic calorimeters can be sensitive to small energy deposition. In theory, they can achieve very low energy resolution because the only irreducible limit on the resolution comes from thermal fluctuations between the absorber and the thermal bath: $\sigma_E^2 \sim k_B T^2 C$ [111], equivalent to sub-eV scale resolutions for the crystals we use. In practice, the energy resolution is dominated by electronic noise and vibrations transmitted to the detector.

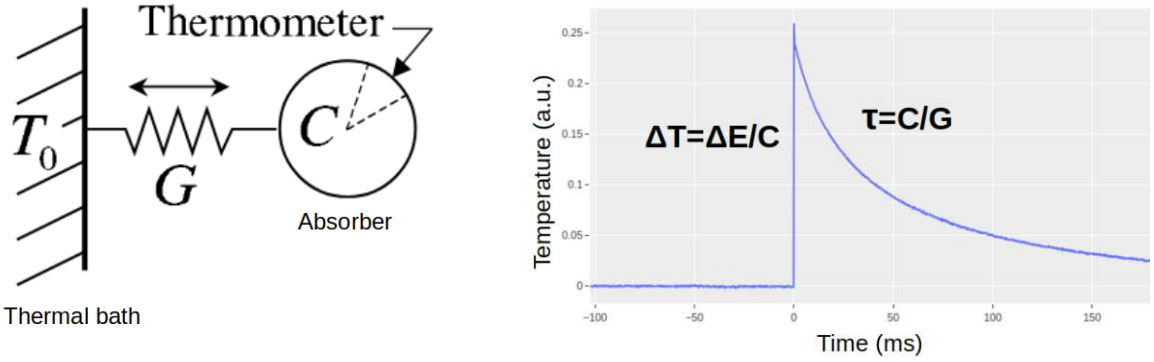

Figure 2.12. Left: Model of an ideal calorimeter with an absorber of heat capacity C, thermally coupled to a heat bath at temperature T_0 via a thermal conductance G. Adapted from [112]. Right: Pulse from data. The amplitude is proportionnal to the deposited energy, and the decay time is the ratio between the heat capacity of the absorber and the conductivity of the thermal link.

2.4.2 Cryogenic sensor: Transition Edge Sensor

A thermal sensor is needed to measure temperature variations of the absorber crystal, and several technologies exist. NUCLEUS uses a Transition Edge Sensor (TES) as a very sensitive thermometer [113]. It is a superconducting material cooled down to its transition temperature T_c. Below this temperature, the material is superconducting, and above it, it is normally conducting. The resistance curve at the transition is shown on the left of Figure 2.13. Cooled down to its transition temperature, the TES experiences a resistance variation induced by the temperature change of the absorber. In NUCLEUS, the TES is made of Tungsten, with a transition temperature of 15 mK.

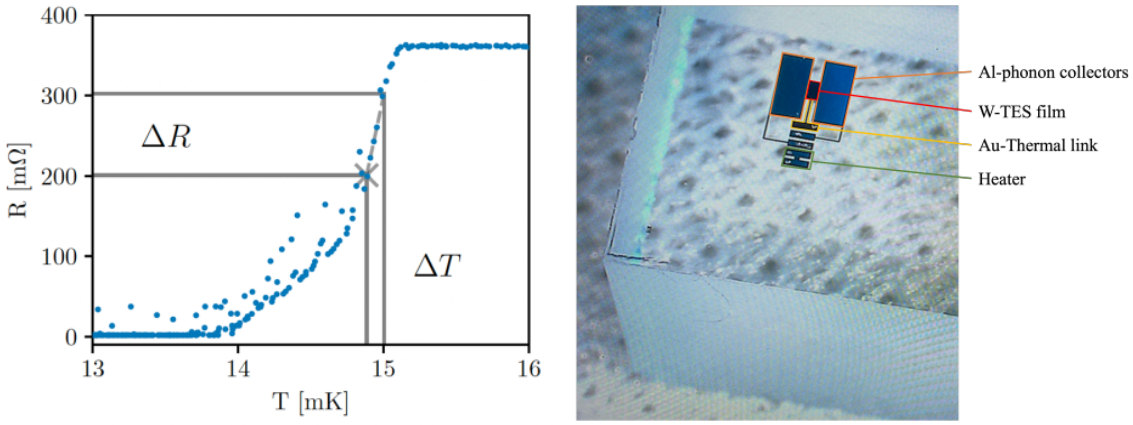

Figure 2.13. Left: Tungsten TES resistance as a function of temperature at the superconducting transition. We can see that a small temperature variation leads to a resistance variation. Figure from [107]. Right: TES design including the tungsten film, the Al-phonon collectors, the gold thermal link to the heat sink, and the heater. More details about these components in the text. Picture from [90].

The TES is cooled down to its superconducting state, and we aim to stabilize it at the operating point located in the middle of the transition curve, where the detector response is linear. To achieve this, the TES is heated both by the bias current required for its operation and by an additional constant heater current passing through an ohmic resistance deposited on the crystal surface (see right panel of Figure 2.13). This current is regulated by a proportional–integral–derivative (PID) controller. The stabilization procedure is detailed in Section 2.4.4. The sensitivity of the TES is quantified by the dimensionless parameter [114]:

$$\alpha = \frac{dR}{dT}\frac{T_0}{R_0} \tag{2.6}$$

where T_0 and R_0 are respectively the temperature and resistance at the working point. For Tungsten, we have $\alpha = 63$ [107]. Its high sensitivity allows for good energy resolution. We can see on the right of Figure 2.13 that the tungsten film is deposited (through electron beam evaporation) on the crystal and attached to Aluminum pads used to collect the phonons. The TES is connected to a gold strip weakly coupled to the heat sink to restore thermal equilibrium.

2.4.3 TES signal

The TES signal corresponds to a very small change in resistance, on the order of ~ 100 mΩ. To better understand the pulse shape induced by temperature variations, I will first detail the thermal detector model. Following this, I will describe how the SQUID readout such signal.

2.4.3.1 Thermal detector model

The model described in Section 2.4.1 is simplified. In reality, the thermometer is not perfectly coupled to the crystal, and two types of signals can be distinguished in the thermometer: phonons and electrons. The model described in [107, 109] is schematized on the left hand side of Figure 2.14. The heat capacity of the thermometer is dominated by the electron heat capacity C_e, while the phonon heat capacity C_{ph} is negligible. The thermometer is coupled to the crystal in two steps: first, there is the transmission of the crystal phonons to the TES, modeled by $G_K = \frac{1}{R_K}$, where R_K is the Kapitza resistance of the crystal-TES interface, and then the interaction of the phonons with the TES electrons, modeled by G_{ep}. Finally, the coupling of the crystal phonons with the electrons of the TES can be modeled by the thermal conductance $\frac{1}{G_{ec}} = \frac{1}{G_K} + \frac{1}{G_{ep}}$.

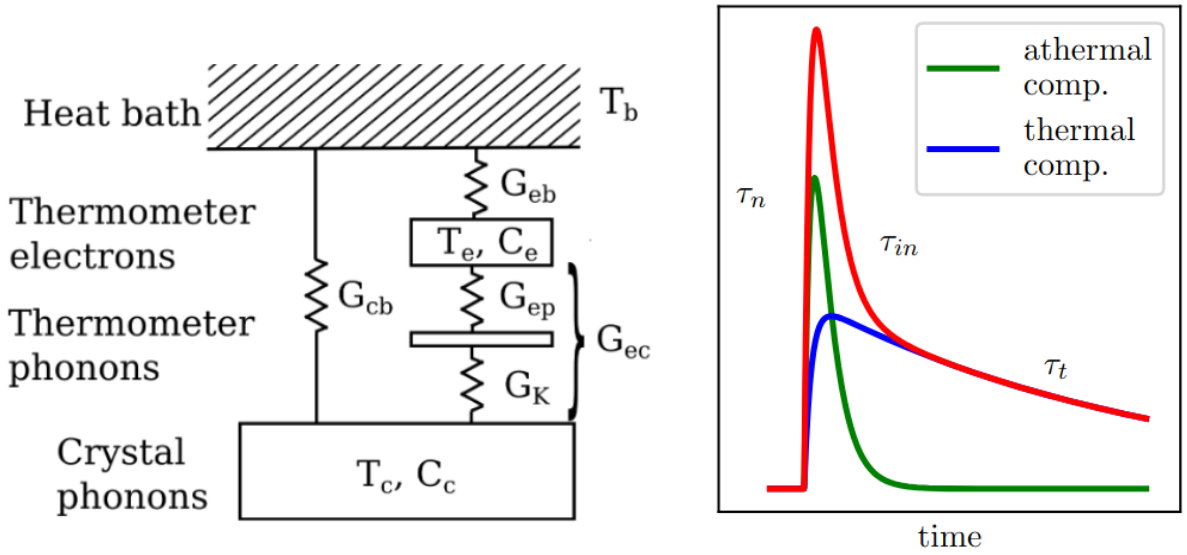

Figure 2.14. Left: thermal detector model, all quantities are described in the text. Right: pulse model for a TES in "calorimetric" mode. Figures from [107].

At low temperatures, the electron-phonon coupling is highly suppressed and therefore, we have a very low conductivity G_{ec}. Finally, the thermometer is connected to the thermal bath via a coupling G_{eb} provided by a gold stripe. The crystal can also be connected to the thermal bath via G_{cb}. This conductivity has to be negligeable for a good operation of the detector. Within this model, the response of the thermometer is as follows [109]:

$$T(t) = \Theta(t)\left[A_n\left(e^{-\frac{t}{\tau_{in}}} - e^{-\frac{t}{\tau_n}}\right) + A_t\left(e^{-\frac{t}{\tau_t}} - e^{-\frac{t}{\tau_n}}\right)\right] \tag{2.7}$$

We can see two terms: a fast component $A_n(e^{-\frac{t}{\tau_{in}}} - e^{-\frac{t}{\tau_n}})$ and a slow component $A_t(e^{-\frac{t}{\tau_t}} - e^{-\frac{t}{\tau_n}})$. $\Theta(t)$ is the Heaviside function. This pulse shape is plotted on the right of Figure 2.14. Let's break down these terms

using the thermal model. When a particle deposits energy in the crystal absorber, high-frequency optical phonons are generated, which then decay to ballistic phonons at around a hundred GHz. These phonons are very energetic and are referred to as "athermal". Following collisions in the crystal and reflections on the surfaces, these phonons thermalize within a few milliseconds. Some athermal phonons can hit the aluminum pads and be collected before they thermalize in the crystal. These phonons have enough energy to break a Cooper pair in the aluminum and bypass $G_{ec} \approx 0$, leading to free electrons that can heat the W-film, thus producing the fast component of the TES signal. Afterward, the temperature of the thermometer relaxes to equilibrium through its coupling to the heat bath, the fast decay time is then:

$$\tau_{in} = \frac{C_e}{G_{eb}} \tag{2.8}$$

As for the phonons that thermalize in the crystal, they heat it up. Despite the small conductivity G_{ec}, the TES thermometer remains sensitive to the increase in the temperature of the crystal, which corresponds to the slow component with a decay time:

$$\tau_t = \frac{C_c}{G_{ec}} \tag{2.9}$$

Finally, the signal rise time τ_n results from a competition between the film thermalization time τ_f (time to collect phonons) and the crystal surface thermalization time τ_c (time for phonons to thermalize) [85]. There are two possible cases:

- $\tau_{in} < \tau_n$: The TES reaches equilibrium before the end of the input signal. The detector is fast enough to measure the heat power input during a particle interaction. This is called "bolometric" mode.
- $\tau_n < \tau_{in}$: The TES reaches equilibrium after the end of the input signal. The detector is slow enough to integrate all the energy deposited by a particle. This is called "calorimetric" mode, which is the one used by NUCLEUS.

In this calorimetric mode, the total amplitude is proportional to the energy deposited:

$$A_n + A_{th} = \frac{\Delta E}{C_e} \tag{2.10}$$

We also have $A_{th} = \frac{1-\epsilon}{\epsilon} A_n$, where ϵ is the proportion of athermal phonons collected by the TES and thus depends on τ_f and τ_c by the relation [109]:

$$\epsilon = \frac{\tau_c}{\tau_c + \tau_f} \tag{2.11}$$

2.4.3.2 SQUID readout

The TES signal is a resistance variation that needs to be measured with an accuracy of a few milliohms. Since the currents must remain below 10 μ A to avoid overheating the crystal, the only option is to use a Superconducting Quantum Interference Device (SQUID) [115], which allows for converting magnetic flux into voltage. The readout circuit converting resistance into magnetic flux is presented on the right of Figure 2.15. A bias current I_B is split into a shunt resistance R_S and the TES. In series with the TES is a coil L_{in}. A variation in the resistance of the TES causes a change in current in the branch, and therefore in the coil. The magnetic flux generated by the coil is then measured using a SQUID. A SQUID is a superconducting ring broken by two Josephson junctions [115, 116]. The current-voltage characteristic of a SQUID is a modulated signal with a period equal to one magnetic quantum flux, as seen on the left of Figure 2.15. To linearize the SQUID response, a "flux-locked loop" (FLL) circuit is used [117]. This consists of a feedback coil in which a current is passed, adjusted so that the SQUID voltage remains at zero. Thus, the FLL output signal is the feedback voltage, proportional to the magnetic flux being measured. If the input signal changes very rapidly and by more than half a magnetic flux quantum ϕ_0, the flux-locked loop may jump to the next working point. We refer to this as a “Flux Quantum Loss”, because the difference between the input and feedback flux changes by one ϕ_0. After the particle event, when the input flux returns to its steady-state value—the SQUID output voltage will be shifted by approximately 1 V resulting in a baseline jump in the recorded pulse.

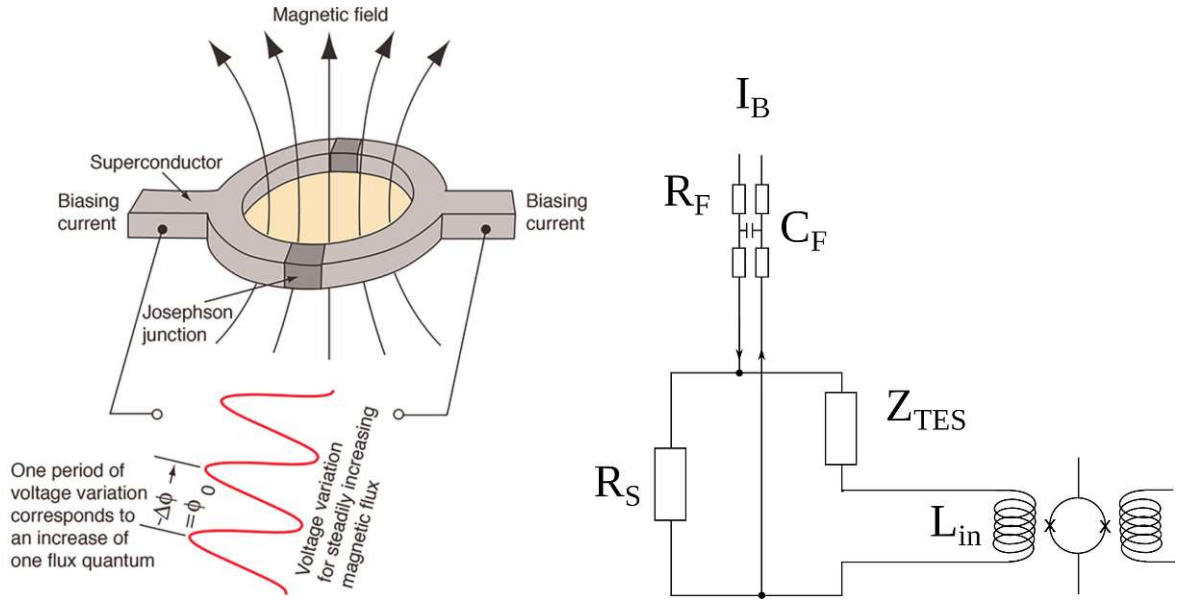

Figure 2.15. Left: SQUID made of a superconducting ring broken by two Josephson junctions. The SQUID voltage versus the magnetic flux in the loop is periodic with a period equal to one flux quantum. Figure from [118]. Right: Electrical readout circuit.

2.4.4 Heater pulses for stabilization

The TES is cooled by the cryostat to a temperature below its transition temperature. Therefore, it needs to be slightly heated. This is done through electrothermal feedback, caused by the heater DC current that heats the TES via the Joule effect. We should fine-tune the heater DC current to place the working point in the middle of the transition. A variable current is sent through a resistance called the "heater" (see right of Figure 2.13). This way, we can send heater pulses of different amplitudes.

There are two types of heater pulses:

- Control pulses: Heater pulses that meant to reach saturation up to the normal conducting phase for a direct measurement of the position of the working point of the TES in the transition. The crystal's response to a control pulse of fixed amplitude gives us information about the initial working point in the transition and can be used as input for a PID control loop on the heater current. This way, the TES temperature can be stabilized against drifts.

- Test pulses: Heater pulses with various amplitudes from near the threshold up to the saturation level. This is used to monitor the linearity and time stability of the detector.

Once the working point is stabilized and the response to the test pulses does not drift, we can achieve a robust energy calibration, providing stable gain during a data-taking segment.

2.4.5 Energy calibration

The energy calibration of cryogenic detectors is crucial for the study of CEνNS and is a challenge for NUCLEUS. A standard method is to use the Mn K_α and K_β lines at 5.9 and 6.5 keV$_{ee}$, respectively, from the decay of ^{55}Fe following electron capture. A ^{55}Fe source is therefore placed inside the detector box. This method has the advantage of being simple to implement experimentally, and the two peaks appear clearly in the energy spectrum. However, it only provides two calibration points that are relatively close in energy, and extending this calibration to lower energies in the sub-keV region assumes that the detector is linear (which is not guaranteed). Furthermore, this method calibrates electron recoils rather than nuclear recoils, so it must be assumed that there is no difference in the detector's response to electron and nuclear recoils. Finally, the interactions of emitted gamma rays mostly occur near the detector surface, which can introduce an additional calibration bias.

Other methods for lower energy calibration are being developed by NUCLEUS. The use of X-ray fluorescence sources, such as copper, aluminum, silicon, and fluorine fluorescence, provides calibration peaks between 677 eV and 6.4 keV [119, 120]. Another method is to use a monochromatic LED source. The photon statistics emitted by the source allow the delivery of multiple "packets" of photons to obtain several calibration peaks accross the full region of interest. The application of this method for the First Commissioning Run of NUCLEUS is detailed in Chapter 4.

All of these previous methods do not calibrate nuclear recoils. A new innovative method has been developed: Calibrated Recoil for Accurate Bolometry (CRAB), which allows for the calibration of low energy nuclear recoil O(100 eV) in all the crystal [9, 121]. This method is presented in Chapter 5.

2.5 Simulation framework: Choozerent

The simulation of the NUCLEUS experiment plays a crucial role, as in all low-background experiments. Its main objective is to provide benchmarks for the expected background and to validate its rejection through the NUCLEUS setup, which includes both active and passive shielding components. Particles are propagated through the NUCLEUS geometry using Monte Carlo simulations based on the GEANT4 toolkit [122–124]. The GEANT4 simulation process consists of several steps. First, a primary event is generated with a defined initial position, energy, and direction. The particle is then transported through the implemented detector geometry. A step-by-step tracking approach enables precise description of the particle trajectory and the energy it deposits in the different materials.

The NUCLEUS simulation code Choozerent, written in C++, integrates the GEANT4 toolkit with the ROOT analysis framework [125], allowing for the storage and post-processing of all relevant simulation variables. The NUCLEUS geometry is implemented within Choozerent, and users can select the appropriate physics lists depending on the simulated particles, the materials in the geometry, and the physical processes being studied. This choice is particularly important for estimating the background in a specific energy region of interest. Neutron-induced backgrounds, require modeling of hadronic interactions, for which the G4HadronPhysicsShielding physics list is used. For electromagnetic interactions, such as those induced by muons or secondary particles, the Livermore physics list is employed. All benchmark simulations for background predictions in NUCLEUS are performed using Choozerent. Although I was not directly involved in the development of the simulation framework for NUCLEUS, I contributed by simulating the exposure of the Muon Veto system to cosmic muons (see Section 3.5).

The predicted background budget for NUCLEUS is shown in Table 2.1 after reduction by active and passive shieldings. We end up with a background level of 235 d.r.u in the [10-100] eV region. In this range, the CEνNS signal is expected to be at 355 d.r.u assuming a 100% reactor duty cycle leading to a signal-to-noise ratios of 1.5. These simulations validate the NUCLEUS shielding strategy for background mitigation. The various contributions to the residual background are shown in the pie chart on the Figure 2.16. As expected, the dominant source of residual background is atmospheric neutrons, due to the shallow overburden at the VNS site.

These results are only based on simulations; however, a measurement of the reactor-OFF background will be essential to support a robust CEνNS observation. Furthermore, the simulation includes only physical background sources. Another significant background, not of particle origin, has been identified in the region of interest. This excess, referred to as the Low Energy Excess (LEE), will be described in the next section.

	Background source	**Rate in [10-100] eV (d.r.u)**
Background	Atm. muons	< 22.0
	Atm. neutrons	214 ± 9
	Env. gamma rays	$10 \pm 5.$
	Material radioactivity	12 ± 2
	Total	235 ± 10
CEνNS 100%		355

Table 2.1. Residual counting rates for all background sources are presented in d.r.u. (events per kg $\cdot$ day $\cdot$ keV). The predicted CEνNS signal is also shown, assuming continuous reactor operation (100% duty cycle). Table adapted from [126].

2.6 Low Energy Excess

In all cryogenic experiments capable of reaching low thresholds, an excess of events in the region of a few hundred eV has been observed [127]. This excess is above the expected CEνNS signal by several orders of magnitude. This is why shared efforts between different cryogenic collaborations have taken place in recent years to understand the origin of the LEE and to mitigate this unexpected background source. A dedicated annual workshop, "EXCESS," has been set up. As shown in Figure 2.17, the excess observed in several experiments exhibits a characteristic exponentially rising spectrum at low energies. It has been demonstrated that the LEE is not of particle origin, as its event rate decreases over time after cooldown, following an exponential decay with both fast and slow components. Moreover, the warmup resets the LEE to a higher rate [128]. It has been shown that one of the sources of the LEE is related to the mechanical stress induced by thermal contraction during cooldown, either in the bulk of the crystal or at its interfaces with the holder of the sensor [129, 130].

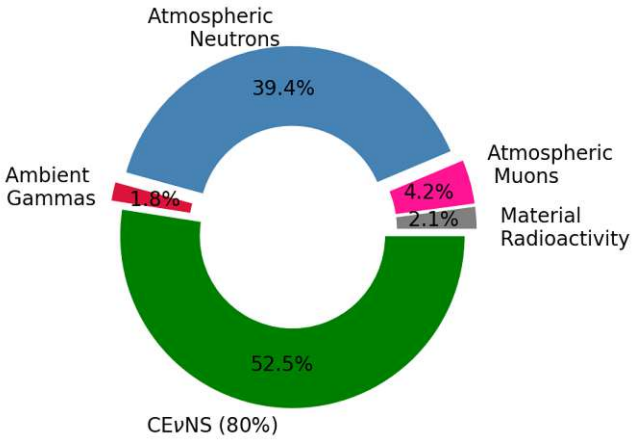

Figure 2.16. Pie chart of the different source of signal and background after passive and active shielding. Credits: C.Goupy.

The Edelweiss and Ricochet collaborations have demonstrated that this LEE is only visible in the heat channel and not in the ionization channel. Their double readout of ionization and phonons provides efficient discrimination against LEE events above the ionization detection threshold [131].

In NUCLEUS, only the phonon channel is readout, so a different strategy is developed to mitigate the LEE background. A first approach is to use a crystal with two TES. This double readout mode allows rejecting events caused by mechanical stress at the interface between the TES sensor and the crystal surface which are seen by only one of the TES, while events induced by particle interactions that occur in the bulk of the crystal are seen by both TES. This method has been the subject of R&D and demonstrated the ability to reject a fraction of LEE events [132–134]. A second option is to use an active support for the target crystals: the Inner Veto, which could be sensitive to events induced by mechanical constraints on the crystal surface.

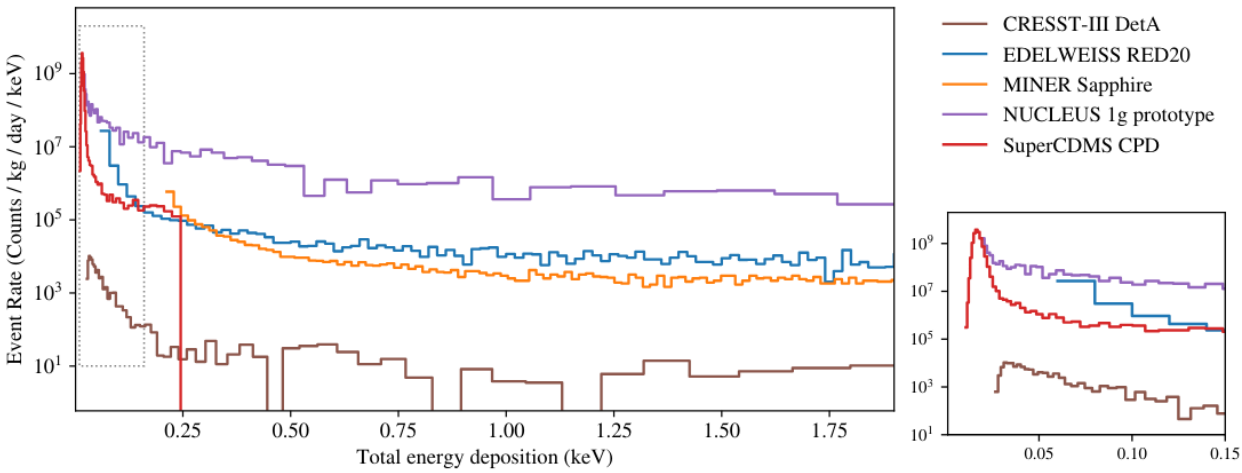

Figure 2.17. Energy spectra from different collaborations. We can see the LEE rising at very low energy. LEE is far above the CEνNS signal expected at O(10^3) dru. Figure from [127].

2.7 Inner Veto

The Inner Veto is an instrumented holder for the crystals, covering a 4 π solid angle around the detector surface. Figure 2.18 shows a mockup; it consists of silicon plates and two silicon wafers placed just above and below the 9 crystals. The first is a thick wafer, while the second is a thin wafer and therefore more flexible. The contact points with the crystals are pyramidal in shape, and sapphire balls are used at the contact points between the silicon wafers and the holding plates [135]. This mockup has shown its robustness against the thermal contraction of the materials over successive cooldowns. The Inner Veto is instrumented with a TES and operated in anticoincidence with the cryodetectors. It allows vetoing α and β decay events occurring on surfaces, which deposit part of their energy in the crystal and the rest in the Inner Veto [85, 135]. The Inner Veto must also be capable of rejecting LEE events originating from mechanical stress at the contact points with the crystal. The operation of the crystals and the Inner Veto simultaneously is still under R&D.

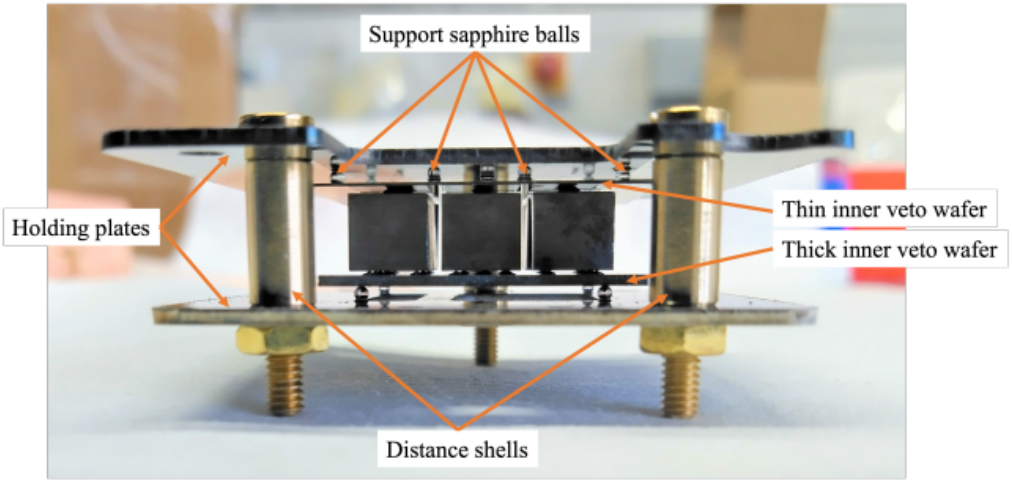

Figure 2.18. One array of nine crystals mounted in an instrumented holder: the Inner Veto. Credits: N.Schermer [135].

2.8 Schedule of NUCLEUS

In this section, I detail the schedule of NUCLEUS and the different phases. After a blank assembly in Munich at the Technical University of Munich (TUM), NUCLEUS is currently being dismantled to be relocated to the VNS at Chooz.

2.8.1 Blank assembly at Munich: First Commissioning Run

In order to validate the background rejection, we conducted a blank assembly in Munich at the UnderGround Laboratory (UGL) [136]. The UGL benefits from 15 m.w.e shielding against cosmic radiation thanks to 6 meters of gravel and soil (see Figure 2.19). The goal was to commission each detector individually and to operate the cryodetectors in anticoincidence with all veto systems before relocating to Chooz. This blank assembly led to the First Commissioning Run (FCR) of NUCLEUS during summer of 2024 (see Figure 2.20). Part of my thesis was dedicated to the commissioning of the Muon Veto, which is discussed in Chapter 3. My works on the preparation of the FCR and subsequent analysis results are presented in Chapter 4.

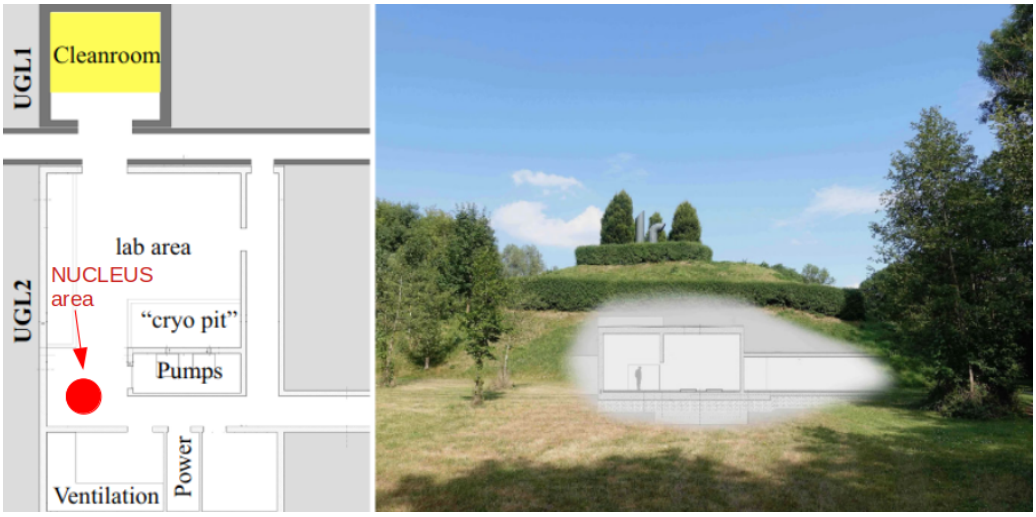

Figure 2.19. Left: Top view of the UGL, showing the NUCLEUS area. Right: Hill beneath which the UGL is located, providing 15 m.w.e shielding. Figure from [136].

2.8.2 Future of NUCLEUS

Currently, the NUCLEUS experiment is in its relocation phase. Once installed at Chooz, a technical run will be conducted at the VNS. While the schedule is subject to potential adjustments, the plan is to operate a Minimal Detector Module consisting of four $CaWO_4$ cubes equipped with dual TES sensors, all housed within the full COV cage. The total target mass is 6.7 g. This phase aims to provide an on-site background measurement, especially in the keV energy region, to validate the background rejection using both passive and active shielding, and to demonstrate the achievable background level. This will serve as a valuable benchmark for simulations. In addition, a measurement of the LEE rate and its rejection efficiency using the double-TES configuration will be investigated. In parallel, R&D on the Inner Veto system will take place in Munich. Due to the limited target mass, the signal statistical is low, limiting the sensitivity to CEνNS. Thus, significant reactor OFF-OFF data is required to extract a meaningful signal. Therefore, a CEνNS detection is rather foreseen for the upgraded NUCLEUS-100 g phase, which will use 18 detectors of $1 \times 1 \times 1\,\mathrm{cm}^3$.

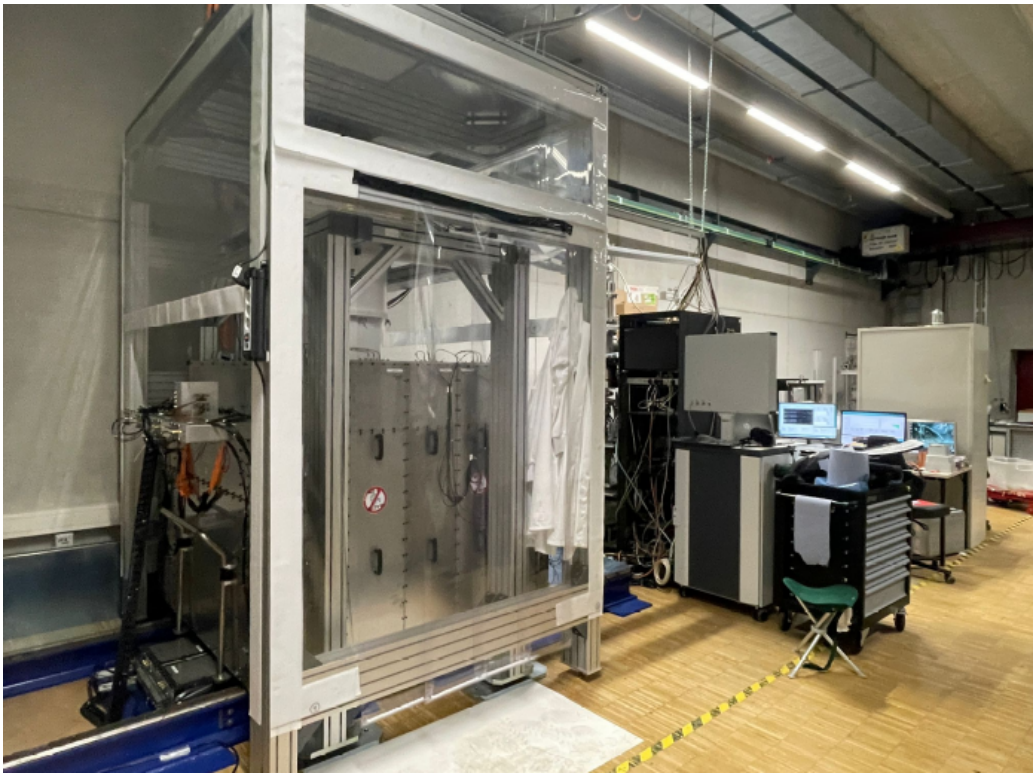

Figure 2.20. Picture of the NUCLEUS experimental setup in the UGL for the First Commissioning Run.

3

The NUCLEUS Muon Veto

As explained in Chapter 2, cosmic muons can induce spallation reactions in the lead shielding and generate neutrons with energies of a few keV, which can reach the target detectors and mimic the CEνNS signature. Therefore, a Muon Veto is needed to suppress such background. The Muon Veto modules were first designed at CEA Saclay where they were tested individually before assembly in Munich in December 2022 and commissioned before the First Commissioning Run. Finally, the Muon Veto has been installed at the Very Near Site beginning of 2025 (see Figure 3.1). In this chapter, after detailing the interaction of muons with matter (Section 3.1), I present the different components of the NUCLEUS Muon Veto (Section 3.2), the key parameters used to quantify the performance of the panels (Section 3.3), and the installation in Munich in the final cubic configuration, which covers almost the entire solid angle around the cryodetector (Section 3.4). Then first comparisons with simulations are presented (Section 3.5). All those steps led to the final commissioning of the Muon Veto during the First Commissioning Run(FCR) (Sections 3.6 and 3.7). The chapter ends with the Muon Veto installation at the Very Near Site (Section 3.8).

Figure 3.1. Schedule of the NUCLEUS Muon Veto (MV).

3.1 Cosmic muons through matter

3.1.1 From the scintillation mechanism...

The muon, like any charged particle, undergoes "electronic energy loss" when passing through a scintillator via ionization or excitation during collisions with the absorber's electron cloud. For thick absorbers such as scintillators, energy is deposited through a series of collisions with the medium's electrons resulting in scintillation light. We can define W, the average energy lost in a single collision transferred to an electron (W $<$ 100 eV). The interaction of a muon with free electrons is described by the Rutherford differential cross-section [33]:

$$\frac{d\sigma_R(W,\beta)}{dW} = \frac{2\pi r_e^2 m_e c^2}{\beta^2} \frac{1-\beta^2 \frac{W}{W_{max}}}{W^2} \tag{3.1}$$

where $W_{max} \approx 2m_e c^2\beta^2\gamma^2$ is the maximum energy transferable to a single collision, r_e is the classical electron radius, m_e is the electron mass, $\beta = \frac{v}{c}$ with v being the muon's velocity and c the speed of light and $\gamma = \frac{1}{\sqrt{1-\beta^2}}$ the Lorentz factor. In reality, electrons in matter are not free, one has to take into account the electronic binding with the correction factor B(W) from Born theory [137]:

$$\frac{d\sigma_B(W,\beta)}{dW} = \frac{d\sigma_R(W,\beta)}{dW} B(W) \tag{3.2}$$

The number of collisions with an energy loss between W and W+δW is given by: $N_e \delta x (\frac{d\sigma}{dW}) dW$, where N_e is the electron density of the scintillator and δx its thickness. We can define the moments as follows:

$$M_j = N_e \delta x \int W^j \frac{d\sigma_B(W,\beta)}{dW} dW \tag{3.3}$$

M_0 is the average number of collisions in the thickness δx and M_1 is the average energy deposited in this same thickness. M_1 is similar to the mass stopping power well described by the Bethe equation for intermediate-Z materials and in the region $0.1 < \beta\gamma < 1000$ [33]:

$$< -\frac{dE}{dx} >= 4\pi N_e r_e^2 m_e c^2 \frac{1}{\beta^2}\frac{Z}{A}\left[\frac{1}{2} ln(\frac{2m_e c^2\beta^2\gamma^2 W_{max}}{I^2}) - \beta^2\right] \tag{3.4}$$

where I is the mean excitation energy, Z and A are respectively the charge number and the atomic mass of the medium. We can consider that most cosmic muons are at minimum ionization, so the relevant value is $< \frac{dE}{dx} >_{min}$. Actually, the mean rate of energy loss is not that accurate in describing the energy deposited by muons, as it is affected by rare events with high energy deposition. We instead use the Most Probable Value (MPV) of energy loss. Additionally, there are some fluctuations in the energy loss described in Section 3.1.2.

3.1.2 ...toward the Landau-Vavilov distribution

In a thin absorber, the probabilistic treatment of successive collisions between a muon and the electrons in the medium leads to fluctuations in the energy loss. The energy loss probability distribution in a detector with thickness x is well described by the Landau-Vasilov distribution [138, 139]. The most probable value Δ_p of this distribution is given by [140]:

$$\Delta_p = \xi\left[ln(\frac{2m_e c^2\beta^2\gamma^2}{I}) + ln(\frac{\xi}{I}) - \beta^2 + 0.2\right] \tag{3.5}$$

where $\xi = \frac{Kx<Z>}{2\beta^2<A>}$ with x the thickness of the absorber and $K = 4\pi N_e r_e^2 m_e c^2$ with N_e the electron density of the medium.

It should be noted that this is a theoretical distribution that needs to be weighted by other physical effects to get the actual energy deposition spectrum in a scintillator. Indeed, due to their interactions with the material, muons will have different paths in the scintillator. More importantly, the angular distribution of the cosmic muon flux induces different thicknesses of scintillator traversed (see Figure 3.2). Measurements have shown that the angular distribution of the muon flux follows a $cos^2\theta$ law [141–143]. There are also "clipping muons" (shown in red in Figure 3.2) that traverse only a small thickness of the scintillator. Figure 3.3 shows an example of simulated energy spectrum deposited by cosmic muons passing through a scintillator block with a thickness of 5 cm. This spectrum accounts for the different orientations of the incident muons and possible clipping.

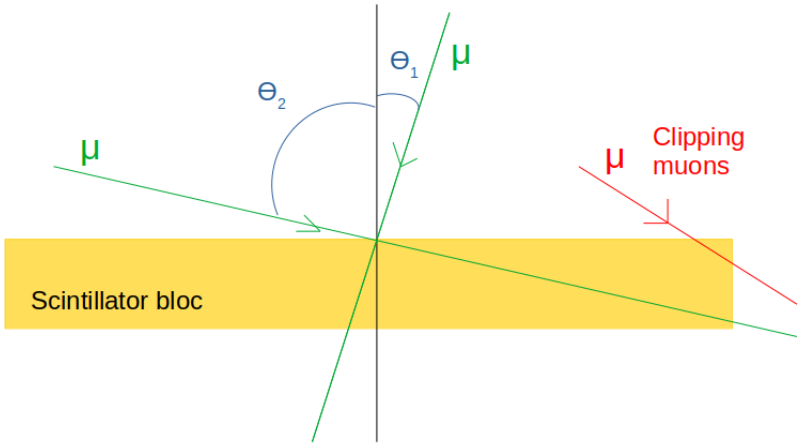

Figure 3.2. Example of different paths taken by muons in a scintillator block. Also shown the 'clipping' of muons that traverse a corner of the scintillator.

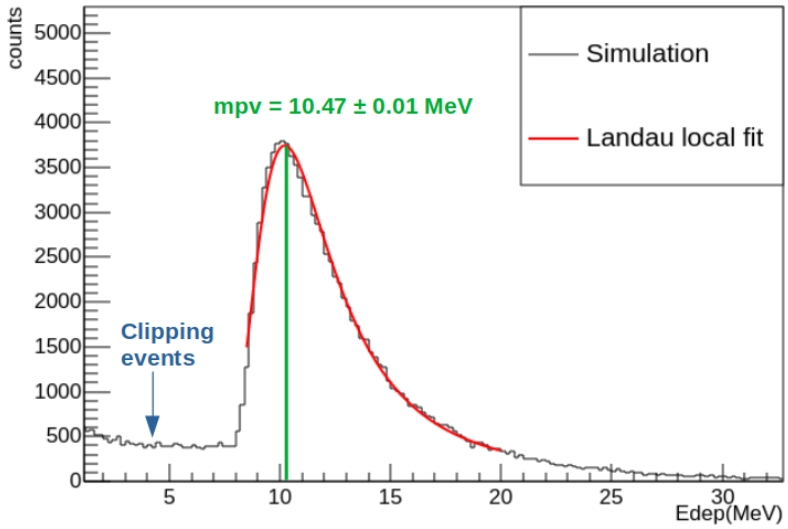

Figure 3.3. Spectra of energy deposited including clipping muons traversing a corner of the scintillator. Also shown the Landau fit with the most probable value (mpv).

3.2 Presentation of the NUCLEUS Muon Veto

3.2.1 Specifications

The Muon Veto must fulfill specific design and performance requirements, which are summarized here. The first requirement is the muon rejection efficiency, which must exceed 90% to ensure sufficient suppression of muon-induced backgrounds. This demands an angular coverage close to 4π around the cryogenic detector, requiring a hermetic geometry. Each muon passing through the veto must be efficiently detected, which is why plastic scintillators are used — they must provide both a good light yield and efficient light collection. Additionally, the system must maintain a low dead time, below 10%, which necessitates minimizing the muon rate and favors a compact geometry. Consequently, the Muon Veto must form a fully enclosed cube around the cryogenic detectors, as shown in left of Figure 3.4. This dead time constraint also requires the ability to

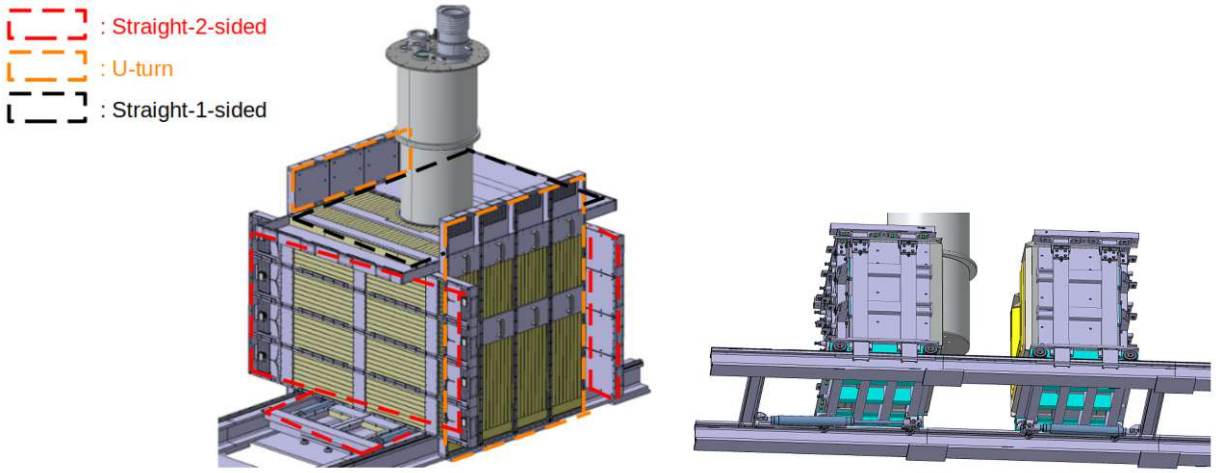

Figure 3.4. Left: Final design of the NUCLEUS Muon Veto. We can see the 28 scintillator panels in yellow, covering the largest solid angle around the crystal target detector inside the cryostat. The optical fiber configuration for all panels is distinguished by dashed outlines (see Section 3.2.2.1). Right: Support structure of the Muon Veto sliding on rails.

discriminate muon events from ambient gamma rays up to 2.6 MeV, so that only muon-induced events are vetoed. For this purpose, thick scintillators (∼5 cm) are used. A Figure of Merit for this criterion will be introduced in Section 3.3.2. To allow access to the cryostat, the Muon Veto is split into two half-cubes mounted on rails, enabling the structure to slide open when needed (see right of Figure 3.4).

3.2.2 Panel description

To meet the design specifications, the Muon Veto consists of 28 panels arranged to form a cube around the cryostat. Each panel is composed of a 5 cm thick plastic scintillator block equipped with wavelength-shifting (WLS) fibers that guide the scintillation light, induced by the passage of a particle (e.g., μ, γ, etc.), towards one or two Silicon Photomultipliers (SiPMs).

3.2.2.1 Plastic scintillator read out by WLS fibers

The scintillator is made of polyvinyltoluene-based BC-408 with characteristics listed in Table 3.1. Such a scintillator produce $\sim 10^4$ photons per deposited MeV. Considering that muons are at minimum ionization, they should deposit an average energy of 10 MeV through the 5 cm thickness of the module, producing approximately $\sim 10^5$ photons. Nine grooves separated by a distance of 30 mm were carved into the surface of each scintillator panel to accommodate wavelength-shifting (WLS) fibers. These fibers are designed to capture the primary blue scintillation light produced by incident particles such as muons or gammas. The WLS material becomes excited and re-emits light isotropically in the green wavelength range, where the SiPMs have a higher detection efficiency. A portion of this green light is then guided toward the SiPMs through total internal reflection within the fiber. This requires the fiber core refractive index n_1 to exceed that of the scintillator plastic n_0, and only rays with an incidence angle θ greater than the critical angle $\theta_c = arcsin(\frac{n_1}{n_0})$ will undergo total internal reflection. To relax this condition and improve light trapping, graded-index fibers are employed. To ensure optimal optical coupling between the fibers and the SiPMs, we applied optical grease at each interface. The optical fibers used in the

system are multi-clad fibers from Saint-Gobain [144]. They are responsible for the light collection efficiency of the scintillator. There are several possible configurations for arranging the WLS fibers: **straight-2sided**, **u-turn**, and **straight-1sided**. A schematic illustration of these configurations, along with some photographs, is shown in Figure 3.5.

In the **straight-2sided** configuration, there is 9 fibers crossing the panels connected at each extremity to one SiPM. This configuration provides the best light collection efficiency. It is used for the four bottom panels $(25.9 \times 5.0 \times 124.3)$ cm^3 and the eight left/right side wall panels $(28.2 \times 5.0 \times 118)$ cm^3. For the eight front and rear panels $(24.3 \times 5.0 \times 125.4)$ cm^3, which are positioned along the sliding rails, no SiPM is placed at the bottom. Instead, this area is covered entirely with scintillating material to preserve the hermeticity of the Muon Veto. To maintain good light collection, a **u-turn** configuration is employed. In this setup, four of the five WLS fibers are bent back into a loop (U-shape), while the central fiber remains straight. All fibers are read out at one end by a single SiPM. Studies of the panel response revealed some local inhomogeneities in the light collection, with variations on the order of 10%, which were acceptable. Finally, for the top modules, smaller scintillator panels are used to allow the Muon Veto cube to open. This design constraint eliminates the possibility of using either **straight-2-sided** or **u-turn** configurations. Instead, a **straight-1sided** configuration is adopted, where all 9 fibers are read out from only one end by a SiPM. The reduced size of these panels compensates for the loss of light at the other fiber ends. Although light collection efficiency varies across the different fiber configurations, it has been demonstrated to be sufficient in all cases [97].

Material	polyvinyltoluene
Atomic composition	$[CH_2CH(C_6H_4CH_3)]_n$
Density (g/cm^3)	1.032
$< Z/A >$	0.54141
$\frac{dE}{dx}$ $(MeV \cdot cm^2/g)$	1.956

Table 3.1. Characteristics of polyvinyltoluene [145].

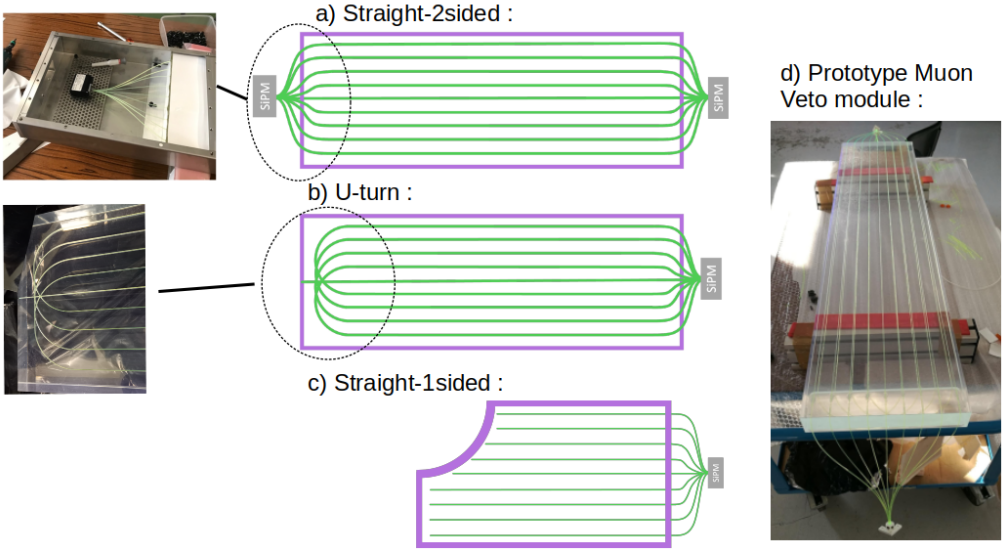

Figure 3.5. a–c) Schematic views of Muon Veto panel with different fiber configurations: **straight-2sided**, **u-turn**, and **straight-1sided** (Credit: C. Goupy). d) Photograph of a Muon Veto module [97].

3.2.2.2 SiPM

The light sensors we use are Silicon PhotoMultipliers (SiPM) PE3325-WB-TIA-SP from KETEK [96]. They are made of arrangement of 13920 Single Photon Avalanche Diodes (SPAD) of dimension 25×25 μm^2; forming a 3×3 mm^2 active area. Each SPAD is a silicon p-n junction, creating a depletion region as depicted in Figure 3.6. When a photon passes through the depletion region, a current is generated. At the microscopic level, the current generation is due to the absorption of a photon in the silicon, resulting in the creation of an electron-hole pair at the junction by photoelectric effect. This is called a PhotoElectron (PE). Under the influence of a strong electric field in the junction, the primary electron-hole pair triggers an ionization cascade. The charge collection with electrode allows to measure the generated current. Consequently, the SPADs operate in Geiger mode. In this mode, the depletion zone becomes an avalanche zone. We lose information about the energy of the incident photon, but we can accurately count the number of scintillation photons reaching the SiPM. This count is proportional to the energy deposited by the incident particle, taking into account the light yield, the light collection and the quantum efficiency of the SiPM. A voltage called the breakdown voltage V_{break} generates the necessary electric field to operate in Geiger mode. In addition to this voltage, we can apply an overvoltage ΔV(**controle voltage**) that will increase the gain of the SiPM. Then, the bias voltage applied is $V_{bias} = V_{break} + \Delta V$. In our case we apply V_{break} =**5V** and ΔV =**0.81V** as controle voltage.

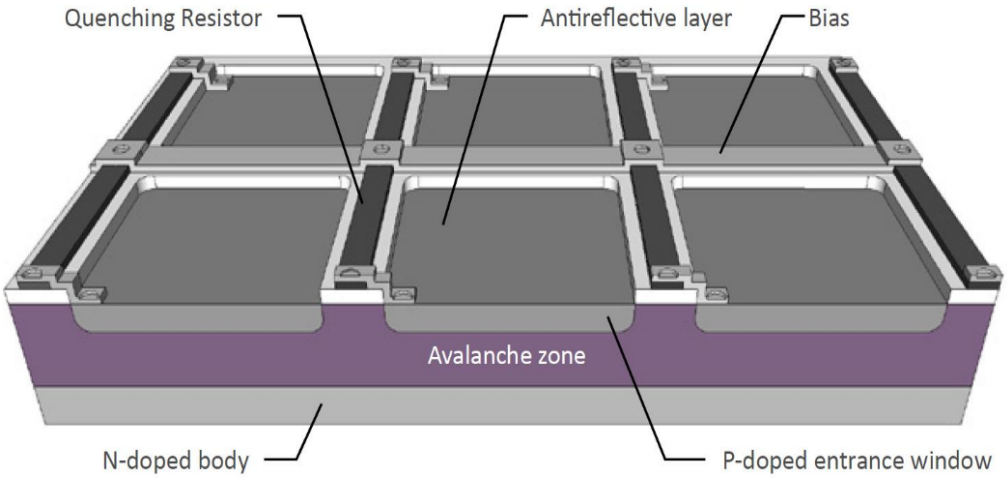

Figure 3.6. Schematic of a SiPM composed of several SPADs. Each SPAD consists of a silicon p–n junction that forms an avalanche zone. Figure from [146].

3.3 Muon Veto tests at Saclay

Before the blank assembly in Munich, all modules were tested individually in Saclay. The tasks included calibrating the SiPMs, testing the performance of the modules, and developing the initial analysis scripts to calculate the parameters useful for monitoring the Muon Veto. It should be noted that at Saclay, the modules were not arranged in a cubic configuration but were placed horizontally on a test bench.

3.3.1 SiPM calibration

When a photon hits a cell of the SiPM, a photoelectron may be created, and the output current of the SiPM is measured. The calibration of the SiPM allows converting the measured charge or amplitude into the number of detected photons, which are photoelectrons: N_{PE}.

3.3.1.1 Dark count rate and SPE spectrum

To calibrate the SiPM, I use the Dark Count Rate (DCR) of the SiPM. This is the output signal of the SiPM when not exposed to any light. This signal comes from electrons that have entered the conduction band due to thermal excitation. They trigger an ionization cascade in the avalanche region. This signal detected by a cell is identical to that of electrons extracted by the absorption of a photon. After amplification, the signal associated with 1, 2, 3... photoelectrons can be obtained. The avalanche process induces a Gaussian-shaped response for each photoelectron peak. On the left of Figure 3.7, one can see the spectrum of the amplitudes of the pulses (in ADC units). Up to six photoelectron Gaussian responses are visible, forming what is known as the Single-PhotoElectron (SPE) spectrum.

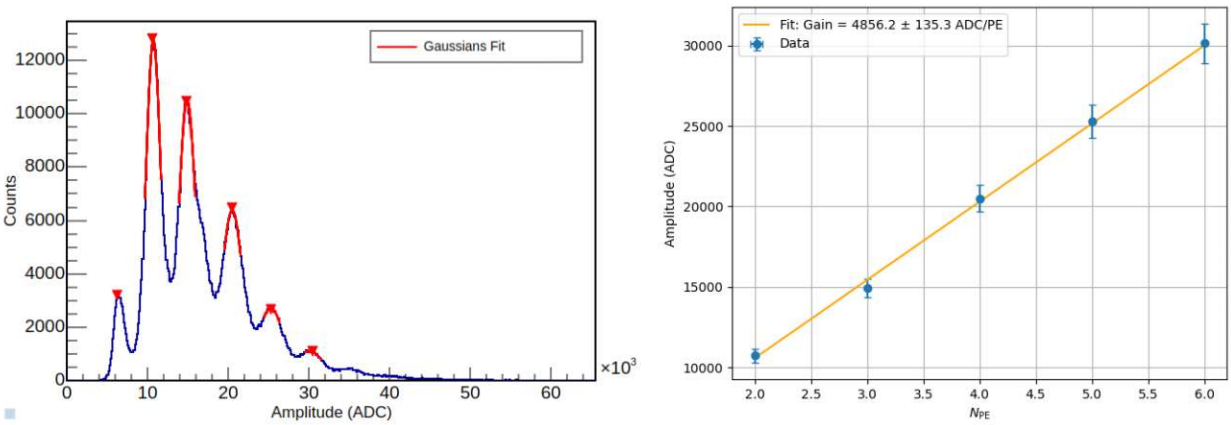

Figure 3.7. Left: SPE spectrum of a SiPM, showing distinct peaks up to 6 photoelectrons. Red curves indicate individual Gaussian fits to each peak. Right: Linear fit of the peak positions as a function of N_{PE}, used to extract the SiPM gain.

3.3.1.2 Determination of SiPM's gains

The gain of a SiPM is the number of ADC (or QDC) channels created by incident PE. To determine it, we fit the peak positions of the SPE spectrum with gaussian function defined in a window around each peak (see left of the Figure 3.7). The first peak is not fitted because its position is potentially biased by trigger threshold effects, which cuts off part of the signal, causing the actual peak position to be lower than observed. Thus, we can plot the number of ADC channels produced by incidents PE (see right of the Figure 3.7). The slope gives the gain of the SiPM. All SiPM's gains are plotted on the Figure 3.8. Most SiPMs have gains within a 10% range around the mean, except for SiPMs number 2, 51, 52, and 53, which have a different design featuring SPADs of size 15×15 μm^2 and are kept as spare units. Nevertheless, this has no impact on the quality of the reconstructed spectrum of the modules.

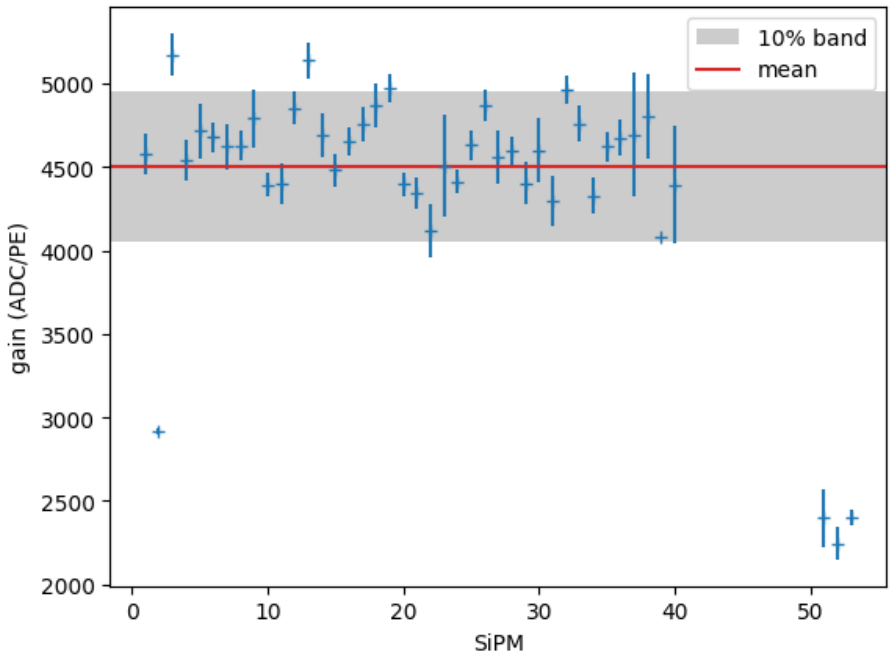

Figure 3.8. Gains of all SiPMs. Also shown are uncertainties from linear fit error and a gray band of 10% around the mean value. One can see the low gain for SiPMs 2, 51,52 and 53 because of their different design (different pixel size).

With this calibration, we can convert the charge spectra into N_{PE} spectra for **u-turn** and **Straight-1sided** using the SiPM gain g:

$$N_{PE} = \frac{N_{ADC}}{g} \tag{3.6}$$

For the double readout panel (**Straight-2sided**), we can compute the sum of the output from both SiPMs $N_{ADC,1}$ and $N_{ADC,2}$ weighted by their respective gain g_1 and g_2:

$$N_{PE} = \frac{N_{ADC1}}{g_1} + \frac{N_{ADC2}}{g_2} \tag{3.7}$$

This summation method allows to mitigate the vertex dependance of the panel response.

3.3.2 Panel performance

The Muon Veto modules are also sensitive to ambient γ-rays from natural radioactive sources, with energies reaching up to 2.6 MeV from ^{208}Tl. This γ background produces a rise at low energy in the spectrum, which must be separated from the muon spectrum. Indeed, it's of utmost importance to be able to discriminate muons from γ-rays because the γ rate is significant and would critically affect the dead time of the experiment, which we aim to keep as low as possible. In Figure 3.9, we can see the exponential distribution of γ-rays at low N_{PE}, the valley corresponding to clipping muons, and the Landau distribution of muons traversing an average of 5 cm of scintillator. The analysis of this spectrum primarily relies on establishing a threshold beyond which events will be tagged as muon events and on a separation criterion between the rise of the γ distribution and the muon peak called the Figure of Merit (FoM). The performance of a panel depends on this FoM.

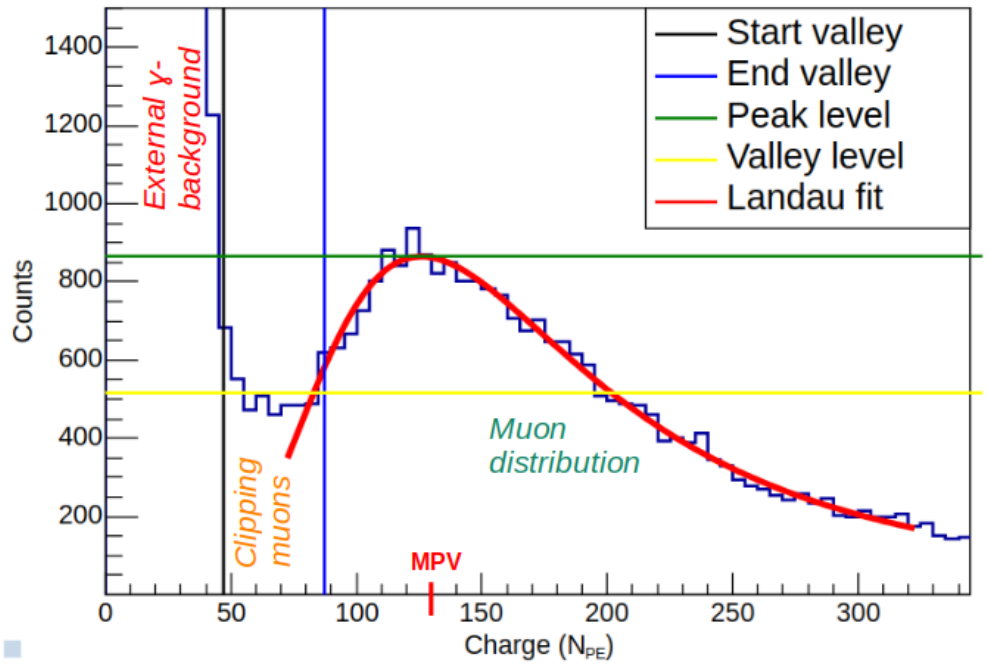

Figure 3.9. Spectrum with relevant parameters for the performance analysis. All parameters are described in the text. In this spectrum we see a good ratio peak-to-valley and good separation between the γ and μ distributions.

In order to quantify the performance of the Muon Veto panel, let's introduce some parameters:

- **MPV**: Most Probable Value, corresponding to the position of the muon peak
- **Peak level**: amplitude of the muon peak (green line in Figure 3.9)
- **Valley level**: mean value of the valley (yellow line in Figure 3.9)
- **Start valley**: arbitrary threshold below which the signal raise up to 33 % above the valley-level (black line in Figure 3.9). Above this threshold, the events are tagged as muons!
- **End valley**: arbitrary threshold above which the counts is more than 33 % above the valley-level (blue line in Figure 3.9)
- $\boldsymbol{\sigma}$: Width of the Landau distribution

We can then build the FoM:

$$FoM = \frac{\textbf{End valley} - \textbf{Start valley}}{\sigma} \tag{3.8}$$

It can be observed that the FoM does not explicitly depend on the position of the muon peak, but the end valley is related to the muon peak position and its width. A high FoM corresponds to a wide valley and a narrow Landau width, indicating good separation between the muon signal and the gamma background. An acceptable

FoM value is typically above 1. The distribution of the FoM for the 28 modules is shown on the left side of Figure 3.10 and does not exhibit any significant dependence on the fiber configuration. However, the position of the muon peak (MPV) is sensitive to light collection efficiency and is therefore higher for the **straight-2sided** and **u-turn** modules, as shown on the right side of Figure 3.10.

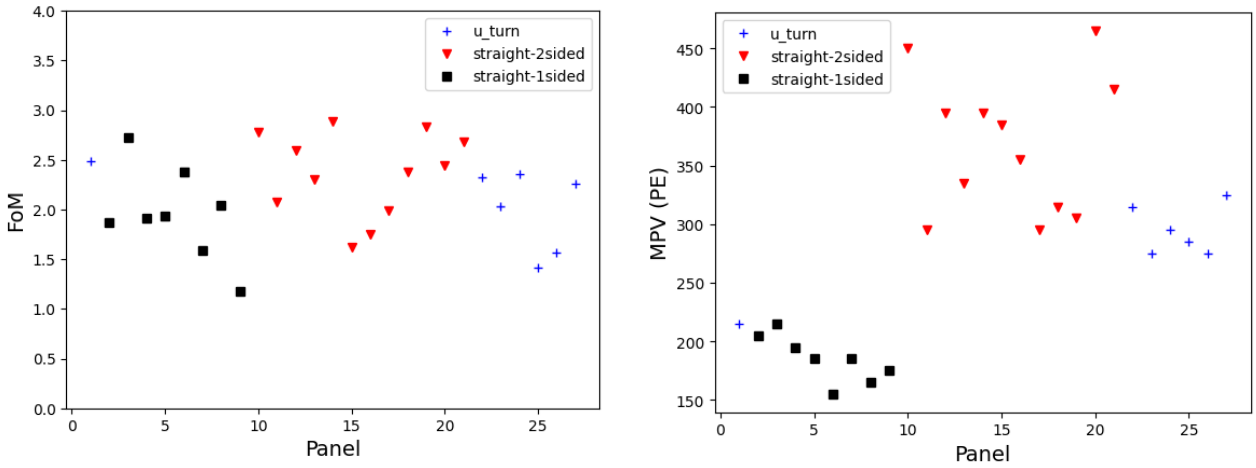

Figure 3.10. Left: Figure of merit for all panels. Right: Most probable value for all panels. One can see that the muon peak is at higher position for double readout module and **u-turn** which ensure a better light collection.

3.4 Muon Veto at the UnderGround Laboratory

Before the installation of NUCLEUS at Chooz, a commissioning run with the cryodetector in anticoincidence with the veto systems was carried out in Munich at an UnderGround Laboratory (UGL) located under a hill providing an overburden of 15 m.w.e [93]. In this section, I present the installation of the Muon Veto at the UGL in the complete cubic configuration and the acquisition system.

3.4.1 Installation in a new cubic configuration

In December 2022, we assembled the Muon Veto modules to form the cube with the technical team from DEDIP (Département d'Electronique des Détecteurs et d'Informatique pour la Physique). Figure 3.11 shows photos of the assembly process and the final configuration of the Muon Veto. A nomenclature for the Muon Veto panels is introduced in Figure 3.12. In this new configuration, the shape of the spectra recorded for the vertical modules (B and C panels) significantly changes since the length of scintillator traversed by the muons is now greater. This results in a higher energy position of the muon peak (see Figure 3.13). However, such geometrical effect also leads to a flattening of the muon peak distribution, resulting in a slightly lower FoM for these modules.

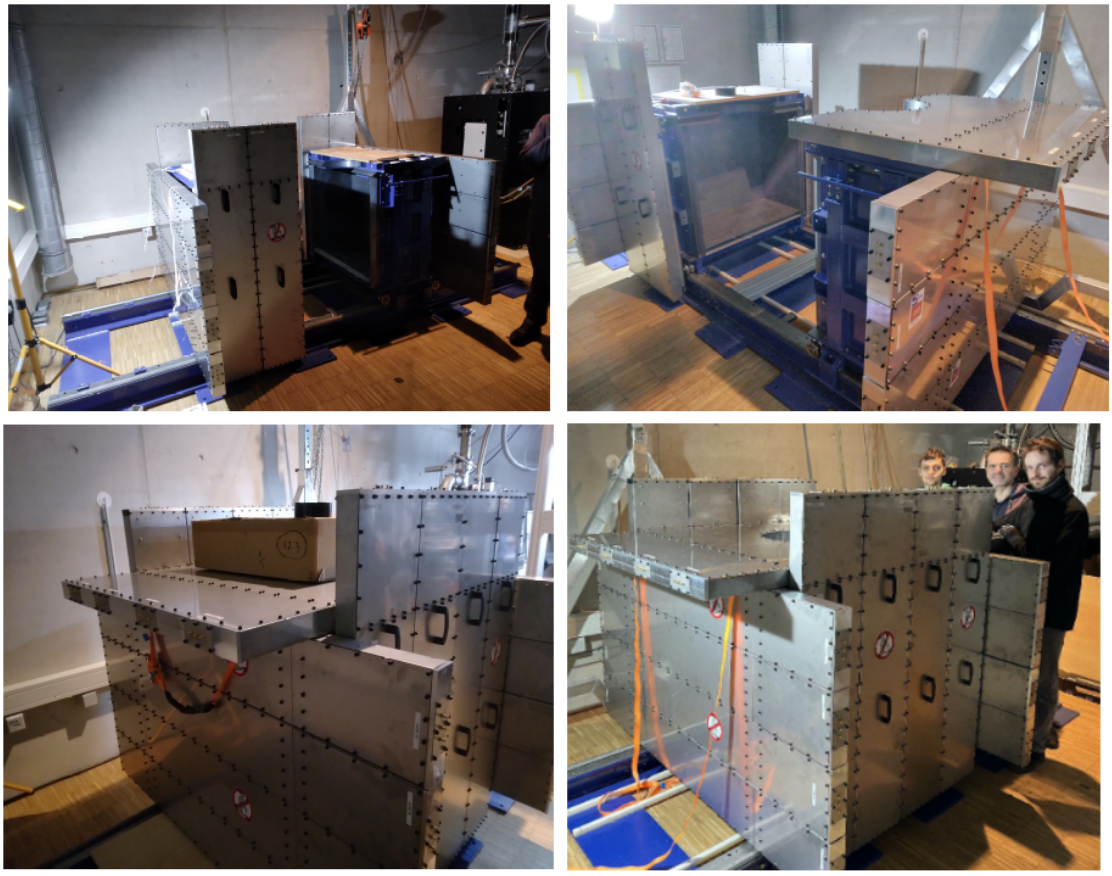

Figure 3.11. Installation of the Muon Veto at the UGL with team from DEDIP. The blue sliding chariots act as support structures for the Muon Veto modules and are installed on rails to allow access to the cryostat.

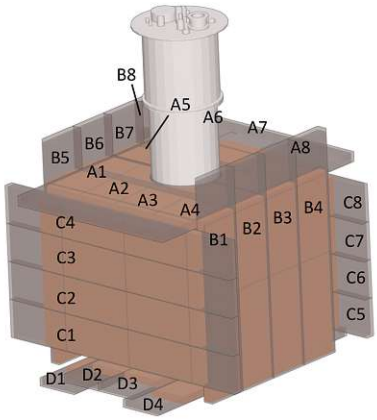

Figure 3.12. Nomenclature of Muon Veto panels. **A1-A8**: roof panels, **straigth-1sided**. **B1-B8**: vertical panels, **u-turn**. **C1-C8**: panels on its edge, **straigth-2sided** (double readout). **D1-D4**: floor panels , **straigth-2sided** (double readout).

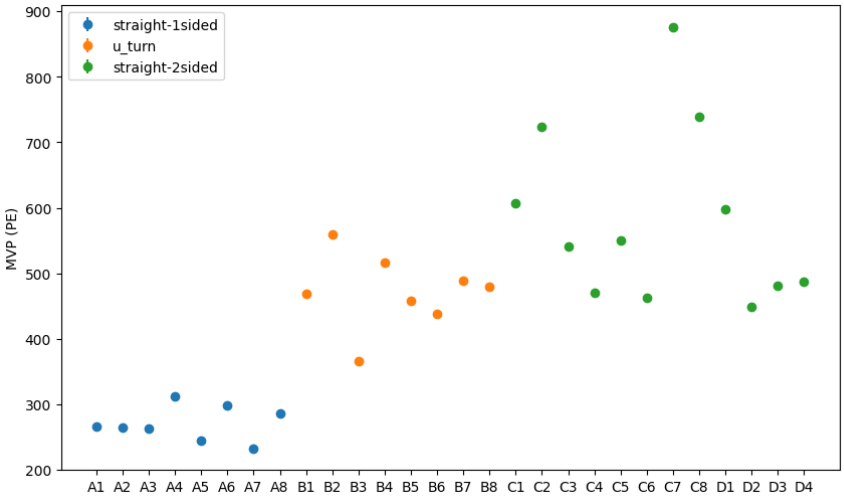

Figure 3.13. Positions of the muon peaks for all panels. The orientation of panels B and C leads to a higher-energy muon peak. The two-sided fiber configuration used for panels C and D, as well as the **u-turn** fiber routing in panel B, improve the light collection resulting in a higher peak energy.

3.4.2 DAQ scheme

A scheme of the Muon Veto electronics is shown in Figure 3.14. Powered by an Arduino module, the Front-end Box (FEE box) role is twofold: it redistributes the necessary voltages to all the SiPMs and collects the signals from each SiPM, transmitting them to the 3 Struck FADC modules which have respectively 16, 16, and 8 channels. Additionally, there is the possibility to remotely enable a gain factor of 10 for reading single photoelectrons during the SiPM calibration runs. The Struck FADC are triggered fast acquisitions that sample and trigger the signals they receive. A trapezoidal FIR filter is implemented for each ADC channel to generate a trigger signal. The filter operates by computing the difference between two sliding average windows, with one window delayed relative to the other. When a pulse occurs, this process produces a trapezoidal-shaped output. If the output exceeds a predefined trigger threshold, a trigger is generated. The signals are then analyzed using an acquisition software installed on the Muon Veto PC. Finally, all the Struck modules are connected to a synchronization module, ensuring a common clock. This is essential for coincident signals in several modules into a single event, and also for synchronizing the Muon Veto clock with an external clock, in view of coincidences/anticoincidences with other NUCLEUS detectors, especially cryodetectors!

The sampling of the signal by the Struck module is done with a sampling frequency of 125 MHz, corresponding to a sample length of 8 ns. Once a sample is above the trigger threshold, the waveform formed by 100 samples is saved, chosen so that the pulse onset is at sample number 60 (a pre-trigger delay allows us to keep in memory the last samples before the pulse onset). Figure 3.15 shows an example of a pulse, one can see that the rise time of the pulse is about few tens of nanoseconds. Thus the time resolution of the Muon Veto is negligeable with respect to cryodetectors time reponse. After a trigger, the electronic dead time is 2 μs due to the data digitizer and data copying processes, and given the global muon rate in the UGL around 200 Hz, the trigger efficiency is 99.96%. We will see in Chapter 4 that the coincidence window between the Muon Veto and the other NUCLEUS detectors is greater than the electronic dead time, so there is no point to account for this trigger efficiency. When one channel triggers, we read all channels, allowing us to measure the charge deposited by a muon in each panel and to have a unique trigger time (the muon time of flight is neglected).

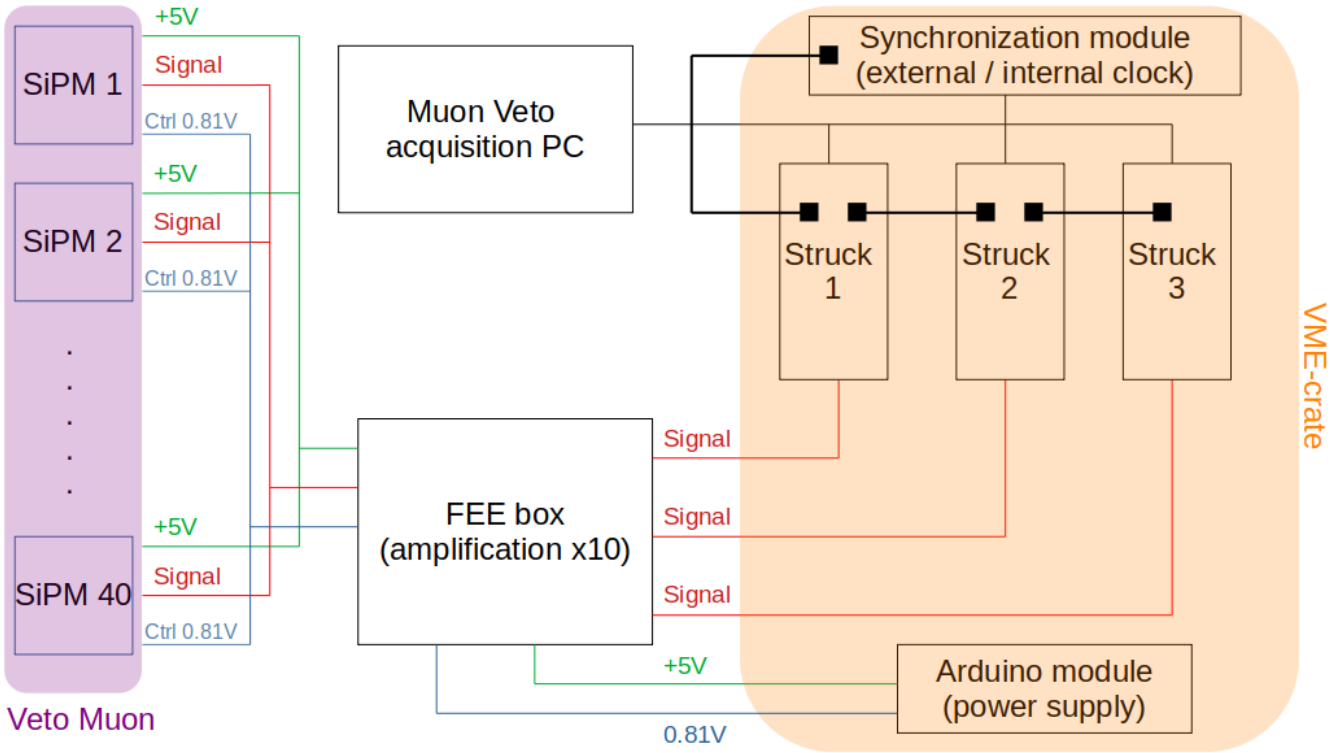

Figure 3.14. DAQ scheme of the NUCLEUS Muon Veto. We can see the main componants: the FEE-box, the struck modules and the Muon Veto PC. More detail in the text.

For the integration of the pulse charge, we define accumulators that sum the charge of each sample over a given window. We define one accumulator (A_1) before the pulse to estimate the baseline level and another accumulator (A_2) containing the pulse (see Figure 3.15). We then obtain the pulse charge Q by subtracting these two accumulators:

$$Q = A_2 - A_1 \tag{3.9}$$

For each events, we store variables from the Table 3.2.

Variable	Type/Unit
Timestamp	Trigger time in ns
A_1	Integrated charge in QDC for all channels
A_2	Integrated charge in QDC for all channels
Charge	Pulse charge in QDC for all channels
Peaktime	Sample Nr of the pulse maximum for all channels
Peakhigh	Amplitude in ADC for all channels

Table 3.2. Stored variables for each events and for all channels of the Muon Veto.

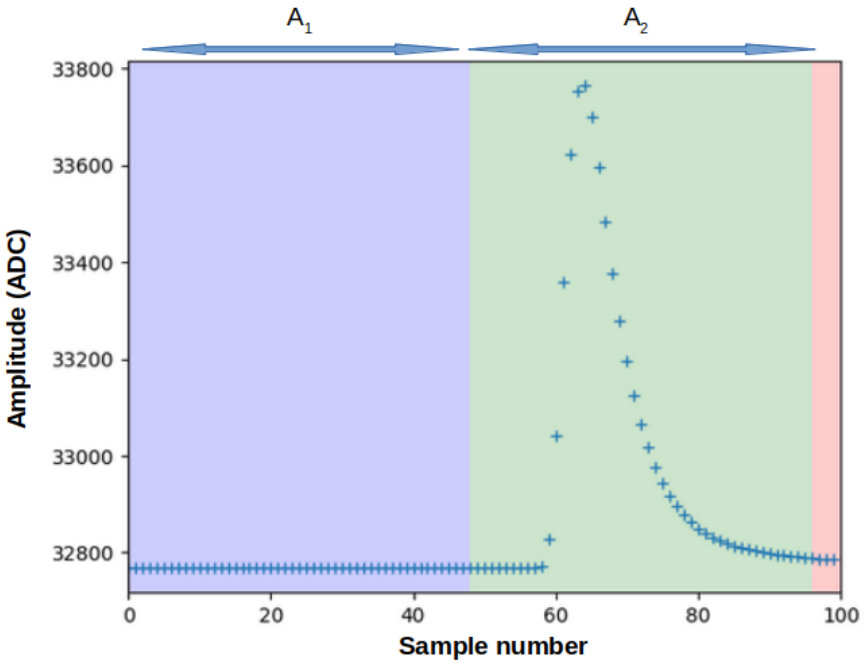

Figure 3.15. Pulse waveform with onset starting at sample number 60. We define two windows for charge integration, one for the baseline (blue) and the second one for the pulse (green).

3.5 Simulations of the Muon Veto

The simulations of the Muon Veto provide access to important informations such as the deposited energy, the rates in all panels, and the geometrical efficiency of the Muon Veto. This latter information is crucial to ensure the Muon Veto's efficiency in rejecting muon-induced background. The simulation framework is Choozerent and has been briefly presented in Section 2.5. It includes the generation of muons and their tracking through the Muon Veto.

3.5.1 Muon simulation with Choozerent

In this section, I briefly describe the Choozerent muon simulation developed in [147]. To account for the angular distribution of the muon flux, a random point is first generated on a hemisphere of radius $R = 2.5\,\mathrm{m}$, centered on the Muon Veto. The polar angle θ is sampled from a probability density function proportional to $\cos^2(\theta)$, while the azimuthal angle ϕ is drawn from a uniform distribution. A tangent plane with a surface area of $2.5 \times 2.5\,\mathrm{m}^2$ is then constructed. The muon is generated at a random point on this plane and emitted perpendicularly towards the Muon Veto, as illustrated in Figure 3.16. Its energy is randomly sampled from the energy spectrum defined by the Gaisser Parametrization [92]. In this framework, the number of generated muons directly corresponds to an equivalent time:

$$t_{eq} = \frac{N_{muons}}{S\phi_0} \tag{3.10}$$

with S the surface of the tangeant plane, N_{muons} the number of generated muons and ϕ_0 is the muon flux at sea level, $\phi_0 = 0.019\ \mu.cm^{-2}.s^{-1}$ [92]. The deposited energy is calculated based on the muon tracks in the different

scintillator volumes. The muon track is divided into steps of length $dx = 0.01$ cm. Then, the deposited energy within this length is computed using the Bethe-Bloch equation (see Equation 3.4).

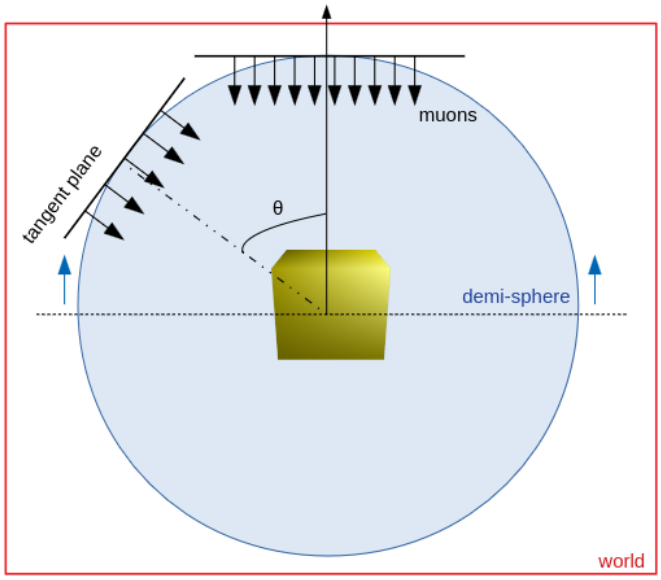

Figure 3.16. Illustrative diagram of muon generation. Muons are shown being generated perpendicularly to the tangent planes on a hemisphere centered on the Muon Veto (yellow cube). Figure from [147].

3.5.2 Data-simulation comparison and calibration

Thanks to the simulations, we can construct the energy deposited spectrum in each panel. Let's define the Light Yield (LY) as the number of photoelectrons per MeV deposited. By comparing the simulated spectrum (in MeV) with the measured one (in PE), we can determine the LY as the ratio between the most probable value in the data and that in the simulation:

$$LY = \frac{MPV_{data}}{MPV_{simu}}(PE/MeV) \tag{3.11}$$

For both simulation and data, the most probable value is extracted with a local Landau fit. The LY depends particularly on the light collection and thus on the fiber configuration as shown in left of Figure 3.17.

For a more accurate comparison of the spectra, it is important to keep in mind, that the equivalent simulation time may be different from the data acquisition live time and, on the other hand, that the simulation spectrum does not account for the detector resolution. The first effect can be corrected by applying a simple amplitude scaling factor. The second is corrected by modeling the detector response. Therefore, for an event depositing energy $E_i = \frac{N_{PE,i}}{LY}$, the Poissonian fluctuations in the number of detected photoelectrons $N_{PE,j}$, responsible for the smearing of the response, are taken into account by the convolution with a Gaussian distribution centered at $N_{PE,i}$ with a standard deviation of $\sigma = \sqrt{N_{PE,i}}$. Thus the detection process converts the number of created photoelectron NPE_i into a detected number of photoelectrons $N_{PE,j}$ following the distribution:

$$N_{PE,j} \sim \mathcal{G}(N_{PE,i}, \sigma) = \frac{1}{\sqrt{2\pi}\sigma} e^{-\frac{(N_{PE,j}-N_{PE,i})^2}{2\sigma^2}} \tag{3.12}$$

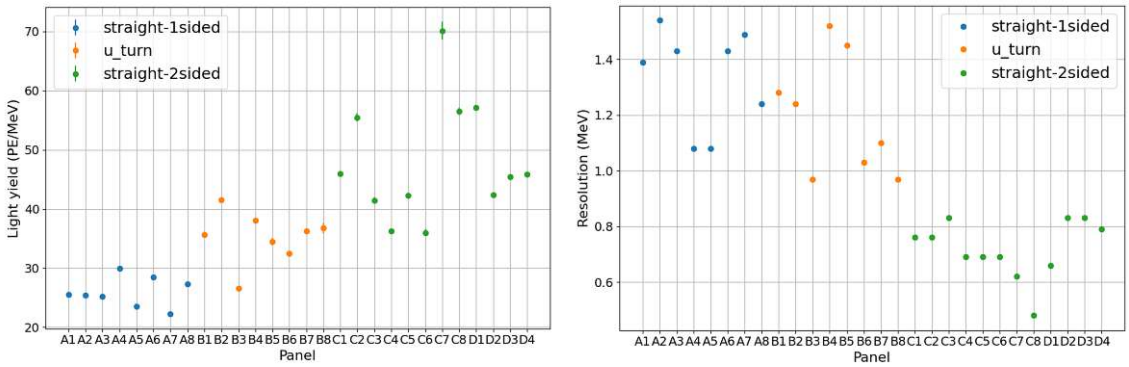

Figure 3.17. Left: Light yield from all panels. Right: Resolution for all panels. We clearly see a higher LY for **straight-2sided** as well as **u-turn** ensuring a better light collection and a better resolution for **straight-2sided panels**.

For each module, the resolution σ and amplitude factor A are free fit parameters adjusted to achieve the best agreement between the model (simulation) and the data spectra. To determine these parameters, a likelihood minimization is employed. For a model with parameters A and σ, the content of each bin n_i is Poisson distributed with mean value equal to the model prediction: $\mu_i(A, \sigma)$. In practice, we minimize the negative logarithm of the likelihood ratio $\lambda(A, \sigma)$[148]:

$$-2ln\lambda(A,\sigma) = 2\sum_{i}^{N_{bins}}\left[\mu_i(A,\sigma) - n_i + n_i ln(\frac{n_i}{\mu_i(A,\sigma)})\right] \tag{3.13}$$

This minimization allows us to extract the amplitude scaling factor A and the resolution σ that can be converted in terms of energy resolution with the LY. Hence, on the right of Figure 3.17 we can see the resolution for all panels. **Straight-2-sided** panels have a better resolution because of a better light collection. After such minimization we can superimpose the simulated and data spectrum. The comparisons for some panels are shown on the Figure 3.18. Around the muon peak positon, we obtain a very good agreement between data and simulated spectra. We can clearly see a saturation effect in the data of the vertical B-panels, as some muons are likely to pass through a large thickness of scintillator and deposit a large charge. For the C-panels, we notice a second peak structure around 50 MeV, which is attributed to a geometrical effect caused by the angular distribution of muons and the panel orientation. Since this is a module read by two SiPMs, the saturation effect is less visible than for the B-panels.

3.5.3 Comparison of single rates and attenuation factors

For each module, we calculate the event rate above the muon threshold, set around 3 MeV. As shown in Figure 3.19, the rate varies between panels due to their different orientations and areas exposed to the muon flux. For example, D-panels register more events than A-panels, which have a smaller surface area.

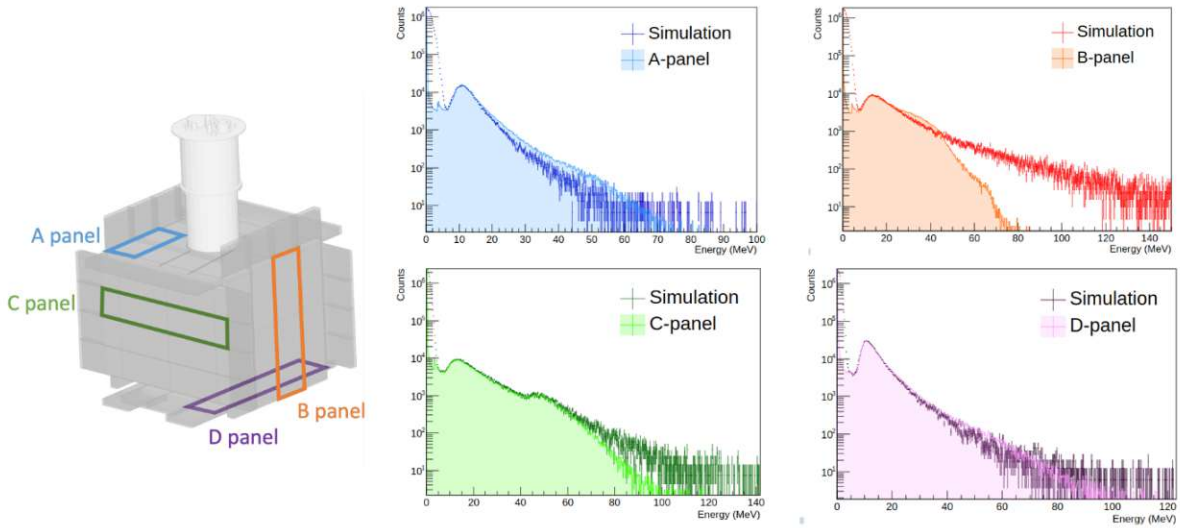

Figure 3.18. Spectrum comparison between data (light color) and simulation (dark color) for different panels, after fine-tuning of LY, resolution, and amplitude scaling factor.

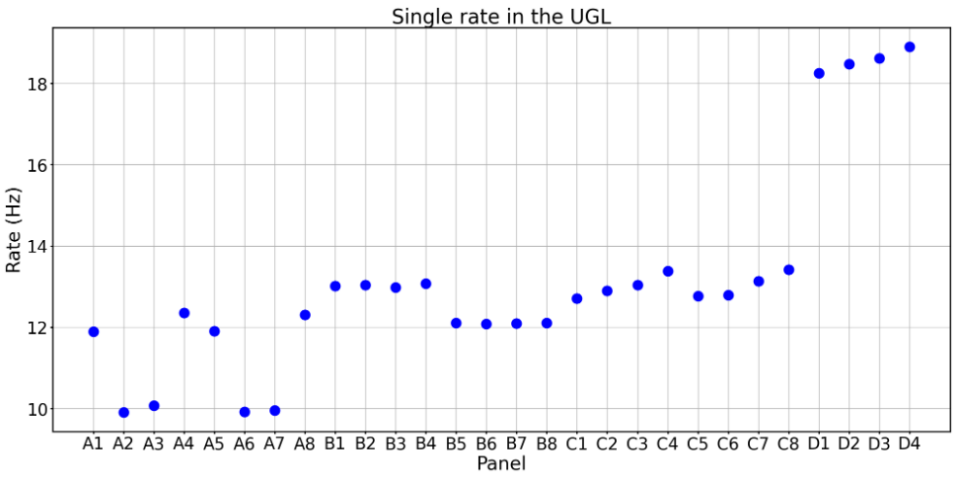

Figure 3.19. Single rate in all Muon Veto panels.

The simulation assume a surface muon flux, therefore comparison with the simulation prediction provides the attenuation factor of the UGL for each panel. It can be translated into meter water equivalent (m.w.e) using the following formula [149]:

$$log\left(\frac{I_{Surface}}{I_{UGL}}\right) = 1.32.log(1+\frac{h}{10}) + 0.26.log^2(1+\frac{h}{10}) \tag{3.14}$$

where h is in m.w.e. The average attenuation factor of the UGL overburden is 2.25, corresponding to 8 m.w.e. Beside, in Figure 3.20, we can observe that the panels located closer to the UGL wall experience a shading effect with a larger attenuation factor. Indeed, the muons passing through these panels must traverse a large thickness of concrete and are slightly more attenuated.

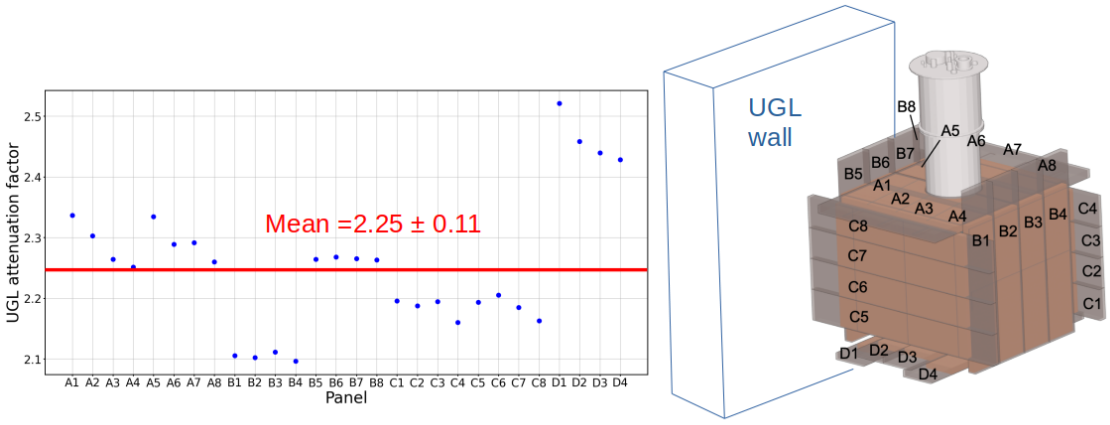

Figure 3.20. Attenuation factor of the UGL overburden in all panels. The shading effect of the UGL wall is clearly visible.

3.6 Monitoring the Muon Veto during the FCR

The core of my work on the Muon Veto has been the development of an analysis chain to produce monitoring plots for the shifters and a reduced file containing the time and energy deposited in all panels for all events tagged as a muon event. This reduced file is then used to perform anticoincidence with the cryogenic detectors.

From the raw data files, the Muon Veto analysis chain computes the parameters listed in Section 3.3.2. These parameters, particularly the FoM, allow for the generation of online monitoring plots to ensure that the shape of the spectra remains nominal and that the muon threshold is correctly set. If a FoM deviates significantly from its nominal value, the corresponding panel is displayed in red on an unfolded sketch of the cube, allowing the shifter to examine the associated spectrum (see Figure 3.21). On the Figure 3.22, one can also observe a very good stability over time of the single rates in all the Muon Veto panels as well as in the Cold Muon Veto (CMV).

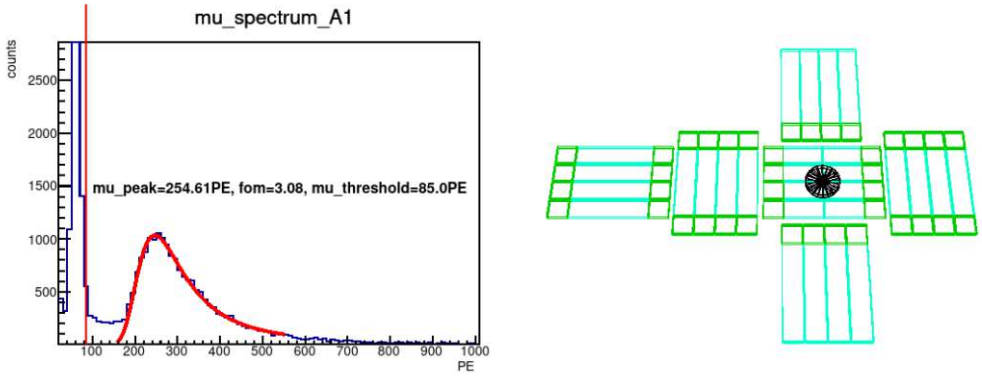

Figure 3.21. Example of online monitoring plots produced during the FCR. The unfolded cube shows in red the panels with non nominal muon spectra, here all muon spectra met specifications.

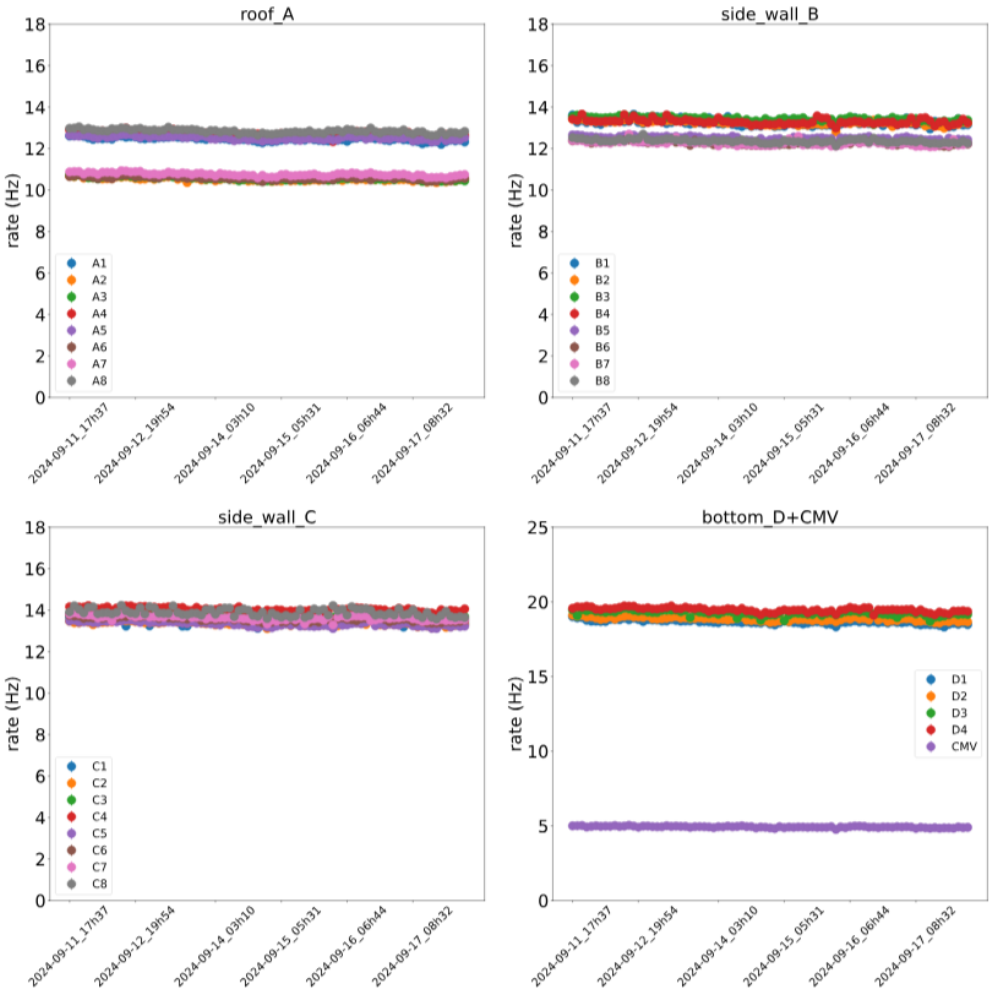

Figure 3.22. Stability of the muon rate in all panels over one week of data taking.

3.7 Muon Veto rate and correlation with pressure and temperature

The total rate of the Muon Veto has shown very good stability, at the percent level, with an average of 196.7 Hz. As seen in Figure 3.23, the muon rate R is anticorrelated with atmospheric pressure P. The meteorological data were obtained using the Python module meteostat, which utilizes open weather data from individual weather stations [150]. On the left side of Figure 3.24, the anti-correlation between the rate and atmospheric pressure is very pronounced. The correlation with temperature, on the other hand, is less pronounced, as seen on the right side of Figure 3.24. However, if we take into account both the dependencies of the rate on pressure and temperature and correct for the correlation with pressure, a higher correlation with temperature emerges. This can be confirmed by performing a joint fit of the muon rate with pressure and temperature using the formula:

$$\frac{R - R_0}{R_0} = \alpha(P - P_0) + \beta(T - T_0) \tag{3.15}$$

where R_0, P_0 et T_0 are mean rate, pressure and temperature. Joint fit as well as indivduals fits results are shown in the Table 3.3. The obtained values are of the same order as those measured in other experiments [151, 152].

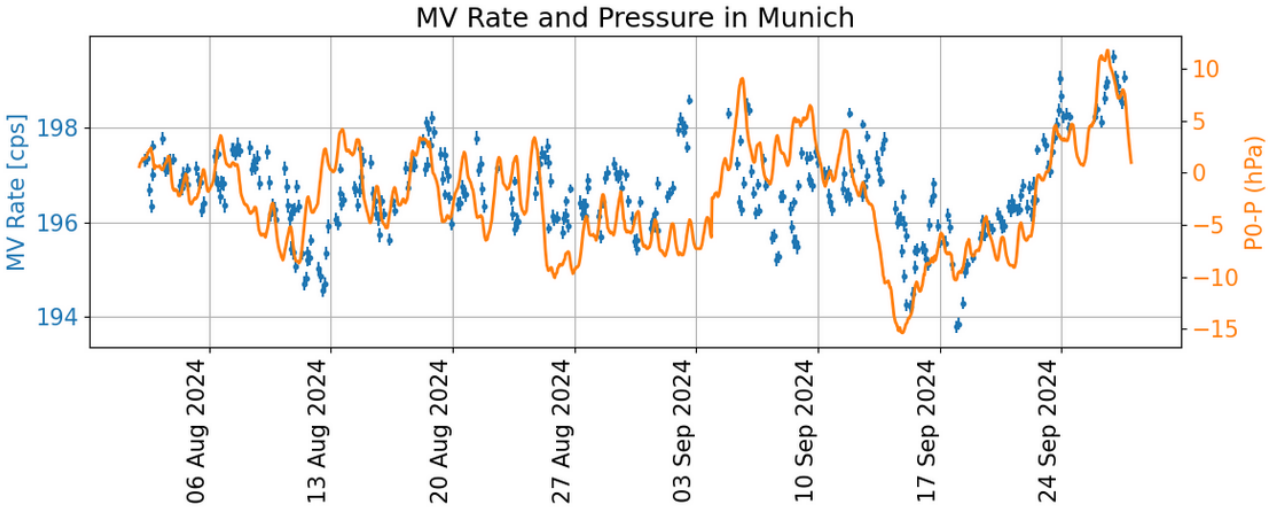

Figure 3.23. Muon rate evolution over time during the FCR. The rate is stable at the percent level and highly anticorrelated with the atmospheric pressure variation. P_0 is the mean pressure: 1013 hPa.

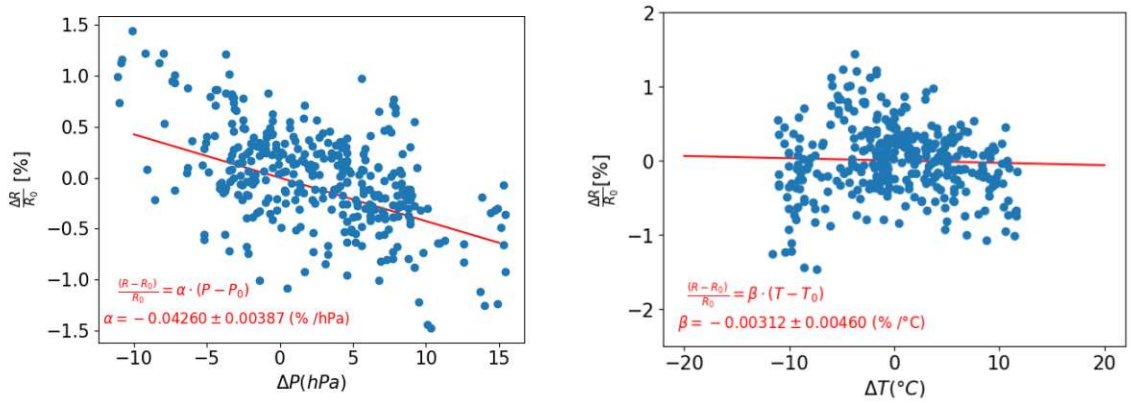

Figure 3.24. Rate correlation with atmospheric pressure (left) and temperature (right). A linear fit is performed and we can see a strong correlation with the pressure while for temperature it's not significant. T_0 and P_0 are the mean temperature and pressure.

Fit function	Parameters
$\frac{R-R_0}{R_0} = \alpha(P - P_0)$	$\alpha = -0.043 \pm 0.004$ [%/hPa]
$\frac{R-R_0}{R_0} = \beta(T - T_0)$	$\beta = -0.003 \pm 0.004$[%/°C]
$\frac{R-R_0}{R_0} = \alpha(P - P_0) + \beta(T - T_0)$	$\alpha = -0.050 \pm 0.004$ [%/hPa] $\beta = -0.0205 \pm 0.004$ [%/°C]

Table 3.3. Results of individual and joint fits with the Equation 3.15.

3.8 Muon Veto at the VNS

In Spring 2025, the Muon Veto and the passive lead and polyethylene shielding were the first components of NUCLEUS to be installed at the Very Near Site (VNS) in Chooz. Figure 3.25 shows the first pictures of these components at the experimental site. During a first commissioning phase following the installation in June, we verified that each SiPM was responding. The Muon Veto was cabled and reconnected to the acquisition system and the Muon Veto server. This commissioning step will need to be continued, as some electronic issues prevented the correct and simultaneous operation of all panels. Nevertheless, several panels were successfully operated and showed good deposited energy spectra.

A very preliminary estimate of the muon rate was extracted from the operational panels. Figure 3.26 shows the measured rate for some working panels, along with a comparison to the corresponding rate measured at the UGL. The subplot displays the rate ratio between Chooz and UGL, showing that, on average, the muon flux is 1.61 times higher at Chooz, slightly below the simulation prediction of 1.66. Rescaling to the full Muon Veto cube yields a total muon rate of $R_{\mathrm{MV}} = 312\,\mathrm{Hz}$. This value is close to the predicted rate of 325 Hz from simulations. The subsequent dead time, DT, as a function of the muon rate and the anticoincidence time window Δt with the cryodetectors, can be expressed as:

$$DT = 1 - \exp(-R_{\mathrm{MV}} \cdot \Delta t) \tag{3.16}$$

Assuming an anticoincidence time window of $\Delta t = 240\,\mu\mathrm{s}$ (as achieved during the FCR in Munich), the resulting dead time would be approximately 7.2%.

Figure 3.25. Pictures of the Muon Veto installation and cabling at the VNS.

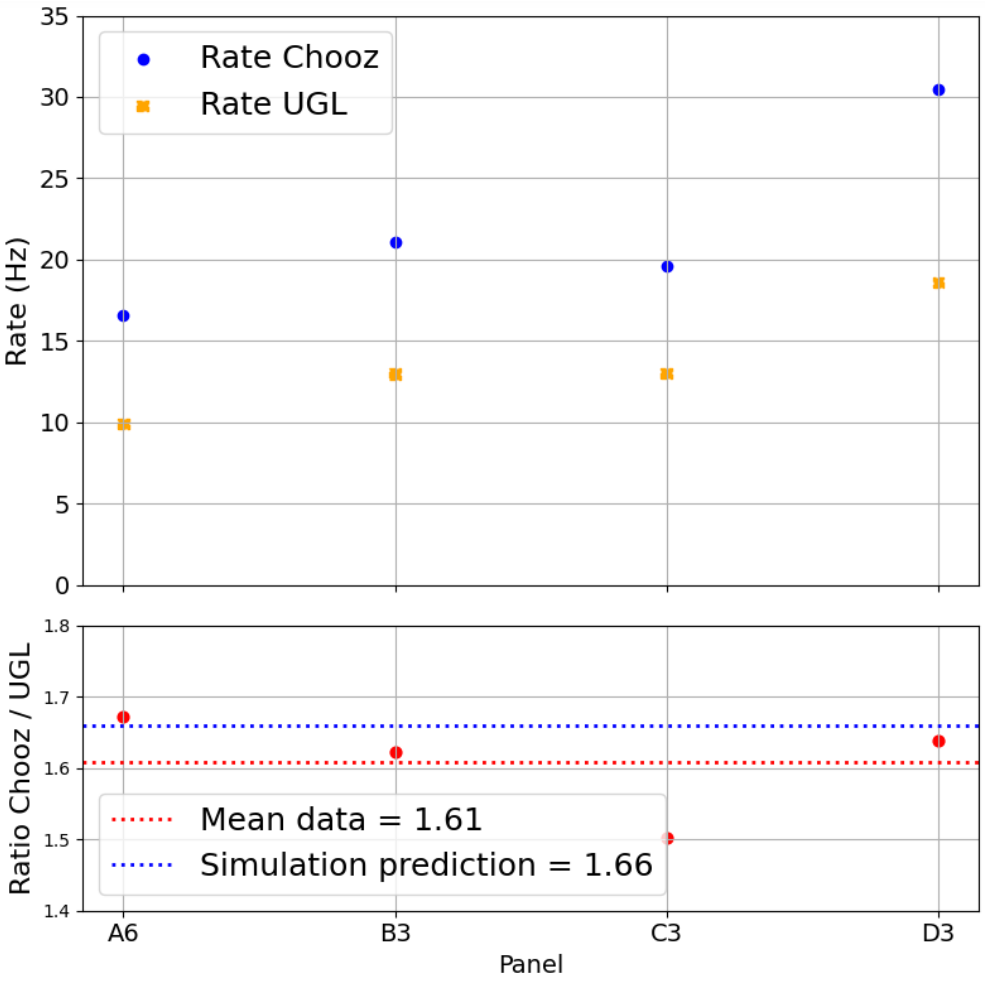

Figure 3.26. Top: Comparison of the measured muon rates at the UGL and at the VNS (Chooz). Bottom: Ratio of the two rates, compared to the simulation expectation.

4

First Commissioning Run at TUM

Before moving to Chooz, a blank assembly of a simplified version of the NUCLEUS experiment took place at the shallow UnderGround Laboratory (UGL) of the Technical University of Munich. This chapter is dedicated to the First Commissioning Run (FCR), which is an important validation step of NUCLEUS experiment as we performed simultaneous operation of all detection and vetoes components. The experimental setup is shown in Figure 4.1. Many challenges were successfully addressed in preparation for the FCR: the assembly of the various detectors, handling cryogenics, thermalizing the inner shielding, and getting the cryodetectors running. This commissioning run lasted nearly two months during the summer of 2024, during which two cryogenic target detectors were tested with the shielding. A background measurement in the cryodetectors was conducted over 9 weeks to provide a benchmark for NUCLEUS. In this chapter, I provide an overview of the FCR: motivations, experimental configurations, data, acquisition systems, and synchronization. Then, I present the results of the first coincidences between the two vetoes systems: the Cryogenic Outer Veto (COV) and the Muon Veto (MV). The analysis methods for the cryodetectors and their application to the LED calibration runs paved the way for obtaining a deposited energy spectrum in both cryodetectors and the subsequent background rate estimation. Finally, the operation of the cryodetectors in anticoincidence with the vetoes systems validated part of the background rejection.

Figure 4.1. Picture of the NUCLEUS experiment installed at the UGL for the FCR.

4.1 Overview of the FCR

4.1.1 Goals of the FCR

The goals of this commissioning run are manyfold. The first challenge was to operate the NUCLEUS detectors in a configuration as close as possible to the final one to ensure that we could turn a theoretical setup into reality. Before installing the experimental setup at Chooz, it was important to conduct a first medium-scale run to identify potential problems that could arise in the future. The FCR led to significant achievements for the operation of the cryodetectors, such as the stability of their response over a month-long period and the commissionning of the LED optical calibration [153].
On the other hand, the main challenge of NUCLEUS is the background rejection. The shielding strategy, presented in Section 2.3, involves multi layer passive shielding and vetoes systems. The FCR allowed, for the first time, the simultaneous operation of the different detectors: the cryodetectors, the COV, and the MV. Work on the synchronization of data acquisitions (see Section 4.1.3) is therefore necessary in order to study coincidences/anticoincidences between the detectors. One motivation of the FCR is the validation of the particle background rejection, which notably depends on the veto attenuation factor of the COV and the MV, which can be compared to the simulation expectations.
In the region of interest for CEνNS, we are dominated by the Low Energy Excess (LEE), and therefore, background rejection cannot be validated with vetoes systems and shielding alone. Studies for the rejection of the LEE were performed using a double-TES readout on one of the cryogenic detector (see Section 2.6). At higher energies (above 1 keV), it is still possible to measure the particle background rate and apply all vetoes systems to identify and reject the different contributions from muons and gamma rays. This background characterization aims to understanding the origins of the particle background, fine-tune and validate the NUCLEUS simulation framework.
It is important to note that the contribution from atmospheric neutrons, the main source of the background budget in Chooz, is suppressed by the overburden of the UGL and thus the background rejection during the FCR focuses on muons and gammas only. A measurement at Chooz when the two reactors are OFF will be of major importance. Finally, although neutrino detection at Chooz remains challenging, the FCR has given the green light to relocate the setup to Chooz and proceed with a technical run.

4.1.2 Configurations of the detectors

During this FCR, two cryogenics target detectors were operated, inside passive and active shielding. The experimental configuration of the FCR is presented in Table 4.1 and in Figure 4.2. Table 4.1 outline for each component the physics goals that help to address the motivations of the FCR presented in Section 4.1.1. The chosen target materials are a cube of $CaWO_4$ and a cube of Al_2O_3 with respective masses of 0.76 g and 0.75 g. The Al_2O_3 crystal was cut larger because it is instrumented by two TES. This dual TES readout, still under R&D, should help to reject a fraction of events from the LEE as explained in Section 2.6. As for the shielding, the Muon Veto is complete with its 28 panels and the Cold Muon Veto (CMV). The external as well as internal lead and polyethylene shielding are installed, only the B_4C piece around the COV is missing. The COV is incomplete, with only one out of the six crystals installed directly above the target detectors. Finally, there is no inner veto as this system is still under development.

Component	Physics goals	Target	Mass	Size
Cryodetectors	• Stability • Background rate estimation • Energy resolution • Calibration	$CaWO_4$	0.76 g	$5 \times 5 \times 5\ mm^3$
	• Stability • Background rate estimation • Rejection of LEE with double TES readout • Energy resolution • Calibration	Al_2O_3	0.75 g	$5 \times 5 \times 7.5\ mm^3$
			Status	
MV	• Stability • MV efficiency • Dead time • Veto attenuation factor		Full MV + CMV	
Passive shielding	• Shielding efficiency		External and Inner Shielding. B_4C missing	
COV	• Stability and regeneration • Detection threshold • γ background measurement		1/6 crystal	
IV	• Surface background rejection • LEE rejection		Missing	

Table 4.1. Experimental configuration of the FCR. For each component, the main physics goals are highlighted.

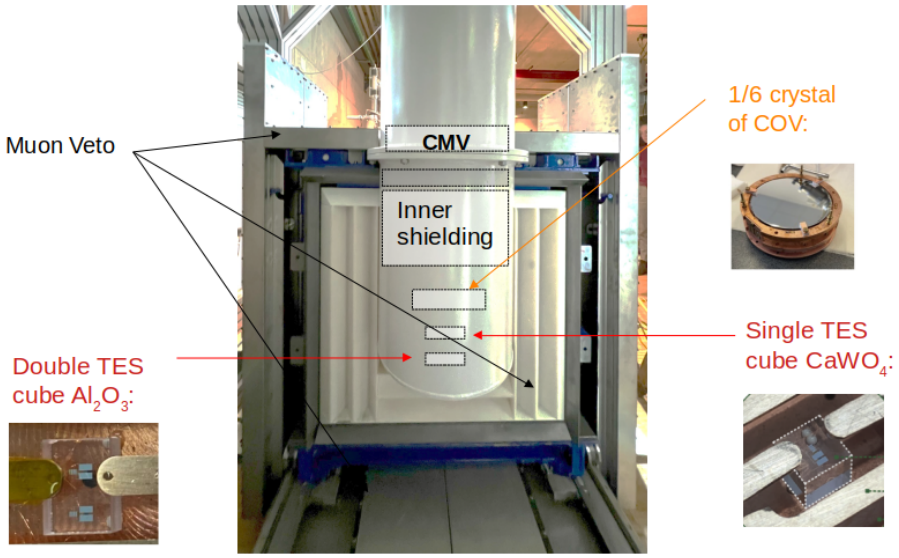

Figure 4.2. Cut view of the NUCLEUS experimental configuration during the FCR.

4.1.3 Acquisition systems and synchronization

The simultaneous operation of multiple detectors involves different acquisitions that must be synchronized, otherwise preventing us from performing coincidence analysis between detectors. The DAQ rack is shown in Figure 4.3. Let's describe some important systems for the acquisition of all detectors.

- **Muon Veto DAQ:** The Muon Veto DAQ consists of 3 Struck FADC modules that sample the signal at 125 MHz and save all traces that contain a trigger above the threshold. More details are provided in Section 3.4.2.

- **VDAQ-v2 (Versatile Data AcQuisition,v2):** The VDAQ is an acquisition system coupled with software developed by NUCLEUS collaboration at HEPHY and TU Wien, specifically for cryogenic detector experiments. We use the VDAQ to acquire both the cryodetectors and COV data streams. This acquisition samples and saves the continuous stream of data. The chosen sampling frequencies are 10 kHz for $CaWO_4$, 50 kHz for Al_2O_3 and 100 kHz for COV. The VDAQ also provides additionnal features, such as bias current and a PID loop over the injected heater current necessary to lock the working point position in the TES transition, ensuring a good stability (see Section 2.4.4). The main limitation of the VDAQ-v2 used in this run concerns the number of available readout channels, limiting the acquisition to two detectors. The upgraded version, VDAQ-v3, will lift this constraint by supporting a larger number of readout channels and will be deployed for the upcoming technical run at Chooz.

- **Synchronization:** The synchronization between the Struck-FADC for the muon signals and the VDAQ for the cryodetector signals is done through a synchronization module. This module takes the VDAQ clock and feeds it to the Struck modules. This prevents any relative clock drift, as there is a common reference clock (the VDAQ clock). The next step is to define a common time origin t_0, since the acquisitions can not be started simultaneously at the microsecond level. This is done by sending a synchronization pulse with the VDAQ, that resets the clocks to zero and ensure that all timestamps are aligned after. This action is performed at the beginning of each data acquisition segment. Left panel of the Figure 4.4 shows the timestamp evolution of the Muon Veto with two resets (only one is needed, but two resets are sent for safety). The second last reset is taken as the time origin t_0.

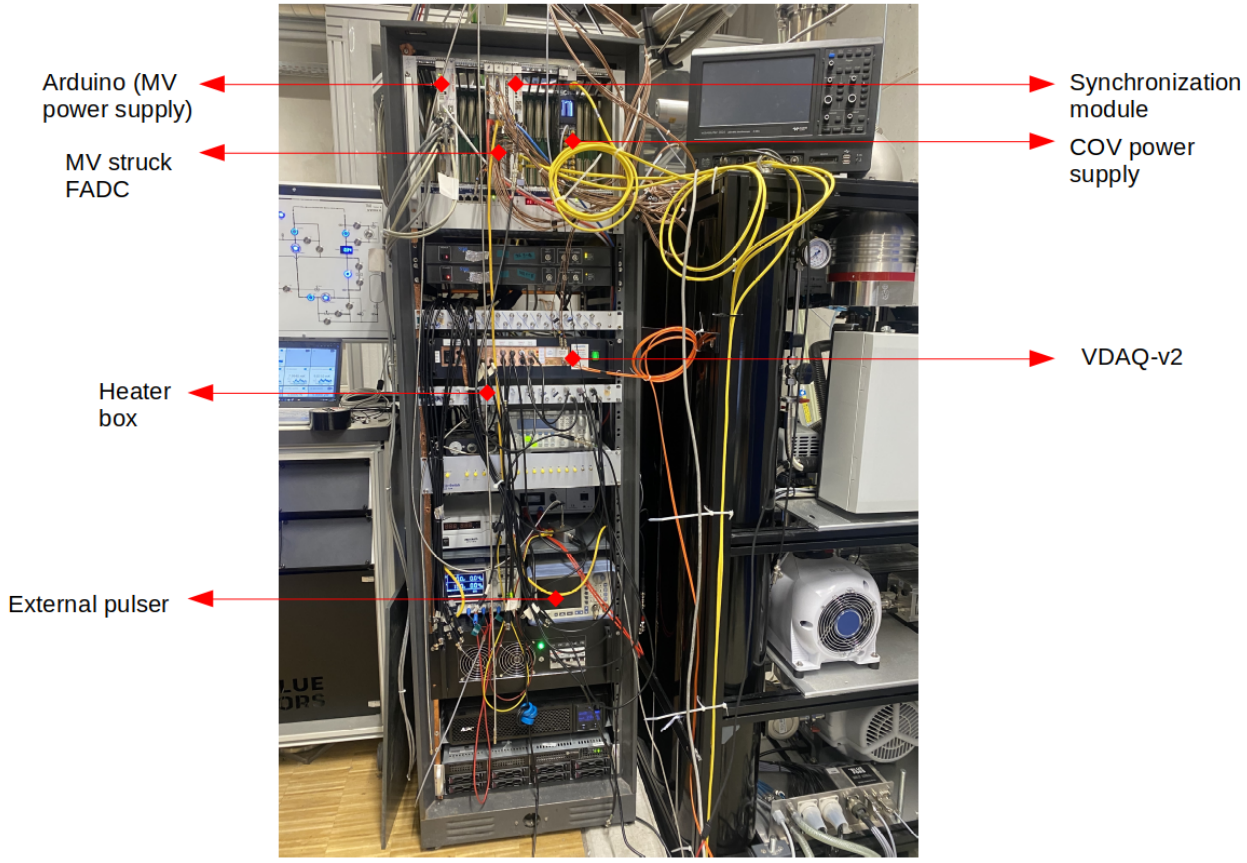

Figure 4.3. NUCLEUS acquisition rack. The top crate contains the electronics of the Muon Veto and the COV power supply. In the middle, there is the electronics for the cryodetectors: the VDAQ-v2 and the heater box. At the bottom there is the external pulser sending pulses to both the Muon Veto struck and the VDAQ-v2 to monitor the synchronization.

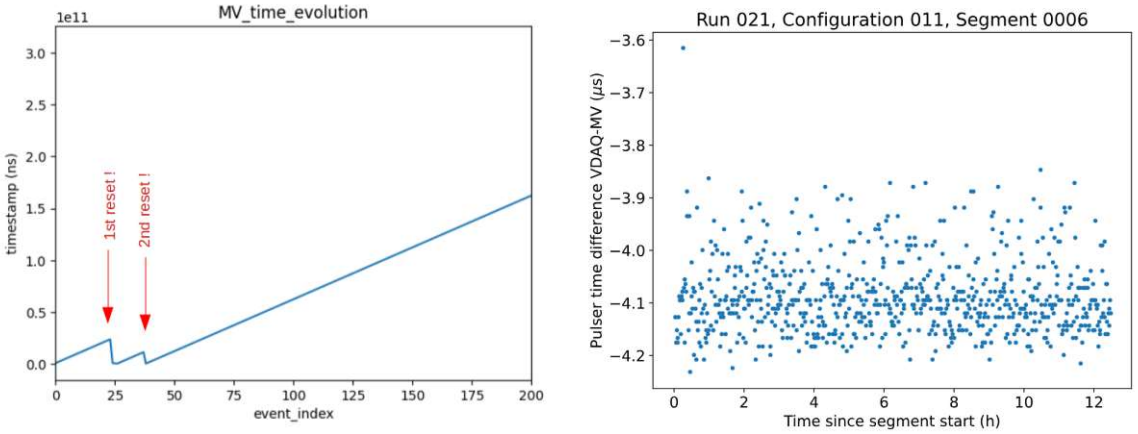

Figure 4.4. Left: Evolution of MV timestamps versus event index. The last time reset sent by the VDAQ-v2 defines the time origin. Right: Time difference between pulser time in VDAQ-v2 and MV. Synchronization is ensured for the entire segment at the 100 ns level, width of the displayed distribution.

The synchronization is continuously monitored with an external pulser that generates pulses every 60 seconds in both acquisitions. This allows us to verify during each segment that the times of the pulses reconstructed in each acquisition are identical. In right-hand side of the Figure 4.4, we can see an example of monitoring plot showing the time difference between the generated pulses in the VDAQ and the MV. The difference remains constant throughout 12 hours, at approximately 4 μs, with a time jitter of 100 ns well below the time coincidence window of 240 μs driven by the time resolution of the cryodetectors.

4.1.4 Datasets

As mentioned earlier, two cryodetectors were operated during this nine-week FCR. Due to constraints on the maximum number of readout channels available with the preliminary version of the VDAQ, data acquisition had to be carefully organized. The issue is that we only had 2 available readout channels for both cryodetectors (totalizing 3 TES to read) and the COV. This is why we had to alternate data collection between the $CaWO_4$ and Al_2O_3 cubes. Since the Al_2O_3 cube is read by two TES, it was not possible to record the COV in parallel. The data acquisition was thus segmented as follows: alternating weeks between either [$CaWO_4$ + COV + MV] or [Al_2O_3 + MV]. Thus, the run is divided into different configurations depending on the hardware settings. Each configuration is further split into segments, which correspond to the data acquisition files.

In total, 562.59 hours of data were acquired with the $CaWO_4$ cube in coincidence with the MV (including 369.74 hours with COV) and approximately 571.88 hours with Al_2O_3 in coincidence with the MV, as shown in Figure 4.5. Tables 4.2 and 4.3 summarize the data collection for the $CaWO_4$ and Al_2O_3 cubes, listing all configuration and segment numbers. Some segment numbers are missing due to issues encountered during data acquisition, such as human errors or DAQ synchronization problems. Short runs were conducted at the beginning and end of each week to perform an LED calibration. I personally focused on analyzing the $CaWO_4$ data. The datasets I analyzed include the LED calibration configurations (see Section 4.4) and the configurations with COV (indicated in bold in Table 4.2).

4.2 MV–COV coincidence analysis

Physical coincidences between the COV and the MV were studied using data from configurations 4, 8, 10, and 12. The COV and MV data have been preprocessed, producing reduced HDF5 files containing the energy and time of each event. The analysis of the MV data and the production of the subsequent HDF5 file were presented in Chapter 3. The preprocessing of COV data was developed in [90]. These reduced files allow for high-level analysis, which is presented in this section.

4.2.1 Coincidence selection

Events depositing energy simultaneously in both the COV and the MV are called "coincidence". They are selected based on the time difference between COV and MV events. For each COV event, we look for the closest event in the MV, and we can plot the time difference distribution (see top of the Figure 4.6). A peak due to physicals coincidences is visible, on top of a nearly flat background referred to as "accidental coincidences". A Gaussian fit provides the parameters of this peak, it is centered at -12 μs with a width of 3.9 μs. An event is considered coincident if the time difference is within $\pm 3\ \sigma$ around the mean, that is, within the time coincidence window [-23.7, -0.3] μs, represented by the red dashed lines. Strictly speaking, not all events selected this way are physical coincidences, a small fraction of them originating from the background of accidental coincidences.

Configuration number	Type	Segments number	Run time (hours)	MV	COV
3	LED Bkg	4-5 6	- 14.69h	No Yes	No No
4	LED **Bkg**	13-14 **2, 3, 5-11, 15, 17**	- **104.28h**	No **Yes**	No **Yes**
7	LED	3-4	-	No	No
8	LED **Bkg**	18-19 **2, 4-7, 9-17, 20**	- **117.22h**	No **Yes**	No **Yes**
10	LED **Bkg**	1, 2, 21, 22 **3–10, 12–20, 23**	- **148.23h**	No **Yes**	No **Yes**
12	LED Bkg	4-5, 25-26 6, 8–24, 48–52	- 178.17h	No Yes	No No
Total time		562.59h			
Total time with COV		**369.74h**			

Table 4.2. Dataset for $CaWO_4$ cube. Bold text indicates configurations in coincidence with both MV and COV, analyzed in Section 4.6.

Configuration number	Type	Segments number	Run time (hours)	MV
2	LED **Bkg**	1-4, 22-25 **6-17, 19-21, 27**	- **124.56h**	No **Yes**
5	LED **Bkg**	3, 5-6, 8, 39-41, 43 **10, 13, 14, 16, 17, 19-30**	- **154.80h**	No **Yes**
9	LED **Bkg**	2-4, 6-10, 36-39, 44-47 **1, 11-12, 14-20, 22-33, 35**	- **139.20h**	No **Yes**
11	LED **Bkg**	1-4, 23-25, 27-39, 41, 42 **5-21, 46, 47**	- **153.32h**	No **Yes**
Total time			**571.88h**	

Table 4.3. Dataset for Al_2O_3 cube. Bold text indicates configurations in coincidence with MV, presented in Section 4.7.

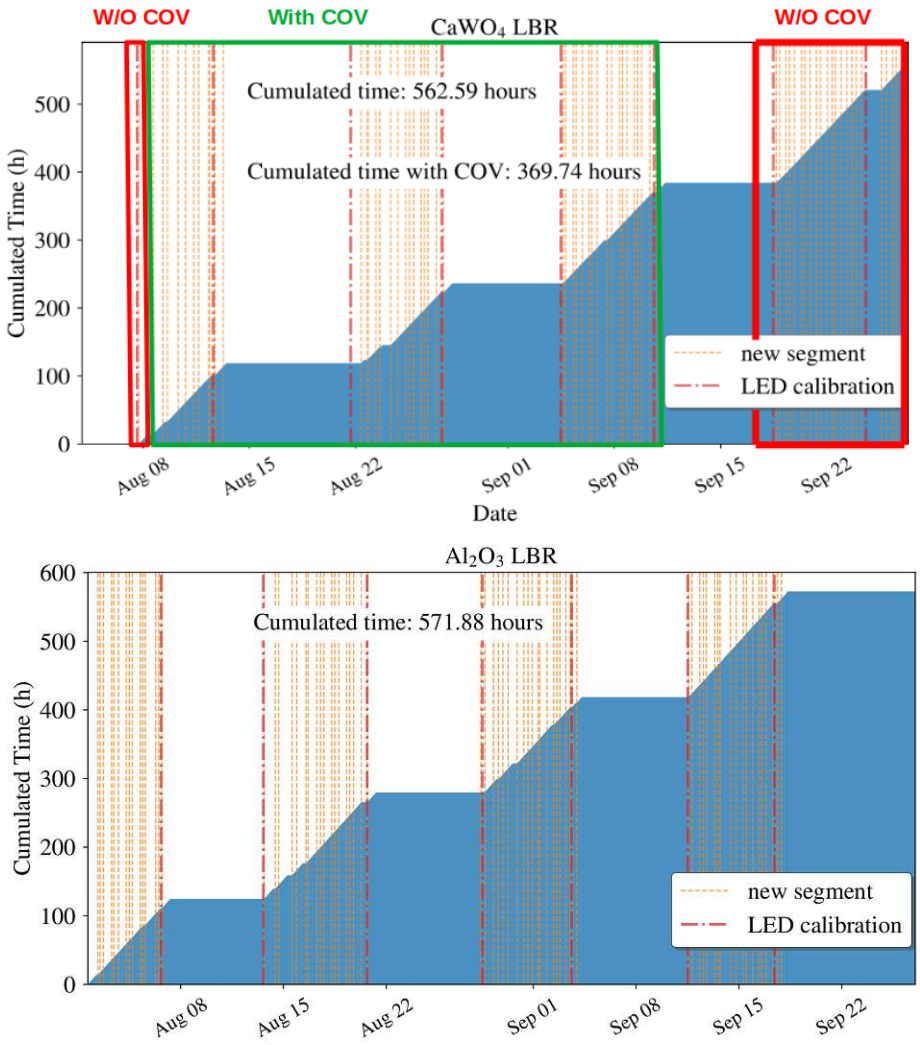

Figure 4.5. Cumulated data taking time in $CaWO_4$ (top) and Al_2O_3 (bottom). Each data file is indicated by an orange line, while the plateau correspond to the data taking with the other cryodetector, as we switched data taking between the two targets. LED calibrations are also indicated by red lines. For $CaWO_4$ only, some configurations are taken with the COV.

The probability that a COV event is in accidental coincidence with the MV can be estimated by:

$$P_{acc} \approx \Delta T \times Rate_{MV} \tag{4.1}$$

where ΔT is the width of the time coincidence window. The choice of the size of this window is a trade-off. A wider window would select all the physical coincidence events but would also increase accidental coincidences. This is why the time resolution of the detectors is important, the better the time resolution, the smaller the time coincidence window. The width of the coincidence peak is driven by the COV time resolution, as the MV time response is on the nanosecond scale while the COV provides only microsecond-level precision due to its sampling frequency. In this case, the probability of accidental coincidences is only 0.46%. Based on this definition of coincidences, we can plot the COV spectra in coincidence or anticoincidence with the MV, as shown on bottom of Figure 4.6. At low energy, in the total COV spectrum, we observe multiple gamma lines, up to the ^{208}Tl peak

at 2.6 MeV. This ambient gamma spectrum is typical of natural material's radioactivity. These gamma rays are not in coincidence with the MV. At higher energies, above 3 MeV, the muons are expected to be the dominant contribution. Indeed, we can see that most of the events in this region are in coincidence with the MV (green spectrum), while the anticoincident events are negligible.

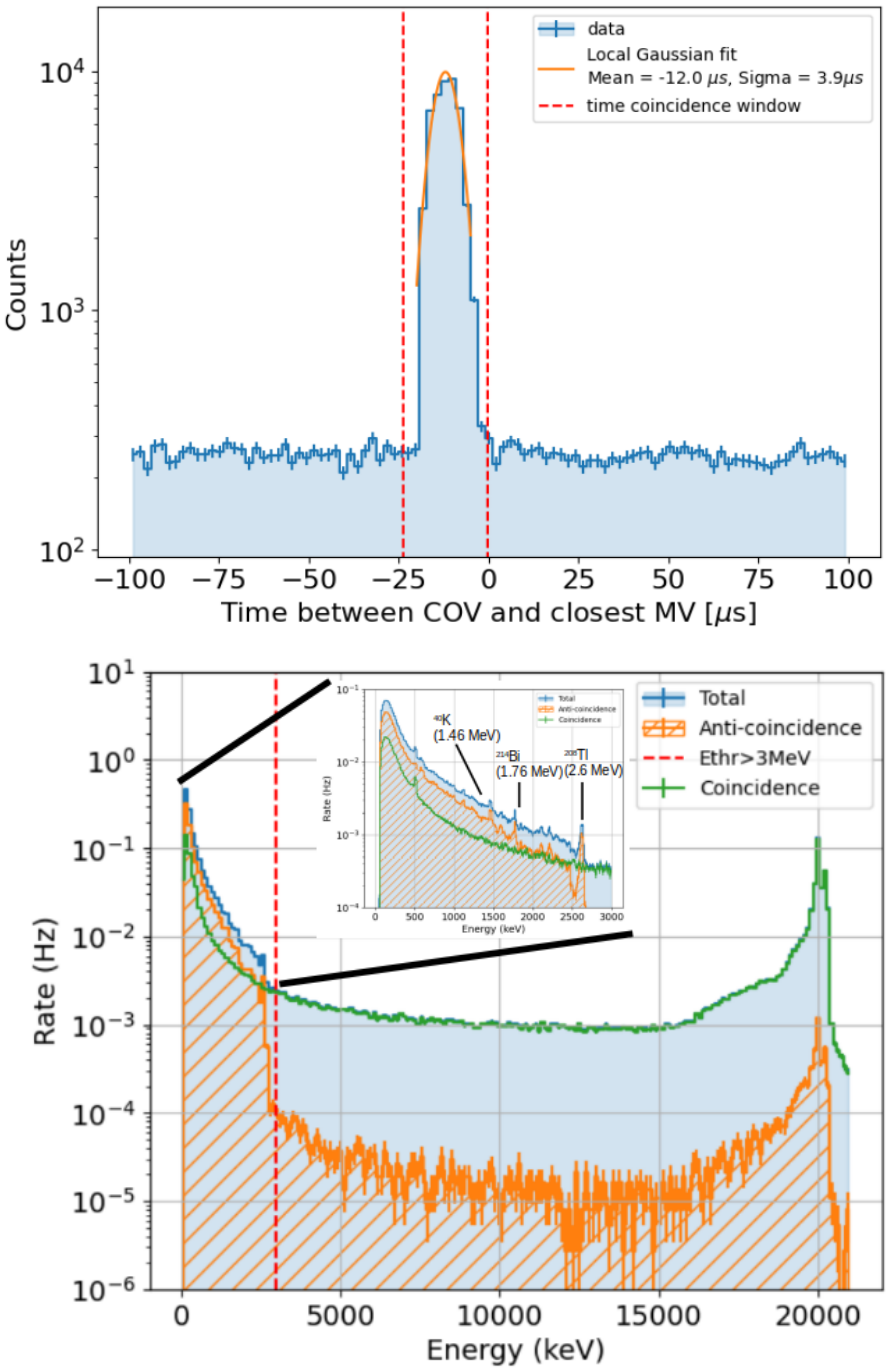

Figure 4.6. Top: Distribution of the time difference between COV events and the closest event in the MV. The time coincidence window is indicated by the red dashed lines. Bottom: Spectrum in COV showing the total, coincidence, and anti-coincidence events with the MV. The data are from configuration 4 totalizing 104.28 hours of data taking.

4.2.2 Efficiency of the MV

The ability to perform COV-MV coincidences paves the way for estimating the efficiency of the MV, i.e., its ability to tag muons. Indeed, the Muon Veto has some geometric inefficiency due to gaps around the cryostat and at the level of the rails in the lower corners. We estimate the total detection efficiency as follows: muon events are selected in the COV (events above 3 MeV), and we compute what fraction of them is also identified by the MV detectors. This method is illustrated in Figure 4.7. Thus the MV efficiency ϵ is defined as:

$$\epsilon = \frac{n_{MV}}{N_{tot}} \tag{4.2}$$

With N_{tot} being the number of muons tagged in the COV and n_{MV} the number of muons also seen in the MV. N_{tot} is determined by integrating the COV total spectrum above 3 MeV, and n_{MV} by integrating the COV coincident spectrum. The uncertainty on ϵ is computed using the standard formula [154]:

$$\sigma_\epsilon = \sqrt{\frac{\epsilon(1-\epsilon)}{N_{tot}}} \tag{4.3}$$

The MV efficiency determined for each data segment shows a very good time stability (see Figure 4.8). Above 3 MeV, the event rate in the COV (dominated by muons) is 0.57 Hz. 98.6% of those events are also seen in the MV, which is close to the simulation prediction of 99.0% and well above the specification of 90%. This is the first major result of my thesis, as it validates all my work on the Muon Veto, both from the hardware and software sides, presented in Chapter 3. This result is important for NUCLEUS, as it validates the rejection of muon-induced backgrounds, which are a major source of background.

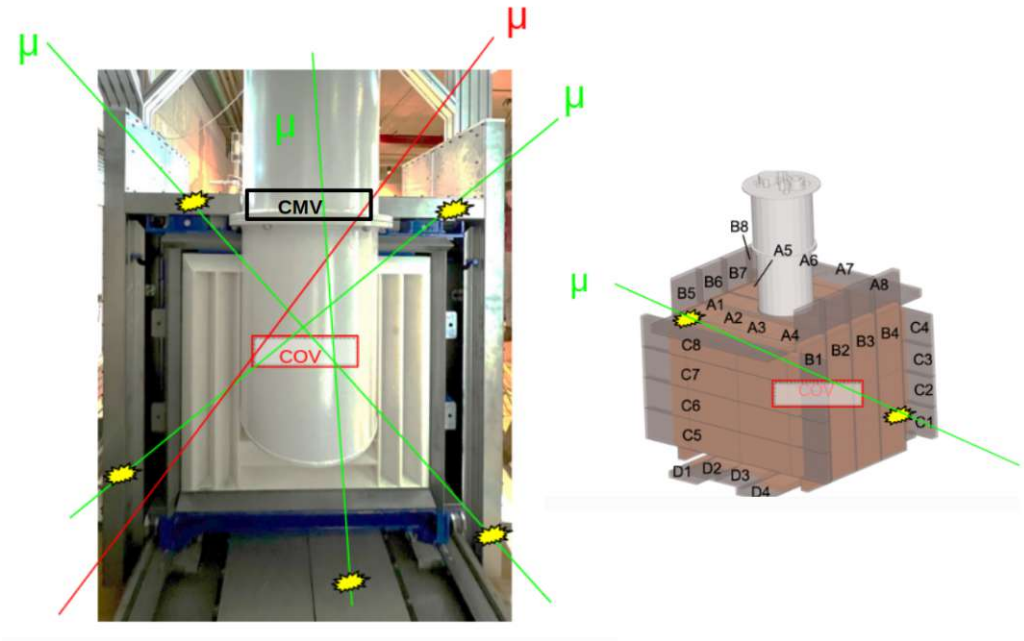

Figure 4.7. Sketch of muons passing through the NUCLEUS setup and crossing the COV. The muons depicted in green passes through the MV as well, while the red muons only deposit energy in the COV, passing through gaps in the mechanics contributing for MV inefficiency.

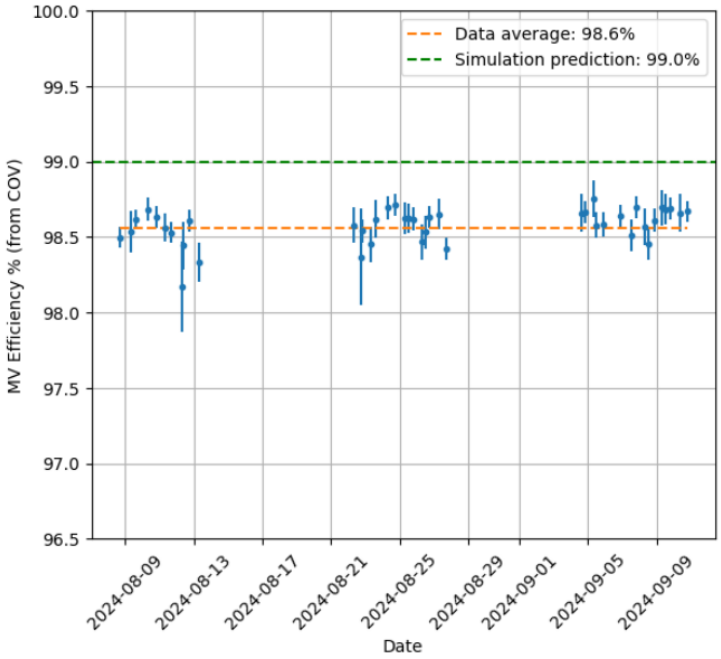

Figure 4.8. Time stability of the MV efficiency. The mean value of 98.6% is in good agreement with simulation prediction of 99.0%, validating the ability of the Muon Veto to efficiently identify muons.

4.3 Cryodetector analysis framework

Now that the FCR has been presented and the performance of the vetoes systems have been validated, let's detail the analysis of cryodetectors data. This analysis aims to draw conclusions on the calibration, performance, and background rate, as well as to identify background sources using the vetoes systems. It's the so-called "high level analysis" that is addressed in Sections 4.4, 4.5 and 4.6. The mechanisms of energy deposition and the response of the thermometers were presented in Section 2.4. Obtaining a deposited energy spectrum from the thermometric signal (raw data) requires standard cryodetector analysis techniques [155, 156], which I briefly review in this section. To present those techniques, I will use the LED calibration data from the $CaWO_4$ cube. I will present the analysis chain and the various steps that were carried out for the FCR analysis. The analysis toolkit I use is CAIT (Cryogenic Artificial Intelligence Tools) [157, 158], which is a Python 3 software package developed at HEPHY for the analysis of raw data from cryogenic experiments. It is a powerful tool to carry out the essential steps of the analysis: triggering, pulse shape parameters calculation, energy reconstruction, and data quality cuts. This software has been adapted within the collaboration to account for specific features of the NUCLEUS experiment like the time reset implementation and LED events identification.

4.3.1 Raw data stream

The VDAQ continuously samples the response of the TES, so we obtain a data stream. An example is shown in blue on top of Figure 4.9. We can see different types of pulses: most of them are responses to the injected heater sent to monitor the detector's response (see Section 2.4.4), a few are particle pulses and some are induced by the LED source. Both LED and heater pulse can be identified by the ADC3 and DAC1 signals. A trigger algorithm uses a moving window of 2048 samples to scan the data stream and build a trace. The baseline is estimated by averaging the first 256 samples and subtracting this value from the entire trace. If at least one sample exceeds the trigger threshold, the trace is saved and counted as an event. This procedure includes some

dead time after a trigger which prevents the trigger on pile-up events (we are triggering only once for the two pulses). The calculation of the trigger efficiency is done in Section 4.6.2. Then, we save all pulse traces and calculate some relevant parameters such as amplitude, decay time, rise time, etc. Figure 4.9 also shows some example of triggered events; we can see a physical pulse but also artifacts that need to be removed by applying data quality cuts (see Section 4.6.1).

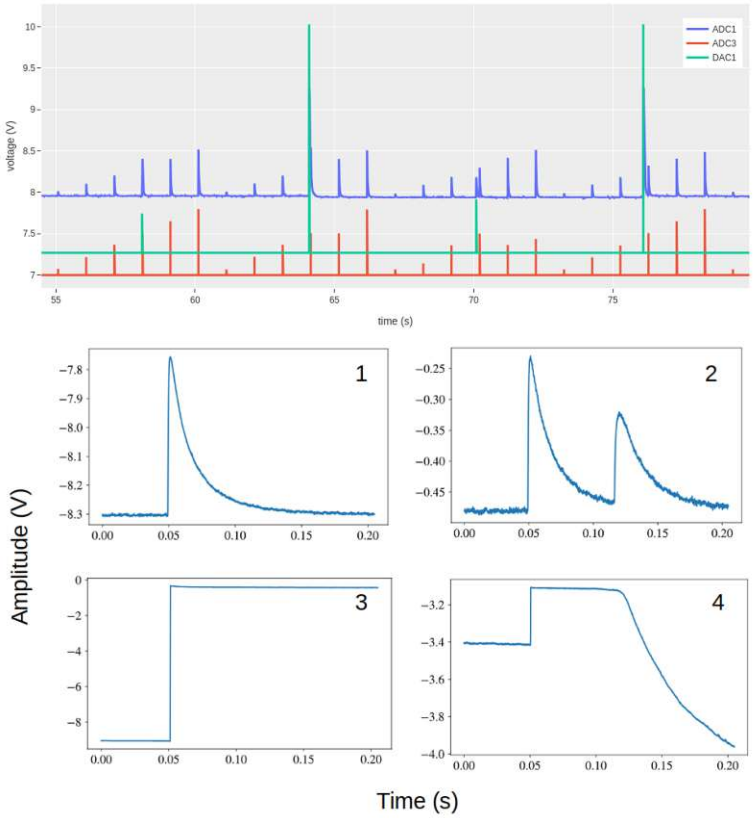

Figure 4.9. Top: Example of a stream showing the signal from the cryodetector on the ADC1 channel. The ADC3 and DAC1 channels are used to identify the timing of LED or heater pulse injections. Bottom: Example of some triggered pulses. Trace 1 is a physical pulse, and trace 2 is a pile-up. Then, there are some SQUID artifacts like SQUID reset (3) or flux quantum loss (4).

4.3.2 Detector response

Several analysis techniques, such as the use of an Optimum Filter for triggering and energy reconstruction, rely on the characterization of the detector's response. This includes knowledge of physical pulse shape and noise conditions of the detector.

4.3.2.1 Standard event

To characterize the detector's response to physical events such as electronic recoils, we aim to determine the typical pulse shape induced. It's the so-called standard event (SEV). To obtain it, we select well reconstructed pulses from the data by applying cuts to remove artifacts, noisy, and saturated pulses. All the pulse traces are then averaged to reduce noise fluctuations, and we can fit this averaged pulse using Pröbst's parametrization [109].

This allows us to obtain the fast and slow decay times of the pulse as well as its rise time. For the $CaWO_4$ cube, the SEV is shown in Figure 4.10, and the fit gives $\tau_{fast} = 9.2$ ms, $\tau_{slow} = 27.5$ ms and $\tau_{rise} = 655$ μs.

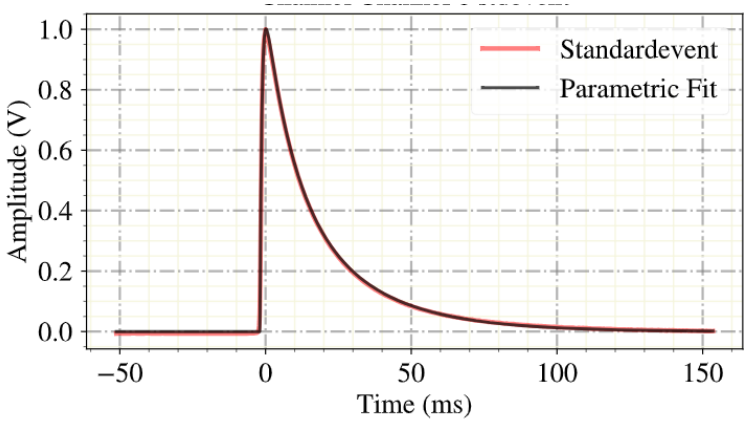

Figure 4.10. Built standard event (red). Also shown is the fit using the Pröbst's parametrization (black). More details in the text.

4.3.2.2 Noise Power Spectrum

To characterize the noise of the detector, we construct its Noise Power Spectrum (NPS). We select clean noise traces $x(t)$ from the data free of pulses, as shown on the left of Figure 4.11. The NPS is the Fourier Transform (FT) of the correlation function of $x(t)$: $R(\tau) =< x(t)x(t+\tau) >$ [159]. Thus, we define the noise power per unit of bandwidth in V^2/Hz:

$$NPS(\omega) = \lim_{T \to +\infty} \int_{-T}^{T} R(t) e^{-j\omega t}\, dt \tag{4.4}$$

It can be demonstrated, using the Wiener-Khinchin theorem, that the expression 4.4 is directly related to the Fourier transform of the noise trace $\hat{x}(t)$ [160]. Thus, we calculate the NPS from selected noise traces $x_i(t)$. We first apply the Fourier transform and then sample-wise average in Fourier space to obtain a reliable NPS [156]:

$$NPS(\omega) = \frac{2}{N.R.F} \sum_{i}^{N} rFFT[x_i(t)](\omega) \tag{4.5}$$

where rFFT is the real fast Fourier transform, N is the number of noise traces used to compute the NPS, R is the record length of those traces, and F is the sampling frequency. The factor 2 comes from the fact that we used a rFFT operator instead of a FT. The obtained NPS is plotted on the right of Figure 4.11 and displays the typical frequencies present in the noise. Notably, we can observe the 50 Hz and its harmonics.

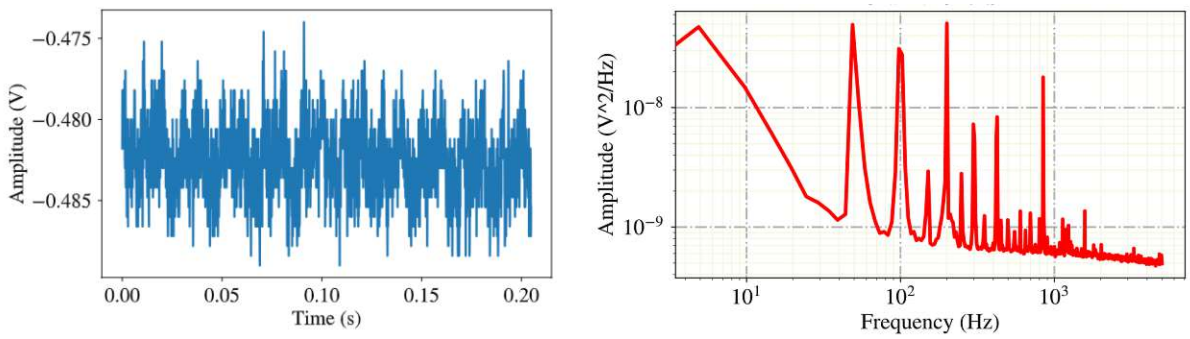

Figure 4.11. Left: Example of a clean noise trace selected to build the NPS. Right: NPS of the $CaWO_4$ cube. The 50 Hz and its harmonics are clearly visible.

4.3.2.3 Optimum filter

Now that we have a template pulse and the NPS, we can construct a frequency filter to enhance signal frequencies and suppress noise frequencies. The technique is called Optimum Filter (OF) or matched filter [161], and it is commonly used in cryogenic experiments to achieve lower detection thresholds were the signal to noise ratio is low. This is essential for experiments aiming to detect CEνNS, such as NUCLEUS, given the very low nuclear recoil energy induced by the neutrino [162]. The OF is therefore a transfer function that can be applied to the stream, and we can re-trigger on it with a lower threshold to be sensitive to low-energy pulses. It can be shown that the optimum filter maximizing the signal-to-noise ratio is the ratio of the SEV and NPS in Fourier space [156]:

$$H(\omega) = h\frac{S^*(\omega)}{NPS(\omega)}\, e^{-2i\pi\omega t_\phi} \tag{4.6}$$

where $S^*(\omega)$ is the complex conjugate of the standard event Fourier transform and $NPS(\omega)$ is the NPS presented in Section 4.3.2.2. t_ϕ is a time delay that allows adjusting the filter phase to align the maximum of the filtered pulse with the maximum of the non-filtered one and h is a normalization factor:

$$h = \frac{1}{\int \frac{|S(\omega)|^2}{NPS(\omega)} d\omega} \tag{4.7}$$

The Optimum Filter obtained is plotted on the left of Figure 4.12. We can see the suppression of the dominant frequencies of the NPS. To filter a pulse trace, we first perform the Fourier transform of the trace, then apply the transfer function (Equation 4.6), and finally transform it back to temporal space. More details about the filtering of the trace can be found in [155, 156]. An example of a filtered pulse is shown on the right of Figure 4.12. Although the filtered pulse is distorted, it preserves the amplitude of the initial pulse.

In addition to lowering the energy threshold and increasing the signal-to-noise ratio, the OF has many advantages. The time estimation of the pulses is more accurate, improving the time resolution of the detector, which allows for reducing the time window to search for coincidences with vetoes systems. Finally, it turns out that the OF is a very good estimator of the pulse amplitude, as we will see in the next section.

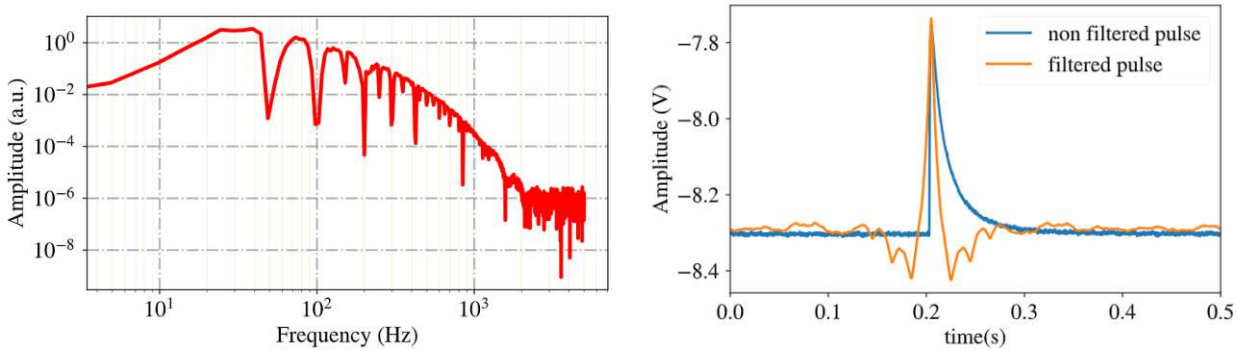

Figure 4.12. Left: The OF transfer function. Noise frequencies are strongly suppressed. Right: Pulse before and after filtering. The OF unshapes the pulse but preserves its amplitude.

4.3.3 Energy reconstruction

All the cryodetector analysis methods presented previously have one goal: to obtain a deposited energy spectrum. As we saw in Section 2.4.1, the pulse amplitude is proportional to the deposited energy. Therefore, a reliable estimation of the pulse amplitude is necessary, especially for low pulses overwhelmed by the noise fluctuations. Let's find a good pulse height estimator. For this, we will use the least squares error minimization method [163]. A pulse trace is the sum of a signal $s(t)$ with amplitude A and a noise $n(t)$:

$$v(t) = As(t) + n(t) \tag{4.8}$$

We can fit this pulse with a signal of amplitude A. Let's define the χ^2 of this fit in frequency space [159]:

$$\chi^2 = \int_{-\infty}^{+\infty} \frac{|\tilde{v}(\omega) - A\tilde{s}(\omega)|^2}{NPS(\omega)} d\omega \tag{4.9}$$

The best estimation for A is obtained by minimizing χ^2 with respect to A:

$$\hat{A} = \frac{\int_{-\infty}^{+\infty} \frac{\tilde{s}^*(\omega)\tilde{v}(\omega)}{NPS(\omega)} d\omega}{\int_{-\infty}^{+\infty} \frac{|\tilde{s}(\omega)|^2}{NPS(\omega)} d\omega} = \int_{-\infty}^{+\infty} H(\omega)\tilde{v}(\omega) d\omega \tag{4.10}$$

The best estimator for $\hat{A}$ is the convolution of the Optimum Filter with the trace $v(t)$, corresponding to the peak amplitude of the filtered trace. The OF amplitude is therefore a very good estimator of the energy, especially for low-energy pulses. At higher energies, close to the saturation level, the pulse shape changes, and thus the OF amplitude is no longer accurate. One common method is the reconstruction of saturated pulses using the SEV template, which can be fitted to a saturated pulse using a truncated fit [155, 156]. In the analysis of this Run, saturated events are discarded since we are interested in the background rate in the keV region, below the saturation. Therefore, all the spectra in this chapter are reconstructed in energy using the OF amplitude.

4.3.4 FCR analysis chain

The NUCLEUS data have been analyzed using different analysis software, and the analysis chain I am presenting here is the one from CAIT. Figure 4.13 illustrates the different steps of the analysis as a block diagram. At the beginning of each week, a LED calibration run is performed, followed by background data taking. First of all, we analyze the LED calibration files to obtain the calibration factor, of course, but also for the pre-trigger analysis. As mentioned earlier, to lower the energy threshold, we need to filter the stream using the OF. This OF was built from SEV and NPS of LED data. The pre-trigger analysis also determines the baseline resolution (BR) (see Section 4.5). In a second step, we analyze the background data, and thanks to the optimum filter pulse height estimation and the calibration factor, we can construct a recoil energy spectrum. Finally, the high-level analysis involves applying data quality cuts to clean the data, particularly to remove artifacts or pile-up. These data quality cuts are defined on the LED calibration data before being applied to the background data. Hence, we can compute the trigger and cut efficiencies using the LED data and correct the energy spectrum from those efficiencies. Finally, we define a coincidence criteria with the vetoes systems that allows us to study the background rate before and after vetoes cuts.

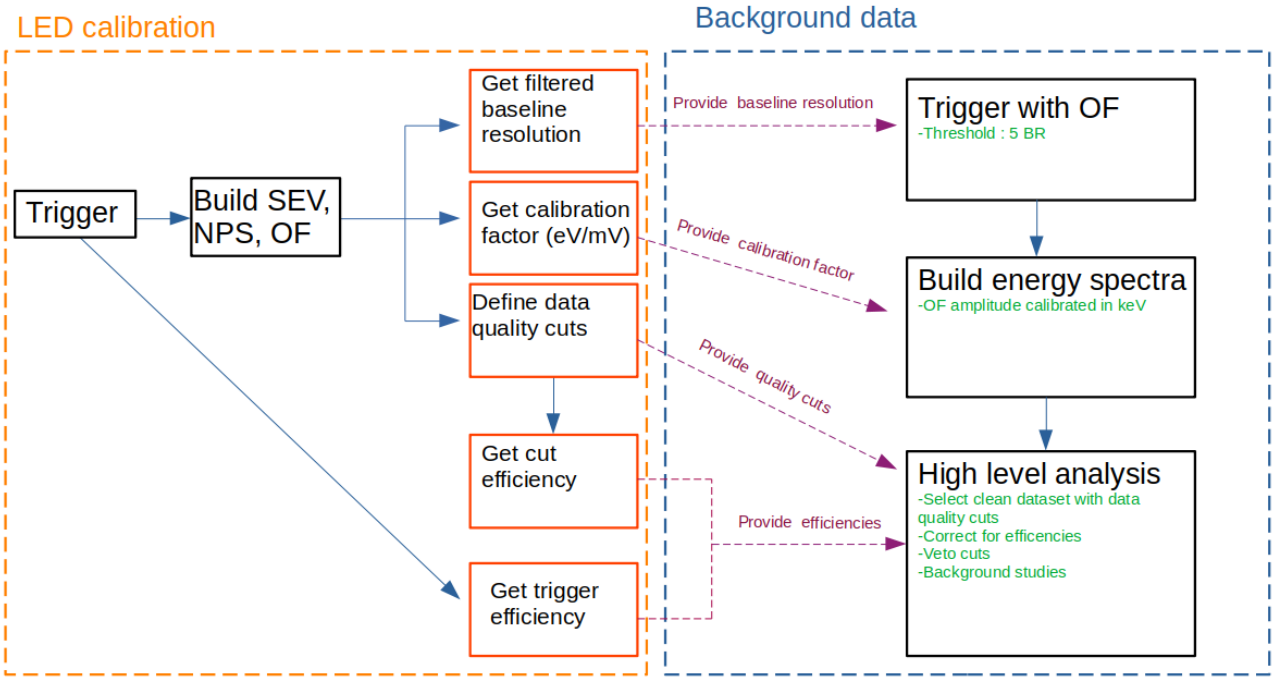

Figure 4.13. CAIT analysis chain for the FCR.

4.4 Energy calibration

To obtain a recoil energy spectrum, the detector response must be calibrated. Several calibration methods exist and have been outlined in Section 2.4.5. During the FCR, we performed regular LED calibrations. This method use optical photons from LED to calibrate the detector. Another method takes advantage of the existence of X-rays lines due to copper activation in background data. However, it is important to keep in mind that both method calibrates electronic recoils, not nuclear recoils. Let's first describe the principle of the LED calibration method before applying it to the FCR data.

4.4.1 LED calibration method

The calibration of the cryodetector at the keV scale needs certain precautions. The common method is to send X-rays to irradiate the detector. However, their low penetration depth in materials requires placing the source in the vicinity of the detector holder. At the same time, such a source could bias the background rate estimation in the keV energy range. This rules out the possibility of using a radioactive source emitting X-rays. The LED calibration addresses this technical challenge: by sending optical photons from an LED, which can be switched on and off, we don't interfere with the background measurement. The experimental setup is as follows: an LED emits optical photons of fixed energy (λ = 255 nm, E = 4.87 eV). The choice of this wavelength is deliberate, as it is just below the gap of $CaWO_4$ ($E_g \sim 4.9$ eV). Still it is possible to excite electrons and produce electronic recoils due to impurities and dynamical effects. The penetration depth of these optical photons allows them to propagate through the crystal and induce electronic recoils in the bulk of the detector: the crystal is semi-transparent. The emitted photons are guided through a fiber towards the detector holder. Special care is taken for the cooling of the fibers, because if thermalization is inadequate, they could become IR hotspots close to the detector, ruining any hope of a physical measurement. To deposit energy in the keV range, photons are sent in packets within a time interval much shorter than the bolometer response time $O(100\ \mu s)$. The LED frequency is therefore set to 290 kHz for $CaWO_4$ and 3 MHz for Al_2O_3, which has a faster time response. These frequencies are chosen such that the cryodetector's time response fully integrates the total energy deposited in a single event. The number of photons N_{ph} sent follows a Poisson distribution with mean value $\langle N_{\mathrm{ph}} \rangle$. Consequently, the detector response follows a Gaussian distribution with mean μ (in mV) given by [153]:

$$\mu = r \, \langle N_{\mathrm{ph}} \rangle \, \epsilon_{\mathrm{ph}} \tag{4.11}$$

The associated variance is:

$$\sigma_E^2 = (r \, \epsilon_{\mathrm{ph}})^2 \, \langle N_{\mathrm{ph}} \rangle = r \, \mu \, \epsilon_{\mathrm{ph}} \tag{4.12}$$

where r is the calibration factor in mV/eV, ϵ_{ph} is the energy of a single photon. Finally, taking into account the baseline resolution σ_0, we have:

$$\sigma_{tot}^2 = \sigma_E^2 + \sigma_0^2 = r\mu\epsilon_{ph} + \sigma_0^2 \tag{4.13}$$

Thus, there is a linear relationship between μ and σ_{tot}^2, where the slope $r\epsilon_{ph}$ directly provides access to the calibration coefficient r. In practice, we generate multiple distributions with different $< N_{ph} >$ and obtain μ and σ_{tot} by fitting the multiple Gaussian distributions, as seen on the top of Figure 4.14.

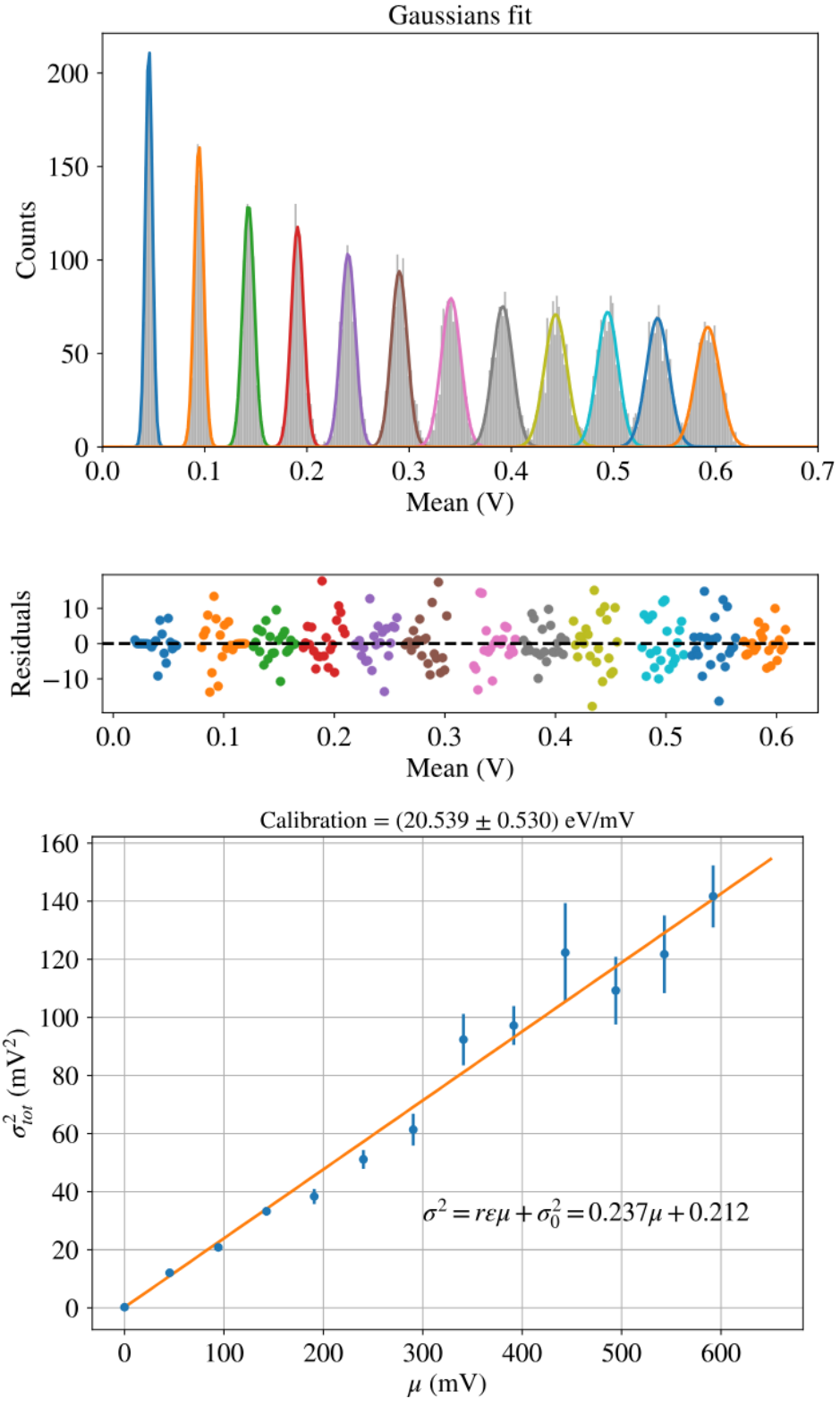

Figure 4.14. Top: Gaussian fits of the Poisson distributions generated by the LED. Bottom: Linear fit of the extracted standard deviation and mean from the previous Gaussian fits. According to Equation 4.13, the slope gives the calibration factor.

A linear fit using Equation 4.13 allows us to determine the detector calibration factor r for the $CaWO_4$ cube, yielding a value of 20.5 ± 0.5 eV/mV for this segment (see bottom of Figure 4.14). The time evolution of this calibration factor, measured during the LED calibration segments, is shown in Figure 4.15. The advantage of this method is that it does not require knowledge of the number of photons sent, as both μ and σ_{tot} depend on $< N_{ph} >$. Therefore, it is robust against uncertainties in fiber transmission or in the LED luminosity.

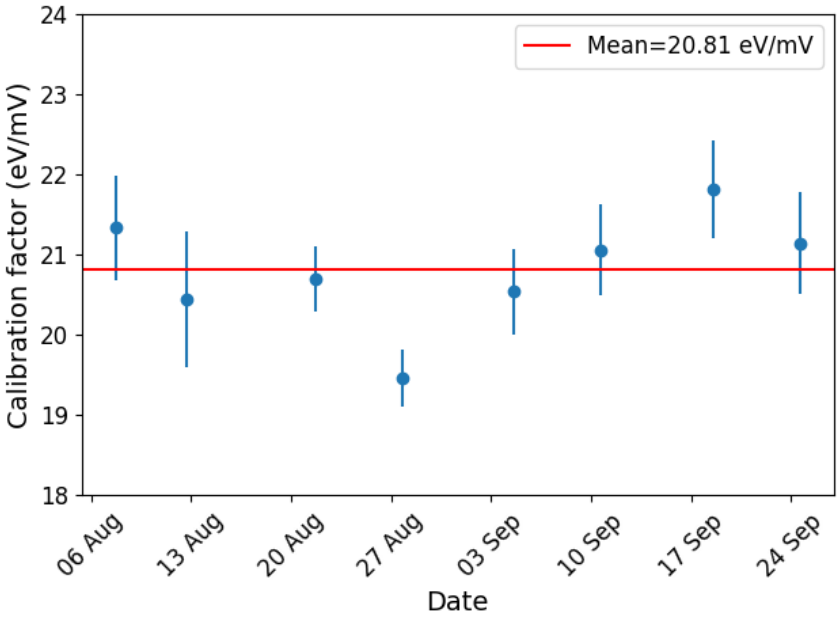

Figure 4.15. LED calibration stability over time.

4.4.2 Copper calibration

The background spectrum of the $CaWO_4$ detector saturates around 25 keV, allowing the observation of the two characteristic X-ray lines, K_α and K_β, from the cosmogenic activation of copper at 8.05 keV and 8.9 keV, respectively. These two peaks are clearly visible above a flat background and can be used to extract a calibration constant, which can then be compared to the one obtained from the LED calibration. Figure 4.16 shows this feature in the background data of $CaWO_4$, along with a fit using two Gaussian functions and a constant background. The peak positions are found to be at $\mu_1 = (459.8 \pm 0.7)$ mV and $\mu_2 = (514 \pm 3)$ mV. The ratios $\frac{\mu_2}{\mu_1} = 1.11 \pm 0.01$ and $\frac{A_1}{A_2} = 7.3 \pm 2.8$ are in agreement with the expected values for Copper K_α and K_β X-rays, namely an energy ratio of 1.11 and an intensity ratio of approximately 7.7 [164]. The obtained calibration factor is (17.51 ± 0.03) keV/V (eV/mV). This value is 15% lower than the one obtained from the LED calibration. This discrepancy is still under investigation and demonstrates the limits of such calibration methods. It highlights the need for a precise calibration of nuclear recoils in the relevant energy range, as proposed by CRAB (see Chapter 5), to calibrate the future CEνNS signal.

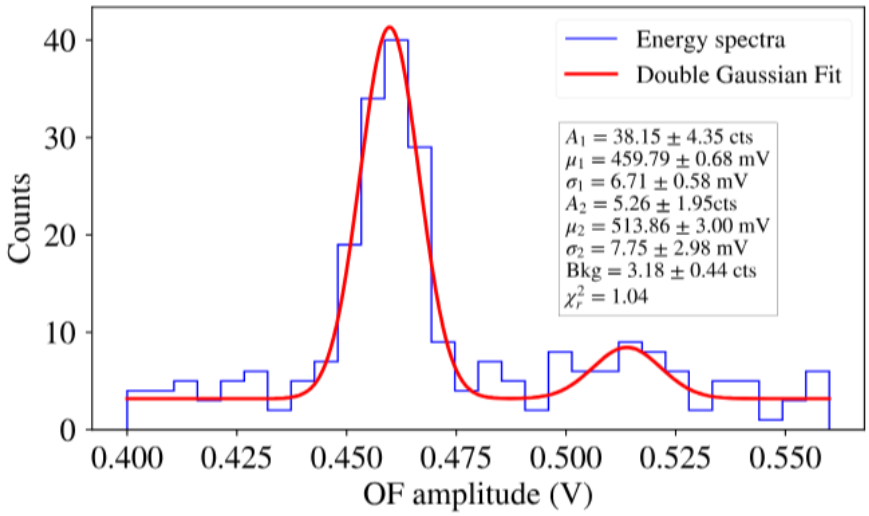

Figure 4.16. Copper K_α and K_β lines identified in the energy spectrum using all background data from $CaWO_4$. The fit parameters are shown. The obtained calibration factor is (17.51±0.03) keV/V (eV/mV).

4.5 Detector performance: stability and resolution

An important parameter for characterizing the performance of a detector is the energy resolution. At high energy, it depends on the deposited energy, however, at low energy, the dominant contribution to the energy resolution is the baseline resolution σ_0. This is also what limits the energy threshold, which is commonly set at 5 σ_0. Naively, it's just the standard deviation of a noise trace. However, one can benefit from the OF, which allows for filtering the noise and reducing the baseline resolution, thereby allowing for a lower energy threshold. With OF, the best possible resolution achievable is [159]:

$$\sigma_0^2 = \frac{1}{\int \frac{|S(\omega)|^2}{NPS(\omega)} d\omega} \tag{4.14}$$

The procedure to obtain the baseline resolution is as follows: several clean noise traces are selected, then filtered using the OF, and the standard deviation of the filtered traces amplitude is calculated. The distribution of those traces for one LED segment is shown on Figure 4.17. The OF has reduced the baseline resolution from 2.3 mV to 0.45 ± 0.01 mV. This translates into an energy resolution of $\sigma_0 = 7.92 \pm 0.13$ eV after applying energy calibration factor of 17.51 eV/mV derived in Section 4.4.2 from copper activation. This baseline resolution remains stable around an average value of $\overline{\sigma}_0 = 7.67$ eV over all LED segments (see Figure 4.18). Our energy threshold is set at 5 $\overline{\sigma}_0$ corresponding to 38.4 eV. For CEνNS detection, this energy threshold is in the ball park of the tens targeted electron volts and sufficient to conduct a background measurement in the keV region. The stability of the detector response is monitored with the reconstructed amplitudes of the injected heater pulses. These amplitudes are very stable during the entire run, with variations among configurations smaller than 1% (see Figure 4.19).

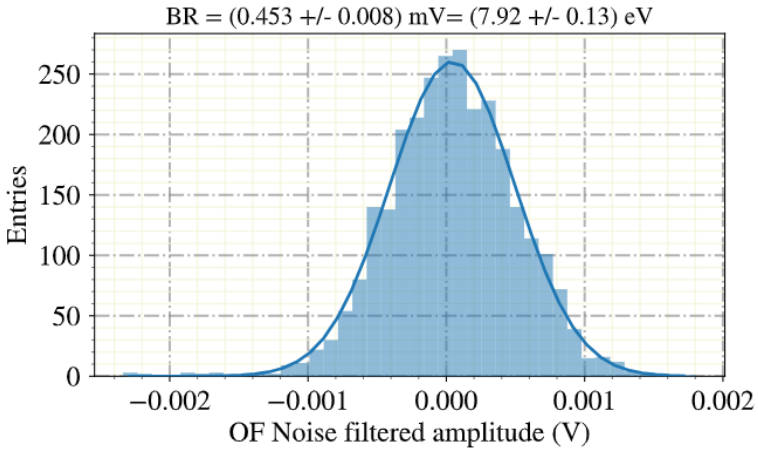

Figure 4.17. The distribution of the filtered noise trace amplitudes for one segment file. The standard deviation gives the baseline resolution of 0.45 mV, corresponding to 7.92 ± 0.13 eV.

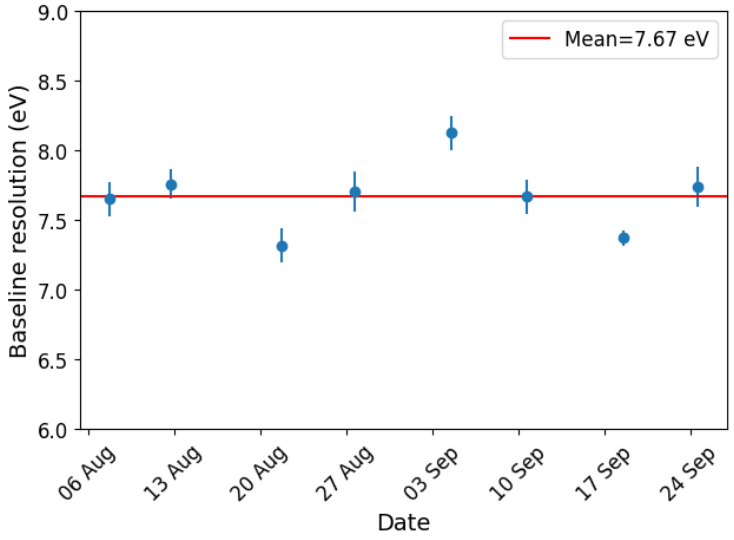

Figure 4.18. Baseline resolution stability over LED calibration configurations.

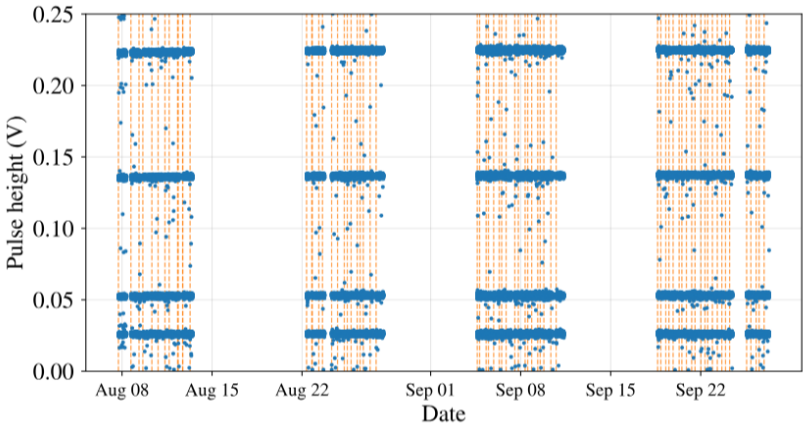

Figure 4.19. Stability of the heater pulses responses. Each data file is indicated by an orange line.

4.6 Background in $CaWO_4$

Now that the pre-trigger analysis has been done, we can finally analyze the background data and build a deposited energy spectrum. A raw spectrum, calibrated using the copper X-ray lines, is shown in grey in Figure 4.20. The high-level analysis presented in this section includes pulse shape cuts to clean the data and estimation of the cut and trigger efficiencies. Finally, the background energy spectrum is used to estimate the event rate in coincidence with the vetoes systems and is compared to simulation predictions.

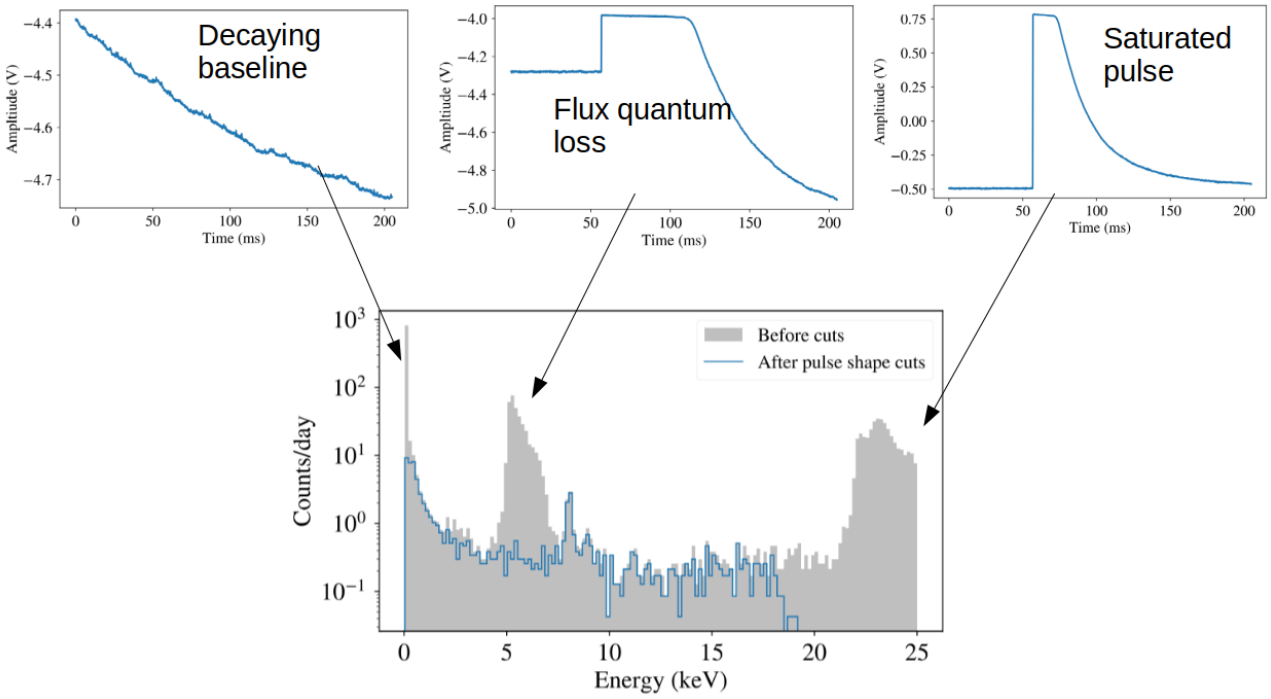

Figure 4.20. Background recoil energy spectra in $CaWO_4$ before (grey) and after pulse shape cuts (blue). These cuts, defined in the text, remove artifacts such as decaying baseline and flux quantum loss. They also discard saturated events with inaccurate energy estimation.

4.6.1 Pulse shape cuts

The grey spectrum shown in Figure 4.20 contains some artifacts, such as a decaying baseline and flux quantum loss, which are reconstructed with fake energy around 6 keV. Additionally, the energy estimation for saturated pulses is not accurate. Therefore, to get the background recoil energy spectrum, I will first apply data quality cuts to select only good pulses and remove artifacts. These cuts are preliminary defined on the LED data before being applied to the background data. Let's now present the parameters used to define these cuts and examples of pulses they allow us to discard.

- **Right-left baseline:** The difference between the average of the last 500 samples and the average of the first 500 samples of the trace. If the pulse has time to decay completely within the selected window, this quantity should be small, comparable to baseline fluctuations. For saturated pulses that don't completely decay within the window, this parameter may differ from 0, indicating an energy dependence. This cut is quite efficient in removing flux quantum loss (see Section 2.4.3.2). We select pulses with a Right-left baseline in the range [-5, 2] mV.

- **RMS of the Optimum Filter:** The RMS between the filtered pulse trace $x_i(t)$ and the filtered standard event trace $\tilde{x_i}(t)$ is calculated as:

$$\sum_{i}^{N_{sample}} (x_i(t) - \tilde{x_i}(t))^2 \tag{4.15}$$

  with N_{sample} being the number of samples forming the trace, here equal to 2048.

  This cut is very effective at rejecting all artifacts with shapes different from thoses of standard pulses. We select pulses with an OF-RMS below 10^{-5} V^2.

- **Decay time:** This is the time difference between the sample that falls below 90% of the maximum amplitude and the one that falls below 36% of the maximum amplitude. This cut is effective in rejecting decaying baselines. However, at low energy, this parameter is not properly calculated, it might results in lower efficiency. We select pulses with decay times in the range [13, 19] ms.

- **Variance of the baseline:** Calculated from the first 1/8 of the trace. If the pulse is sitting on a flat baseline, the variance should be on the order of the detector noise. This cut is effective in rejecting pulses sitting on a decaying baseline due to pile-up. We select pulses with baseline variance below 1.5×10^{-6} V^2.

The distribution of each of these parameters for both LED and background data is shown in Figure 4.21, with the cuts indicated by the red dashed line. It can be seen that these cuts effectively remove the outliers, which are artifacts. The clean spectrum obtained is shown in blue in Figure 4.20. The spectrum is flat above 2.5 keV, exhibits a double-peak structure around 8 keV due to copper X-rays, and shows a high event rate exponentially distributed at low energies called the Low Energy Excess.

4.6.2 Efficiency estimations

The cuts defined previously remove artifacts, but unfortunately also some physical events, mainly due to misestimation of the parameters described above, for example, due to pile-up. A physical pulse has a certain probability of surviving these pulse shape cuts, which is what we call "cut efficiency". Note that this cut efficiency $\epsilon_{cut}(E)$ may depend on the energy.

Moreover, the trigger procedure described in Section 4.3.1 also implies a trigger inefficiency. At high energy, this is mostly due to pile-up. Indeed, if two pulses are too close in time, we only count one event. Given the low particle event rate, pile-up mostly concerns a particle event and an injected heater pulse. A physical pulse has a certain probability of being triggered. This trigger efficiency, $\epsilon_{trigger}(E)$, also depends on the energy. At lower energy, trigger inefficiency also takes into account the misreconstruction of the pulse amplitude. Since my study is limited to the keV range, $\epsilon_{trigger}(E)$ is not estimated at low energy. A more complete study has been conducted for LEE rate estimation in [165]. Finally, the total efficiency is:

$$\epsilon_{tot}(E) = \epsilon_{cuts}(E) \times \epsilon_{trigger}(E) \tag{4.16}$$

We should estimate these efficiencies to correct the event rate. To do so, LED calibration data are used, as the injected LED signal is recorded in a separate read-out channel, allowing us to know exactly the total number of injected LED pulses, N_{LED}, at each amplitude. For each LED amplitude, the number of triggered pulses, N_{trig}, gives the trigger efficiency, while the number of pulses surviving the cuts, N_{cuts}, gives the cut efficiencies. Since the injected energy is between 1 and 13 keV, we can study the energy dependence of the trigger, cut, and

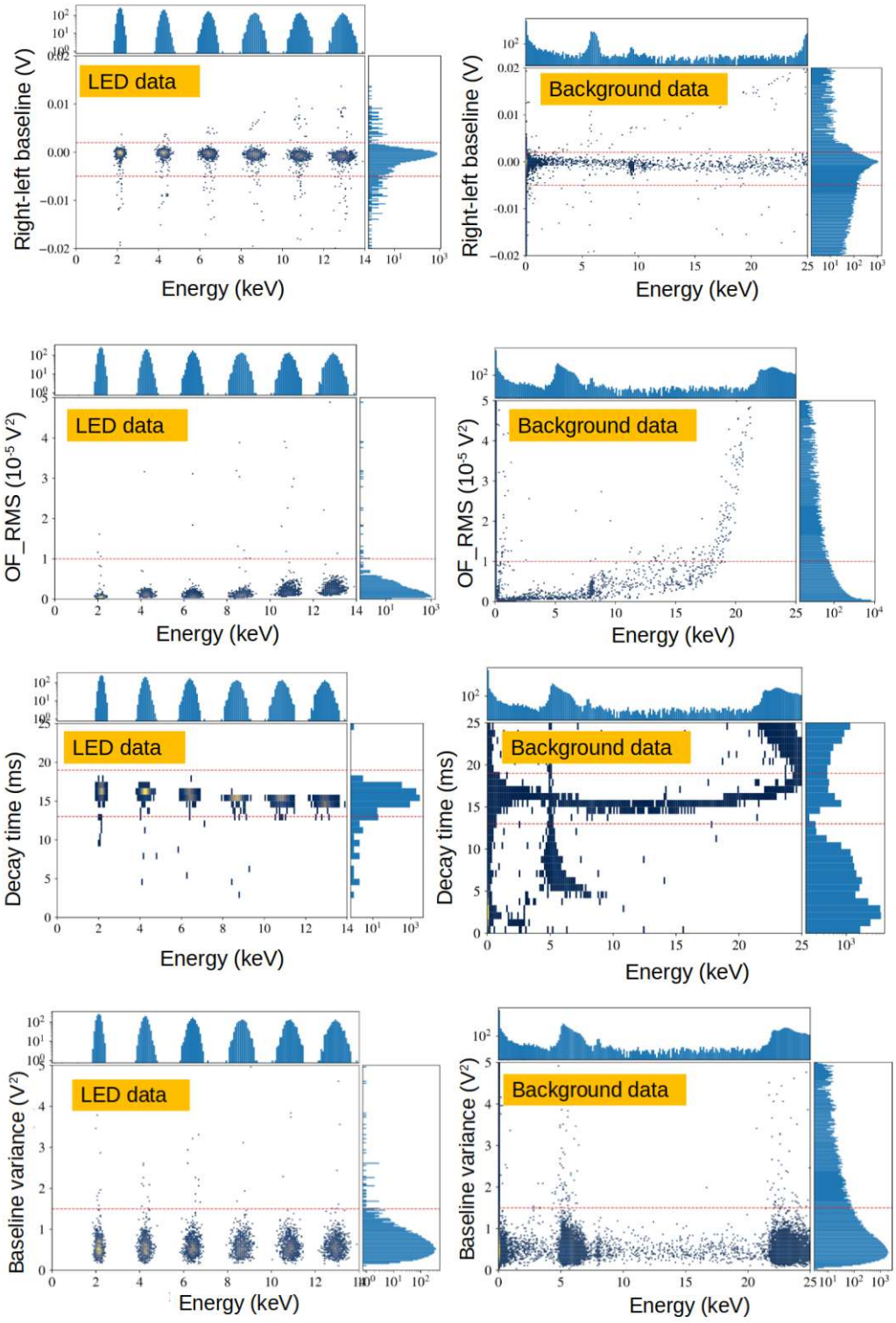

Figure 4.21. Left: Pulse shape cuts defined on LED data. We can see that these cuts are defined to remove outliers and select only physical events (in the blobs). Right: Same cuts applied to the background data.

total efficiencies in this energy range. The trigger and pulse shape cut efficiencies can be extracted for each LED amplitude as:

$$\epsilon_{trigger}(E) = \frac{N_{trig}}{N_{LED}} \tag{4.17}$$

$$\epsilon_{cuts}(E) = \frac{N_{cuts}}{N_{trig}} \tag{4.18}$$

with their uncertainties [154]:

$$\sigma_{\epsilon_{trigger}} = \sqrt{\frac{\epsilon_{trigger}(1-\epsilon_{trigger})}{N_{LED}}} \tag{4.19}$$

$$\sigma_{\epsilon_{cuts}} = \sqrt{\frac{\epsilon_{cuts}(1-\epsilon_{cuts})}{N_{trig}}} \tag{4.20}$$

Figure 4.22 shows the trigger, cut, and total efficiencies as functions of energy. Above 1 keV, the trigger efficiency is almost flat with a slight increase with energy. For the cut efficiency, it's the opposite: the cuts become more stringent at higher energies as the pulse shape is distorted due to the approach to saturation. We obtain a mean trigger efficiency of (95.8 ± 0.5)% and a mean cut efficiency of (96.6 ± 0.8)%. Finally, the total efficiency can be considered as constant, and in the following analysis, I consider the efficiency to be energy independent. Therefore, I use the mean value: 92.5%.

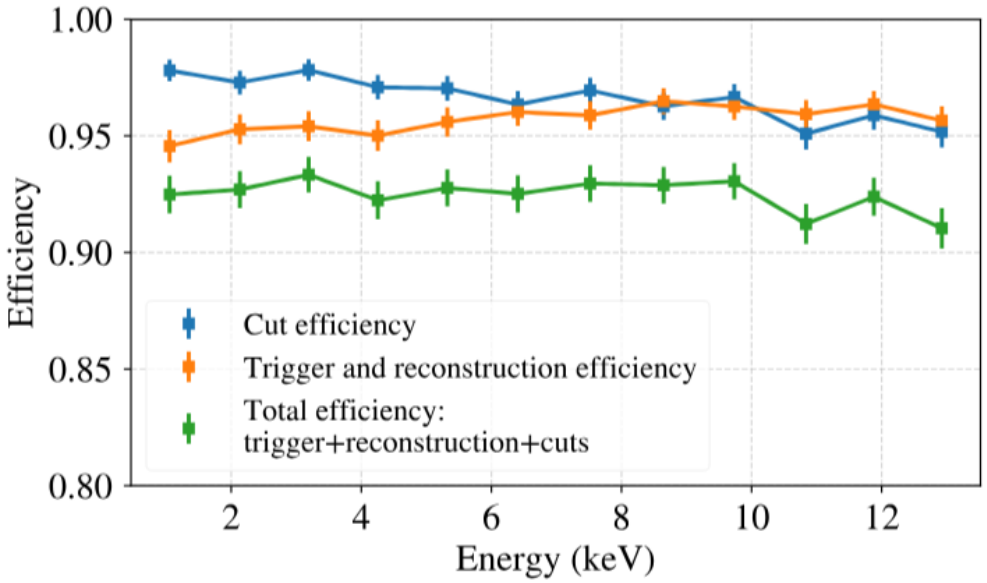

Figure 4.22. Trigger, cut and total efficiencies versus energy. The total efficiency can be considered as constant with a mean value of 92.5%.

4.6.3 Coincidences with the Muon Veto and the COV

The recoil energy spectrum corrected for cut and trigger efficiencies is shown in Figure 4.23. To estimate the background rate, I use the flat part of the spectrum between 2.5 and 7.5 keV. This range is above the low-energy rise and below the copper peaks. The measured rate is **2951 ± 202 dru** (event/keV/day/kg), corresponding to one event every two hours in the [2.5,7.5] keV range. This event rate can be further reduced by taking advantage of the anticoincidence with vetoes systems. As done in Section 4.2.1, the selection of coincidences between the cryodetector and the COV and MV relies on the time differences between all events in the cryodetector and the closest event in the corresponding veto system. Figure 4.24 shows the distributions of these time differences for both MV and COV, where we can clearly see the coincidence peaks. They have a similar mean value of $\mu \approx 120\ \mu s$ and a width of $\sigma \approx 25\ \mu s$. Therefore, the coincidence window is chosen between 0 and -240 μs. The number of accidental coincidences can be evaluated using the accidental probability. With the observed muon rate of 197 Hz and a 240 μs window, one would expect a 4.7% probability of random coincidences. The accidental coincidences expected with the COV, however, are negligible.

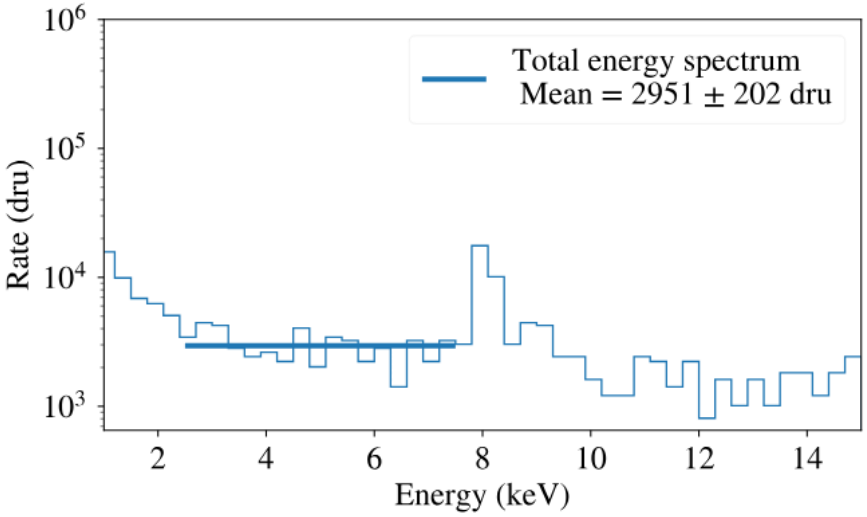

Figure 4.23. Single background energy spectrum in $CaWO_4$. The measured rate in [2.5,7.5] keV is 2951 ± 202 dru.

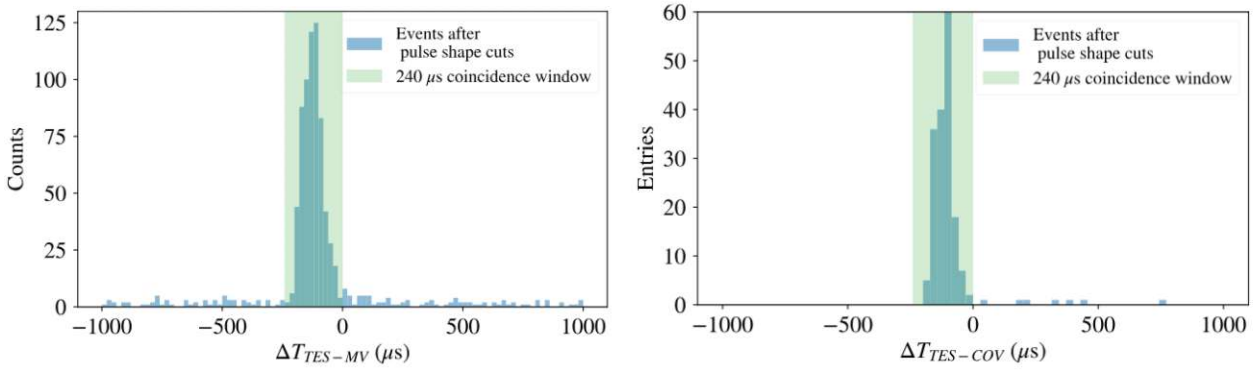

Figure 4.24. Veto coincidence window for MV (left) and COV (right).

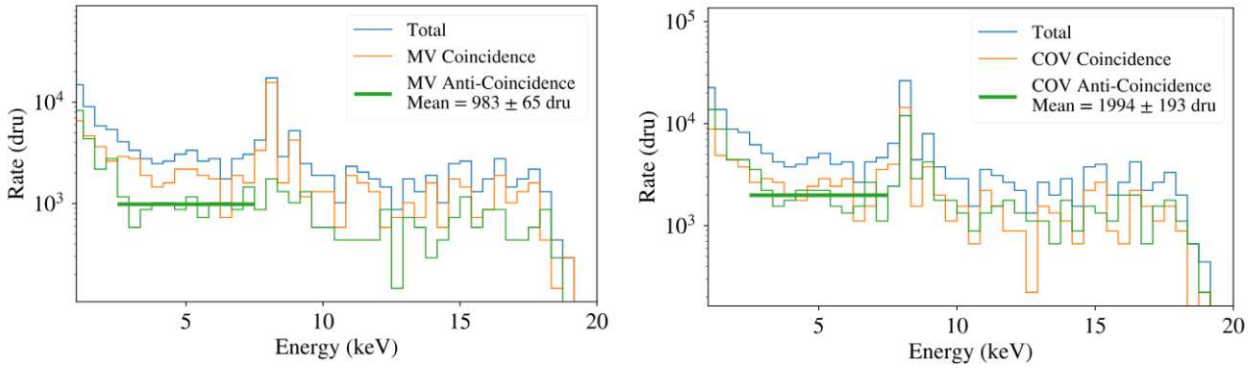

Figure 4.25. $CaWO_4$ spectra in coincidence and anticoincidence with MV (left) or COV (right).

On the left of Figure 4.25, we can see that the two lines around 8 keV are fully in coincidence with MV, as they result from the activation of Copper by muons. The measured rate in the [2.5,7.5] keV range is **983 ± 65 dru** (equivalent to one event every 7 hours). The MV attenuation factor is then 3.0 ± 0.3. Regarding the COV, since only one crystal is installed, the attenuation factor is lower at 1.5 ± 0.2, leading to an event rate in anticoincidence with the COV of **1994 ± 193** dru (equivalent to one event every 3 hours). Finally, when both the COV and MV cuts are applied, we end up with an event rate of **868 ± 88 dru**, as seen in the anticoincidence spectrum in Figure 4.26 (equivalent to one event every 7.5 hours). This is the background level that we were able to reach during this FCR. The MV+COV veto attenuation factor is 3.4 ± 0.4. The discrepancy between data and simulation predictions can be computed as the ratio of the event rate in data to that in simulation. The Table 4.4 summarizes the event rate as well as vetoes attenuation factors in data and simulation and the corresponding discrepencies. While the vetoes attenuation factors matches very well with the simulation predictions, we observe discrepancies in the event rates, with a consistent data-to-simulation ratio (ranging from 1.5 to 1.9) across all vetoes configurations. It is important to note that the measured background do not include atmospheric neutrons, which are stopped by the UGL hill. However, they do include the muon and gamma components. Muons are efficiently rejected thanks to the high Muon Veto rejection power of 98.6%. As for the gamma background, its mitigation has not yet been validated, since only one out of the six COV crystals was installed. This currently constitutes the dominant contribution to the residual background rate measured after vetoes cuts.

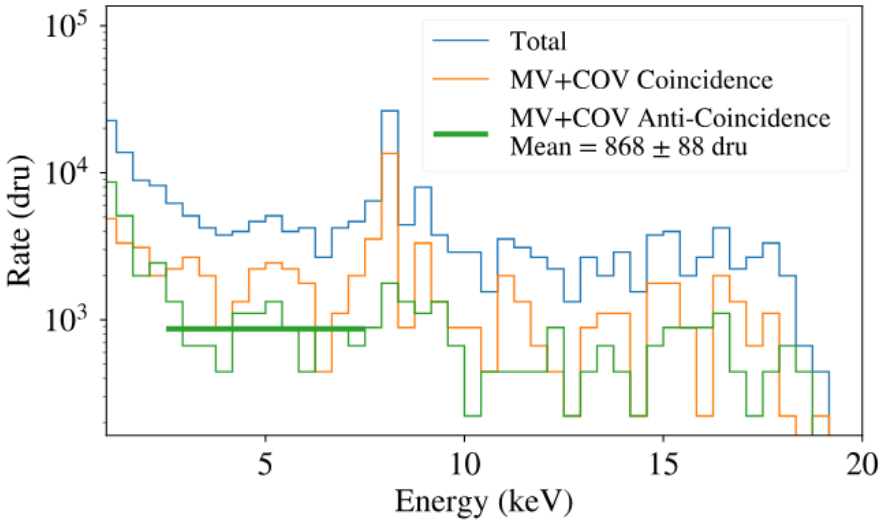

Figure 4.26. $CaWO_4$ spectra in coincidence and anticoincidence with both MV and COV. The measured background after all vetoes is 868 ± 88 dru.

Detector	Veto systems	Rate in [2.5–7.5] keV (counts / (keV · kg · day))			Veto attenuation factor		
		Data	Simulation	Discrepancy	Data	Simulation	Discrepancy
$CaWO_4$	No Veto	2951 ± 202	1969 ± 28	1.5	–	–	–
	MV	983 ± 65	574 ± 18	1.7	3.0 ± 0.3	3.4 ± 0.1	0.9
	MV+COV	868 ± 88	527 ± 17	1.6	3.4 ± 0.4	3.7 ± 0.1	0.9

Table 4.4. Comparison of measured and simulated rates and vetoes attenuation factors in the $CaWO_4$ detector. The discrepancies, defined as the ratios between data and simulation values, are also shown.

4.7 Background measurement in the Al_2O_3 detector

The second cryogenic detector commissioned during the FCR campaign was a Al_2O_3 target instrumented with a double TES readout. A total of 571.88 hours of data were collected in parallel with the MV (without the COV in operation). I was not personally involved in the analysis of this detector and will therefore only briefly present the key results, including the measured background rate and the impact of the anti-coincidence with the MV. These results were analyzed using the DIANA software framework [166, 167] and are discussed in more detail in [165].

Figure 4.27 shows for the Al_2O_3 detector the energy spectra recorded in single and in anti-coincidence with the MV. It saturates above 4 keV, therefore the background rate is estimated in the [1.4,3.5] keV range. The measured and simulated background rates, as well as the MV attenuation factor, are summarized in Table 4.5. In anticoincidence with the Muon Veto a background rate of 2302 ± 256 dru was measured. A similar discrepancy between data and simulation as observed for $CaWO_4$ is also seen. It is also worth noting that the background rates are higher in Al_2O_3 compared to $CaWO_4$, primarily due to the larger volume of the Al_2O_3 detector.

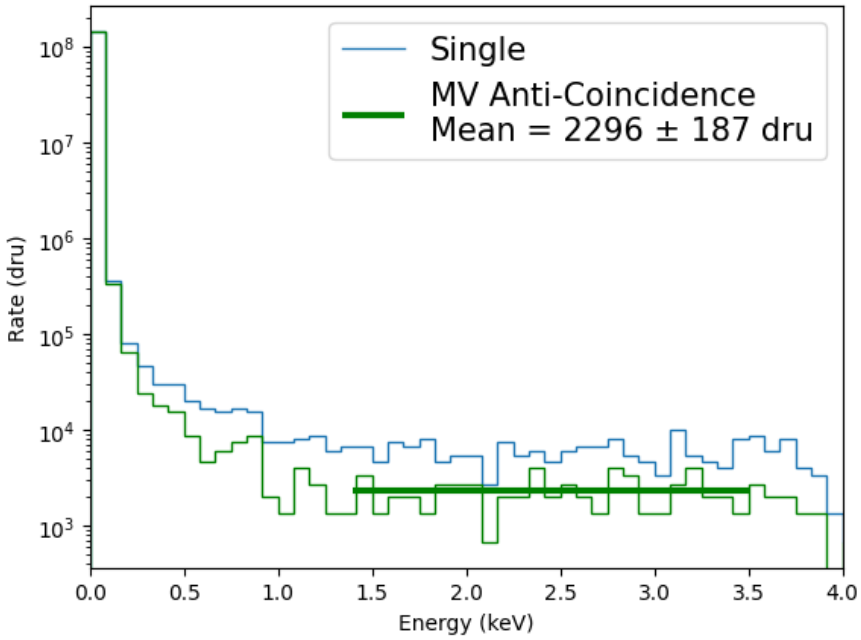

Figure 4.27. Al_2O_3 spectra in single and in anticoincidence with MV. The measured background rate after MV cut is 2296 ± 187 dru.

Detector	Vetoes systems	Rate in [1.4–3.5] keV (counts / (keV · kg · day))			Veto attenuation factor		
		Data	Simulation	Discrepancy	Data	Simulation	Discrepancy
Al_2O_3	No Veto	5970 ± 337	3964 ± 68	1.5	–	–	–
	MV	2296 ± 187	1459 ± 50	1.6	2.6 ± 0.4	2.7 ± 0.1	1.0

Table 4.5. Comparison of measured and simulated rates and MV attenuation factor in the Al_2O_3 detector. The discrepancies, defined as the ratios between data and simulation values, are also shown.

4.8 Conclusion

During the FCR, the detectors forming NUCLEUS operated successfully and the coincidences between them were validated. The muon rejection performance of the Muon Veto was measured for the first time and met the specifications. The measured background rate in both the $CaWO_4$ and Al_2O_3 cryodetectors in the keV energy range was found to be approximately 1.7 times higher than predicted by simulations. This discrepancy has served as an important benchmark for the refinement of the NUCLEUS simulation framework.

However, the neutron background rejection still needs to be validated at Chooz, where the atmospheric neutron background is no longer negligible. Additionally, the particle background in the CEνNS region of interest (ROI) has not yet been studied in detail, as the event rate in this region is currently dominated by the LEE.

The FCR has also provided valuable insights into the origin and rejection of the LEE, thanks in particular to the dual TES readout technology. This configuration allows us to distinguish events depositing energy in one TES, the other, or both simultaneously. Events detected by only one TES are likely due to interface effects between the TES and the crystal, whereas physical energy depositions induce signals in both TESs. Data from the FCR shows the presence of single-TES events and a shared band characteristic of physical events. We believe that another component of the LEE arises from stress between the holder and the crystals, similar to the stress observed between the sensor and the crystal. The rejection of such events is currently being investigated using an instrumented holder: the inner veto. Finally, preliminary analyses indicate that the LEE rate strongly depends on the cool-down duration: the slower the cool-down, the lower the LEE rate. Validation of LEE rejection using the double TES will be part of the technical run planned at Chooz (see Section 2.8.2), while R&D on the inner veto will be carried out in parallel at the cryolab in Munich.

5

The CRAB experiment: Calibration of cryogenic detectors for sub-keV nuclear recoils

The ability of cryogenic detectors to detect sub-keV nuclear recoils makes them promising candidates for the detection of CEνNS or light dark matter. The calibration of these low-energy nuclear recoils is therefore of great importance. In this chapter, I present an innovative new method for calibrating low-energy nuclear recoils in cryogenic detectors: "Calibrated Recoil for Accurate Bolometry" (CRAB).

The CRAB collaboration was established in 2019 and consists of about forty people from several institutes across four European countries: Commissariat à l'Énergie Atomique et aux Énergies Alternatives de Saclay (CEA Saclay and CEA Cadarache, France), Technische Universität München (TUM, Germany), Istituto Nazionale di Fisica Nucleare (INFN, Italy), Institute of High Energy Physics (HEPHY, Austria), and Technische Universität Wien (TUW, Austria). This collaboration started in synergy with NUCLEUS, as $CaWO_4$ (the target material used by NUCLEUS, but also relevant for CRESST) is a favorable case for the CRAB method. Then, the CRAB collaboration has expanded to other experiments (RICOCHET and TESSERACT) to apply the method to a germanium target.

The first section presents the scientific context and motivations for the characterisation of the detector response to low energy nuclear recoils. Section 5.2 then details the principle of the CRAB method which relies on the de-excitation following a neutron capture in the target detector. The following sections describe the prediction of nuclear recoil energy spectra in various target materials. Finally, the last section reports the application of modern Density Functional Theory (DFT) and Molecular Dynamic (MD) techniques to the impact of crystal defects creation and the subsequent energy storage within the material.

5.1 Scientific context and motivations

Recent advances in the field of cryogenic detectors have made it possible to achieve high energy resolution, allowing sensitivity to low-energy nuclear recoils. This opens a window into neutrino and dark matter physics. Indeed, the experimental signatures of Coherent Elastic Neutrino-Nucleus Scattering (CEνNS) [4, 168] and low-mass (sub-GeV) dark matter scattering [169, 170] correspond to sub-keV nuclear recoils. The calibration of cryogenic detectors in this energy range is crucial to understand their energy scale and to probe potential new physics. This represents a challenge for both the dark matter and neutrino communities, which are actively working on innovative calibration methods [171]. Standard techniques, briefly described in Section 2.4.5, face severe limitations. X-ray source calibrations generally produce recoils above keV energies, but recent X-ray fluorescence (XRF) calibrations have been performed in the sub-keV range [119, 120]. LED sources can also be used for calibration down to a few hundred eV [153]. However, both of these methods calibrate electronic recoils, not nuclear recoils, and X-ray calibrations are also sensitive to surface effects.

The detector response depends on the recoil type. When a particle interacts in cryogenic detectors, it can generate phonons, but part of the energy is also detected into other channels: ionization (for semiconductors) or scintillation (for scintillators). The mechanisms of energy deposition differ significantly depending on the type of recoil: electronic or nuclear. These mechanisms are illustrated in Figure 5.1, where it is evident that the two recoil types lead to distinct channels for energy deposition and various leak of energy, highlighted in red. The ionization and light yields for electronic recoils are higher than for nuclear recoils. Nevertheless, nuclear recoils can still transfer part of their energy to electrons (dashed arrow), thereby producing a scintillation or an ionization signal. In semi-conductors like germanium, the ratio of the ionization yield from a nuclear recoil to that from an electronic recoil of the same energy is known as the quenching factor. While the quenching factor of germanium is well known above 1 keV [66, 172], there is a lack of knowledge at lower energies and inconsistent measurements [66, 173].

Nuclear recoil calibration is essential, as it directly mimics the expected detector response to CEνNS and dark matter signals. It also eliminates the need to rely on the quenching factor to extrapolate electronic recoil calibrations to nuclear recoils. The main challenge is to produce nuclear recoils with well-defined energy. A commonly used technique involves the scattering of a fast neutron beam of known energy on a target detector. This scattering induces a nuclear recoil whose energy is defined by the scattering angle of the incident neutron. Operating in coincidence with neutron detectors placed around the target allows selection of the scattering angle and then the reconstruction of the nuclear recoil energy. It has been successfully used to induce nuclear recoils, as demonstrated in [173] and [174], and applied in the measurement of quenching factors in the sub-keV energy range. Nevertheless, it becomes very challenging in the sub-keV range. Nuclear recoils in germanium have been detected down to 400 eV [66] and in silicon down to 100 eV [174], however suffering from significant uncertainties. The CRAB method (Calibrated Recoil for Accurate Bolometry) addresses this lack of sub-keV calibration by providing an in situ calibration, producing low-energy nuclear recoils uniformly distributed within the detector volume [9].

5.2 Principle of the CRAB method

The CRAB method produces a nuclear recoil induced by a thermal neutron radiative capture. The capture of thermal neutrons in a target crystal produces a compound nucleus in an excited state with an energy equal to the neutron separation energy S_n, of several MeV. This compound nucleus then de-excites to the ground state by emitting γ-rays and conversion electrons. The de-excitation involves either a single-γ transition or a multi-γ cascade, associated with a nuclear recoil due to momentum conservation. This method is schematized in Figure 5.2. For a single-γ transition, the two-body kinematics determine the energy of the associated nuclear recoil:

$$E_{NR} = \frac{E_\gamma^2}{2M_n c^2} = \frac{S_n^2}{2M_n c^2} \tag{5.1}$$

where M_n is the mass of the target nucleus and E_γ is the energy of the emitted γ (for single-γ transition $E_\gamma = S_n$). For medium and heavy mass nuclei, this nuclear recoil is on the order of 100 eV. In a cm-sized detector, the high-energy gamma escapes the detector without depositing energy. Therefore, the only energy deposition in the cryodetector comes from the nuclear recoil. The emitted γ can be detected in a γ-detector in coincidence with the cryodetector (see Section 7.2). Single-γ de-excitations are of particular interest for calibration, as they produce calibration peaks in the recoil energy spectrum.

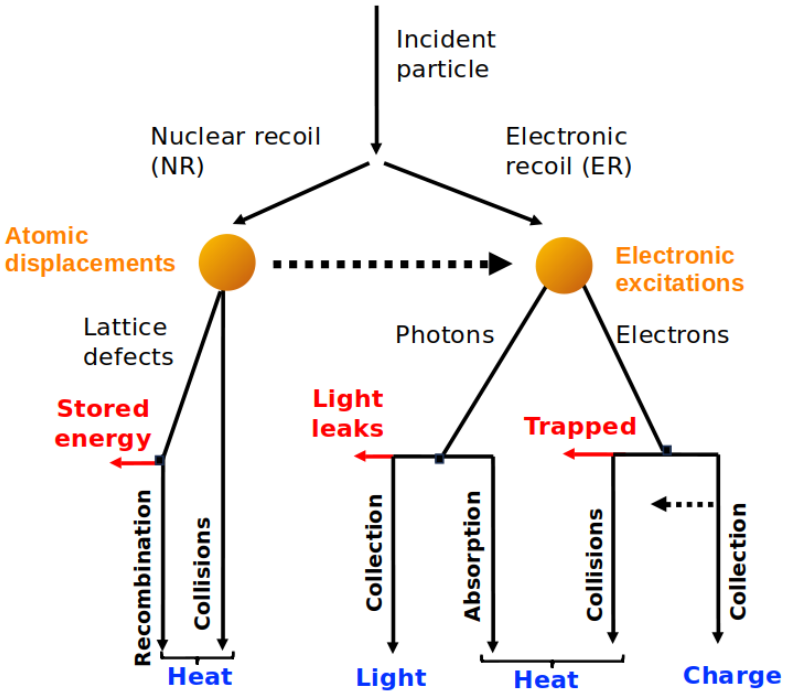

Figure 5.1. Energy deposition mechanisms for nuclear and electronic recoils. Nuclear recoils primarily induce atomic displacements and lattice defects, leading to heat and non-measurable stored energy. A fraction of the energy may transfer to electronic excitations. Electronic recoils directly excite the electronic cloud, producing charge, light, and heat. Energy losses—such as stored energy in defects, light leaks, and trapped charges—are highlighted in red.

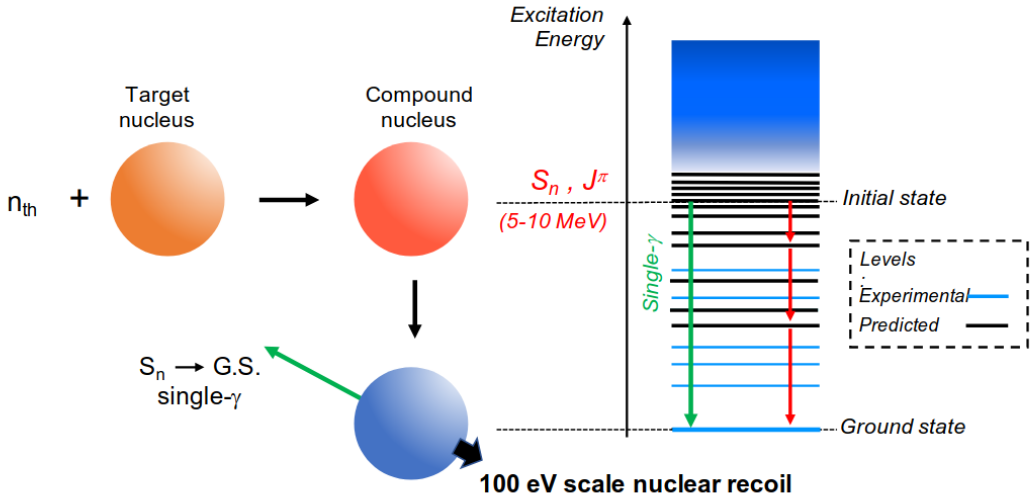

Figure 5.2. Illustration of the CRAB method using radiative neutron capture. The single-γ transition from the initial state to the ground state is associated with a nuclear recoil of well-known energy on the 100 eV scale. Multi-γ cascades, on the other hand, are predicted by FIFRELIN simulations based on nuclear data, such as nuclear level energies and branching ratios. Figure from [9].

The black line in Figure 5.3 shows the nuclear recoil energy as a function of the emitted γ-ray energy S_n, along with the maximum recoil energies expected from various particle scattering processes such as dark matter or neutrinos. For a γ energy of 6 MeV, the corresponding nuclear recoil is on the order of 100 eV, which is comparable to the recoil energies induced by elastic scattering from a 3 MeV neutrino or by a 3 GeV dark matter particle. CRAB is therefore a valuable tool for CEνNS and light dark matter searches. The experimental validation of this method and the detection of a nuclear recoil peak in $CaWO_4$ are presented in Section 6.1.

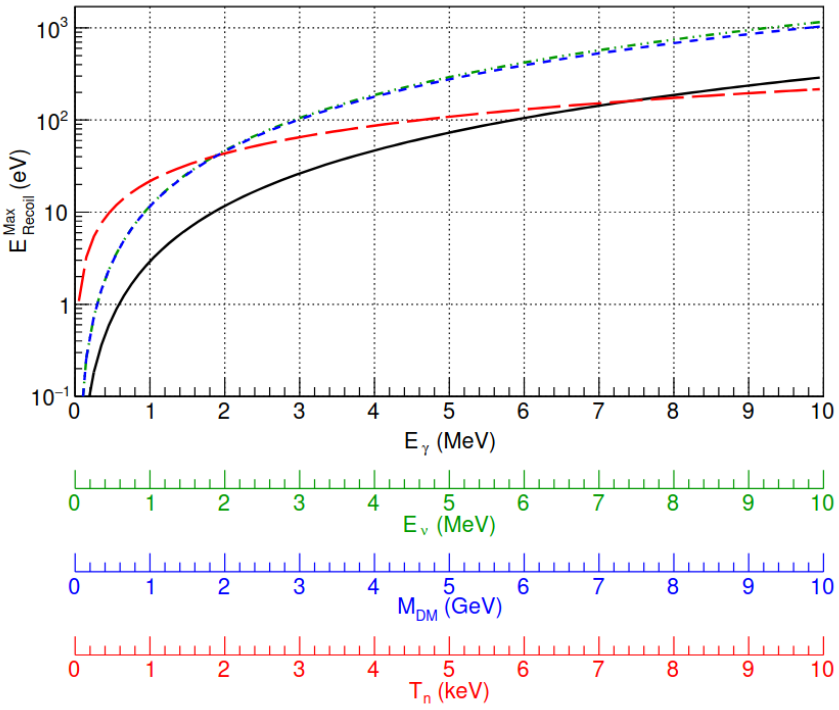

Figure 5.3. Nuclear recoil energy induced by gamma emission in tungsten via two-body kinematics (solid black curve). For comparison, the maximum nuclear recoil energies in tungsten expected from the scattering of various particles are also presented: light dark matter (blue curve), CEνNS (green curve), and elastic neutron scattering (red curve). Figure from [9].

Multi-γ cascades produce a continuum of nuclear recoils (see Section 5.4), which constitute a potential background for the detection of a calibration peak. Let's review the required conditions for the calibration peaks from single-γ transitions to emerge above this continuum. The target material may contain multiple isotopes that contribute to the total nuclear recoil energy spectrum. First, it is necessary to consider the neutron capture probability $\sigma_{n,\gamma}$ for each of them. Then, the branching ratio I_γ to single-γ decay must be sufficiently high. Finally, a suitable isotope should have a high natural abundance Y_{ab}. From these considerations, we can build a Figure of Merit (FoM) for an isotope X_i in a given material as:

$$FoM(X_i) = \Sigma_{n,\gamma}(X_i) \times I_\gamma(X_i) \tag{5.2}$$

with $\Sigma_{n,\gamma}(X_i)$ the macroscopic neutron cross-section for the isotope X_i [175]:

$$\Sigma_{n,\gamma}(X_i) = \frac{\rho N_a}{M_{tot}} n_X Y_{ab}(X_i) \sigma_{n,\gamma}(X_i) \tag{5.3}$$

where ρ is the density of the material, N_a is Avogadro's number, M_{tot} is the total molar mass of the material, n_X is the stoechiometric coefficient of the element X, $Y_{ab}(X_i)$ and $\sigma_{n,\gamma}(X_i)$ are the natural abundance and neutron capture cross-section for isotope i of element X, respectively.

The FoM quantifies the probability that the target isotope captures a neutron and de-excites via a single-γ transition. Table 5.1 presents relevant parameters as well as the FoM for various materials commonly used in cryogenic experiments: $CaWO_4$, Al_2O_3, Si and Ge. In particular, it can be seen that the isotope ^{182}W in $CaWO_4$ is the most promising isotope for CRAB calibration, providing an intense calibration peak at 112.5 eV. This made a $CaWO_4$ detector from the NUCLEUS experiment the best candidate for a first proof-of-concept measurement [121].
The probability of neutron absorption in a target material is given by the following formula:

$$P = 1 - e^{-\Sigma_{n,\gamma} l} \tag{5.4}$$

with l the thickness of the cube and $\Sigma_{n,\gamma}$ the total macroscopic cross-section accounting for all elements and isotopes in the target:

$$\Sigma_{n,\gamma} = \sum_X n_X \sum_i \Sigma_{n,\gamma}(X_i) \tag{5.5}$$

We can also obtain the capture probability of an isotope X_i as:

$$P_{capture}(X_i) = \frac{\Sigma_{n,\gamma}(X_i)}{\Sigma_{n,\gamma}} \tag{5.6}$$

Considering a NUCLEUS $CaWO_4$ cube with dimensions $5 \times 5 \times 5$ mm^3, we obtain an 11% probability of absorption of a neutron in this 5 mm thick target. The captures are predominantly distributed among three main tungsten isotopes: 58% on ^{186}W, 29% on ^{182}W and 7.5% on ^{183}W.

5.3 Prediction of nuclear de-excitations: FIFRELIN code

For de-excitations involving a multi-γ cascade (shown in red in Figure 5.2), the associated nuclear recoil energy is not straightforward to estimate, as it depends a priori on the energies and directions of the emitted γ. Therefore, it requires knowledge of nuclear level energies. The prediction of nuclear de-excitation is challenging due to the complexity of the phenomenon, especially for heavy nuclei, which suffer from a lack of knowledge regarding their level schemes and transition probabilities at high excitation energies.

The CRAB simulations use the FIFRELIN code, developed at CEA Cadarache, which aims to provide an accurate prediction of the de-excitation cascade. It was initially used to predict fission fragment de-excitation [178] but has also proven its ability to describe neutron capture in Gadolinium for the STEREO experiment [179].To predict the de-excitation cascade, the nuclear level scheme must be constructed up to the neutron separation energy S_n, requiring for each level the knowledge of energy, spin, and parity values (E,J,π). Then, the transition probabilities $P_{i\to j}$ from a level i to j, must be determined. Unfortunately, heavy nuclei such as germanium or tungsten suffer from a lack of knowledge at high energies due to high level density. FIFRELIN therefore combines experimental measurements with statistical models to retrieve all the necessary information.

Detector material			Target nucleus (A)			Compound nucleus (A+1)			FoM
Chemical formula	ρ [g/cm^3]	$\Sigma_{n,\gamma}$ [cm^{-1}]	Isotope	Y_{ab} [%]	$P_{capture}$ [%]	I_γ [176] [%]	S_n [177] [MeV]	E_{NR} [eV]	[a.u.]
Al_2O_3	3.970	1.1×10^{-2}	^{27}Al	100	99.89	26.81	7.725	1145	29.5
Si	2.329	8.23×10^{-3}	^{28}Si	92.2	94.60	2.17	8.474	1330	1.7
			^{29}Si	4.7	3.38	6.73	10.609	2016	18.7
			^{30}Si	3.1	2.02	1.47	6.586	777	0.02
Ge	5.323	9.76×10^{-2}	^{70}Ge	20.5	28.30	1.95	7.416	416.2	5.4
			^{72}Ge	27.5	11.11	0	6.783	338.7	0
			^{73}Ge	7.8	51.55	0	10.196	754.9	0
			^{74}Ge	36.5	8.58	2.83	6.506	303.2	2.4
$CaWO_4$	6.1	2.37×10^{-1}	^{182}W	26.5	29.01	13.94	6.191	112.5	95.8
			^{183}W	14.3	7.62	5.83	7.411	160.3	10.5
			^{186}W	28.4	58.11	0.26	5.467	85.8	3.6

Table 5.1. Table of relevant parameters and FoM for various materials used in cryogenic experiments. Only single-γ transitions are shown. For each detector material, the table presents the density and the macroscopic capture cross section $\Sigma_{n,\gamma}$. For each isotope, we can see the natural abundance Y_{ab}, the neutron capture probability $P_{capture}$, the branching ratio of the single-γ transition I_γ and the associated nuclear recoil energy E_{NR}. The FoM is defined in the text.

Let's briefly describe the FIFRELIN code. For more detailed explanations, see [179, 180]. FIFRELIN first generates a nuclear level scheme and then determines transition probabilities, using different methods depending on the energy, as depicted in Figure 5.4. For the building of the level scheme, three energy regions are considered:

- $\mathbf{E < E^{RIPL3}_{cut-off}}$: Below $E_{cut-off}$, all energy levels are known and available in databases such as RIPL-3 [177].

  $E^{RIPL3}_{cut-off}$ appears as an energy beyond which knowledge about energy levels is limited. This energy therefore varies from one isotope to another and is also stored in the RIPL-3 database.

- $\mathbf{E^{RIPL3}_{cut-off} < E < E_{bin}}$: In this region, only certain energy levels are known. Therefore, the discrete nuclear level scheme is completed in such a way that it matches the theoretical density model.

- $\mathbf{E > E_{bin}}$: In this region, we can no longer rely on measured quantities. The nuclear level scheme is not discrete anymore but is considered as a continuum $\rho(E, J, \pi)$, modeled by theoretical level density models such as CGCM [181] or HFB [182]. FIFRELIN builds the nuclear level scheme by drawing levels within the ρ distribution.

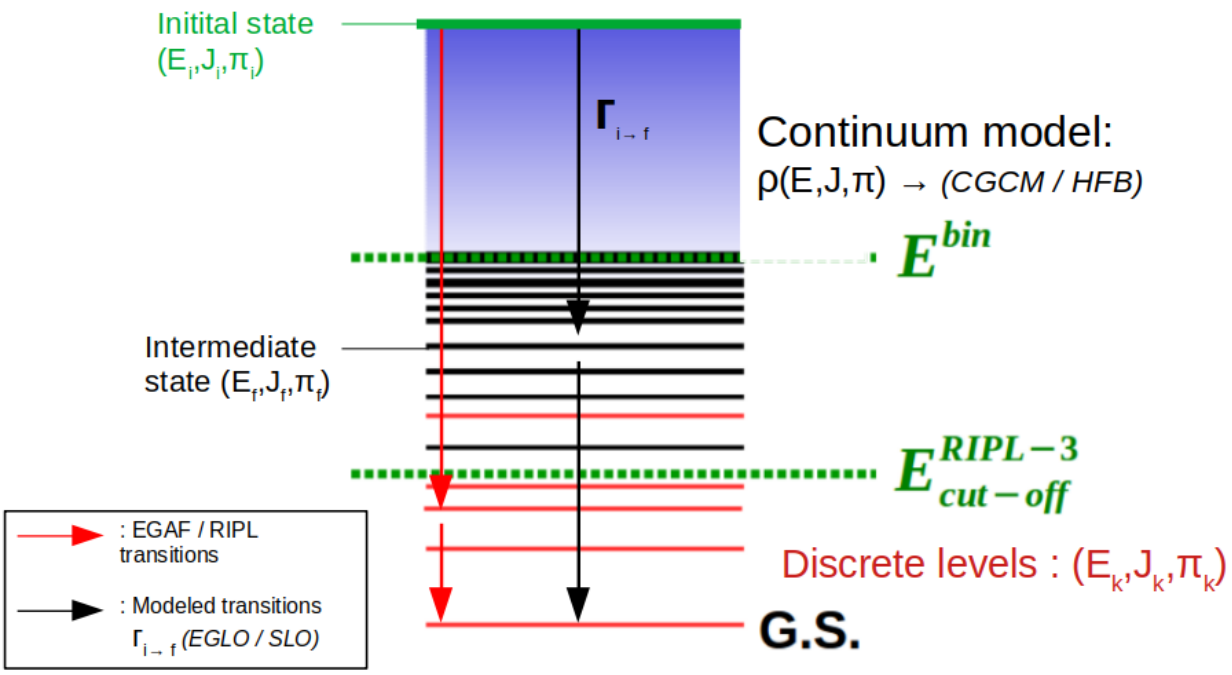

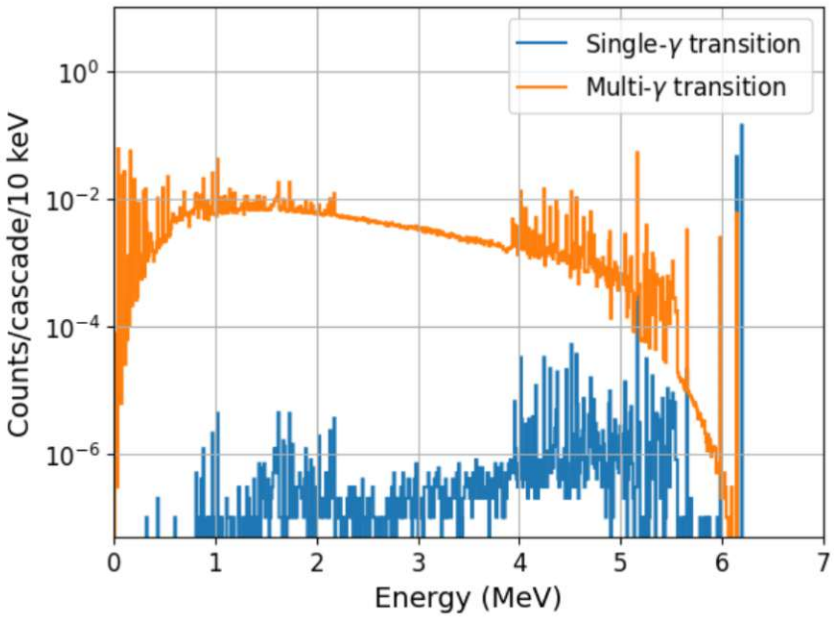

Figure 5.4. Top: Nuclear level scheme generated by FIFRELIN. We can see known discrete levels in red from RIPL and level generated from nuclear models in black. Above E_{bin}, levels are considered as a continuum. Also are shown the transition probabilities either measured by EGAF or RIPL in red or estimated from models like EGLO or SLO in black. Figure adapted from [180]. Bottom: FIFRELIN prediction for the energy distribution of γ-rays emitted following neutron capture on ^{182}W. Multi-γ transitions (orange) are the dominant decay mode. Single-γ transitions (blue) include the line at $S_n = 6.191$ MeV, which accounts for 13.94% of all possible cascades. A few additional, less probable lines are observed between 0 and S_n; these involve cascades that include electron conversion processes to reach the ground state.

Once a level scheme has been constructed, the next step is to determine the transition probabilities. The probability of a γ transition from an initial state i to a final state f is linked to the radiative partial width $\Gamma_{i\to f}$, as follows:

$$P_{i\to f} = \frac{\Gamma_{i\to f}}{\sum_{f'} \Gamma_{i\to f'}} \tag{5.7}$$

For low-lying levels, the radiative partial widths have been experimentally determined. However, at higher excitation energies, in the range $E_{\text{cut-off}}^{\text{RIPL-3}} < E < S_n$, they remain unknown. Therefore, for those transitions, FIFRELIN relies on theoretical models to predict the average partial widths:

$$< \Gamma_{i\to f} >= \frac{f_{XL}(E_\gamma) E_\gamma^{2L+1}}{\rho(E_i, J_i, \pi_i)} \tag{5.8}$$

where the index i refers to the initial state, $f_{XL}(E_\gamma)$ is the Photon Strength Function (PSF) depending on the type of transition X (Electric (E) or Magnetic (M)), its multipolarity L, and the γ energy E_γ. By default, FIFRELIN uses EGLO [183] to model the PSF, but it can also use SLO [184] or QRPA [185]. According to the uncertainty principle, the lifetime of these levels is inversely proportional to the partial width.

Primary γ transition from the level $E = S_n$ are handled using a dedicated approach. Indeed, some transitions from the state S_n to the levels below $E_{cut-off}^{RIPL3}$ have been measured and are taken from EGAF [176]. These transitions, depicted in red in Figure 5.4, reach levels known from RIPL, and therefore, the overall cascade uses well-known transition probabilities. However, other transitions, depicted in black, rely solely on previous theoretical models of the partial width.

In the FIFRELIN procedure, we build a nuclear level scheme and determine the corresponding transition probabilities and associated branching ratios. From these data, a large number of cascades are generated. However, it is important to recall that the built nuclear level scheme is only one statistical realization. Additionally, the partial width is subject to Porter-Thomas fluctuations [186], as nuclear models only predict the average $< \Gamma_{i\to f} >$. Therefore, a nuclear realization consists of a given nuclear level scheme with $\Gamma_{i\to f}$ values fluctuating around their mean. FIFRELIN generates many nuclear realizations and for each of them, de-excitation cascades are simulated and all relevant quantities such as gamma and conversion electron energies are stored. This procedure provides state of the art γ and e^- emission spectra.

The bottom panel of Figure 5.4 shows the γ energy for single and multi-γ transitions from the ^{183}W compound nucleus (corresponding to the highest FoM in Table 5.1). The single-γ line at 6.191 MeV corresponds to a de-excitation from S_n to the ground state and induces a mono-energetic recoil (112.5 eV). A few lines are observed between 0 and S_n; these correspond to cascades that involve electron conversion processes to reach the ground state. Indeed, the lower the intermediate energy level, the higher the probability to decay via conversion electron emission. The conversion coefficients are taken from the BrIcc database [187].

5.4 Nuclear recoil energy computation: Timing effects

For single-γ transitions, the nuclear recoil can be easily reconstructed as $E = \frac{P_\gamma^2}{2M_n c^2}$. But what about multi-$\gamma$ cascades? Every γ emission provides momentum to the emitter nucleus, which recoils in the target crystal and interacts with its neighboring atoms in the crystal lattice through successive collisions. Therefore, the total nuclear recoil from multi-γ cascades also depends on the comparison between the stopping time of the recoiling

nucleus in matter and the lifetime of intermediate levels involved in the γ-cascade. As highlighted in [188], the nuclear recoil energy results from an interplay between the stopping time of the recoil, τ_{recoil}, and the emission time, τ_γ, of subsequents γ-rays. We can simplify the problem by considering two extreme cases, schematized in Figure 5.5, based on different "timing hypotheses":

- **Prompt Hypothesis $\tau_\gamma \ll \tau_{recoil}$**: In this scenario, all γ emissions occur simultaneously before the nucleus starts to recoil. The recoil energy is then the vector sum of the recoil momenta $\vec{p_\gamma}$ of all emitted γ. The total recoil energy is given by:

$$E_{recoil} = \frac{(\sum_\gamma \vec{p_\gamma})^2}{2M_n c^2} \tag{5.9}$$

  Let's consider a simple example of a cascade with two γ of energy E_1 and E_2. If both γ are emitted in the same direction, the situation is equivalent to the single-γ transition: $E_{recoil} = \frac{(E_2+E_1)^2}{2M_n c^2} = \frac{S_n^2}{2M_n c^2}$. However, if they are emitted back-to-back, the total recoil energy is reduced down to $E_{recoil} = \frac{(E_2-E_1)^2}{2M_n c^2}$. This introduces a dependence of the nuclear recoil energy on the emission direction of the γ, with a continuous distribution between the two previous extreme values.

- **Slow Hypothesis $\tau_{detector} \gg \tau_\gamma \gg \tau_{recoil}$**: In this case, the nuclear recoil stopping time is shorter than the lifetime of the intermediate level. Consequently, the nucleus has time to stop in the crystal lattice before emitting another γ. This results in multiple distinct nuclear recoils in the cryodetector. However, the time difference between these recoils is negligible compared to the detector's response time, which only records the total deposited energy. Thus, the total recoil energy is given by:

$$E_{recoil} = \sum_\gamma \frac{P_\gamma^2}{2M_n c^2} \tag{5.10}$$

  In this scenario, a 2-γ emission always results in the same nuclear recoil energy, equal to the sum of the individual recoils. Under this hypothesis, the recoil energy does not depend anymore on the direction of the emitted γ.

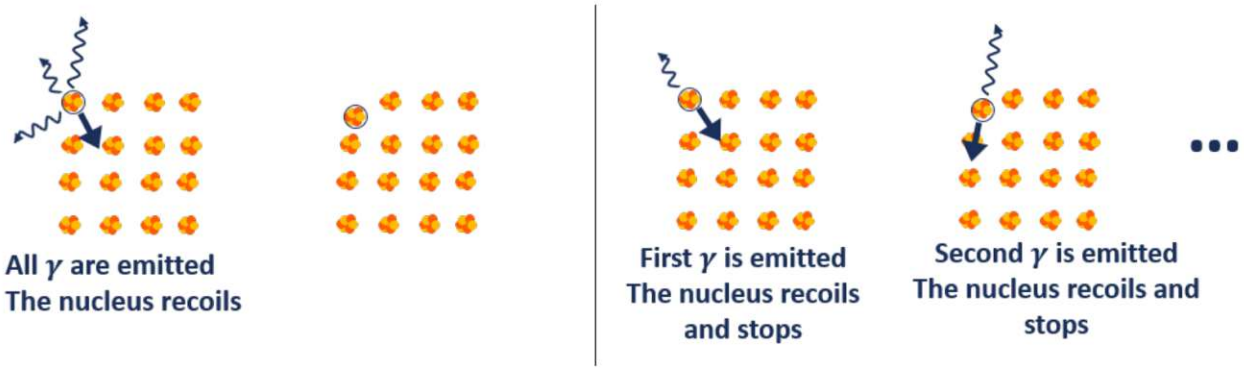

Figure 5.5. Representation of nuclear recoil(s) during a multi-γ cascade for two timing hypotheses: prompt (left) and slow (right). Figure from [175].

Therefore, to estimate the nuclear recoil energy, one must compare nuclear recoil times on the order of $\tau_{recoil} \sim 10^{-13}$ s with the lifetimes of intermediate levels, whose estimates may depend on nuclear models. The left panel of Figure 5.6 shows the half-life of different nuclear transitions in ^{71}Ge in the Weisskopf hypothesis. Depending on whether the lifetimes τ_γ of a transition are above or below τ_{recoil}, the transition will be considered prompt or slow. There also exists intermediate cases where $\tau_{recoil} \sim \tau_\gamma$, known as "in-flight emissions," indicated by the gray band. In this scenario, the emission of the secondary γ occurs after the nucleus begins to recoil but before it stops. The nuclear recoil stopping time, τ_{recoil}, depends on several parameters such like the recoil energy, the material density, the recoiling nucleus and the direction. In our simulations, this stopping time is estimated using the open-source code IRADINA [189], which tracks the position of atoms and follows the atomic cascade induced by the recoil. Let's briefly describe its framework.

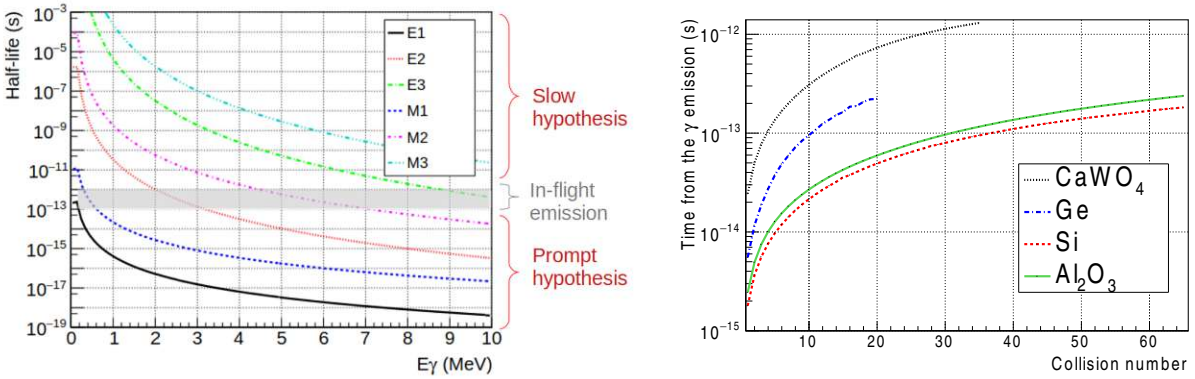

Figure 5.6. Left: Half-life of different γ-transition types and multipolarities according to the Weisskopf formula for ^{71}Ge [190]. The gray shaded area represents the typical range of nuclear recoil stopping times in Ge. Right: IRADINA prediction of the mean time elapsed since the emission of the first γ shown as a function of the number of collisions for recoils associated with single-γ transitions presented in Table 5.1: 112.5 eV recoil of a W atom in $CaWO_4$ (dotted black), 416.2 eV recoil of a Ge atom in pure Ge (dashed dotted blue), 1330 eV recoil of a Si atom in pure Si (dashed red) and 1145 eV recoil of an Al atom in Al_2O_3 (plain green). The end point of each curve corresponds to the number of collisions after which 90% of the initial kinetic energy has been lost. Figures from [191].

IRADINA uses the Binary Collision Approximation (BCA) to simulate displacement cascades. In this approach, the nucleus recoils in a homogeneous gas-like material with a nominal atom density but no lattice structure (isotropic properties). Collisions with atoms are then described by a succession of two-body elastic collisions. If the transferred energy exceeds the threshold displacement energy required to permanently displace an atom from its lattice site, it generates another projectile, whose cascade is simulated using the same procedure as for the primary recoil. Between each collision, the nucleus follows a straight trajectory at a uniform velocity. After traveling a distance d_1, sampled from a Poisson distribution with a mean equal to the interatomic spacing in the lattice, the recoiling nucleus loses part of its energy upon colliding with an atom. It then travels a subsequent distance d_2 at a reduced velocity before undergoing another collision. The time is incremented at each step using the track distance and the velocity. This process continues until the nucleus reaches an energy of $\frac{3}{8}k_B\theta_{DB}$ (<1 eV) with θ_{DB} the Debye temperature of the material. This energy is the lowest possible energy that the system may have. At the end of the cascade the total recoil time is exctracted. On the right panel of Figure 5.6, one can see, for different targets and nuclear recoil energies, the time elapsed since the emission of the first γ as a function of the number of collisions. Each curve stops at the number of collisions after which 90% of the initial kinetic energy has been lost. We clearly see that the stopping time is between few 10^{-13} s and 10^{-12} s. While this framework provides a good estimate of nuclear recoil time, crystallographic effects such as defect creation and subsequent energy trapped in vacancy sites are not properly estimated. Simulations using molecular dynamics [192] have been conducted on this subject and are detailed in [175].

The output of the FIFRELIN code, predicting the energy and emission time of the particles (gamma, electron, positron) in the de-excitation cascade, is coupled to the simulation of the displacement cascade by the IRADINA code leading to the FIFRADINA code. This coupling of IRADINA and FIFRELIN allows us to simulate γ emission during the cascade (in-flight decay), thereby estimating the nuclear recoil energy. A more comprehensive description of in-flight gamma emission implementation in IRADINA can be found in [175, 191]. Note that through the generation of decay schemes, the continuum of recoil energies induced by multi-γ transitions depends on nuclear models. However, they do not affect single-γ transitions or compromise the calibration peaks ensured by the CRAB method. Certain 2-γ cascades benefit from timing effects (especially under the slow hypothesis) leading to the appearance of additional calibration peaks. Table 5.2 summarizes a few decay cascades identified as good candidates for inducing prominent calibration features in target materials commonly used in cryogenic experiments. Among these cascades are, of course, the single-γ transitions listed in Table 5.1, but also two- or three-γ transitions, where a primary γ carries away the majority of the energy, followed by one or two γ rays with energies in the few hundreds of keV range. The half-life of these low energy intermediate levels is above the time required for the nuclear recoil to stop. Therefore, the secondary and tertiary γ rays are emitted at rest (slow hypothesis). When all emitted γ's exit the crystal without depositing energy, we are left with a pure nuclear recoil at fixed energy, resulting in the additional recoil lines listed in Table 5.2. For each recoil line we can associate a Figure of Merit (FoM) as defined in Section 5.2. Note that this FoM is not directly proportional to the count rate expected for each recoil line, as we still need the condition that all γ in the cascade escape the crystal without depositing energy in it. The validity of this condition depends of course on the geometry of each detector.

It can be observed that for $CaWO_4$, the single-γ transition from ^{187}W is very rare, and two 2-γ cascades have been found to be favored. Under the slow hypothesis, these introduce two additional peaks close in energy at 79.5 eV and 81.4 eV. Thus, the main impact of the timing effect is a more prominent peak structure around 80 eV. For Al_2O_3, many peaks emerge around 575 eV due to timing effects. Taking into account the finite detector resolution, they will lead to a single calibration peak feature. For silicon, an additional line appears at 990 eV with high intensity. For germanium, the timing effect is even more pronounced and promising, as it introduces additional calibration lines originating from slow transitions in the 300-600 eV region [191]. This pattern offers a unique opportunity to study the response of Ge detectors in the sub-keV region, allowing both calibration and probing of the germanium quenching factor when combining the readout of heat and ionization channels.

5.5 Simulation of CRAB spectra in cryogenic detectors

Now that FIFRADINA has provided a representative sample of the de-excitation cascades and the subsequents nuclear recoil energies produced by gamma emissions, we need to propagate all particles in the cryogenic detector. This is done by the GEANT4 package [122–124] of the CRAB simulations presented in this section. We use the TOUCANS simulation tool [194] developed at CEA. Neutron interactions in matter are of critical importance for CRAB and are modeled using the Neutron High-Precision (Neutron-HP) package based on ENDF/B-VII.1 nuclear data library [195], as well as the NCrystal library [196]. The simulation of electromagnetic processes, such as gamma and charged particle interactions, is handled by the Livermore physics list. The coupling of TOUCANS with FIFRADINA inputs enables the simulation of the full chain — from neutron irradiation of a target detector to the reconstruction of the resulting energy deposits. These energy deposits fall into two distinct categories: (i) high-energy events, primarily due to conversion electrons emitted during the de-excitation cascade, which deposit all of their energy in the crystal, and (ii) low-energy nuclear recoils, which result from either multi-γ cascades or single-γ transitions. Note that any cascade involving conversion electron leads to an energy deposition of few keV to MeV in the crystal and ruins the chance to detect the nuclear recoil associated with the primary γ of the cascade.

Table 5.2. Summary of the most prominent nuclear recoil peaks induced by radiative thermal neutron capture in four detector materials of various sizes (1st column). The 2nd column shows the macroscopic capture cross section $\Sigma_{(n,\gamma)}$ defined in Equation 5.3. The target isotopes are listed in the 3rd column with their relative probability $P_{capture}$ of neutron capture (4th column). The de-excitation of the compound nucleus is characterized by the branching ratio I_γ (5th column) and energy E_γ (6th column) for each transition, extracted from the RIPL-3 and EGAF databases. Multi-γ cascades span multiple rows, with each row describing one γ-ray of the cascade. Subsequent emissions are signaled by a $\hookrightarrow$ symbol preceding their energy, and the 7th column indicates the associated half-life. The reported half-lives are evaluated values from RIPL-3 database when available, with the Weisskopf estimate used as a fallback, and specified by the notation "(W)". The two last columns present the total recoil energy E_r and the FoM defined in Equation 5.2. Table from [193].

Detector material		**Target nucleus**		**Compound nucleus**				
Formula & Size (mm)	$\Sigma_{(n,\gamma)}$ (cm^{-1})	Isotope	$P_{capture}$ (%)	I_γ (%)	E_γ [176, 177] (MeV)	Half-life [177] (ps)	E_r (eV)	FoM ($\times 10^4$)
Al_2O_3 $5 \times 5 \times 5$	1.10×10^{-2}	^{27}Al	99.89	6.90 11.73	4.133 $\hookrightarrow$ 3.560	- 0.03	571.0	0.89
		^{27}Al	99.89	0.56 46.08	3.825 $\hookrightarrow$ 3.902	- 0.19	572.0	0.28
		^{27}Al	99.89	3.12 78.06	3.849 $\hookrightarrow$ 3.876	- 0.02	572.0	2.68
		^{27}Al	99.89	0.87 40.65	3.789 $\hookrightarrow$ 3.936	- 0.02	572.0	0.39
		^{27}Al	99.89	0.73 37.17	4.015 $\hookrightarrow$ 3.705	- 0.19	573.0	0.30
		^{27}Al	99.89	6.90 59.27	4.134 $\hookrightarrow$ 3.902	- 0.03	575.0	4.49
		^{27}Al	99.89	6.80 87.72	4.260 $\hookrightarrow$ 3.466	- 0.04	578.0	6.55
		^{27}Al	99.89	3.39 100	7.693 $\hookrightarrow$ 0.031	- 2070	1135.7	3.72
		^{27}Al	99.89	26.81	7.724	-	1144.8	29.46
Si $10 \times 10 \times 20$	8.23×10^{-3}	^{28}Si	94.60	7.10 100	7.200 $\hookrightarrow$1.273	- 0.29	990.4	5.53
		^{28}Si	94.60	2.17	8.474	-	1330.1	1.69
		^{29}Si	3.38	6.73	10.609	-	2016.0	0.19

Detector material		Target nucleus		Compound nucleus				
Formula & Size (mm)	$\Sigma_{(n,\gamma)}$ (cm^{-1})	Isotope	$P_{capture}$ (%)	I_γ (%)	E_γ (MeV)	Half-life (ps)	E_r (eV)	FoM ($\times 10^4$)
Ge $10 \times 10 \times 10$	9.76×10^{-2}	^{74}Ge	8.58	11.75 98.52	6.253 ↪0.253	- 1.36 (W)	280.6	9.69
		^{70}Ge	28.30	5.30 78.65	6.117 ↪1.299	- 0.4	296.0	11.51
		^{74}Ge	8.58	2.83	6.506	-	303.2	2.37
		^{70}Ge	28.30	2.62 77.31	6.276 ↪1.139	- 4.00	307.9	5.59
		^{70}Ge	28.30	4.80 95.44	6.708 ↪0.708	- <10.70	344.3	12.65
		^{70}Ge	28.30	3.83 99.30	6.916 ↪0.500	- 0.18 (W)	363.9	10.50
		^{70}Ge	28.30	1.95	7.416	-	416.2	5.39
		^{73}Ge	51.55	1.02 99.95 99.86	8.732 ↪0.868 ↪0.596	- 1.53 12.14	561.8	5.12
$CaWO_4$ $4.8 \times 4.8 \times 4.8$	2.37×10^{-1}	^{186}W	58.11	7.42 27.73	5.262 ↪0.205	- 2.6 (W)	79.6	28.34
		^{182}W	29.01	5.24 52.3	5.165 ↪1.026	- -	81.3	18.84
		^{186}W	58.11	5.26 38.21	5.321 ↪0.146	- 7.1 (W)	81.4	27.68
		^{186}W	58.11	0.26	5.467	-	85.8	3.58
		^{182}W	29.01	13.94	6.191	-	112.5	95.84
		^{183}W	7.62	5.83	7.411	-	160.3	10.53

The simulation is divided into several steps:

- Step 1: A thermal neutron is transported through the geometry of the experiment to the target detector and can eventually be captured. If so, we move to step 2.
- Step 2: From the capture vertex, a de-excitation cascade is drawn from FIFRADINA predictions with its associated nuclear recoil energy.
- Step 3: Reconstruction of energy deposition in the detector. All emitted particles are transported in the geometry. Then restart from step 1.

Basic simulations with a collimated, monoenergetic 25 meV thermal neutron beam incident on various target materials can be used to predict the typical energy deposition spectrum in cryogenic detectors. I simulated four examples of detectors: $CaWO_4$ and Al_2O_3 from the NUCLEUS experiment, germanium from TESSERACT and silicon with the dimensions shown in the Table 5.2. The small size O(mm) of the crystals makes them little sensitive to the external background not taken into account in theses simulations.

$CaWO_4$: In the left panel of Figure 5.7, one can see the energy deposited at high energy in a $CaWO_4$ cube of dimensions $5 \times 5 \times 5$ mm^3. The right panel shows a zoom in on conversion electrons or γ lines produced in the 20-200 keV range during the nucleus de-excitation and interacting in the crystal. Although they lie outside the region of interest (ROI) for low-energy nuclear recoil calibration, they still constitute a source of high energy events that saturate the detector response and induce additional dead time. These features have been measured during the commissioning of the Phase II of CRAB (see Chapter 8). The left panel of Figure 5.8 shows the low energy spectrum, in the ROI (<200 eV) where the contribution of the CRAB events is dominant and the spectrum reveals both the multi-γ continuum and two calibration peaks at 112.5 and 160.3 eV. These originate from single-γ transitions following neutron capture on the isotopes ^{182}W, and ^{183}W, respectively. A peak structure around 80 eV comes from nuclear recoils associated with 2-γ transitions from ^{187}W and ^{183}W. The right panel shows the same spectrum assuming a detector energy resolution of 10 eV. The intense 112 eV peak stands out clearly, making it an excellent candidate for calibration. The first experimental validation of the CRAB method took place in 2022, resulting in the observation of this nuclear recoil peak. The 160 eV peak requires high statistics to be visible. Finally, the structure at 80 eV is a bit overwhelmed by the multi-γ continuum and depending on the achieved energy resolution could be unresolved in single-mode operation. However, as discussed in Section 7.2, γ-tagging techniques help suppress the multi-γ continuum background, thereby relaxing the constraints on the required energy resolution.

Al_2O_3: Figure 5.9 shows the energy deposition in a $5 \times 5 \times 5$ mm^3 cube without energy resolution (left panel) and with a 40 eV resolution (right panel). A prominent calibration peak is observed at 1144.8 eV, corresponding to the single-γ emission from ^{28}Al. This peak is intense enough to remain clearly visible even with a 40 eV resolution. Its relatively high energy makes it less demanding in terms of the energy resolution required for detection. As a result, this peak is clearly distinguishable, both from a hardware perspective and in data analysis, as the associated pulses significantly exceed baseline fluctuations. Table 5.2 also shows the presence of several lines around 570 eV. After applying resolution effects, these lines produce a noticeable bump in the recoil energy spectrum. Its observation would not only provide additional validation of the CRAB method, but also constitute the first-ever observation of a spectral feature arising from timing effects.

Silicon: Figure 5.10 shows the energy deposition in a $10 \times 10 \times 20$ mm^3 silicon crystal, without energy resolution (left panel) and with a 40 eV resolution (right panel). The larger crystal dimensions are chosen to compensate for the relatively low neutron capture cross-section in silicon. Table 5.2, when considered alongside the capture probabilities, indicates that the CRAB energy spectrum is dominated by contributions from neutron capture in ^{28}Si. The single-γ transition gives rise to a peak at 1330.1 eV, while a 2-γ transition produces a

more prominent peak at 990.4 eV. A distinctive feature of silicon is that the peak associated with the single-γ transition is no longer visible when a 40 eV resolution is applied. In contrast, the 990 eV peak, resulting from the 2-γ transition with the secondary gamma emitted in flight, is intrinsically broadened. This unique feature makes it less sensitive to the detector's energy resolution and allows it to remain clearly observable. The lower rate of the third peak makes it very demanding in terms of background level.

Germanium: For germanium, as shown in Table 5.2, the timing effects produce several lines, plotted on the left side of Figure 5.11. This constitutes a valuable feature, as it opens the door to measurements using simultaneous readout of the ionization and phonon channels to probe the germanium quenching factor. Notably, these calibration lines lie in the sub-keV range, where several quenching factor measurements have yielded to inconsistent results [66, 173]. The known energies provided by the CRAB calibration lines thus offer the possibility of measuring this quenching factor with unprecedented precision and control over uncertainties. However, all these peaks are already smeared out with a 20 eV energy resolution as shown on the right side of Figure 5.11. We will see in Section 7.3 that γ-tagging helps to recover some of these peaks.

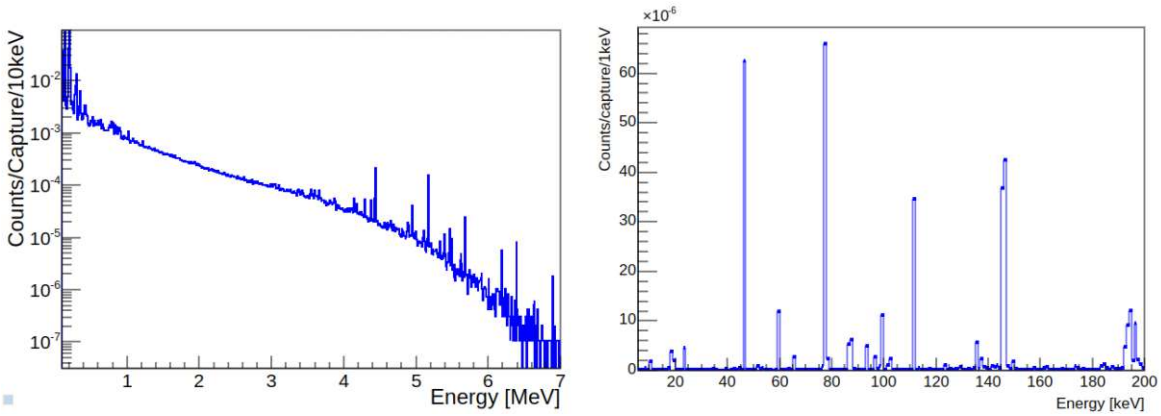

Figure 5.7. Left: Energy deposited in a $5 \times 5 \times 5$ mm^3 $CaWO_4$ crystal from simulation. Right: Zoom in the keV region showing electron conversion lines.

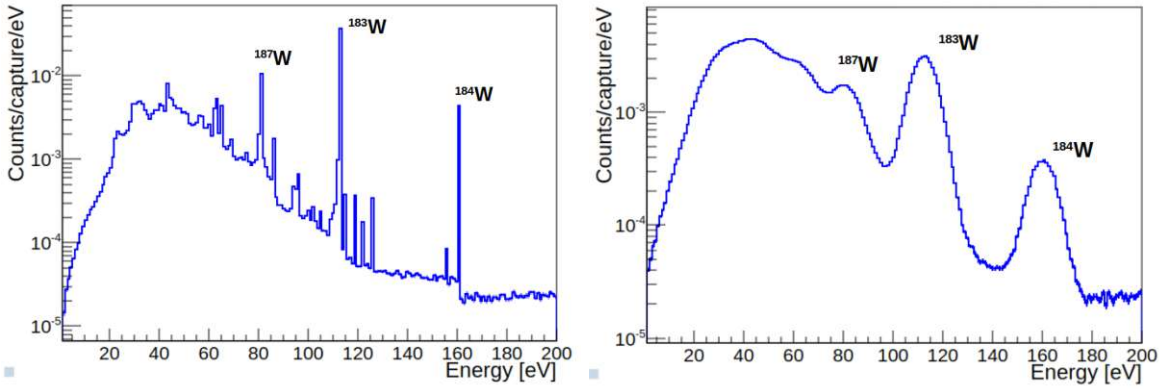

Figure 5.8. Left: Energy deposited in a $5 \times 5 \times 5$ mm^3 $CaWO_4$ crystal in the ROI showing three calibration peaks. Right: Energy deposited taking into account a 5 eV energy resolution. One can see that the peaks at 112.5 eV and 160.3 eV are visible while the peak at 80 eV is already a bit overwhelmed by the multi-γ background. The labeled isotopes represent the compound nuclei formed after neutron capture.

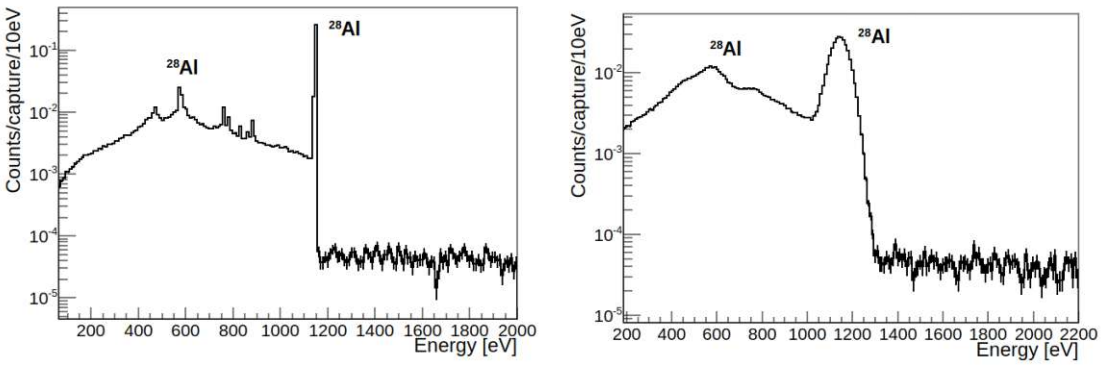

Figure 5.9. Left: Energy deposited in a $5 \times 5 \times 5$ mm^3 Al_2O_3 crystal in the ROI showing two calibration peaks. Right: Energy deposited taking into account a 40 eV energy resolution. The peak at 1144 eV is still visible. A peak at 570 eV originating from the 2-γ transitions of Table 5.2 could also be detected. The labeled isotopes represent the compound nuclei formed after neutron capture.

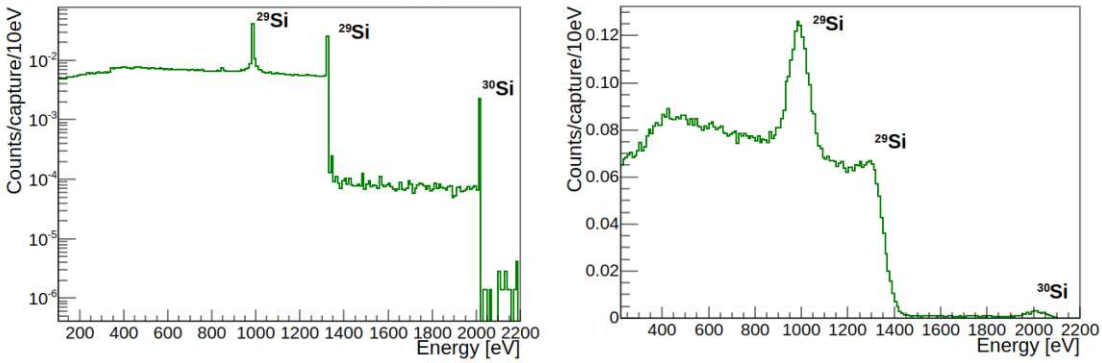

Figure 5.10. Left: Energy deposited in a $10 \times 10 \times 20$ mm^3 silicon crystal in the ROI showing three calibration peaks. Right: Energy deposited taking into account a 40 eV energy resolution. The peak at 990 eV originating from a 2-γ transition is more prominent than the peak at 1330 eV associated with a single-γ transition. The labeled isotopes represent the compound nuclei formed after neutron capture.

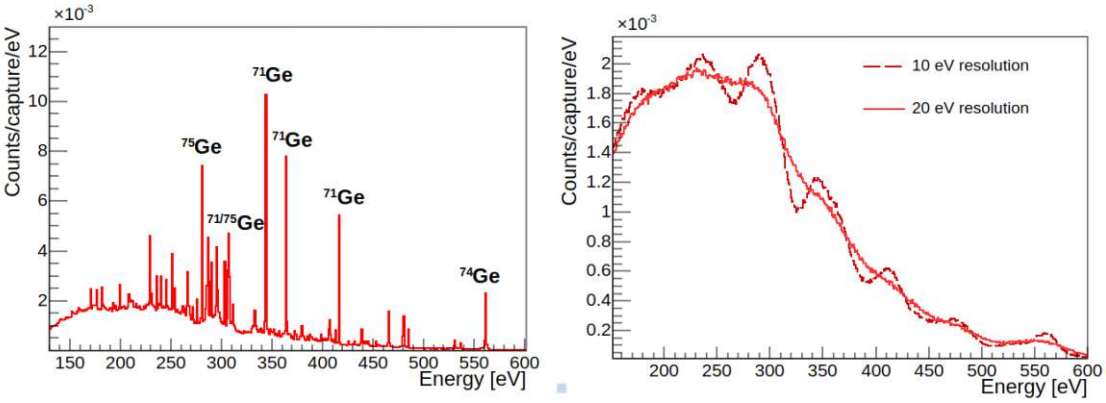

Figure 5.11. Left: Energy deposited in a $10 \times 10 \times 10$ cm^3 germanium crystal in the ROI showing severals calibration peaks listed in Table 5.2. Right: Energy deposited taking into account 10 or 20 eV energy resolution. One can see that all the calibration lines are smeared out with 20 eV energy resolution. The labeled isotopes represent the compound nuclei formed after neutron capture.

5.6 Detector response

The previous section provided predictions of the energy deposited by nuclear recoils induced by neutron captures in several target materials. However, before comparing the predicted and measured spectra, one must consider that all the deposited energy in the detector is not necessarily read out. The deposited energy can be distributed across three readout channels: phonon, ionization, and scintillation, with proportions that depend on both the material and the recoil energy. For germanium, quenching effects result in a very low ionization yield for nuclear recoils in the sub-keV region. For $CaWO_4$, in the CRAB ROI (<200 eV), the only relevant readout channel is the phonon channel. However, not all of the deposited energy will be converted into this channel. A fraction of the nuclear recoil's kinetic energy is stored in the form of crystal defects created during the displacement cascade. This stored energy is invisible to the detection with direct impact on the spectrum of reconstructed recoil energy. Therefore, it is crucial to account for the defect creation effects. Many defect configurations are possible including a Frenkel pair (an interstitial atom and a vacancy), a lattice distortion or a broken atomic bond. To quantify the energy stored by such defects, molecular dynamics simulations are used. A simulation box consists of a system containing thousand atoms arranged in a crystalline lattice. In this box, the recoil of an atom during a cascade is simulated step by step, estimating the force acting on the atom at each step. To determine this force, an interatomic potential is required.

There are three main methods for determining this potential. The first method relies on the Density Functional Theory (DFT) framework providing highly accurate results, accounting for the quantum nature of electrons, but it is computationally infeasible. The second approach uses empirical interatomic potentials for the calculation of the exerted force on the recoiling atom. This potential depends on few parameters fine tuned on experimental data or DFT predictions. While this method is computationally efficient, its accuracy can be limited by the approximate description of the potential. The third approach aims to maintain high accuracy while significantly reducing computational cost compared to DFT. It involves training a Machine Learning (ML) potential on DFT data so that the resulting potential reproduces DFT-like predictions. More details on this approach can be found in [175]. Simulations using this ML potential have been performed for various nuclear recoil energies and directions in a $CaWO_4$ target to determine the energy stored in defects at the end of the simulated cascades. The energies of the simulation boxes before and after the cascade give access to the stored energy expressed as:

$$E_{\text{stored}} = E_{\text{box with defect}} - E_{\text{box without defect}} \tag{5.11}$$

We can also infer the probability of defect creation with the fraction of cascades that do not store any energy in defects [197]. The left panel of Figure 5.12 shows the defect creation probability in $CaWO_4$ as a function of nuclear recoil energy. It follows a Fermi-like distribution, with the threshold displacement energy - defined as the minimum energy required to create a defect - set at the inflection point, around 40 eV. The right panel of Figure 5.12 displays the distribution of energy stored in defects for different nuclear recoil energies. Energy storage in defects can induce non-linearity effects in the detector response. Below the threshold displacement energy, the detector remains linear as no defects are formed. At high energies (above ~1 keV), enough defects are created such that the resulting missing energy scales linearly with the initial energy. In this regime, the missing energy is a constant fraction of the initial recoil energy, leading to no spectral distortion, it simply results in a renormalization of the calibration factor. However, at intermediate energies around 100 eV, the progressive formation of various types of defects leads to non-linearity in the detector response. $CaWO_4$ offers three calibration peaks in this region — at 81 eV, 112 eV, and 160 eV — which are particularly useful for probing this effect. Figure 5.13 shows both the raw deposited energy spectrum and the spectrum corrected for defect-induced missing energy. Although the absolute energy shift caused by these defects may not be directly observable, CRAB remains sensitive to the resulting spectral distortions. In particular, the positions of the three peaks deviate from a linear relation with the initial recoil energy, providing a clear signature of non-linearity.

Therefore, the application of CRAB to $CaWO_4$ offers a unique opportunity to probe the physics of crystal defect formation. Most of the current calibration techniques, involving electronic recoils, are not sensitive to this important physics of very low energy nuclear recoils. This measurement is particularly important, as it directly affects the reconstructed energy spectra from CEνNS and low-mass dark matter interactions, as demonstrated in [197, 198] and illustrated in Figure 5.14. Accounting for this effect is essential to avoid misinterpreting detector-induced distortions as signatures of new physics.

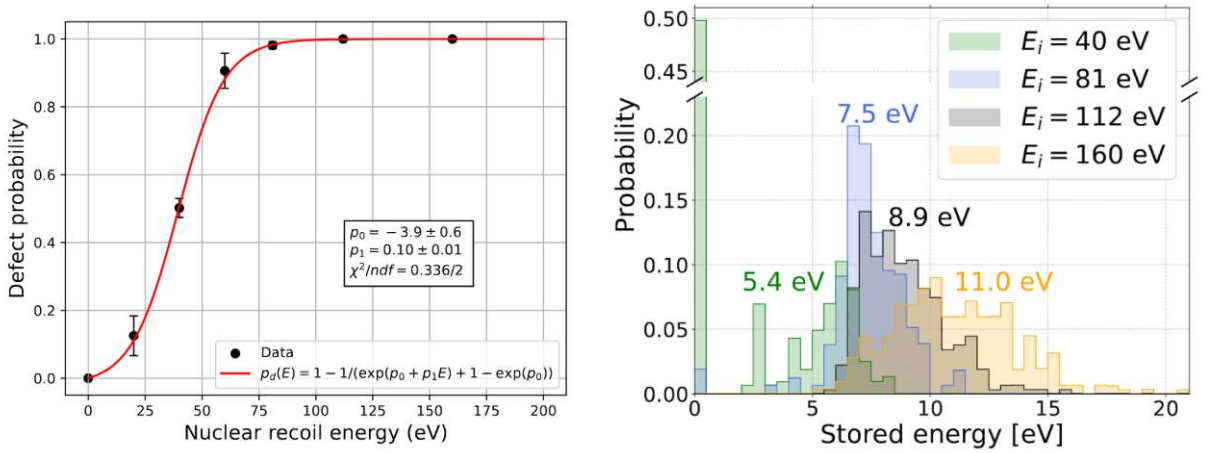

Figure 5.12. Left: Evolution of the crystal defect creation probability versus the initial recoil energy. A fit by a Fermi function has been performed (red curve) and the parameters are shown in the inset. Right: Predicted distributions of energy stored in crystal defects in $CaWO_4$ for different recoil energies of interest: 40 eV (green, 320 simulations), 81 eV (blue, 160 simulations), 112 eV (grey, 320 simulations), and 160 eV (orange, 320 simulations). The number next to each distribution indicates the average of the non-zero stored energies. Figures from [197].

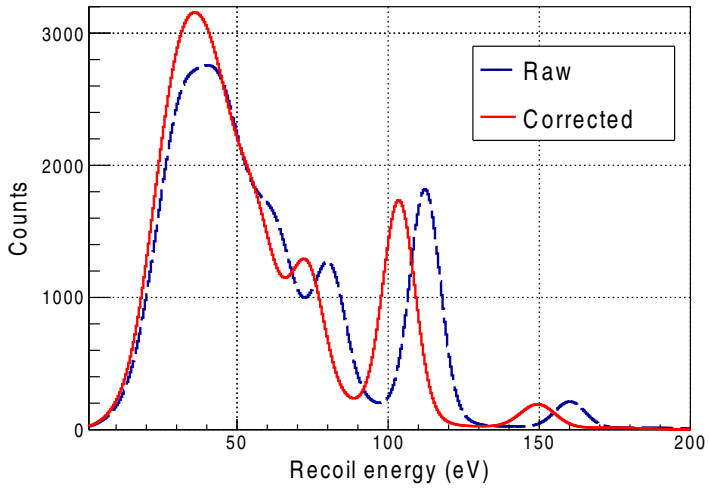

Figure 5.13. Predicted recoil energy spectra induced by neutron capture in a $CaWO_4$ cryogenic detector with 5 eV resolution (blue dashed line) and corrected for the energy stored in crystal defects (red solid line). Figure from [197].

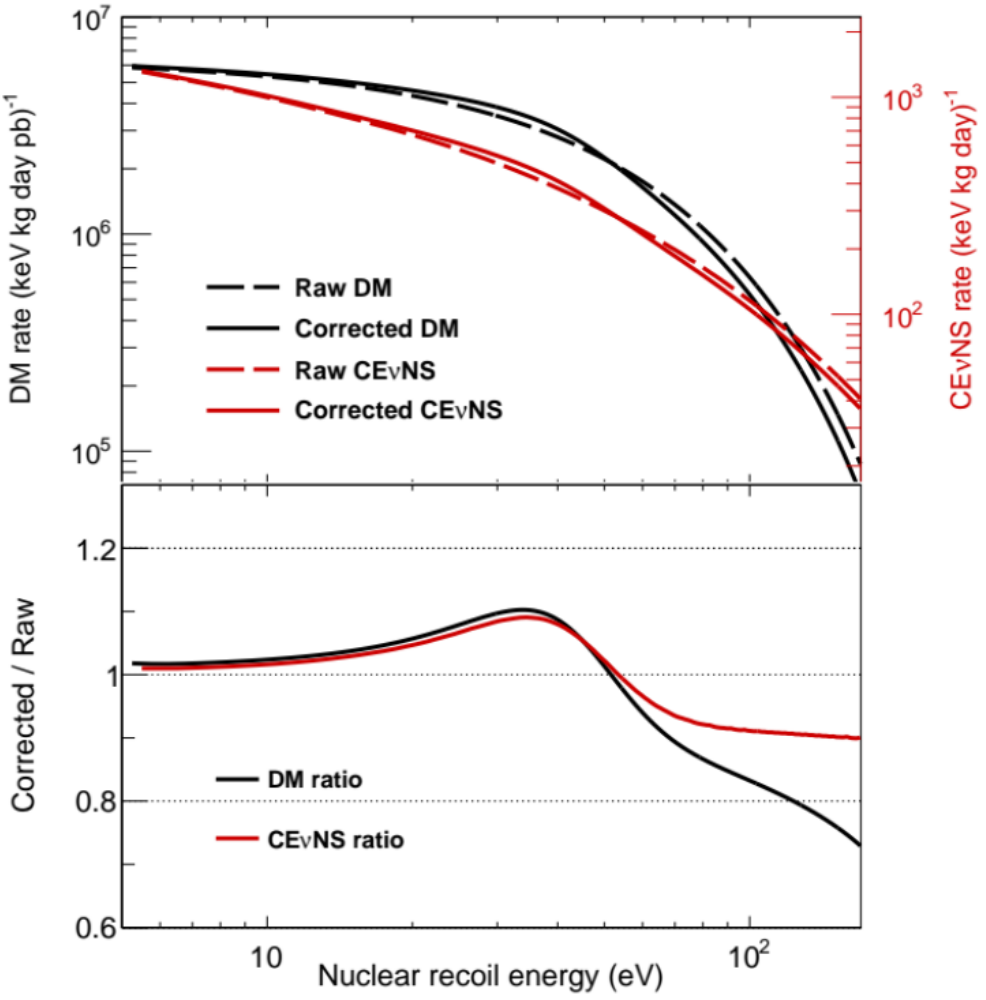

Figure 5.14. Predicted nuclear recoil spectra from elastic scattering of 2 GeV dark matter particles (black lines) and reactor neutrinos via CEνNS (red lines), shown both with (solid lines) and without (dashed lines) accounting for the impact of lattice defects. The dark matter rate is scaled to an arbitrary DM–nucleon interaction cross-section. Also shown is the ratio between the corrected and the raw spectra. Figure from [197].

6

Experimental validations of the CRAB method

The use of neutron capture to induce nuclear recoils has already successfully been employed by several experiments in germanium [173] and silicon detectors [199, 200]. However, none has clearly identified a well-defined nuclear recoil peak arising from this process. In 2022, the CRAB collaboration has been the first to observe such a peak. Section 6.1 summarises this first validation on a $CaWO_4$ target. Section 6.2 presents a second validation performed with a Al_2O_3 target. I was highly involved in the cryostat commissioning as well as in the analysis of cryodetector data acquired during this run.

6.1 CRAB phase I: Experimental validation

During the summer of 2022, the first experimental validation of the CRAB method on a $CaWO_4$ target took place at the Technical University of Munich (TUM) [121].

6.1.1 Experimental setup

An illustration of the setup is shown in Figure 6.1. The target is a 0.75 g cubic $CaWO_4$ crystal equipped with a Transition Edge Sensor (TES) developed for the NUCLEUS experiment. It is installed in a dry dilution refrigerator (Bluefors LD400) [98]. The operation of the cryodetector, including its design and the associated readout chain, has been described in detail in Chapter 2. For continuous electronic recoil calibration, the detector is exposed to an ^{55}Fe source glued onto the copper lid of the cryodetector. This source emits characteristic K_α and K_β X-ray lines at 5.985 keV and 6.490 keV, originating from the daughter nucleus ^{55}Mn.

A ^{252}Cf portable neutron source with an activity of 3.54 MBq was positioned next to the cryostat at a distance of 80 cm from the cryogenic detector. This californium source emits mainly alpha particles, which, due to their low penetration depth in matter, do not induce any background. ^{252}Cf also decays by spontaneous fission with a branching ratio of 3%. On average, each fission event produces 3.77 fast neutrons with a mean energy of 2.12 MeV [178, 201], along with MeV-range γ-rays.

To thermalize neutrons and stop γ-rays, a compact moderator with dimensions $(32 \times 34 \times 42)$ cm^3 was designed, surrounding the neutron source (see left panel of Figure 6.1). The source is embedded in a 10 cm polyethylene cube. In the direction of the cryostat, there is a 5 cm thick PE layer for additional neutron thermalization. A 7 cm thick lead layer reduces the γ flux from the source. To enhance the neutron flux through the collimator, graphite blocks are positioned above, below, and behind the source, reflecting neutrons that would otherwise be lost. An outer layer of borated polyethylene surrounds the source to reduce the radiation dose of the environment. The resulting thermal neutron rate at the cryodetector is 0.25 n_{th}/s.

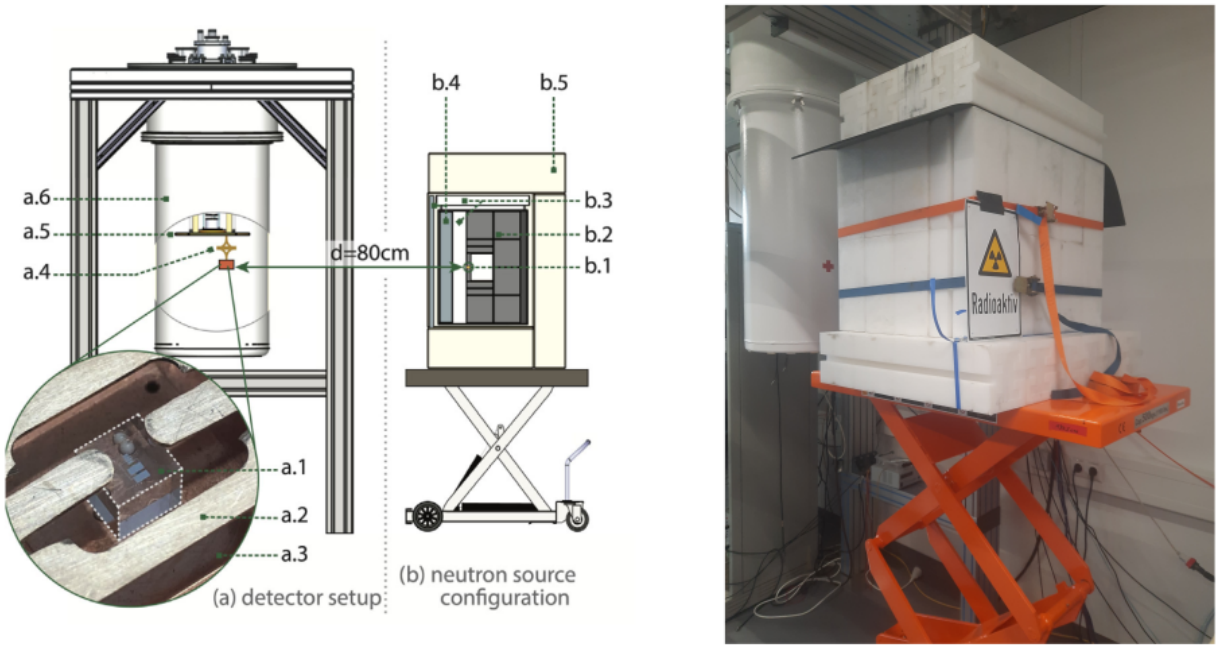

Figure 6.1. Left: Scheme of the experimental setup including the cryostat, the cryogenic detector and the portable neutron source. Figure from [121]. Right: Picture of the experimental setup with the ^{252}Cf portable thermal neutron source.

6.1.2 Data analysis

A background run is first used to characterize the ambient background, with a total runtime of 25.3 h corresponding to a live-time of 13.8 h after taking into account detector efficiency. Then a second run was acquired with the neutron source with a runtime of 40.2 h and a corresponding live-time of 18.6 h. Two independent analyses were conducted using the DIANA and CAT frameworks. The DIANA software was developed for the neutrinoless double beta decay CUORE experiment [166, 167] and adapted for the NUCLEUS experiment [202], while the CAT software was developed for the CRESST experiment [203]. The results presented here are based on the DIANA analysis and are consistent with those obtained using CAT, within uncertainties.

A baseline resolution of $\sigma_{\mathrm{BR}} = (6.54 \pm 0.02)$ eV was achieved during the source run. The energy conversion uses a calibration factor of 9.296 ± 0.0023 eV/mV, obtained from the two iron calibration lines. Left panel of Figure 6.2 shows the reconstructed recoil energy spectra for both the background data (dark grey) and the source data (light grey). The source spectrum exhibits a peak feature near the expected energy of 112.5 eV. The energy scale was calibrated using iron, so the peak is not expected to appear exactly at 112.5 eV due to non-linearity effects and the difference between nuclear and electronic energy scales.

The steep rise at low energies originates from the continuum of nuclear recoils induced by multi-γ de-excitations, combined with an increasing background. At higher energies, an additional contribution arises from the scattering of fast neutrons emitted by the source. These two background components are modeled by two exponential functions. The peak itself can be fitted with a Gaussian. Therefore, two binned likelihood fits are performed in the range [60, 300] eV: the null hypothesis H_0 without a Gaussian component (dashed blue line), and the alternative hypothesis H_A including the Gaussian (red line). The statistical test $t = 2\ln\left(\frac{\mathcal{L}_{\mathrm{Bkg+sig}}}{\mathcal{L}_{\mathrm{Bkg}}}\right)$ follows a χ^2 distribution with 3 degrees of freedom and is used to determine the significance of the peak. The null

hypothesis is rejected with a significance of 3.1 σ. The fit yields a peak position of $\mu_{\text{peak}} = 106.7^{+1.9}_{-2.0}$ eV and a standard deviation of $\sigma_{\text{peak}} = 6.0^{+1.7}_{-1.4}$ eV [121].

This result is promising, as it represents the first direct measurement of a neutron-capture-induced nuclear recoil at the 100 eV scale. However, this measurement still suffers from limited statistics due to the low intensity of the neutron source, as well as background from fast neutrons, which prevents the observation of the second calibration peak at 160 eV. More details about the analysis of this run can be found in [121, 175].

A similar measurement was performed by the CRESST collaboration, where three $CaWO_4$ detectors were exposed to a thermal neutron flux from an AmBe source. The CRAB peak at 112 eV was observed in all three detectors, with respective significances of 3.6, 5.8, and 6.6 σ (see right panel of Figure 6.2) [204].

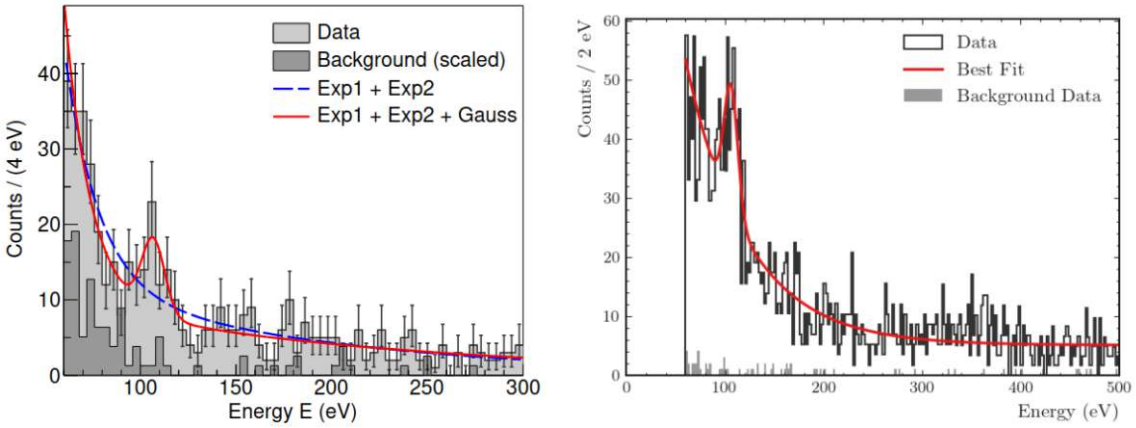

Figure 6.2. Left: Recoil energy spectra recorded by the NUCLEUS experiment in a $CaWO_4$ detector. The background dataset is in dark gray and the source dataset in light gray. Two fit models are shown: the dashed blue line represents the background model, and the solid red line represents the background plus signal model. Figure from [121]. Right: Energy deposited in the CRESST TUM93A $CaWO_4$ detector. Figure from [204].

6.2 CRAB measurement on a Al_2O_3 target

At the beginning of 2024, another source run was taken at the UnderGround Laboratory (UGL) in Munich with a Al_2O_3 detector of the NUCLEUS experiment. This effort was part of the preparatory work for the phase II of CRAB presented in the next chapter. This section first describes the cryogenic setup and the cryodetector. It then presents the data analysis and results.

6.2.1 Experimental setup

The experimental setup is shown in Figure 6.3. The cryostat is surrounded by a 14 cm thick lead shielding. The same neutron source as used in the previous validation with the $CaWO_4$ target is placed 48 cm from the cryodetector.

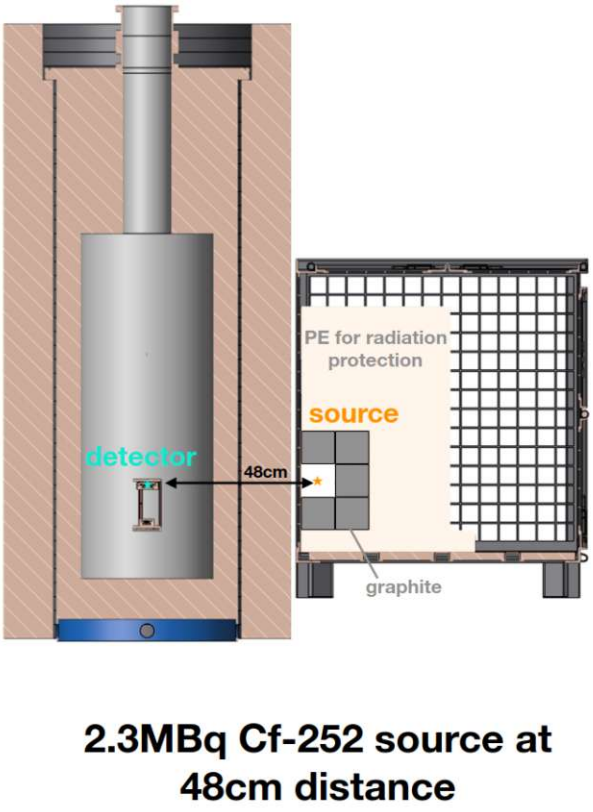

Figure 6.3. Overview of the experimental setup including the cryostat and the portable neutron source. Credits: A.Erhart.

6.2.1.1 Wet cryostat

The cryostat selected for phase II of the CRAB project is a wet ^{3}He–^{4}He dilution refrigerator, the Kelvinox-100 model from Oxford Instruments plc. This cryostat was initially operated by the CRESST experiment and has since been made available to the CRAB collaboration for the phase II. Prior to its relocation to the new experimental site dedicated to this phase, it was installed in the pit of the UGL. Technical details on the cooling principle of the wet cryostat can be found in Appendix A. Despite the need for regular liquid helium refills, long-term measurements with cryogenic detectors are feasible over several months, under very stable thermal conditions. The cryogenic system consists of an insert placed at the center of a dewar capable of holding up to 60 liters of liquid helium (see Figure 6.4). The insert is enclosed in the Inner Vacuum Chamber (IVC), which comprises several temperature stages: the 4 K stage, the 1 K stage containing the 1 K pot, the still stage operating at approximately 800 mK and the mixing chamber (MXC) reaching a base temperature below 10 mK. The refrigerator provides a cooling power of approximately 140 μW at 100 mK. Below the mixing chamber lies a cylindrical experimental volume with a diameter of 130 mm and a height of 80 mm. Multiple detectors can be installed on two NOSV copper mounting plates within this volume, which is shielded by a 1 mm thick copper enclosure at the MXC stage to block thermal radiation from higher-temperature stages. Temperature monitoring is achieved using two diodes read by a Lakeshore 325 controller for the 4 K stage and 1 K pot during cool-down. Two additional ruthenium oxide (RuOx) thermometers from Bluefors, read out by a Lakeshore 372 AC resistance bridge, are used to monitor the MXC stage and the detector box during steady-state operation. The cryostat is equipped with a 3-channel DC-SQUID (Superconducting Quantum Interference Device) system from Magnicon for TES readout. Dedicated bias and heater lines are integrated into the readout circuit.

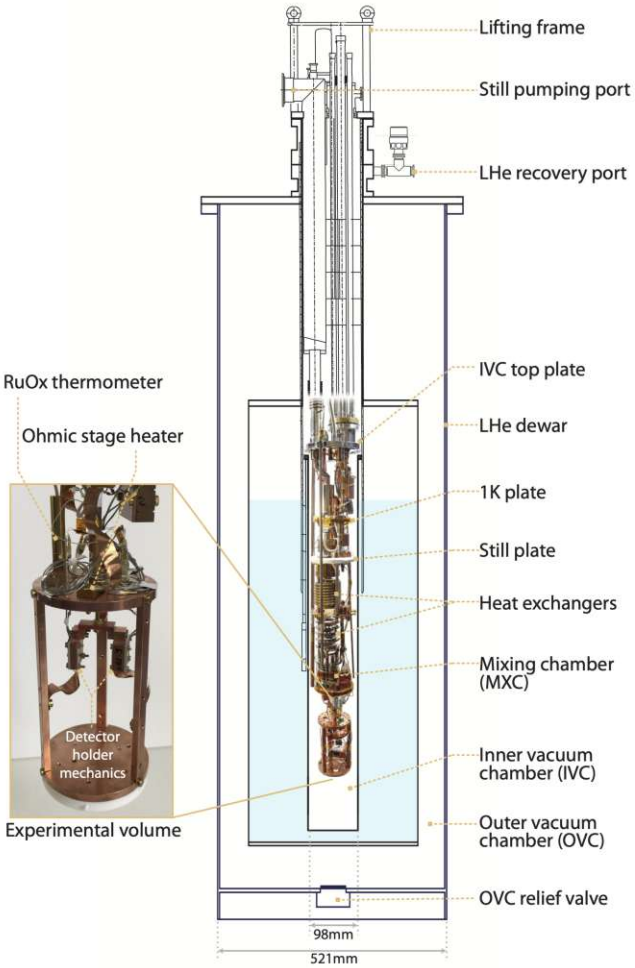

Figure 6.4. Schematic overview of the wet ^{3}He–^{4}He dilution refrigerator (Kelvinox-100, Oxford Instruments plc). The figure shows the different temperature stages of the cryostat, including the heat exchangers used for thermalization. The experimental volume, located at the bottom of the IVC, houses the cryodetector. Figure from [193].

6.2.1.2 Cryodetector

Before moving to Vienna for measurements with the reactor neutron beam, performance tests of the cryodetectors were carried out. In particular, during this commissioning phase, valuable data were acquired with a Al_2O_3 cube, providing additional validation of the CRAB method on a different target material. The cryodetector cube of $5 \times 5 \times 5$ mm^3 is enclosed in a copper housing that serves as the detector holder. The cryodetector is mounted on a Printed Circuit Board (PCB) and secured using flexible bronze clamps. Sapphire balls are placed at the contact points for thermal isolation. The PCB, which acts as the electrical interface, is composed of glass fiber reinforced epoxy.

The thermal and electrical connections are implemented as described in Section 2.4.2. A picture of the copper detector housing and the PCB is shown in Figure 6.5. The copper top plate of the detector holder includes a ^{55}Fe source deposited on a copper strip. This source continuously emits the K_α and K_β X-ray lines at 5.985 keV and 6.490 keV, allowing for an online calibration and monitoring of the detector's electronic recoil response.

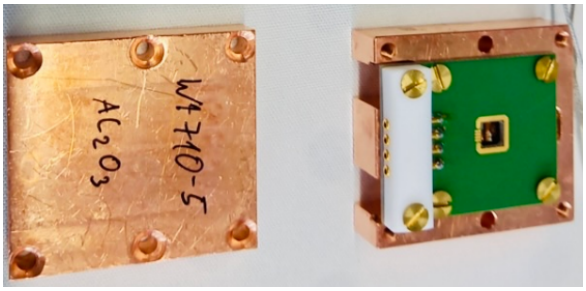

Figure 6.5. Pictures of the Copper detector holder hosting the PCB and the Al_2O_3 crystal. Credits: A.Erhart.

6.2.2 Datasets

Over a two-month period at the beginning of 2024, three configurations were used, as described in Table 6.1. Configuration 4 corresponds to background data, with a total of 212.28 hours of data taken with no source. Configuration 7 includes the neutron source, with a cumulative runtime of 362.14 hours. Finally, configuration 8 also includes the neutron source, but with an additional 5 mm boron loaded rubber mat to capture thermal neutrons emitted by the source, totaling 158.12 hours of data. This last configuration serves as a reference for source-induced background, as it specifically suppresses the signal from thermal neutrons while leaving the fast neutron and gamma backgrounds mostly unaffected. This enables a differential comparison with configuration 7. The acquisition system records only pulse traces that exceed the trigger threshold, with a sampling frequency of 200 kHz. Each trace consists of a window of 8192 samples, corresponding to a total duration of 40.96 ms.

Configuration	Type	Run time (h)	Goals
4	Background data, no source	212.28	• Background estimation • Iron calibration • Stability
7	Source data	362.14	• CRAB calibration • Stability
8	Source data with B_4C	158.12	• Source background estimation • Stability

Table 6.1. Overview of run configurations and their goals.

6.2.3 Low level analysis

The cryodetector analysis methods are similar to those described in Section 4.3. The selection cuts used to build the Standard Event (SEV) and the Noise Power Spectrum (NPS) were developed using background configuration 4, and subsequently applied to the source configurations. The SEV is shown on the left of Figure 6.6; its fit using the Pröbst's parametrization [109] yields the parameters $\tau_{\text{rise}} = 42$ μs, $\tau_{\text{fast}} = 0.79$ ms, and $\tau_{\text{slow}} = 6.2$ ms, highlighting the fast response of the cryodetector. From noise traces, the NPS is calculated and shown on the right of Figure 6.6. The data contain artifacts that are removed through a data cleaning procedure. I initially defined these cuts using the background data of configuration 4 and then applied them to configurations 7 and 8. The cuts applied are as follows:

- **Onset:** Position of the maximum of the trace in the window. I select pulses with onset of ±1 ms.
- **Rise time:** It is calculated backward in time as the difference between the time of the maximum of the trace and the last sample that remains above 80% of the maximum value. I select pulses with rise time below 300 μs.
- **Decay time:** Already defined in Section 4.6.1. I select pulses with decay times less than 20 ms.
- **Right-left baseline:** Already defined in Section 4.6.1. I select pulses with a right-left baseline of above -0.01 V.

The recoil energy spectra, estimated from Optimum Filter (OF) amplitudes before and after data cleaning, are shown in Figure 6.7. The iron peak is within the detector's saturation region, emphasizing the necessity for a reconstruction method capable of accurately recovering the amplitudes of saturated pulses at higher energies.

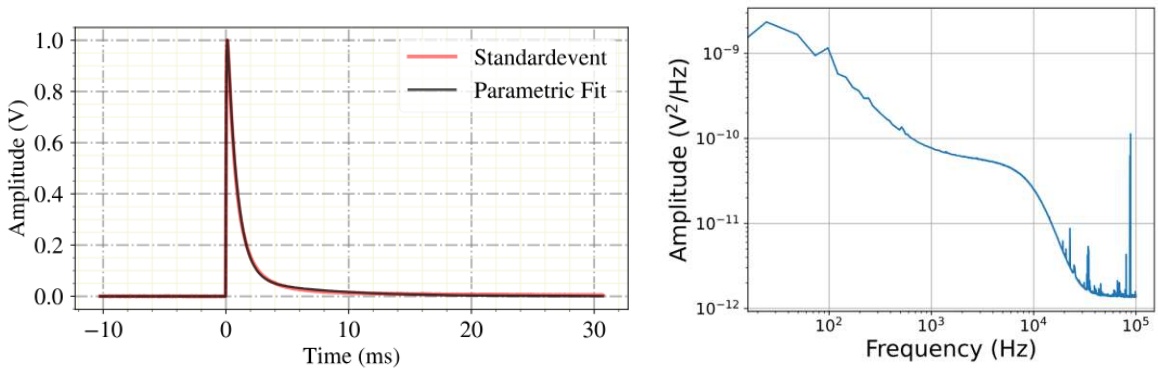

Figure 6.6. Left: Built standard event, also shown is the fit by the Pröbst's parametrization [109]. Right: NPS obtained for configuration 4.

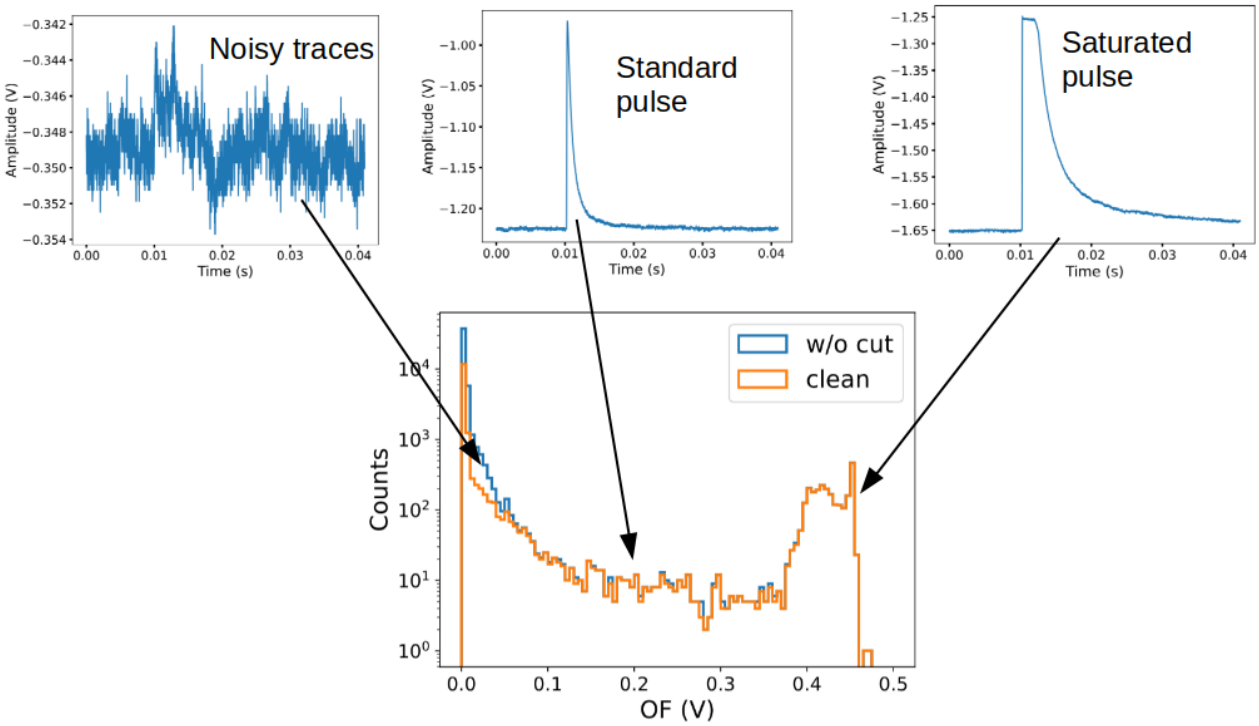

Figure 6.7. Recoil energy spectra for configuration 4, estimated with OF amplitude before (blue) and after (orange) cleaning procedure removing noisy traces. At high energy we observe the saturation of the pulse amplitudes.

6.2.4 Saturated pulse amplitude reconstruction

High-energy events can excessively heat the TES, driving it out of its superconducting transition into the normal conducting state. This results in a saturation plateau in the recorded pulse. To address this situation, a truncated fit method is applied to reconstruct the pulse amplitude [155, 156]. As long as the pulse returns to the baseline within the recorded trace window, it is possible to fit the signal using a scaled SEV template. This is done by minimizing the mean squared error (MSE) between the pulse trace and the SEV pulse shape. The fit includes four parameters to model the baseline with a third-degree polynomial, one onset parameter for the pulse start time and one amplitude parameter for scaling the SEV. Since saturated pulses differ significantly in shape from the SEV template at high amplitudes, the MSE minimization is restricted to the unsaturated part of the pulse. This is achieved by excluding all samples exceeding a predefined voltage threshold, known as the truncation limit. The truncation limit must be low enough to remain within the linear regime where the SEV pulse shape remains valid, but also high enough to include a sufficient number of samples to allow for a reliable pulse reconstruction at higher amplitudes. An appropriate choice of this limit can be made by studying the detector's response to heater pulses, as illustrated in the left panel of Figure 6.8. A truncation limit of 250 mV represents a good compromise. The right panel of the figure illustrates the truncated fit performed below this threshold and its extrapolation beyond, up to 1.5 V. The reconstructed pulse amplitude spectrum for configuration 4 is displayed in the left panel of Figure 6.9, revealing two distinct peaks around 0.75–0.80 V. These correspond to the K_α and K_β lines of the ^{55}Fe source.

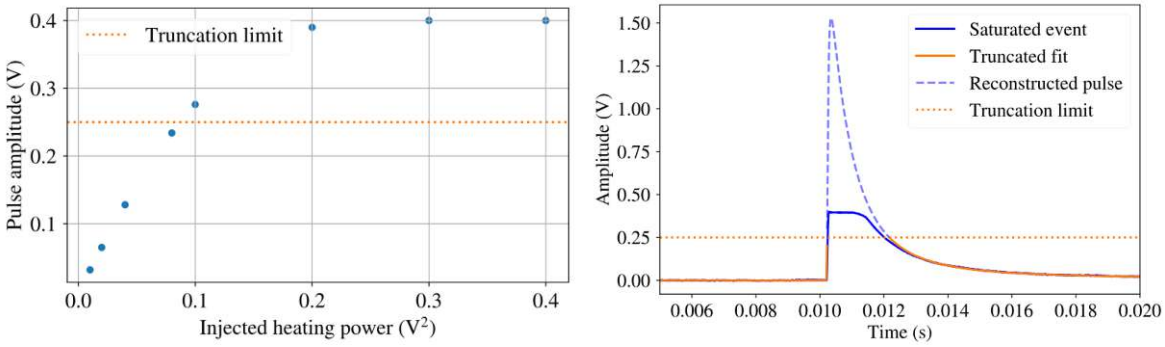

Figure 6.8. Left: Amplitude of heater pulses as a function of injected heater power. This curve illustrates the saturation effect of the TES above the truncation limit at 250 mV. Right: Example of a truncated fit. The saturated pulse (blue) is fitted only below the truncation limit (orange dotted line) on the pulse trace (orange solid line). The reconstructed pulse is shown as the dashed blue line. More details are provided in the text.

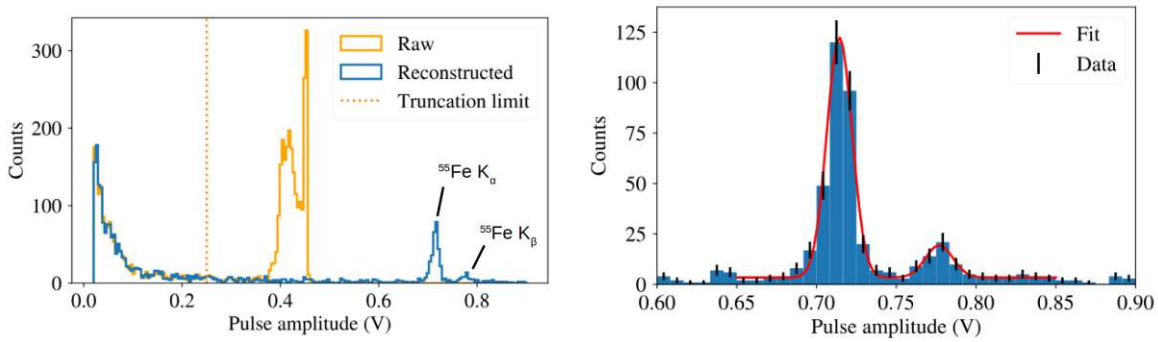

Figure 6.9. Left: Pulse amplitude spectra before (blue) and after (orange) saturated pulse amplitude reconstruction. After reconstruction, two calibration lines from iron become clearly identifiable. Right: Fit of the iron K_α and K_β peaks using two Gaussian functions. The resulting calibration factor is 8.04 ± 0.02 eV/mV.

6.2.5 Detector performance

The detector exhibited excellent stability during all three configurations since the response to heater pulses (see Figure 6.10), demonstrates sub-percent level variations in amplitude throughout each configurations. A noticeable shift in the TES operating point occurred between configuration 7 and configuration 8, leading to a gain variation of approximately 10%. An independent iron calibration was thus performed for each configuration. The stability of the heater pulse amplitudes within each configuration validates the robustness of the calibration over time. For the calibration, I fit the iron spectrum by two Gaussian distributions plus a constant background. The result of the fit for the configuration 4 is shown on the right panel of Figure 6.9. The corresponding parameters are listed in Table 6.2. The ratios $\frac{\mu_\beta}{\mu_\alpha} = 1.091 \pm 0.003$ and $\frac{I_\alpha}{I_\beta} = 7.8 \pm 2.0$ are in good agreement with the expected theoretical values of 1.10 and 7.7, respectively. This fit results in a calibration factor of 8.04 ± 0.02 eV/mV. The baseline energy resolution remained very stable across all three configurations, with a remarkable average value of 4.1 eV, as shown in Figure 6.11.

Parameter	K_α	K_β
Integral I [counts]	417 ± 34	54 ± 13
Mean μ [V]	0.734 ± 0.001	0.801 ± 0.002
Width σ [V]	0.013 ± 0.001	0.016 ± 0.003

Constant background: $C = 3.0 \pm 0.6$ counts

Table 6.2. Fit parameters for the K_α and K_β peaks from iron.

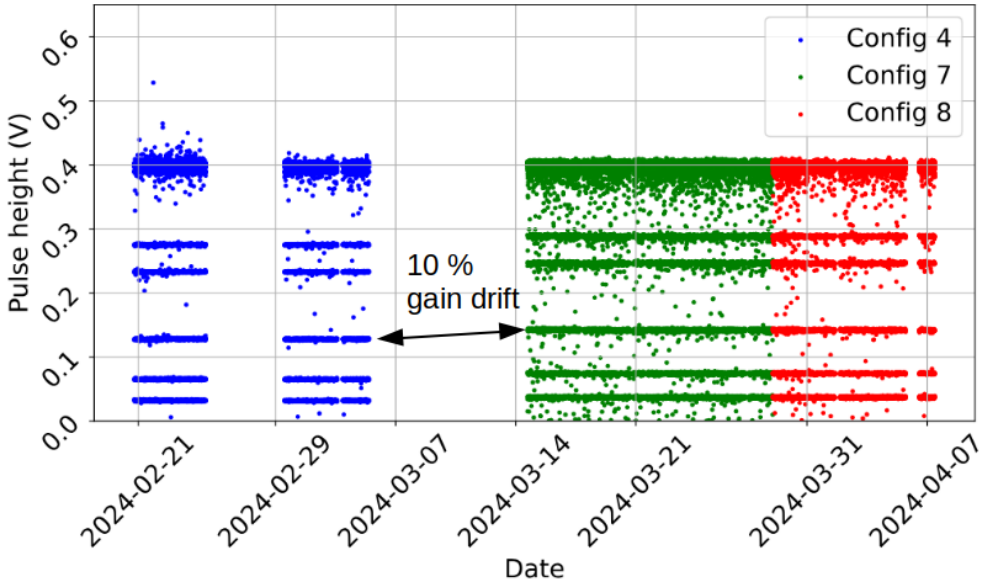

Figure 6.10. Stability of the heater pulse response across the three configurations. Apart from a noticeable shift of the operating point within the TES transition curve causing a gain drift of about 10% between configurations 4 and 7, stability at the sub-percent level is demonstrated.

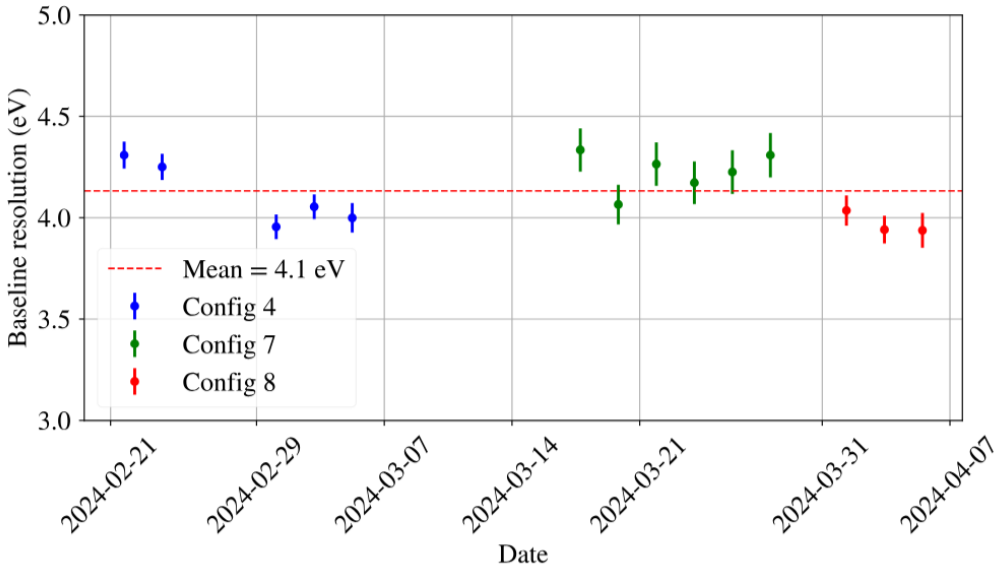

Figure 6.11. Baseline resolution stability over the three configurations.

6.2.6 Source analysis

Figure 6.12 shows the recoil energy spectra for the configurations with the neutron source, without (Config 7) and with B_4C shielding (Config 8), which is used to absorb thermal neutrons. In both spectra, the iron K_α peak is visible at 0.81 mV, corresponding to a calibration factor of 7.28 $\pm$0.02 eV/mV. At lower amplitudes, a peak appears below 200 mV, as highlighted in the inset. To quantitatively assess this observation, I now perform a blind peak search and apply a χ^2 test to identify statistically significant peaks in the low energy region.

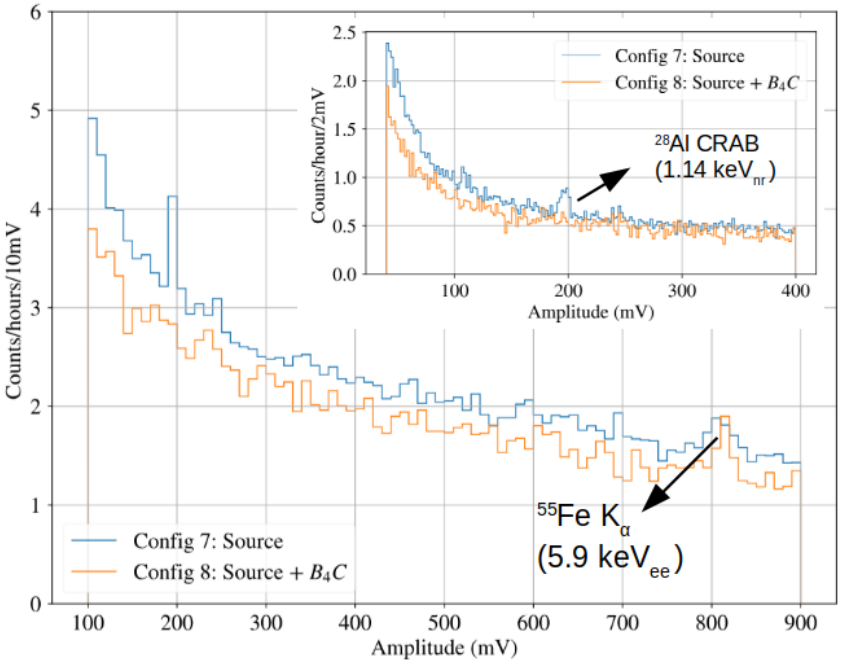

Figure 6.12. Recoil energy spectra for Configuration 7 (without B4C, blue) and Configuration 8 (with B4C, orange). The iron Kα calibration peak is clearly visible in both spectra. The inset shows a zoomed-in view of the low-energy region, where a candidate CRAB peak emerges below 200 mV.

6.2.6.1 Blind Peak Search

To perform a blind peak search, a *sliding window* approach is used to identify statistically significant peaks on top of the expected background. For this purpose, I define a background-only model, f_{bkg}, composed of two exponential components to account for the steep rise at low energies due to γ interactions and elastic scattering of fast neutrons from the source, along with a constant offset:

$$f_{\text{bkg}}(x; A_1, A_2, \tau_1, \tau_2, C) = A_1 e^{-x/\tau_1} + A_2 e^{-x/\tau_2} + C \tag{6.1}$$

The background-plus-signal model, $f_{\text{bkg+signal}}$, includes an additional Gaussian peak:

$$f_{\text{bkg+signal}}(x; \theta_{\text{bkg}}, I_{\text{peak}}, \mu_{\text{peak}}, \sigma_{\text{peak}}) = f_{\text{bkg}}(x; \theta_{\text{bkg}}) + \frac{I_{\text{peak}}}{\sqrt{2\pi}\sigma_{\text{peak}}} \exp\left[-\frac{(x-\mu_{\text{peak}})^2}{2\sigma^2_{\text{peak}}}\right] \tag{6.2}$$

where, I_{peak}, μ_{peak}, and σ_{peak} represent the integral of the peak, its position, and its standard deviation, respectively. The background parameter set is defined as $\theta_{\text{bkg}} = (A_1, A_2, \tau_1, \tau_2, C)$.

We define the likelihood ratio test statistic t as:

$$t = -2 \ln \left(\frac{\mathcal{L}_{\text{bkg}}}{\mathcal{L}_{\text{bkg+signal}}} \right) \tag{6.3}$$

where $\mathcal{L}_{\text{bkg}}$ and $\mathcal{L}_{\text{bkg+signal}}$ are the likelihoods of the background-only and background-plus-signal hypotheses defined as follows [33]:

$$\ln \mathcal{L}_{\text{bkg}} = \sum_{i=1}^{N_{\text{bins}}} \left[D_i \ln \left(\frac{D_i}{S_{i,\text{bkg}}} \right) + S_{i,\text{bkg}} - D_i \right] \tag{6.4}$$

$$\ln \mathcal{L}_{\text{bkg+signal}} = \sum_{i=1}^{N_{\text{bins}}} \left[D_i \ln \left(\frac{D_i}{S_{i,\text{bkg+signal}}} \right) + S_{i,\text{bkg+signal}} - D_i \right] \tag{6.5}$$

In these expressions:

- D_i is the observed number of events in bin i
- $S_{i,\text{bkg}} = f_{\text{bkg}}(V_i; \theta_{\text{bkg}})$ is the expected count from the background-only model at the bin center V_i
- $S_{i,\text{bkg+signal}} = f_{\text{bkg+signal}}(V_i; \theta_{\text{bkg}}, I_{\text{peak}}, \mu_{\text{peak}}, \sigma_{\text{peak}})$ is the expected count from the background-plus-signal model at the bin center V_i

According to Wilks' theorem [33], under the null hypothesis H_0, the test statistic t follows a χ^2 distribution with 3 degrees of freedom (corresponding to the difference in the number of free parameters: 8 - 5 = 3).

A sliding window of 20 bins (corresponding to 40 mV) is applied from 40 mV to 300 mV, with a step size of 5 bins between windows. The scan starts at 40 mV, as searching for peaks below this value is not meaningful due to the exponential rise in the event rate. For each window, both background-only and background+signal models are fitted, and the test statistic t is computed. A value of t that is too high to be consistent with a chi-squared distribution with 3 degrees of freedom indicates the presence of a signal peak within that window.

For each window, the peak position is initially set to the center. The width is initialized to approximately 10 mV, which is within the expected resolution range for this energy domain. The amplitude is randomly assigned a value between 0 and the maximum bin value in the window. As for the background parameters, a first global background-only fit is performed on the entire spectrum to determine initial values. The resulting fits for each window are shown in green in Figure 6.13. Three distinct local peak features are identified with a significance above 2 σ (their corresponding fits are shown in red). An intense peak is observed around 200 mV. When applying the iron-based calibration, its position shows a slight discrepancy with the expected location of the CRAB signal at 1144.8 eV. Nevertheless, the observed proximity supports its identification as the CRAB peak. The calibration mismatch between the CRAB and iron energy scales will be further discussed in Section 6.2.6.2. Another peak is found near 100 mV, potentially compatible with the predicted feature at 570 eV in the simulated Al_2O_3 spectrum (see Figure 5.9). The pulse amplitude reconstruction method creates a third artificial peak near the truncation level of 250 mV, which passed the blind analysis. This peak is an artifact that does not appear when using the OF estimator and will not be considered further in the analysis.

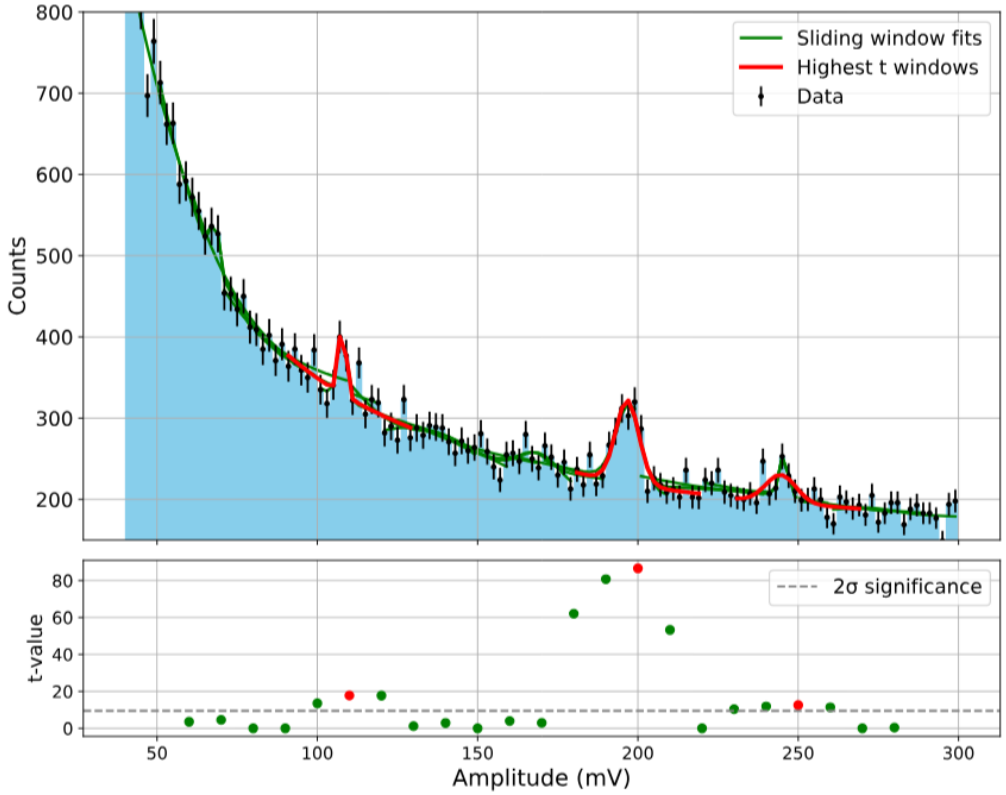

Figure 6.13. Blind peak search using a sliding window approach. For each window, the value of the statistical test t is shown in the bottom plot. In the top plot, solid lines represent the fits within each window: green lines correspond to regular sliding window fits, while red lines highlight the window with the highest t-value within the three-peak regions.

For the two candidate CRAB peaks identified in the blind analysis, I evaluate their statistical significance through a global fit over the full amplitude range. The gaussian parameters obtained from the local fits are used as initial conditions. The fits shown in Figure 6.14, yield the following values:

- **First peak:**
  - $I_{\text{peak}} = 141 \pm 57$ counts
  - $\mu_{\text{peak}} = 107.7 \pm 0.4$ mV
  - $\sigma_{\text{peak}} = 1.3 \pm 0.6$ mV
- **Second peak:**
  - $I_{\text{peak}} = 403 \pm 53$ counts
  - $\mu_{\text{peak}} = 196.7 \pm 0.7$ mV
  - $\sigma_{\text{peak}} = 3.4 \pm 0.5$ mV

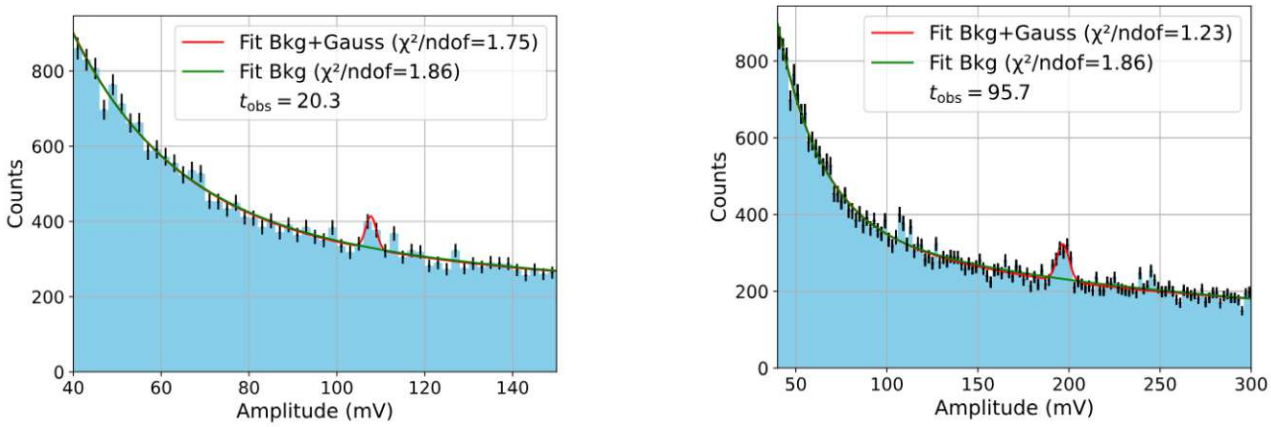

Figure 6.14. Fits of the two candidate CRAB peaks using the f_{bkg} (green curves) and $f_{\text{bkg+signal}}$ (red curves) models. The corresponding test statistics t yield significances of 3.6 σ (left) and 9.2 σ (right), respectively.

The observed test statistics $t_{\text{obs}} = 20.3$ and $t_{\text{obs}} = 95.7$ have to be compared with a χ^2_3 distribution with 3 degrees of freedom plotted on Figure 6.15. The p-value is computed as the probability, under the null hypothesis H_0, of obtaining a value of t as extreme or more extreme than t_{obs} (red-shaded area) [205]:

$$p = \int_{t_{\text{obs}}}^{\infty} f(t|H_0)\, dt \tag{6.6}$$

Finally, we convert the p-value into a significance Z in standard deviations using:

$$Z = \Phi^{-1}(1 - p) \tag{6.7}$$

where Φ is the cumulative distribution function of the standard normal distribution. The resulting significances for the two peaks are 3.6 σ and 9.2 σ, respectively.

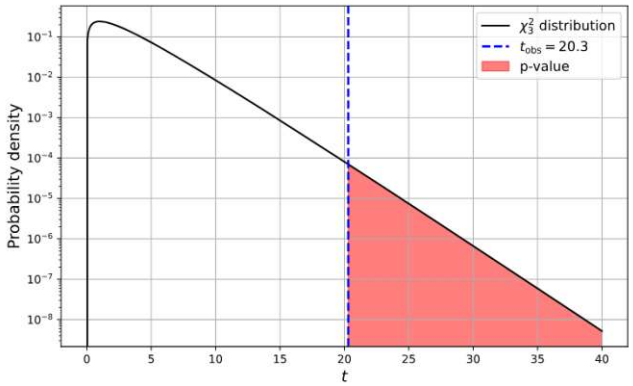

Figure 6.15. Distribution of χ^2_3 (black solid line). The observed value $t_{\text{obs}} = 20.3$ is indicated by the blue dashed line. The p-value is the integral of the χ^2_3 distribution above t_{obs}, corresponding to the red shaded area.

6.2.6.2 Discussion on energy scales

In the source configuration, several calibration lines are visible: two from CRAB and one from the ^{55}Fe source. Figure 6.16 shows the measured pulse amplitudes as a function of the corresponding theoretical energies. Notably, the CRAB peaks at 107.7 mV and 196.7 mV appear overestimated by approximately 36% and 25%, respectively, when compared to the energy scale derived from the iron calibration. This result highlights the limitation of extrapolating an iron-based calibration to lower-energy nuclear recoils. Several effects contribute to this discrepancy. First, the detector response differs between nuclear and electronic recoils. Additionally, in a separate run, this same detector exhibited strong non-linearity in the 500 eV to 10 keV range when exposed to an X-ray fluorescence sources producing calibration lines within this energy region (see [119] for more details on this calibration method). This may explain the failure of the iron extrapolation at low recoil energies. Nevertheless, the CRAB signal provides a local calibration anchor for nuclear recoils. This underlines the need for in-situ CRAB calibration in the region of interest, avoiding reliance on extrapolations from higher-energy X-ray sources with limited accuracy for low energy nuclear recoils. Finally, combining CRAB calibration with X-ray fluorescence sources could enable a direct comparison between nuclear recoils at 1140 eV_{nr} and electronic recoil lines at 927.7 eV_{ee} (Cu Lα) and 1486.4 eV_{ee} (Al K$_\alpha$). Such a comparison would provide new insight into the difference in detector response between electronic and nuclear recoils with unprecedented precision.

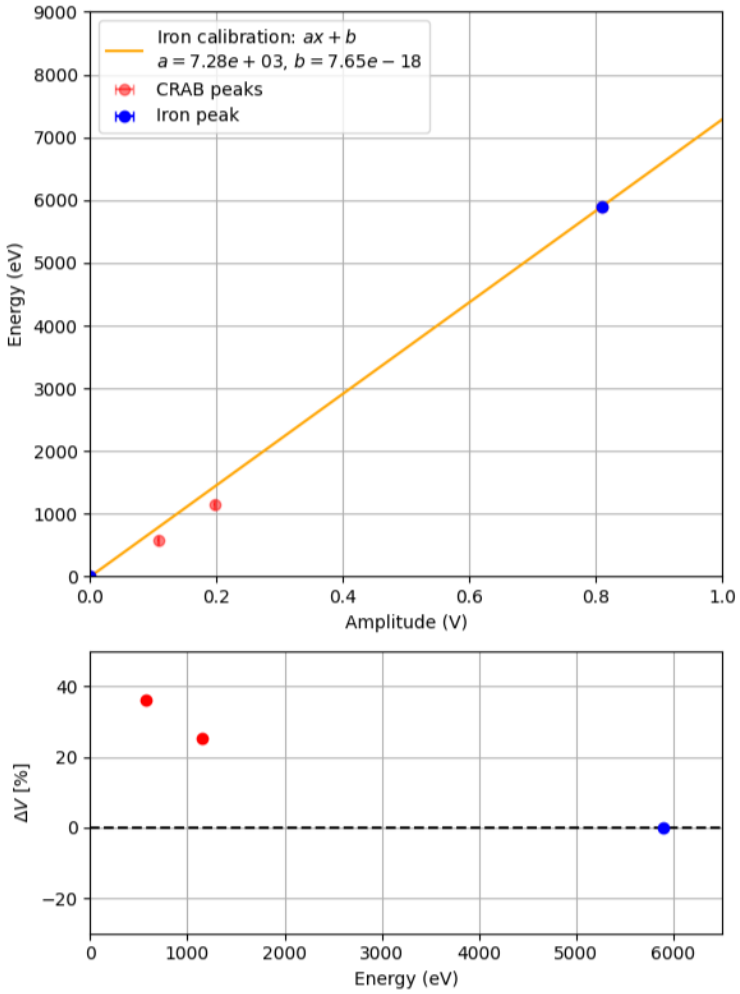

Figure 6.16. Linear extrapolation of the iron calibration down to low recoil energies. The bottom panel highlights the discrepancy between the CRAB peaks and the iron calibration.

6.3 Conclusion

These initial experimental validations represent a significant milestone for the CRAB project and are very promising, especially considering the simplicity of the experimental setup. Although the neutron source introduced a notable background, which limited the precision of our measurements, these results clearly demonstrate the feasibility of the method. The data analysis for this run is still ongoing. In particular, the 570 eV peak, if confirmed, would represent the first observation of a timing-induced peak from 2-γ cascades. Its amplitude results from the interplay between the lifetimes of the intermediate nuclear levels and the stopping time of the nuclear recoil in the material. Comparing this amplitude with simulations currently underway could thus provide valuable insights. These achievements pave the way for phase II of the CRAB project, which will benefit from high statistics and a pure thermal neutron beam, enabling a substantial reduction in background and improved measurement accuracy. The next two chapters will focus on the detailed presentation of this phase II, including its commissioning and first results.

7

CRAB phase II

Phase II of the CRAB project is the natural continuation of the experimental validation performed on the $CaWO_4$ target in 2022. For this second phase, the collaboration moved to a new experimental site: the Atominstitut in Vienna, leveraging its research reactor, which provides a flux of pure thermal neutrons. This chapter begins by outlining the motivations and requirements of this second phase (Section 7.1). It then presents the simulations I conducted during the first year of my PhD, which were particularly focused on demonstrating the relevance of coincidences between γ and the Nuclear Recoil (NR) (Sections 7.2 and 7.3). The experimental setup ultimately deployed at the Atominstitut is described in Section 7.4. As part of my joint PhD program with the Technical University of Vienna (TU Wien), I had the opportunity to spend my second year on-site at the Atominstitut to work on the preparation and commissioning of this phase II, detailed in the next chapter.

7.1 Motivations and requirements

The experimental validations presented in the previous chapter highlighted a major limitation: the inability to achieve high-precision results due to the background level. This background is primarily linked to the neutron source, which generates both fast neutrons and γ-rays. Phase II of the CRAB project specifically addresses this issue by utilizing a pure and collimated thermal neutron beam provided by the TRIGA Mark-II research reactor at the Atominstitut in Vienna (ATI) [206]. The absence of fast neutrons and the collimation of the beam drastically reduces the background compared to previous experimental setups.

While a high neutron flux improves statistical precision, it can also lead to significant pile-up due to the decay of detector pulses on the order of several tens of milliseconds. Thus, a limiting neutron flux of a few hundred neutrons per second per cm^2 is required at the crystal position. A low reactor power of 250 kW is required to meet this specification. Figure 7.1 illustrates the principle of Phase II. A collimated, pure thermal neutron beam is reflected by a graphite crystal toward the cryostat, which is positioned along this secondary beamline. The beam passes through the cryostat, enabling neutron captures within the cryodetector.

In Figure 7.1, γ-detectors are shown surrounding the cryostat. This additional feature of Phase II allows for the detection of nuclear recoils in coincidence with their associated high energy γ-ray. As demonstrated by the simulations in Sections 7.2 and 7.3, such γ–NR coincidences enable the extraction of calibration peaks otherwise overwhelmed by the multi-γ background due to detector resolution effects. This coincidence tagging thus relaxes the energy resolution requirements needed for the calibration.

Leveraging all these improvements, Phase II of the CRAB project provides a dedicated facility for the calibration of various cryogenic detector materials — including $CaWO_4$, Al_2O_3, Ge, and Si — and for conducting high-precision measurement campaigns to gain deeper insight into the physics underlying cryodetector responses.

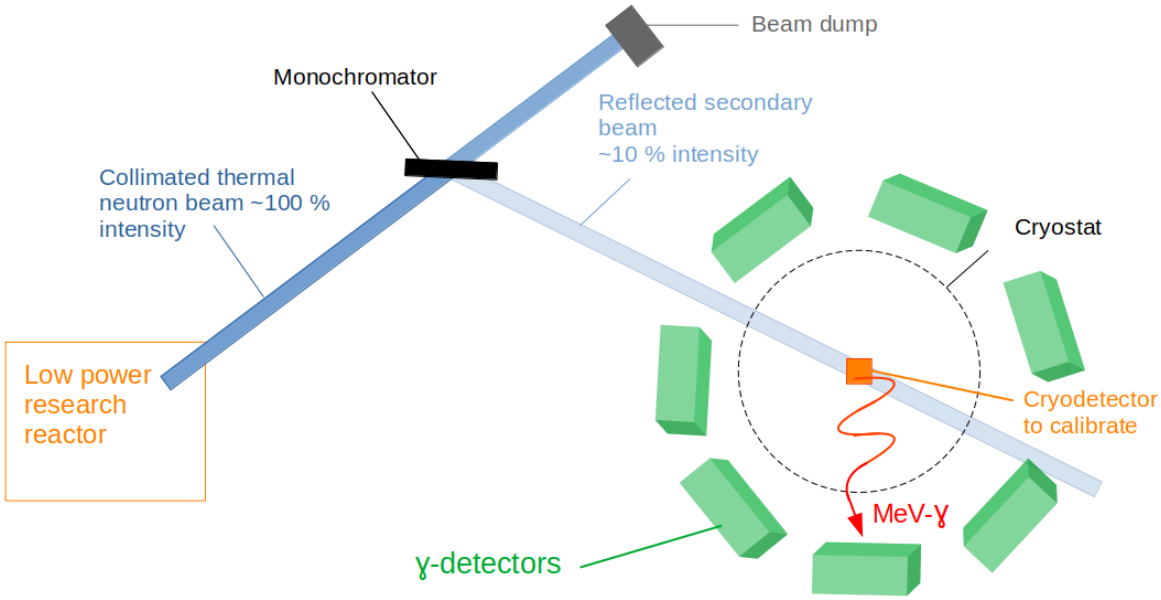

Figure 7.1. Illustration of the experimental concept for CRAB phase II. A low-power research reactor is used to produce a low-intensity, collimated, and purely thermal neutron beam, which is reflected toward the cryodetector. Surrounding γ-detectors positioned near the cryostat enable the detection of nuclear recoils in coincidence with their associated γ-ray.

7.2 Coincidence γ-NR

In this section, I present a simulation with a $CaWO_4$ target and γ-detectors clusters from the PARIS collaboration [207]. I first describe the simulation framework, with a focus on the implemented geometry in GEANT4. Then, I investigate the coincidence between the cryogenic detector and the PARIS detectors. This simulation work has two purposes: to define the energy window for coincidence events, and to validate the concept of γ-tagging as a method for extraction of calibration peaks from the multi-γ continuum.

7.2.1 Simulation framework

The geometry shown on the right side of Figure 7.2 has been implemented in GEANT4. It consists of a $CaWO_4$ target with dimensions of $5\times5\times5$ mm^3 inside a cryostat. The cryostat walls are modeled as three concentric cylindrical layers of aluminum with respective thicknesses of 5 mm, 1 mm, and 1 mm, along with an additional 1 mm layer of copper. This configuration is a simplified model and does not accurately represent the actual cryostat that will be used in Phase II. In particular, neutron attenuation through the cryostat is underestimated in this simplified configuration. The simulation presented here involves sending 10^8 thermal neutrons with an energy of 25 meV onto a $CaWO_4$ crystal, accounting for their passage through the cryostat. The simulated neutron beam is a collimated disk with a radius of 2.5 mm without any divergence. The equivalent time of the simulation is given by:

$$t_{eq} = \frac{N}{\phi.S} \tag{7.1}$$

with N the number of simulated neutron, S the surface of the simulated neutron beam, and ϕ the experimental neutron flux. Assuming a neutron flux of 450 n/cm^2/s, this corresponds to a data-taking period of 10 days. About 10% of the neutrons are captured by tungsten isotopes within the crystal. As for the γ-detectors, the initial plan was to use PARIS detectors (Photon Array for studies with Radioactive Ion and Stable beams [207]). A proposal has been sent to the PARIS collaboration to loan few clusters [208]. The default PARIS configuration studied here consists of 4 clusters, each composed of a 3×3 matrix of phoswich detectors read out by PMTs. Each phoswich detector includes a $LaBr_3$ crystal at the front ($2 \times 2 \times 2$ inches), optically coupled to a NaI(Tl) crystal at the back ($2 \times 2 \times 6$ inches), as illustrated on the left side of Figure 7.2. These detectors offer the advantages of high detection efficiency and fast time response ($\sim 1\ \mu s$). The distance between the cryodetector and the top face of the PARIS clovers is 12 cm. The beamline sits at a height of about 90 cm above the floor, which provides enough space to insert the PARIS clovers underneath the cryostat using a simple mechanical support resting on the ground. Since the PARIS detectors are located outside the cryostat, they operate independently from it and avoid all related issues typically encountered with detectors placed inside the cryostat (such as thermalization, electronic readout complications, etc.). Although these detectors were ultimately not used in CRAB phase II, the conclusions of the simulation remain valid and support the use of coincidence measurements with the emitted γ-rays. Their future use is not excluded and remains a possible option for later phases of the project. At the end of the simulation process described in Section 5.5, the energy deposited in both the target crystal and the PARIS detectors are obtained on an event-by-event basis. In PARIS clusters, the total deposited energy is obtained by summing the energy measured in all $LaBr_3$ and NaI crystals from the 4 clusters, as high-energy γ cause multiple energy depositions in different crystals. I then account for detector resolutions by convoluting the signal with a gaussian of standard deviation equal to the detector resolution. For PARIS detectors the resolution depends on the energy and can be expressed as [209]:

$$\frac{\sigma(E_\gamma)}{E_\gamma}(\%) = \frac{1}{2.35}\sqrt{a + \frac{b}{E_\gamma}} \tag{7.2}$$

with a= 3.8 and b=15.5 MeV for $LaBr_3$ and a=0 and b=79 MeV for NaI. At 6 MeV, the resolution is $\sigma(E_\gamma) = 65$ keV for LaBr3 and $\sigma(E_\gamma) = 90$ keV for NaI. Each energy deposit is convolved with its respective energy resolution before being summed to obtain the total energy spectrum in the PARIS detector. For the cryodetector, I assume a constant 10 eV resolution, because at this energy, the resolution is dominated by the constant baseline energy resolution.

7.2.2 Selection cuts on the γ energy in PARIS from $CaWO_4$

The coincidence analysis aims to identify nuclear recoil events in the crystal that are induced by high-energy γ emissions, simultaneously detected in the PARIS detector. The goal is to isolate, within the PARIS detector, signals associated with relevant γ transitions from tungsten isotopes following neutron capture. We examine here the impact of the γ energy selection cuts on the positions of coincident recoil peaks to assess systematic effects arising from such selection cuts. A simple approach would consist in applying an energy cut centered on the theoretical energy of the single-γ transition $E_\gamma \approx S_n$, with a window width of a few times the PARIS energy resolution. However, Compton scattering and pair production cause partial energy losses outside the PARIS detector. As a result, the choice of the lower edge of the energy window involves a trade-off. A wider energy window increases the number of selected nuclear recoils in the calibration peak, but it also introduces contamination from multi-γ cascades, which can distort the peak shape and bias the calibration.

Figure 7.3 shows the energy deposited in PARIS in the simulation for selected γ transitions of ^{183}W, ^{184}W and ^{187}W, with respective energies of 6.2 MeV, 7.4 MeV and 5.3 MeV. For the first two isotopes, it's a single-γ transition. In the case of ^{187}W, the transition proceeds via a two-γ cascade, with the primary 5.3 MeV γ being

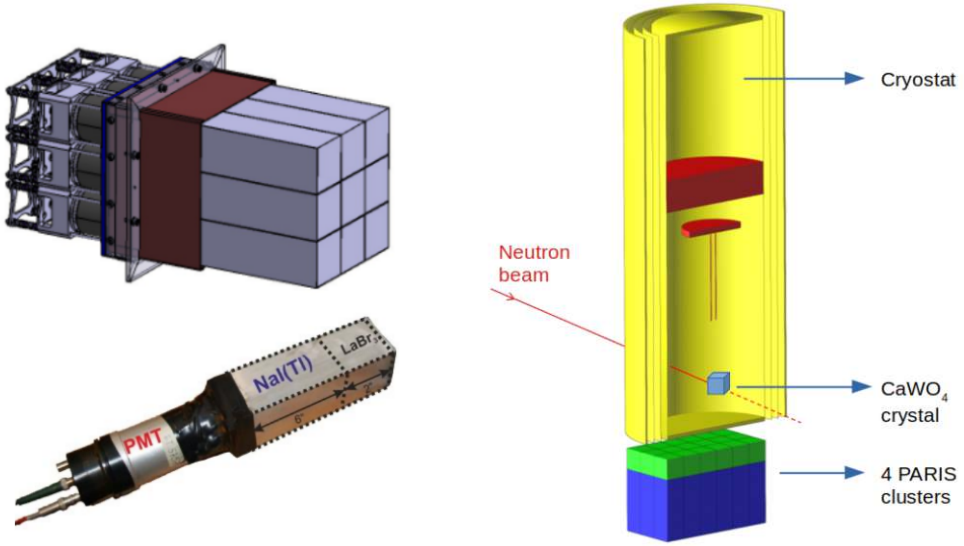

Figure 7.2. Left: A PARIS cluster consisting of a 3 × 3 matrix of phoswitch detectors, each composed of $LaBr_3$ and NaI crystals optically coupled to a photomultiplier tube (PMT). Figure from [210]. Right: Cut view of the experimental setup geometry implemented in the simulation. The neutron beam (red line) is aligned on the small $CaWO_4$ target crystal. The thin vessels of the cryostat (yellow) induce little disturbance on the beam. The $LaBr_3$ (green) and NaI (blue) crystals are visible underneath the cryostat.

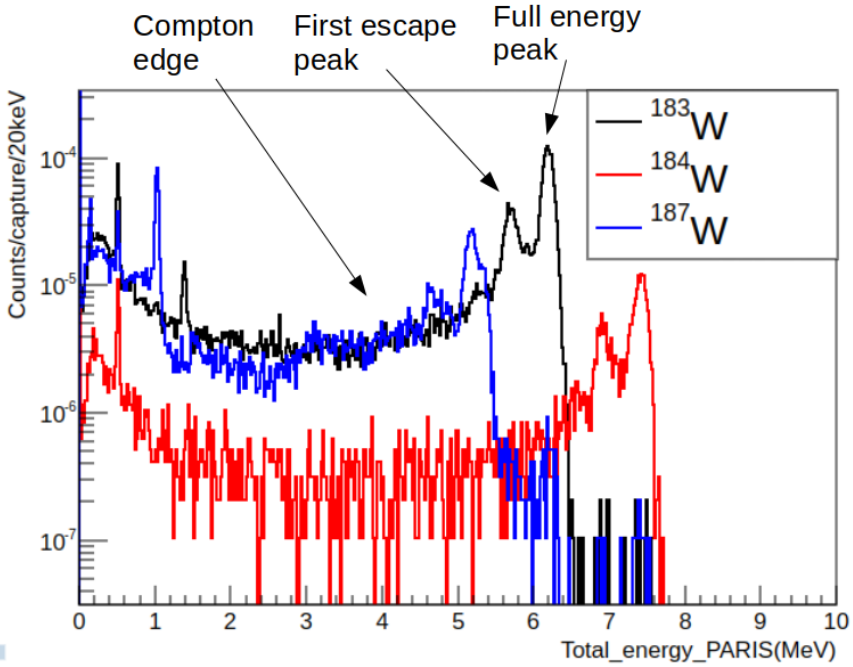

Figure 7.3. Total energy deposited in the PARIS clusters by γ-rays from the relevant nuclear transitions of the main tungsten isotopes: ^{183}W, ^{184}W, and ^{187}W. Each distribution shows a full-energy peak, the single escape peak, and a Compton edge. Although it is not possible to perfectly separate contributions from each isotope using γ-tagging alone, specific energy windows can still isolate the dominant contribution of each isotope to the recoil spectrum in the cryodetector (see Section 7.2.3).

the one tagged in the PARIS detector. As discussed in Chapter 5, this isotope provides a calibration peak around 80 eV, which is overwhelmed by the multi-γ continuum. The distributions in Figure 7.3 exhibit the full-energy peak, a single escape peak (511 keV below), and a Compton continuum. A clear separation is observed between the spectra of each isotope, with minimal overlap. This feature opens the possibility of selecting γ energies to isolate the contribution of individual transitions to the recoil energy spectrum. In particular, it will be possible to define specific coincidence energy window to isolate the calibration peak of ^{187}W from the recoil continuum induced by multi-γ transitions.

The upper threshold is fixed at $E_\gamma + 2\sigma$. Figure 7.4 quantifies how the estimated recoil peak position in the cryodetector varies with the lower threshold of the γ energy cut in PARIS. The resulting coincident recoil spectra are fitted with a local Gaussian function, without assumptions on the true underlying distribution. As the lower energy cut is relaxed, more multi-γ events are included, introducing a low-energy tail in the cryodetector signal. This causes a systematic shift of the fitted peak to lower energies as shown in the right panels of Figure 7.4. A more sophisticated analysis could, in principle, model and correct for this distortion.

A practical compromise consists in including the first escape peak in the selection. As such, the coincidence energy window for ^{187}W is set to [4.7–5.5] MeV. Using the same methodology, the coincidence energy windows [5.5–6.4] MeV and [6.3–7.6] MeV are defined for the ^{183}W and ^{184}W isotopes, respectively. With these selection cuts, the systematic uncertainty on the recoil peak position in the cryodetector is kept below the sub-percent level.

7.2.3 Coincidence energy spectra for CaWO4

The resulting coincidence recoil spectra expected in the target crystal are shown in the insets of Figure 7.5. Thanks to γ-tagging, the recoil peaks associated with the single-γ emissions from the ^{183}W and ^{184}W isotopes, as well as with the primary γ from the de-excitation of ^{187}W, can be clearly resolved with a favorable signal-to-background ratio. Table 7.1 summarizes the γ selection cuts along with the recoil peak positions extracted from Gaussian fits. Even with a relatively simple fitting procedure based on a local Gaussian approximation, the results show excellent statistical precision on the peak positions and only minor systematic bias. In particular, the extraction of a third peak at 81.4 eV—only visible in coincidence and not in single mode with a 10 eV resolution—demonstrates the potential of this technique to study the linearity of the cryodetector response and its sensitivity to defect formation in the crystal (see Section 5.6). At such low energies, the number of defects created is typically 0, 1, or 2 on average. As a result, the spacing between the peaks may carry valuable information: if the energy crosses a threshold where a new defect is formed between two peak positions, a deviation from linearity is expected. Although the analysis assumes a 10-day runtime, the high event statistics indicate a comfortable margin, suggesting that good precision could be achieved with shorter data-taking periods.

Isotope	Primary E_γ (MeV)	γ selection (MeV)	Recoil (eV)	Fit (eV)
^{183}W	6.2	[5.5-6.4]	112.5	112.1± 0.2
^{184}W	7.4	[6.3-7.6]	160.3	159.4± 0.4
^{187}W	5.3	[4.7-5.5]	81.4	80.7± 0.4

Table 7.1. 1^{st} column: tungsten isotope after neutron capture. 2^{nd} column: primary γ energy. 3^{rd} column: selected γ-energy window. 4^{th} column: theoretical recoil peak positions. 5^{th} column: fitted recoil peak positions with sub-percent statistical uncertainties, showing good agreement with the theoretical values.

Figure 7.4. Left: Energy deposition spectra in the PARIS detector in coincidence with nuclear recoils of 81.4, 112.5 and 160.3 eV in the cryodetector. These spectra represent the PARIS response to the de-excitation γ-rays from ^{187}W (5.3 MeV), ^{183}W (6.2 MeV), and ^{184}W (7.4 MeV). Right: Variation of the relative error on the fitted recoil peak position E_{fit} in the cryodetector with respect to the theoretical energy E_{th}, as a function of the lower edge of the energy window for the coincident γ detected in PARIS.

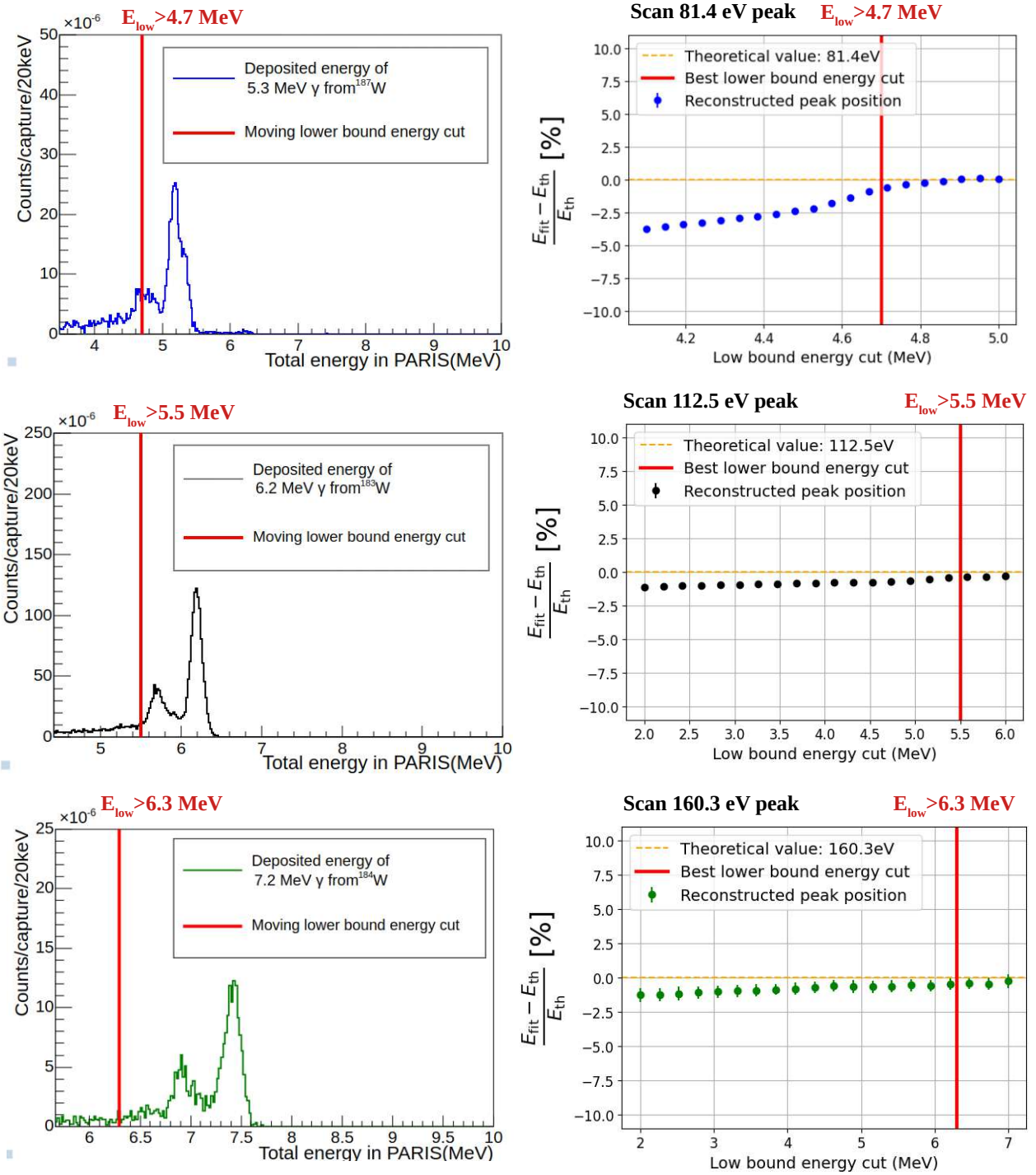

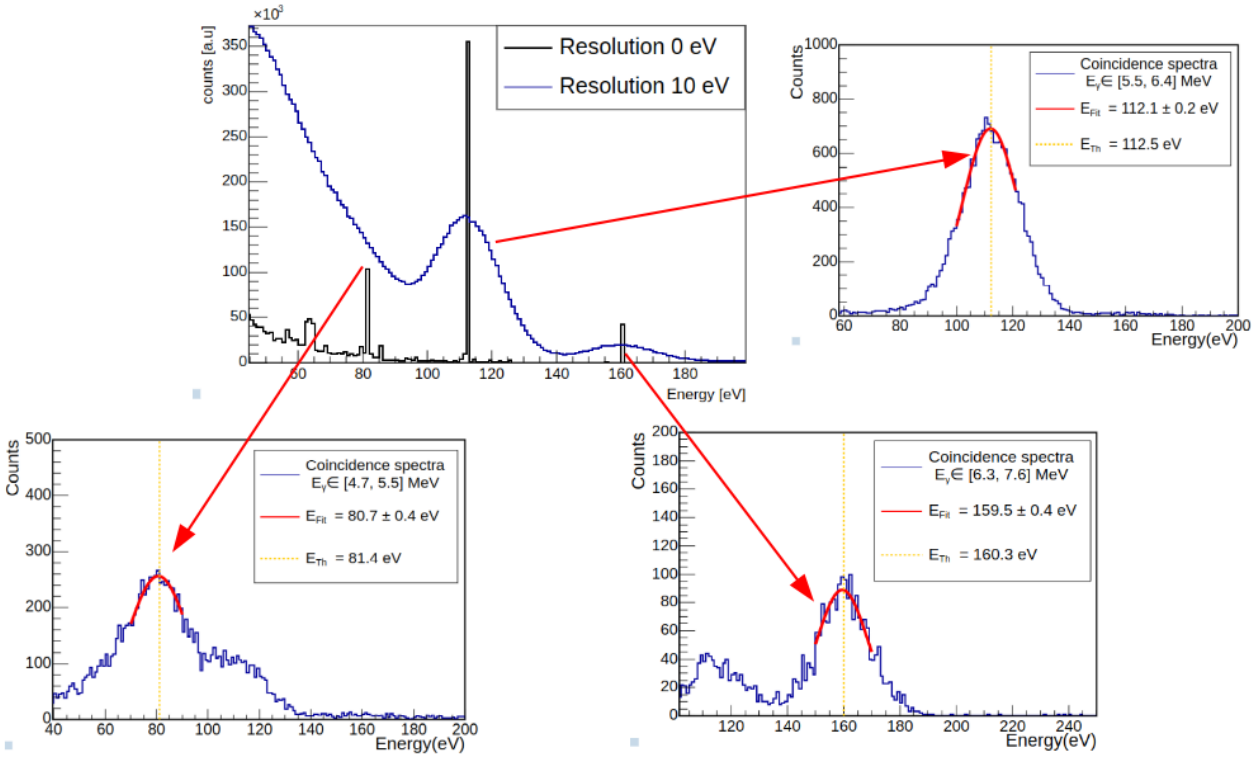

Figure 7.5. The main panel (top left) shows the total nuclear recoil energy spectrum, with and without a 10 eV detector resolution applied. For visualization purposes, an arbitrary scaling factor is applied to the unresolved spectrum. The inset plots display the recoil spectra expected in the cryodetector when applying the three γ energy selection windows defined in Table 7.1. These selections allow the clear isolation of the three expected recoil peaks at 81.4, 112.5, and 160.3 eV, each with an enhanced signal-to-noise ratio. The red curves correspond to local Gaussian fits to the peaks, demonstrating high-precision determination of their positions in good agreement with theoretical values. As shown in Figure 7.3, the ^{183}W isotope contributes to the γ spectrum across all selected energy windows, which explains the presence of the 112.5 eV peak in all three recoil spectra.

7.3 Application to a germanium target

The coincidence method makes the measurement of calibration peaks a lot more robust with respect to the energy resolution of the cryo-detector, relaxing the main experimental constraint of the detector. In practice it would open unique perspectives of accurate calibrations of other crystals widely used in the community. A particularly relevant case is that of the germanium. Simulations of the neutron capture induced nuclear recoils in this material, conducted in Section 5.5, show that up to 8 intense recoil peaks are present in the recoil energy spectrum plotted on left panel of the Figure 5.11. The list of isotopes and associated recoil energies was provided in Table 5.2.

To illustrate the power of coincidence detection applied to the CRAB method I consider the practical case of a germanium crystal of dimension $10 \times 10 \times 10$ mm^3 from TESSERACT collaboration [211]. This cubic crystal is larger than a NUCLEUS crystal, partly compensating for the smaller mean n-capture cross section. However the price to pay for this larger size is a larger energy resolution here assumed to be 20 eV. While still being an amazing resolution in itself, it is already insufficient to distinguish individual recoil peaks (see right panel of Figure 5.11). As in the $CaWO_4$ case, a coincidence analysis between the germanium target and the PARIS detector enables the recovery of distinct calibration peaks in the 300–600 eV energy range. This is particularly valuable for future CEνNS and dark matter searches, where precise calibration in this region is crucial. However, some γ-lines are very close in energy, and even with coincidence tagging, they cannot be fully resolved. This is partly due to the energy resolution of the germanium detector, but more importantly, because the primary γ themselves are too close in energy to be discriminated by the PARIS detectors. This limitation arises from the energy resolution of the PARIS clusters. As a result, nearby lines tend to merge. To mitigate this, we define averaged recoil energies for clusters of closely spaced γ-transitions. Specifically, the quadruplet at 280.6, 296.0, 303.2, and 307.9 eV is combined into a single weighted average recoil at 292.9 eV, as is the doublet at 344.3 and 363.9 eV combined into a weighted average recoil at 352.9 eV, with weights determined from their relative intensities in the simulated spectrum. Table 7.2 reports the theoretical and fitted recoil energies for both individual lines and these grouped transitions, after applying the appropriate γ-energy selection in PARIS. Figure 7.6 shows that coincidence analysis restores four well-defined calibration peaks, each measurable with potential percent-level precision. This capability offers a promising route to study the quenching factor at sub-keV energies (see Section 8.6.2).

Isotope Isotope	**Primary E_γ (MeV)**	**Selection cut (MeV)**	**Recoils (eV)**	**Mean recoil (eV)**	**Fit (eV)**
^{75}Ge	6.252		280.6		
^{70}Ge	6.117		296.0		
^{75}Ge	6.506		303.2		
^{75}Ge	6.276	[5.5,6.5]	307.9	292.9	294.7 ± 0.6
^{71}Ge	6.707		344.3		
^{71}Ge	6.916	[6.3,7.0]	363.9	352.9	353.1 ±0.6
^{71}Ge	7.416	[7.1,7.6]	416.2	416.2	416.8 ±1.3
^{74}Ge	8.732	[8.6,8.9]	561.8	561.8	561.0 ±1.1

Table 7.2. Most intense recoil peaks induced by n-capture in a germanium crystal. 1^{st} column: germanium isotope after neutron capture. 2^{nd} column: Energy of primary γ to be selected in the PARIS detector. This primary γ can be either from a single-γ transition or a 2-γ cascade. 3^{rd} column: associated selection cuts in γ detector. 4^{th} column: expected recoil peaks. 5^{th} column: for the four first lines and then the two following lines, the recoil energies are considered too close to be resolved by the cryodetector. In that case a mean recoil value is computed from the weighted sum of the individual lines. 6^{th} column: fitted positions using a local gaussian function.

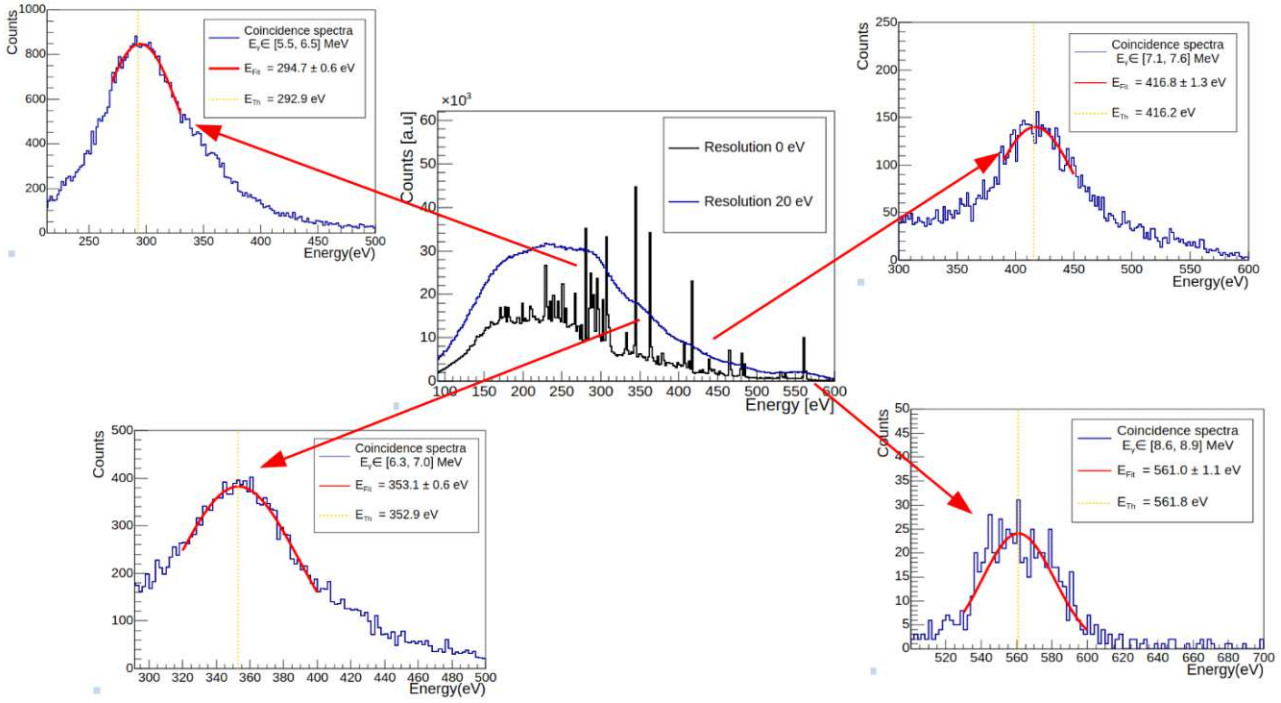

Figure 7.6. The main panel shows the total nuclear recoil energy spectrum in a TESSERACT germanium crystal, with and without the detector resolution applied. For visualization purposes, an arbitrary scaling factor is applied to the unresolved spectrum. The inset plots display the recoil spectra expected in the cryodetector when applying the four γ energy selection windows defined in Table 7.2. Using the same simple approach as for $CaWO_4$, local gaussian fits (red curves) provide the four peak positions with percent level accuracy and in good agreement with the theoretical values.

7.4 Phase II at the Atominstitut

For the phase II of the CRAB experiment, it was decided to install the setup at a new experimental site near the TRIGA MARK-II research reactor at the Atominstitut in Vienna (Austria), which meets the requirements outlined in Section 7.1. The experimental setup for this second phase includes several components (see Figure 7.7). I present them in more detail in the following. A similar description of the setup can be found in [193].

7.4.1 TRIGA MARK-II reactor

TRIGA (Training, Research, Isotopes, General Atomics) reactors constitute a class of nuclear reactors developed in the 1950s for research purposes and student training. Designed to be installed within university facilities, these reactors are relatively simple and inherently safe. The fuel is enriched to 20% in ^{235}U, and the use of a zirconium hydride (UZrH) moderator has proven to be an effective safety feature, as its moderating efficiency decreases at high temperatures [206, 212]. The TRIGA Mark-II nuclear research reactor at the Atominstitut (ATI) operates at a nominal thermal power of 250 kW for seven hours per day, approximately 220 days per year. A schematic of the reactor is shown in Figure 7.8. The reactor core is surrounded by graphite, which serves as a neutron reflector, and is immersed in a water-cooled reactor tank. The water acts both as a primary coolant and as an additional neutron moderator, contributing to neutron thermalization. As a result, the reactor produces a thermal neutron flux of $\phi \approx 10^{13}\text{cm}^{-2} \cdot \text{s}^{-1}$. This flux is distributed to multiple experimental stations via four beam tubes. Beam tube D is oriented tangentially with respect to the reactor core, rather than directly facing it, which significantly reduces the background of γ-rays and fast neutrons. This beamline is used for the CRAB experimental setup and provides a thermal neutron beam, whose energy spectrum follows a Maxwell-Boltzmann distribution with an effective temperature of approximately 300 K. The thermal neutron beam emerging from the reactor core is thus guided through beam tube D into the neutron beam line, which includes components for energy selection, collimation, flux attenuation and guide the neutron beam towards the CRAB cryostat.

7.4.2 Neutron beam line

The transport of neutrons from the reactor beam tube to the cryodetector is achieved using two Highly Oriented Pyrolytic Graphite (HOPG) crystals that reflect the neutron beam (see Figure 7.7). The first crystal is mounted in a fixed position inside the concrete shielding of the reactor. The neutron beam it reflects is referred to as the primary beam. Positioned within this primary beam is the second HOPG crystal, which is mounted on an M-037.DG rotary table [213]. This rotary table is itself mounted on an H-820 six-axis hexapod [214], which is installed on a DL-SLW linear translation stage [215]. This setup, illustrated in inset (ii) of Figure 7.7, allows fine-tuned adjustment of the neutron beam direction, particularly by translating the hexapod along the linear stage, so that the reflected beam is precisely directed toward the cryodetector, which has dimensions on the order of a few millimeters. This reflected beam is referred to as the secondary beam.

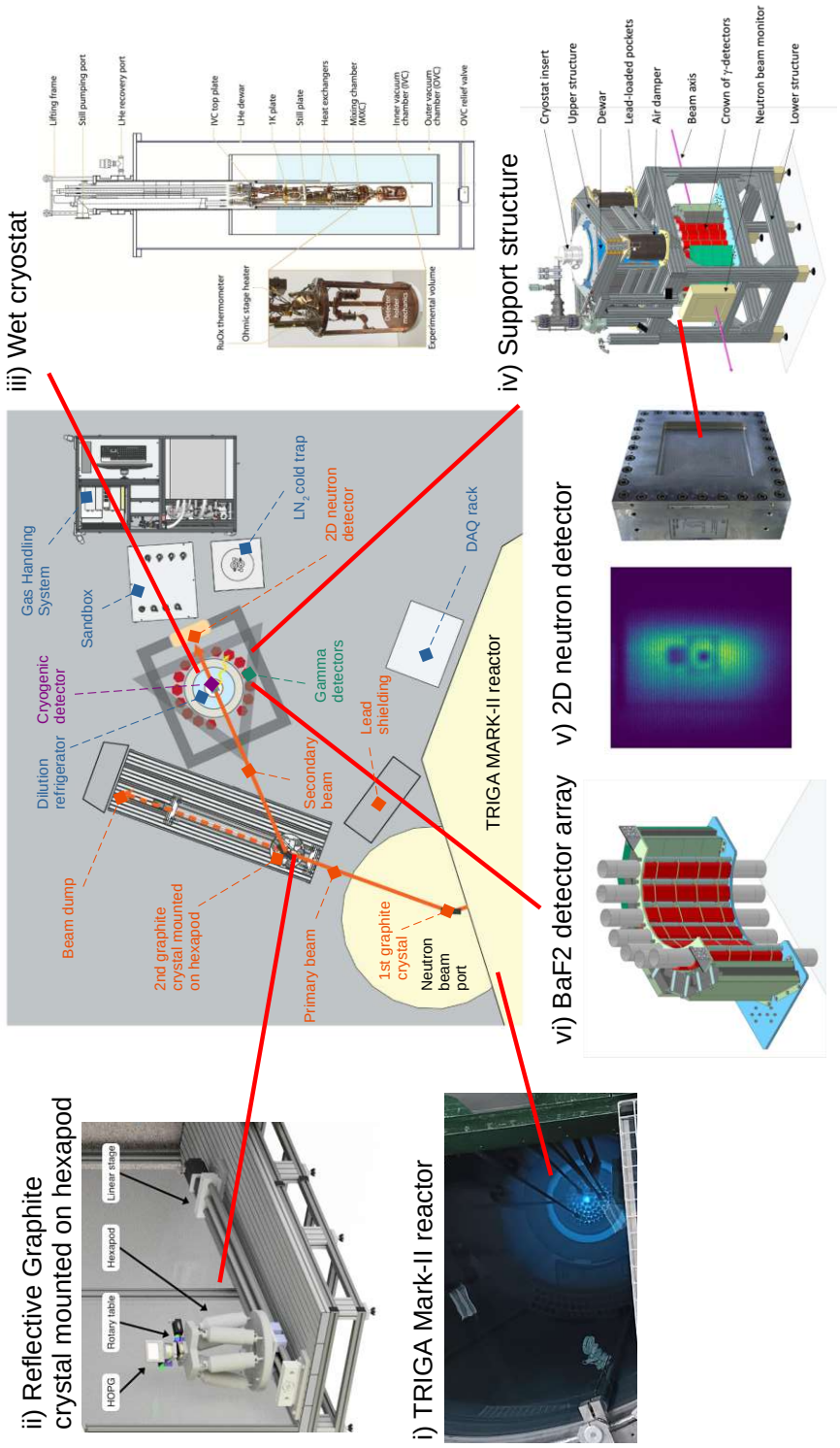

Figure 7.7. Schematic overview of the CRAB phase II experimental setup, illustrating the main components: (i) the TRIGA MARK-II reactor, (ii) the neutron beamline (Credits: S.Dorer), (iii) the wet cryostat, (iv) the cryostat support structure, (v) the 2D neutron detector and (vi) the BaF_2 γ-detectors array. Further details about these components are provided in the text. Figures adapted from [193].

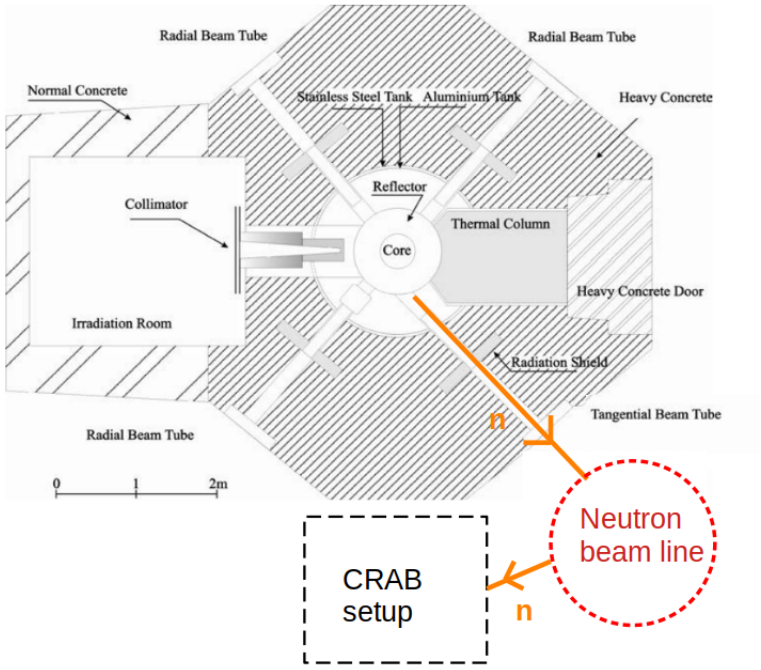

Figure 7.8. Sketch of the TRIGA MARK-II reactor showing the reactor core and the neutron beam tubes. The CRAB setup is shined by reflected neutrons from the tangential beam tube. Figure from [206].

Let's now describe in more detail how reflection by the HOPG crystal works. Both neutron reflection and energy selection are governed by Bragg diffraction on such crystal. The first crystal of dimensions $5 \times 5 \times 0.4$ cm^3 is set at a fixed angle of $\theta = 23.17°$ with respect to the incident beam, a constraint imposed by the geometry of the reactor layout. Consequently, the beam is reflected at an angle of 2θ relative to its incoming direction. According to Bragg's law, neutron reflection occurs only when the incident neutron energy satisfies the diffraction condition [216]:

$$\lambda_n = \frac{2dsin(\theta)}{n} \tag{7.3}$$

where λ_n is the neutron wavelength diffracting at a fixed incident angle θ, n is the diffraction order and $d = 3.355$ Å is the lattice spacing of the HOPG crystal. This Bragg condition inherently leads to a reduction of the neutron flux due to its selective nature.

The primary beam includes neutron from first order diffraction but also second and third order. For a Bragg angle of $\theta = 23.17°$, the selected wavelengths for orders $n = 1$, 2, and 3 are:

$$\lambda_1 = \frac{2.64}{1} = 2.64 \text{ Å}, \quad \lambda_2 = \frac{2.64}{2} = 1.32 \text{ Å}, \quad \lambda_3 = \frac{2.64}{3} = 0.88 \text{ Å}$$

These wavelengths correspond to neutron energies of approximately 12 meV, 47 meV, and 106 meV, respectively. The relative contributions of these components are currently under investigation using time-of-flight measurements. Although the CRAB method does not require a strictly monoenergetic neutron beam, knowledge of the energy spectrum remains essential for simulation signal prediction, as the neutron capture cross section is highly energy-

dependent. Quantitative neutron flux measurements are performed using a VacuTec proportional ^{3}He counter tube [217]. In the primary beam, a neutron flux of $\phi \approx (4296 \pm 430)\ \mathrm{cm}^{-2} \cdot \mathrm{s}^{-1}$ has been measured. A second HOPG crystal is placed in the primary beam to reflect neutrons toward the cryostat. This second HOPG must be aligned at the same Bragg angle θ as the first HOPG to reflect neutrons of the same wavelengths λ_1, λ_2 and λ_3. Since this condition can never be perfectly fulfilled in practice, the alignment leads to a reduction of the neutron flux in the secondary beam by approximately a factor of 10. As a result, the neutron flux measured at the cryostat location is $\phi \approx (469 \pm 47)\ \mathrm{cm}^{-2} \cdot \mathrm{s}^{-1}$.

A DENEX 200-TN two-dimensional neutron detector [218] is used to monitor the beam position and to align it with the cryodetector (see Section 8.2). The detector is a large-area $20 \times 20\ \mathrm{cm}^2$ multi-wire proportional chamber filled with ^{3}He. It allows for millimeter-scale reconstruction of neutron capture vertices, enabling precise imaging of the neutron beam. These beam images allow us to determine the size of the beam spot. In the primary beam, the full width at half maximum (FWHM) of the horizontal and vertical projections of the neutron beam is approximately $6.3 \times 12.0\ \mathrm{cm}^2$ (width $\times$ height). In the secondary beam, at the cryostat location, the beam spot is reduced to $3.0 \times 6.4\ \mathrm{cm}^2$. A collimator made of B_4C and lead is placed at the entrance of the cryostat, upstream the detector with a circular aperture of 2 cm radius, to further reduce the beam to the minimum dimensions. This minimizes neutron capture on cryostat materials and subsequent background and improves the signal-to-noise ratio in the cryodetector. More detail about the neutron beam line can be found in [219].

7.4.3 Cryogenic infrastructure

The cryostat used for phase II of the CRAB experiment is a wet ^{3}He–^{4}He dilution refrigerator (Kelvinox100) from Oxford Instruments plc, previously introduced in Section 6.2.1.1. A wet cryostat relies on the use of cryogenic liquids, making its operation more complex; however, this technology has proven to provide highly stable conditions due to the absence of internal vibrations. As a result, the performance of the cryodetector depends on its isolation from external mechanical disturbances. To achieve this, the cryostat insert and its dewar are suspended from a triangular frame constructed from aluminum profiles provided by Alvaris [220]. This upper structure rests on a lower square-base frame via Newport S-2000 air dampers [221], which are positioned at each corner of the triangle (see inset (iv) of Figure 7.7). For optimal damping performance, the suspended mass—originally 250 kg—is increased to approximately 500 kg by attaching lead-filled compartments beneath each side of the upper triangle. Midway up the lower structure, a support plate holds the γ-detectors and the 2D neutron detector positioned downstream of the cryostat. Additionally, the cryostat is electrically isolated from the supporting metal structure by a plastic insulating ring mounted at the top flange of the dewar, which prevents ground loops between different components of the setup. Cryostat operation involves connecting pumping lines and hoses to a Gas Handling System (GHS). To minimize vibration transmission from the pumps, the tubing passes through a sandbox, decoupling mechanical noise from the cryostat.

7.4.4 BaF_2 detectors array

The detection of high-energy γ in coincidence with nuclear recoils induced in the cryodetector significantly improves the signal-to-background ratio, as demonstrated in Sections 7.2.3 and 7.3. Although the PARIS clusters—widely used by the nuclear physics community—were initially envisioned for the second phase, their short-term unavailability led us to revise our plans. We ultimately turned to an alternative solution, using a total of 40 BaF_2 crystals from the "Château de Cristal" experiment, originally developed for nuclear spectroscopy in the 1980s [222, 223], and kindly made available for the CRAB project.

7.4.4.1 Detector description

BaF_2 is an inorganic scintillator known for its fast time response (on the nanosecond scale), good energy resolution, and high detection efficiency for MeV γ-rays, owing to its relatively high density of 4.88 g/cm^3. From the initial set of 40 BaF_2 detectors, 28 were selected to form two half-crowns arranged along the outer wall of the dewar, as illustrated in inset (vi) of Figure 7.7. GEANT simulations performed with the TOUCANS code [194] demonstrated that this arrangement offers the best compromise between solid-angle coverage and intrinsic γ-detection efficiency. Additionally, the compact configuration around the dewar allows the implementation of lead shielding to protect the γ-detectors from the ambient high-energy γ-ray background generated in the experimental hall during reactor operation (see Section 8.1.1). Each BaF_2 crystal has a hexagonal base with 50 mm sides and a height of 140 mm, and is optically coupled to a photomultiplier tube (PMT) with a quartz window transparent to the UV scintillation light (see left panel of Figure 7.9). The PMT device must be supplied by a -2 kV voltage. Due to its chemical affinity with Barium, BaF_2 crystals are contaminated with Radium [224]. The decay chain of ^{226}Ra involves α-decays with characteristic energies and half-lives obtained from [225]:

$$^{226}_{88}\mathrm{Ra} \xrightarrow[1600\ \mathrm{yrs},\ 4.78\ \mathrm{MeV}]{\alpha} {}^{222}_{86}\mathrm{Rn} \xrightarrow[3.8\ \mathrm{d},\ 5.59\ \mathrm{MeV}]{\alpha} {}^{218}_{84}\mathrm{Po} \xrightarrow[3.1\ \mathrm{min},\ 6.11\ \mathrm{MeV}]{\alpha} {}^{214}_{82}\mathrm{Pb} \xrightarrow[27.1\ \mathrm{min}]{\beta^-} {}^{214}_{83}\mathrm{Bi}$$

$$^{214}_{83}\mathrm{Bi} \xrightarrow[19.7\ \mathrm{min}]{\beta^-} {}^{214}_{84}\mathrm{Po} \xrightarrow[163.6\ \mu\mathrm{s},\ 7.83\ \mathrm{MeV}]{\alpha} {}^{210}_{82}\mathrm{Pb} \xrightarrow[22.2\ \mathrm{yrs}]{\beta^-} {}^{210}_{83}\mathrm{Bi} \xrightarrow[5.013\ \mathrm{d}]{\beta^-} {}^{210}_{84}\mathrm{Po} \xrightarrow[138.4\ \mathrm{d},\ 5.407\ \mathrm{MeV}]{\alpha} {}^{206}_{82}\mathrm{Pb}$$

Therefore, the associated α-decay results in four main energy lines at 4.78, 5.59, 6.11, and 7.83 MeV. They induce a significant total rate of ≈195 Hz above 1 MeV on each counter (see right panel of Figure 7.9). It is worth noting that the fifth alpha transition at 5.407 MeV has a negligible contribution to the energy spectrum due to the long half-life of $^{210}_{82}$Pb (22.2 years).

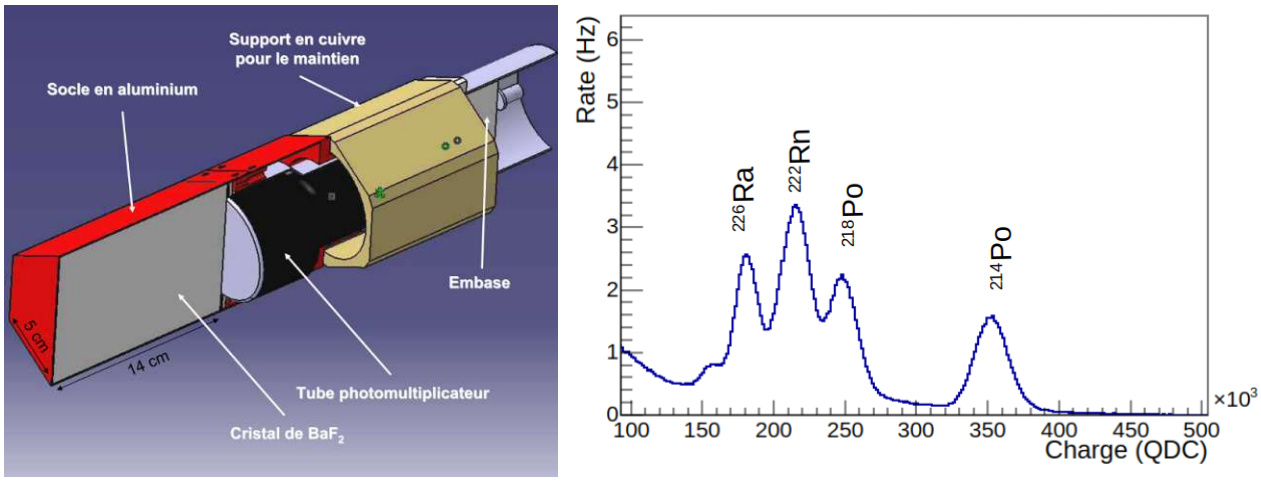

Figure 7.9. Left: 3D sketch of a BaF_2 module, showing the BaF_2 crystal optically coupled to a photomultiplier tube. Figure from [223]. Right: Charge spectrum measured in a BaF_2 detector, showing four distinct α peaks arising from internal radioactive contamination.

7.4.4.2 Scintillation mechanism

The BaF_2 crystal is a scintillation detector. When a γ is absorbed by the scintillator, it transfers its energy to a valence-band electron, which is then excited to the conduction band. This process creates an electron-hole pair, also known as an exciton. Two mechanisms contribute to the scintillation process. First, upon recombination, the electron de-excites and emits a photon with a wavelength of approximately 200 nm. The de-excitation time is around 0.6 ns, which corresponds to the so-called fast scintillation component [226]. Alternatively, the exciton can be trapped in the crystal lattice, forming a Self-Trapped Exciton (STE) [227]. The radiative decay of these STEs results in the emission of photons with a wavelength around 310 nm, and a much longer decay time of approximately 630 ns [226]. As a result, the scintillation signal in BaF_2 consists of both fast and slow components. The slow component typically accounts for about 80–90% of the total emitted light. The relative contributions of these two components depend on the type of ionizing particle, which enables pulse shape discrimination (see Section 7.4.4.4).

7.4.4.3 BaF_2 data acquisition system

The BaF_2 signals are read out using FASTER electronic modules developed by LPC Caen [228]. A μTCA crate houses a motherboard, which defines the system clock, and seven CARAS daughter boards, each providing four readout channels. These CARAS boards include a charge integration QDC module implemented on an FPGA. The FASTER system is a fast digitizer capable of sampling signals at 500 MHz using a 12-bit flash ADC over a ± 1.15 V range. With seven CARAS boards, up to 28 BaF_2 detectors can be read out simultaneously. A trigger is defined by a signal exceeding a channel-specific amplitude threshold for at least 28 ns. Only channels that fulfill this condition are read out. If the trigger times of two channels occur within a time window of 100 ns, they are merged into a single event. For charge integration, two time windows can be defined to measure both the fast component charge (Q_{fast}) and the total charge (Q_{tot}) of the signal. In accordance with the fast and slow scintillation decay times discussed in the previous section, Q_{tot} is integrated over the interval $[-30$ ns; 1500 ns$]$ around the trigger time, while Q_{fast} is computed over a shorter interval $[-30$ ns; 8 ns$]$.

7.4.4.4 Pulse shape discrimination

The dual-component nature of the BaF_2 scintillation pulse, discussed in Section 7.4.4.2, enables the use of pulse shape discrimination (PSD) to distinguish between events originating from γ and those from internal α-radioactivity within the crystal. It has been shown in [229, 230] that α particles don't have a fast scintillation component. Therefore, discrimination can be performed by looking at the charge in the fast component Q_{fast}. During the calibration of these detectors, a ^{60}Co source was used to produce γ-rays with energies of 1.17 and 1.33 MeV. As shown in the left panel of Figure 7.10, γ events are clearly separated from α events by plotting the relative contribution of the fast component, $Q_{\text{fast}}/Q_{\text{tot}}$, versus the total charge Q_{tot}. A simple cut on $Q_{\text{fast}}/Q_{\text{tot}} > 0.016$ is sufficient to select γ events while rejecting α contamination. The right panel illustrates the effect of this cut, showing how it isolates both the γ and α-particle contributions in the total energy spectrum. This discrimination capability is particularly useful for accurately determining γ peak positions for energy calibration (see Section 8.4.1).

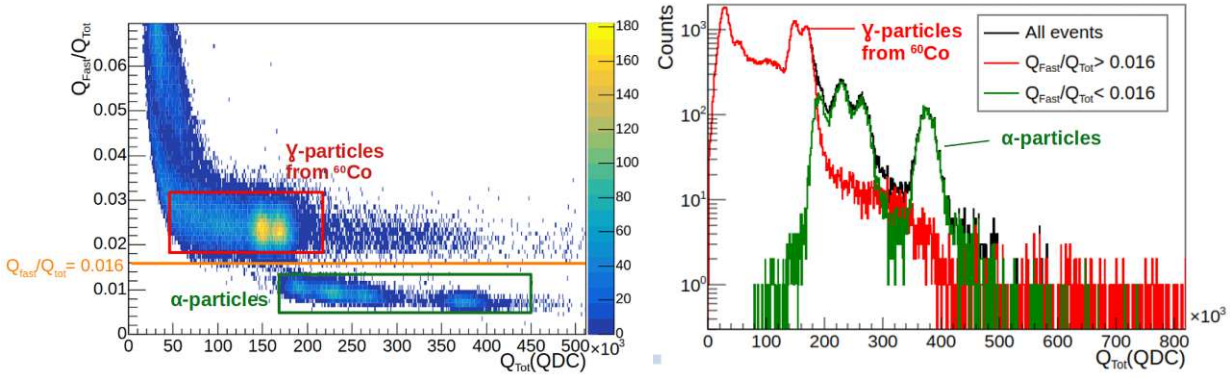

Figure 7.10. Left: 2D histogram showing the relative fast component ($Q_{\text{fast}}/Q_{\text{tot}}$) as a function of the total charge (Q_{tot}). A clear separation is observed between α particles from internal background and γ-rays from the ^{60}Co source. A pulse shape cut on $Q_{\text{fast}}/Q_{\text{tot}}$ enables efficient discrimination between α and γ events. Right: Total deposited charge spectrum, highlighting the contributions from α and γ events after applying the pulse shape discrimination cut.

7.5 Conclusions

This chapter has highlighted the strengths of the phase II setup, in particular the advantages of a pure, thermal, and collimated neutron beam. Simulations demonstrating the benefit of γ-tagging motivated the integration of γ-detectors in phase II to detect nuclear recoils in coincidence with the emitted γ. The various components of the phase II setup, implemented at the Atominstitut, have been presented. The next chapter will focus on the on-site preparation and installation of this setup, and will present the first promising commissioning data.

8

Preparation, installation and commissioning of the phase II

This chapter is dedicated to the preparation, on-site activities, and initial commissioning results related to the second phase of the CRAB project. During my time at the facility, I actively contributed to the preparation of phase II (see Section 8.1), especially characterizing the reactor site backgrounds. I also took part in the installation of the experimental setup during summer 2024, as detailed in Section 8.2. The resulting experimental setup was simulated to serve as a benchmark for comparison with the data (see Section 8.3). The following two sections describe the commissioning of the BaF_2 detectors and the cryodetectors. These initial data are promising and validate our understanding of the cryodetector's signal components. Notably, the first coincidences between a cryodetector and the BaF_2 detectors have been successfully observed. The final section provides an outlook and discusses future directions for the continued development of the CRAB experiment. Apart from the preparation of the cryogenic detector and the simulations, I was actively involved in all other parts of the work presented in this chapter. It forms part of a submitted article describing this second phase [193].

8.1 Preparation of the phase II

Phase II required extensive preparation. On the experimental site itself, I conducted a background characterization. Preparatory work also involved operating the cryostat before its relocation to the reactor site, as well as the commissioning of two $CaWO_4$ cryogenic detectors and an Al_2O_3 cube, the latter of which exhibited a clear CRAB peak (see Section 6.2). We further investigated the internal structure of the cryostat dewar to ensure accurate modeling in the GEANT4 simulation framework.

8.1.1 On site background characterisation

On-site background characterisation is a critical step for enabling coincidence measurements with the γ-detectors. A high background rate in the γ-detectors, dominated by high-energy γ-rays from reactor neutron captures on surrounding materials, populate the CRAB region of interest (ROI). This would significantly increase the probability of accidental coincidences with the cryodetectors—potentially compromising the benefits of γ-tagging. This accidental coincidence probability P_{acc} depends on the background rate R_{Bkg} and the width of the time coincidence window Δt, following the relation:

$$P_{acc} \approx R_{Bkg} \times \Delta t \tag{8.1}$$

While Δt is driven by the time resolution of the cryodetector, the background rate can be measured and mitigated by identifying and addressing its sources. To this end, a first BaF_2 γ-detector and a FASTER acquisition module were preliminarily shipped to Vienna to conduct an initial background characterisation. In the ROI for tagging high-energy γ from CRAB events (4.7–7.6 MeV), it is crucial to maintain the background rate per detector below 3 Hz to keep accidental coincidences at an acceptable level. An initial measurement was performed close to the future cryostat location using a table-mounted setup under various experimental conditions:

- Reactor OFF (upper left panel of Figure 8.1)
- Reactor ON
- Reactor ON with a boron carbide (B_4C) carpet surrounding the detector to shield against neutrons
- Reactor ON with both B_4C and 10 cm of lead shielding to suppress γ-rays (upper right panel of Figure 8.1)

The resulting spectra are shown in the lower panel of Figure 8.1. The ROI is highlighted by the red shaded area. The corresponding counting rates in this region are summarized in Table 8.1. The measurements reveal that, when the reactor is ON, the background rate increases drastically—from 0.5 Hz to 31.2 Hz—leading to an unacceptably high accidental coincidence rate. This reactor-induced background originates largely from the neutron beam and subsequent captures in surrounding materials. The B_4C shielding slightly reduces the rate to 26.7 Hz, indicating the presence of a neutron contribution. However, the most significant reduction is achieved by adding 10 cm of lead, bringing the rate down to 1.6 Hz. This confirms that the majority of the background is due to γ-rays. Spectral features observed in the 7–8 MeV range suggest the presence of high-energy γ-rays produced by thermal neutron capture on iron. This hypothesis is supported by complementary measurements using a portable high-resolution germanium detector. Additional measurements at various positions helped identify the likely sources of this iron and provided further insight into the spatial distribution of the background.

The left panel of Figure 8.2 shows a picture of the three different positions used to measure the background rate at increasing distances from position 1, which is located near the monochromator shielding and close to the neutron beam exit. The corresponding background rates are plotted in the right panel. The data exhibit a clear trend consistent with a $\frac{1}{r}$ dependence, where r is the distance from position 1, suggesting that the monochromator shielding acts as a dominant radiation source illuminating the CRAB experimental area.

A complementary measurement involved scanning the background rate along the monochromator shielding at different heights (see left panel of Figure 8.3). The highest background rate was recorded at the height of the neutron beam. Further investigation revealed that the reactor tank and some beam tubes are made of stainless steel and iron, located in regions with high neutron flux. A lead wall was installed, consisting of two rows of five bricks each, with a thickness of 5 cm (see right panel of Figure 8.3). This shielding significantly reduced the background rate at position 2, which corresponds to the future cryostat location, and strongly motivated the construction of a permanent lead wall next to the monochromator shielding for phase II. Additionally, an increase in the background rate was observed near the floor due to a small unshielded gap at the base of the monochromator shielding. This gap was subsequently filled with lead bricks. The presence of iron beneath the concrete floor, potentially activated by ambient neutrons, also motivated the installation of lead shielding on the floor at the cryostat location.

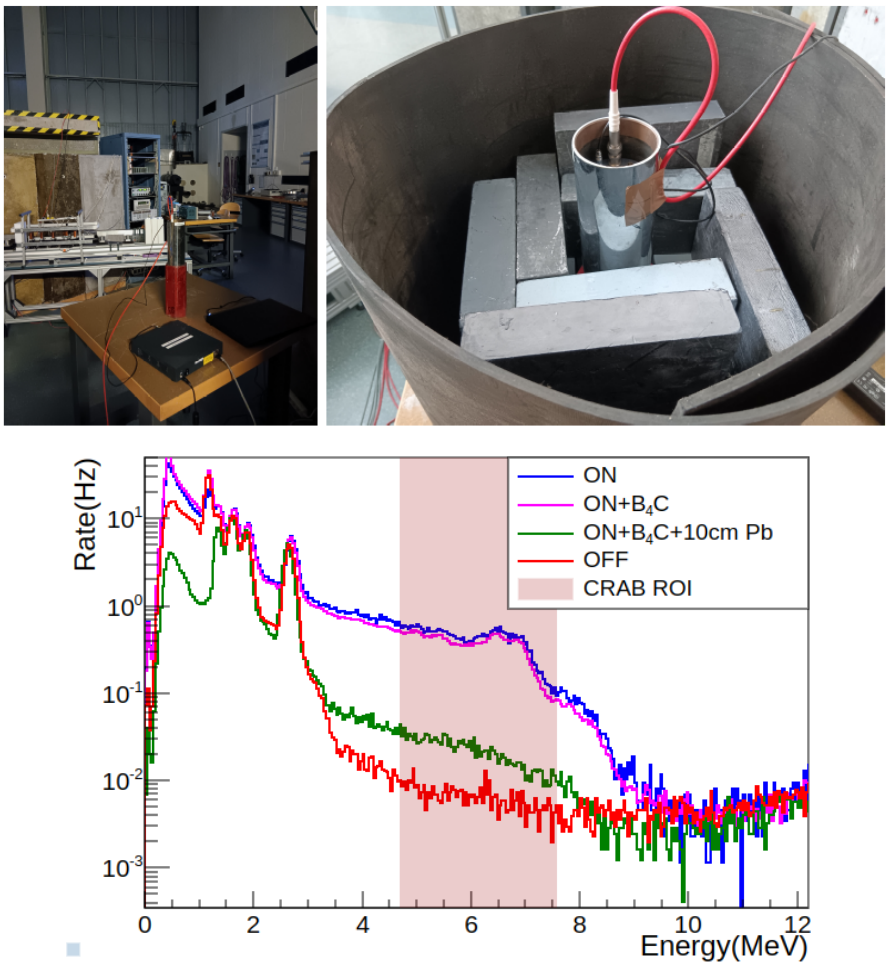

Figure 8.1. Top left: Background measurement in the CRAB area using a BaF_2 detector. Top right: Additional 10 cm of lead shielding around the detector to attenuate ambient gamma radiation, along with a boron carbide (B_4C) layer to shield against neutrons. Bottom: Measured energy spectra for all configurations (various shielding setups and reactor statuses). Under reactor operation, a significant background is observed in the CRAB ROI (red shaded area). This background is strongly suppressed by the combined lead and B_4C shielding.

Configuration	Rate in [4.7,7.6] MeV
OFF	0.5 Hz
ON	31.2 Hz
ON & B_4C	26.7 Hz
ON & B_4C & 10cm Pb	1.6 Hz

Table 8.1. Background rate in the CRAB ROI for various configurations. The neutron component is reduced by the B_4C shielding, while ambient gamma radiation—identified as the dominant background source—is significantly attenuated by the lead bricks.

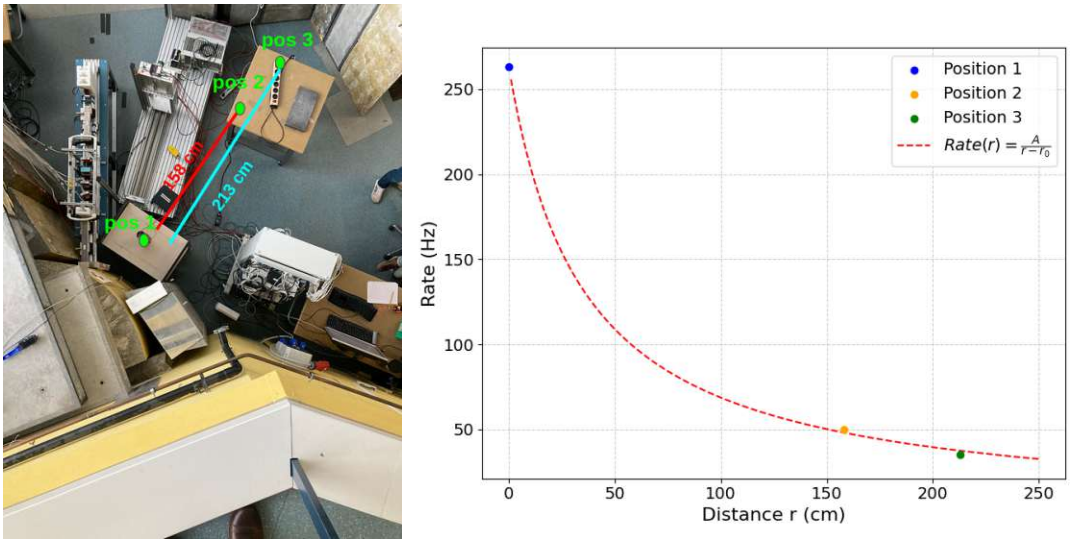

Figure 8.2. Left: Top view of the CRAB area showing the positions of background measurements and their distances from the monochromator shielding. Right: Background rate in the ROI at these positions. The rates follow a $\frac{1}{r}$ dependence, where r is the distance from the monochromator shielding, indicating that it is the primary source of the background.

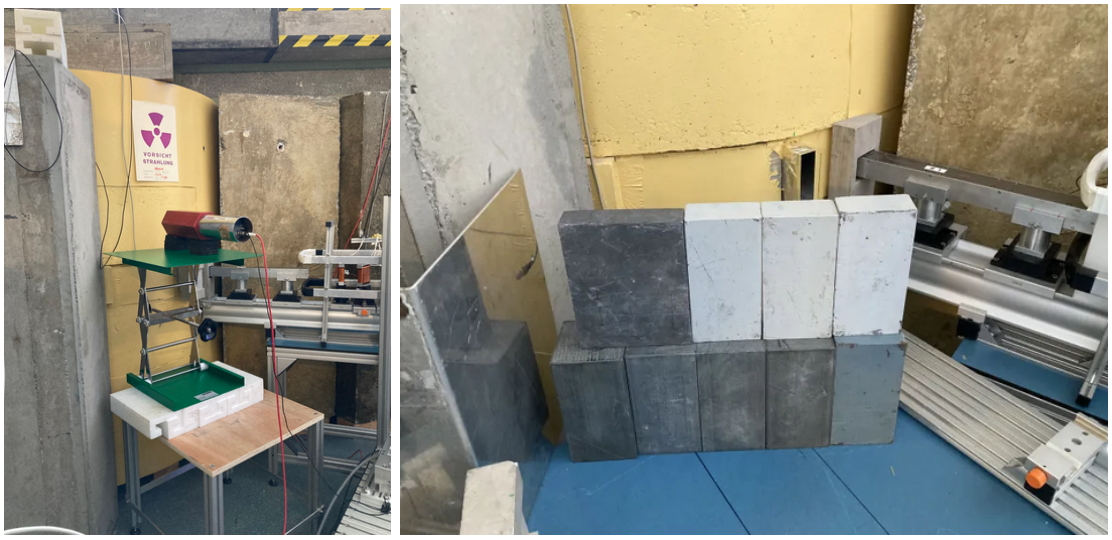

Figure 8.3. Left: Scan of the background rate along the height of the monochromator shielding. Right: Test using lead bricks placed near the monochromator shielding to shield the CRAB area from emitted radiations.

8.1.2 Dewar attenuation measurement

The cryostat, originally manufactured in the 1990s, lacks detailed documentation regarding the thickness and material composition of its internal dewar walls. Yet, this information is critical for our high-precision measurements, as the thermal neutron beam passes directly through the cryostat to reach the target detector. To compensate for the limited manufacturer data, we conducted dedicated γ-attenuation measurements. Various radioactive sources were placed at the location of the cryodetector inside the empty dewar, using a long U-shaped aluminum structure. This same structure held a CLYC detector (Cs_2LiYCl_6:Ce scintillator [231]) at a fixed position outside the dewar. Transmission factors were determined by comparing count rates with and without the

dewar in place. Measurements were performed using five γ-lines from the following isotopes: ^{137}Cs (661.7 keV), ^{133}Ba (356.0 keV, 160.6 keV, 81.0 keV), and ^{241}Am (59.5 keV). The experimental setup is shown on left of the Figure 8.4. In the right panel of this figure, the resulting transmission factors are compared with simulated transmission curves computed using GEANT4 with the Livermore physics list, considering various material combinations and thicknesses (specifically aluminum and stainless steel). The shape of the measured curve provides clear discrimination, ruling out a single-material composition for the dewar walls. The best agreement is found for a combination of a 6 mm thick aluminum layer and a 1 mm thick stainless steel layer.
The thermal insulation of the dewar consists of multiple interleaved layers of mylar and aluminized mylar surrounding the liquid helium (LHe) vessel. Although this low-density material has negligible impact on γ attenuation, its overall thickness can be probed through neutron transmission measurements using the CRAB neutron beam at Atominstitut. To account for this, an intermediate mylar layer was included in the GEANT4 geometry. A thickness of 2 mm provided the best agreement with the observed neutron transmission through the dewar of 6.7%.

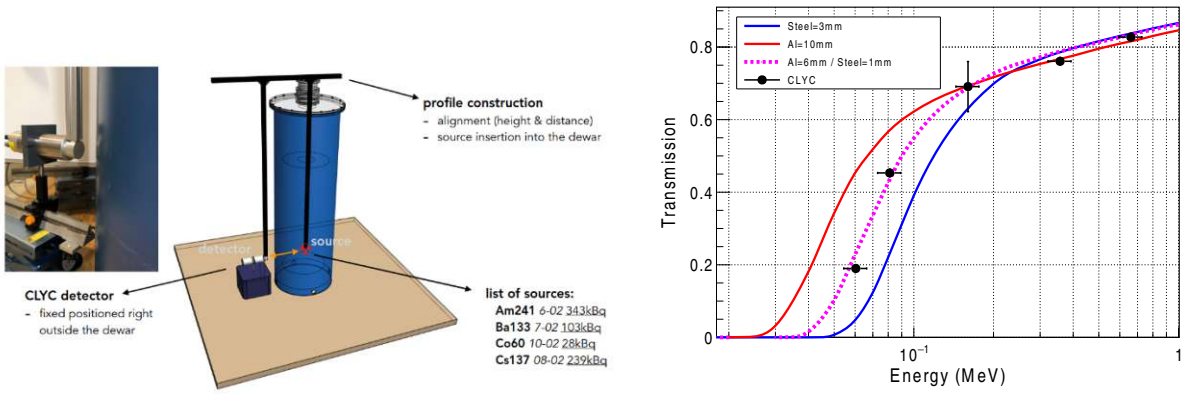

Figure 8.4. Left: Experimental setup for estimating the dewar wall material. A long U-shaped aluminum structure is used to align radioactive sources inside the dewar with a CLYC γ-detector positioned outside. For each source, measurements are taken with and without the dewar to determine the transmission factor. Right: Transmission factors of γ-rays measured by the CLYC detector (black points), compared with GEANT4 simulations for various wall materials and thicknesses. The best agreement between data and simulation is obtained with a dewar wall composed of 6 mm aluminum and 1 mm steel. Figures from [193].

8.1.3 Cryogenic detectors

In preparation for phase II of the CRAB experiment, characterisation measurements of three ultra-low-threshold cryogenic detectors were conducted at the UnderGround Laboratory (UGL) of the Technical University of Munich (TUM), using the wet cryostat (described in Section 6.2.1.1), prior to its relocation to the TRIGA Mark-II reactor site in Vienna. Two $CaWO_4$ crystals and one Al_2O_3 crystal, each with different geometries, were mounted in dedicated CRAB low-mass mechanical holders and tested in two separate runs. Their dimensions are listed in Table 8.2, and the crystals are referred to as follows: $CaWO_4$ cube (W1-682-9), small wafer $CaWO_4$ (IPP27-Ca-c1), and Al_2O_3 cube (W1-710-5). The low-mass holder design was optimized to minimize neutron capture in the holder mechanics. It consists of an aluminum Printed Circuit Board (PCB), which serves both as a structural support and as an electrical interface. The detectors are shielded against thermal radiation by a housing made of NOSV copper to ensure proper thermalization. The PCB is thermally coupled to the heat bath via interleaved high-conductivity copper foils. Displayed at the top of Figure 8.5 are an exploded 3D view and a picture of the detector holder. The two different $CaWO_4$ geometries required distinct mounting

solutions. For the cube geometry, a bronze clamp attached to a segment of the holder wall presses the crystal onto the PCB. Aluminum spheres provide point-like contact between the crystal and the bronze clamp, ensuring thermal isolation from the holder. For the wafer geometry, the crystal is held by two side-mounted bronze clamping arms that apply gentle lateral pressure. Pictures of the two mounted and wire-bonded $CaWO_4$ crystals are displayed at the bottom of Figure 8.5.

During benchmark performance measurements in Munich, all three detectors were continuously exposed to a ^{55}Fe X-ray source for energy calibration. They demonstrated excellent performance in terms of baseline energy resolution and energy threshold. As shown in Table 8.2, the achieved baseline resolutions were below 6 eV, leading to detection thresholds as low as 30 eV. These results meet the requirements for high-precision measurements of ∼100 eV nuclear recoil peaks. The success of these preliminary tests paved the way for relocating the cryostat to the Atominstitut in Vienna. A more complete description of the cryodetectors and their development can be found in [232].

Detector	**IPP27_Ca-c1**	**W1-682-9**	**W1-710-5**
Target material	$CaWO_4$	$CaWO_4$	Al_2O_3
Dimensions (mm)	4.75 × 1.7 × 0.6	4.8 × 4.8 × 4.8	5.0 × 5.0 × 5.0
Mass (g)	0.03	0.67	0.50
Transition temperature (mK)	14	13	18
Baseline resolution (eV)	3.8 ± 0.4	5.5 ± 0.1	3.7 ± 0.1

Table 8.2. Overview of characteristics and benchmark performance of the cryodetectors selected for the CRAB experiment. Baseline resolutions meet the required specifications. Table adapted from [193].

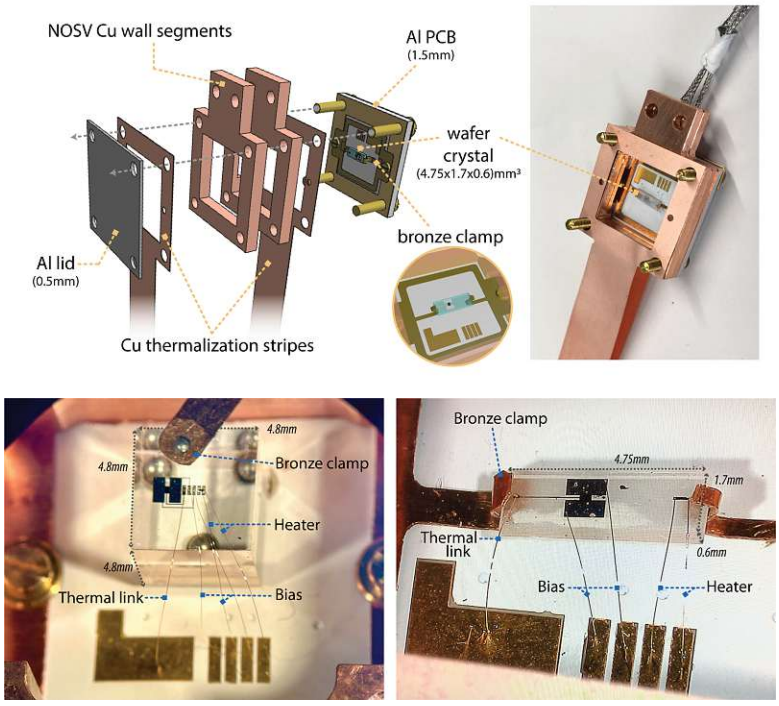

Figure 8.5. Top left: Exploded 3D view of the detector holder showing the aluminum PCB, the minimal housing, and the interleaved copper strips providing thermal conductance between the PCB and the heat bath. Top right: Picture of the assembled detector holder. Bottom: Picture of the $CaWO_4$ cube (left) and the wafer-shaped crystal (right), with dimensions listed in Table 8.2, each mounted in their respective detector holders. Electrical contacts for the heater and bias lines use aluminum wire bonds, while thermal links gold wire bonds. Images from [193].

8.2 Installation of the CRAB experimental setup

After several months of preparation for phase II and close collaboration with the technical teams from CEA, TU Wien and TU Munich, the cryostat support structure as well as the gas handling system were successfully designed and manufactured. The installation steps of the setup are illustrated in the insets of Figure 8.6. At the end of 2023, the linear stage and the hexapod were installed in the primary beam (see inset i). In spring 2024, the upper triangular section supporting the cryostat and its air dampers was mounted (see inset ii). A few weeks later, the full support structure was completed (see inset iii). In summer 2024, the cryostat and its dewar were transported to Vienna. Once the cryostat was installed, beam alignment with the cryodetector had to be addressed. To achieve this, a 2D neutron detector was placed downstream of the cryodetector box, and a dummy LiF crystal—chosen for its high neutron absorption—was installed inside the detector box to enhance image contrast in the 2D neutron detector (inset iv). Thanks to the hexapod on which the second reflective graphite crystal is mounted, the neutron beam could be finely adjusted. The resulting image was striking: it clearly showed that the detector box was properly aligned with the beam, and that the dummy crystal was located precisely at the beam's intensity maximum.

Then, the dewar was integrated into the support structure (see insets v and vi). A compact and mobile gas handling system has been developed for operation at the reactor site to manage helium gas circulation (see inset vii). It includes two circuits—the "auxiliary circuit" and the "mixing circuit"—integrated into the central KelvinoxIGH unit, a commercial intelligent gas handling system from Oxford Instruments plc. This unit is equipped with internal valves and pressure sensors to regulate the flows of ^{3}He and ^{4}He, that can be monitored and controlled remotely via a dedicated software. The auxiliary circuit incorporates a 1 K pot and a pumping line powered by two multi-stage roots pumps (Pfeiffer ACP 40) connected in series. In the mixing circuit, circulation of the ^{3}He–^{4}He mixture is driven by a turbomolecular drag pump (Pfeiffer HiPace 400) positioned near the still outlet on the cryostat insert rack to ensure optimal pumping performance. A separate turbomolecular pumping station—comprising a Pfeiffer HiPace 400 pump and a Pfeiffer ACP 40 backing pump—is dedicated to evacuating the Inner Vacuum Chamber (IVC) prior to cool-down. For monitoring purposes, the system is equipped with eight additional pressure gauges (Pfeiffer PCR 280) and a liquid helium level sensor to track the fill level of the LHe dewar.

The BaF_2 detector array was then installed (see inset viii), positioned in two concentric crowns around the cryostat and surrounded by 10 cm thick lead shielding to reduce ambient γ-ray background (see inset ix). Additional 4 cm thick lead bricks were placed on the floor beneath the cryostat to shield against radiation from below. To block thermal neutrons and suppress radiative neutron captures near the detectors, boron-doped rubber mats were mounted across the entire cryostat support structure (inset x). To further limit neutron captures on materials surrounding the cryodetectors, a collimator was installed upstream of the cryostat along the neutron beam axis. It consists of a 2 cm radius circular aperture made of boron-loaded material, followed by 5 cm of lead to absorb γ-rays emitted from neutron capture on boron (inset xi). This configuration allows the neutron beam to shine exclusively on the cryodetectors (inset iv). In addition, a 10 cm-thick mobile lead screen was mounted on a movable cart to shield the solid angle subtended by the reactor wall at the beam exit, which constitutes a background hot spot (see inset xii).

Finally, the detector acquisition systems were installed on two racks (see inset xiii). The cryodetectors use the VDAQ-3 system, an improved version of the VDAQ-2 system used by the NUCLEUS experiment (see Section 4.1.3). The rack also houses the SQUID readout electronics and the heater control box. The second rack contains the high-voltage power supply for the γ-detectors as well as the FASTER data acquisition crate. Electronics for neutron beam-related components—including the linear stage, hexapod, and 2D neutron detector—are also located in this rack. To ensure proper electrical ground isolation, an Uninterruptible Power Supply (UPS) was installed at the interface between the lab power supply and the acquisition systems.

Figure 8.6. Steps of the experimental setup installation are shown in insets i–xiii. i) Linear stage intended to hold the hexapod and second graphite crystal (not installed here). ii) Upper section of the cryostat support structure with air dampers for vibration isolation. iii) Fully assembled cryostat support structure. iv) Installation of the cryostat and alignment verification with the neutron beam using the 2D neutron detector. The neutron beam imaging after the installation of the collimator is also shown (Credits: S.Dorer). v) and vi) Dewar installation. vii) Gas handling system containing the pumps and tubing connected to the cryostat. viii) Installation of the BaF_2 detector array surrounding the cryostat. ix) Lead shielding protecting the γ-detectors crown from ambient γ-ray background. x) Boron-carbide (B_4C) mat fixed to the structure to mitigate ambient thermal neutron background. xi) Collimator at the cryostat entrance, consisting of a B_4C aperture followed by a lead brick, designed to reduce neutron beam-induced background. xii) An additional mobile lead wall was positioned at the neutron beam exit to shield this known background hot spot. xiii) Rack hosting all cryodetector electronics, including the VDAQ-3 system, heater box, and external pulser. A second rack houses the electronics for the γ-detectors and neutron beam line components.

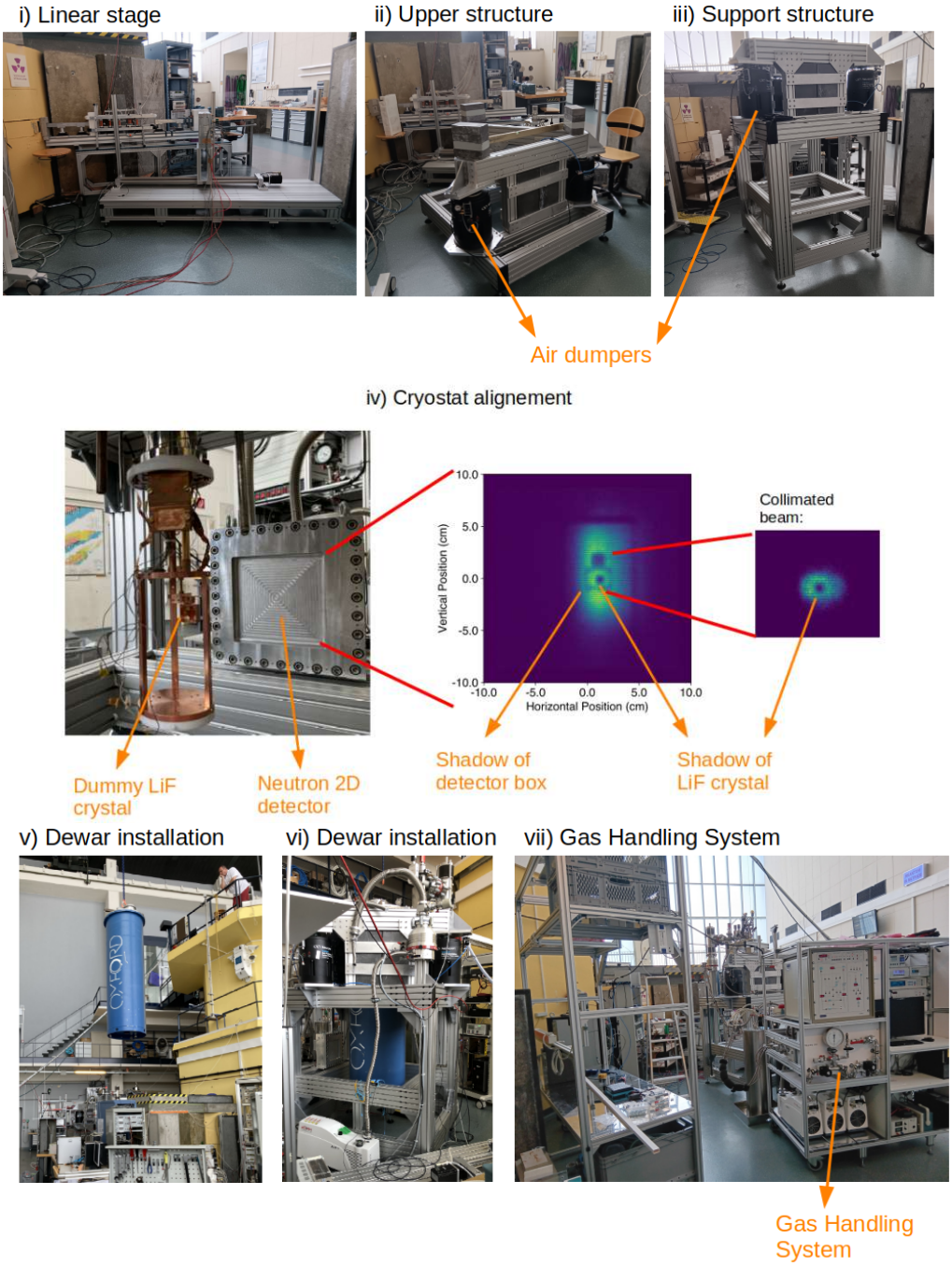

viii) BaF_2 implementation ix) Lead shielding x) B_4C shielding

BaF_2 crown

xi) Collimator xii) Lead wall

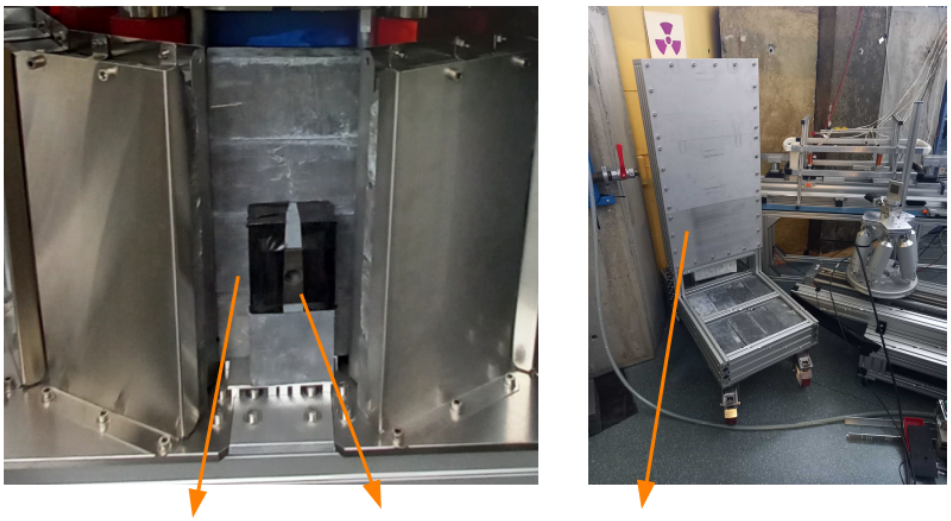

Lead B_4C Lead wall

xiii) Electronic racks

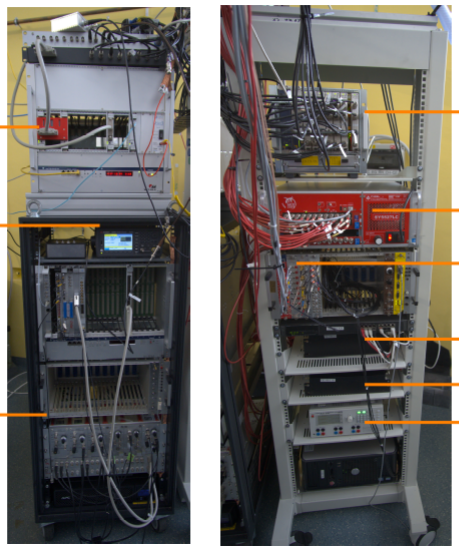

VDAQ 3

External pulser

Heater box

FASTER crate

HV power supply (BaF_2)

2D neutron detector power supply

Hexapod electronics

Rotational stage electronics

Linear stage power supply

8.3 Simulation of the phase II

The phase II geometry has been implemented in the GEANT4 simulation. It includes the cryostat, its dewar, the support structure, and a detailed description of the IVC. The passive shielding as well as the collimator are also taken into account. On the detector side, the two $CaWO_4$ cryodetectors (cube and small wafer crystal) described in Table 8.2, along with the 28 BaF_2 detectors, are included in the simulation. Neutrons are injected from the position of the secondary graphite crystal, with their energies sampled from an energy spectrum obtained via time-of-flight measurements. The neutron beam is predominantly bi-energetic, composed of neutrons at 12 and 47 meV. A divergence angle of 0.8° is applied. The neutron flux transmission through the dewar vessel and the liquid helium is approximately 25%. In total, 3.5×10^9 neutrons were transported through the simulated geometry, corresponding to an equivalent data-taking time of 141.5 hours. Table 8.3 presents the event rates in the two cryodetectors, both in single mode and in coincidence with the γ-detectors, across different energy regions. At low energies, the event rate is dominated by CRAB events, particularly those producing the three calibration peaks. At higher energies, the signal consists of two main components: one from external background induced by neutron capture on surrounding materials, and a second, dominant component from CRAB events. These CRAB events correspond to multi-γ transitions following neutron capture, involving either a low-energy γ or, more frequently, a conversion electron. These particles, with energies in the [10-100] keV range have a high probability to deposit their energy within the crystal. A detailed study of these events is conducted in Section 8.5.

While the small wafer crystal, due to its small size, is expected to achieve superior energy resolution, the higher event rate in the $CaWO_4$ cube provides high statistics. This simulation predicts the detection of CRAB peaks with high significance within just a few days of data-taking, depending on the achieved energy resolution. In particular, with an energy resolution of 5 eV, a single day of data-taking is sufficient to observe the 112 eV peak in the $CaWO_4$ cube.

Cryodetector	Energy region		Single rates [mHz]	Coincidence rates [mHz]
IPP27_Ca-c1 ($4.75 \times 1.7 \times 0.6$) mm^3	CRAB ROI	81 eV	1.16	0.07
		112 eV	3.04	0.20
		160 eV	0.35	0.02
	High energy	> 10 keV	Total = 64.1 CRAB = 49.7	Total = 2.57 CRAB = 1.96
W1-682-9 ($4.8 \times 4.8 \times 4.8$) mm^3	CRAB ROI	81 eV	24.29	1.39
		112 eV	82.80	5.38
		160 eV	9.63	0.40
	High energy	> 10 keV	Total = 1990 CRAB = 1650	Total = 78.0 CRAB = 64.0

Table 8.3. Single and coincidence rates measured in the small wafer crystal and in the $CaWO_4$ cube across different energy regions. At high energies, two main contributions are identified: (1) background from neutron capture in cryogenic materials, and (2) CRAB events originating from the de-excitation cascade following neutron capture in the target detector.

8.4 Commissioning of the BaF_2 detectors

In this section, I review the full commissioning of the BaF_2 detectors following their installation. This includes energy calibration, time stability, and detection efficiency. An external background characterisation is also presented. Finally, work was carried out to achieve clock synchronization between the FASTER acquisition system and the VDAQ cryodetector readout system.

8.4.1 BaF_2 characterisation

The monitoring of the energy response of all detectors is performed online using the fourth α peak from radioactive internal contamination. Due to the quenching effect—that is, the reduced light yield of α-induced scintillation compared to that from γ interactions of the same energy—no absolute energy calibration can be derived from this α peak alone. The quenching factor, defined as the ratio of the measured scintillation energy to the theoretical energy, varies by up to $\pm 10\%$ between detectors. Therefore, an absolute calibration using known γ lines is necessary. This calibration enables determination of the position of the fourth α peak on a γ-equivalent energy scale for all detectors, thus allowing for reliable online calibration.

The absolute calibration is performed using known γ-lines from radioactive sources: ^{137}Cs (0.662 MeV), ^{60}Co (1.173 and 1.332 MeV) and Am-Be (4.440 MeV), as well as the 2.2 MeV line from neutron capture on hydrogen contained in the low-density material shielding the Am-Be source (see Figure 8.7). A simple Gaussian fit is applied to extract the peak positions, and a linear fit is then used to determine the detector gains (see left panel of Figure 8.8). After adjusting the photomultiplier high voltages, all gains are aligned to a mean value of 7.9 eV/QDC channel within $\pm$ 5% (see right panel of Figure 8.8).

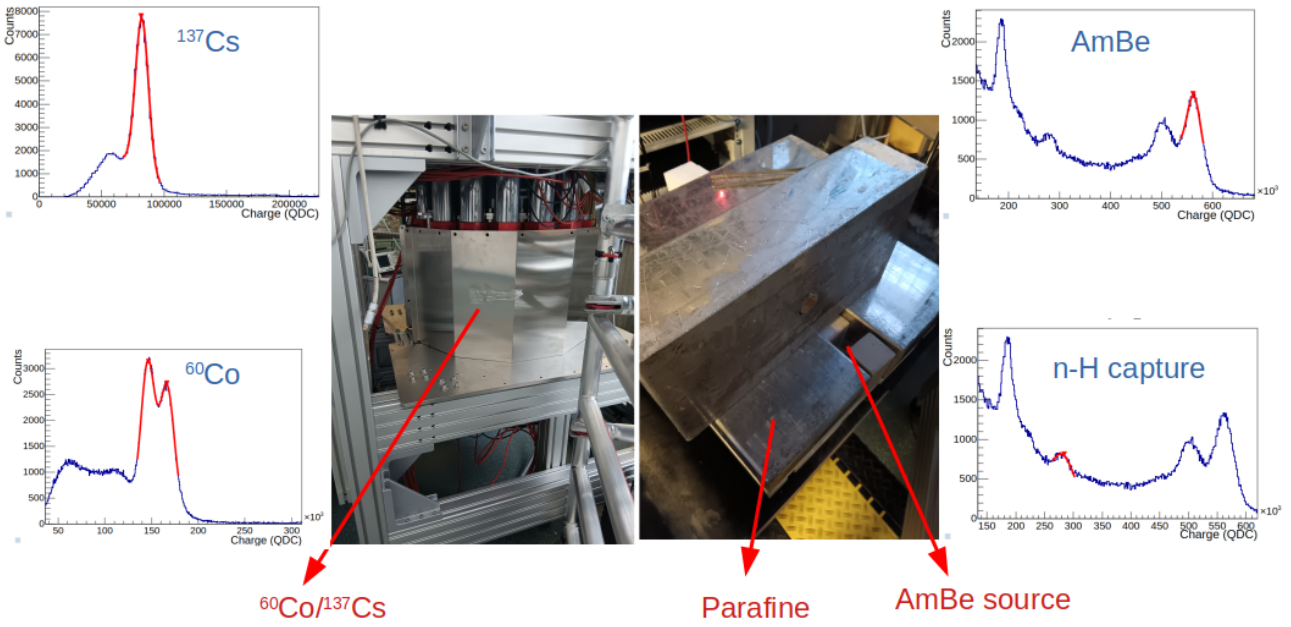

Figure 8.7. Middle left: Exposure of the γ-detectors to ^{137}Cs and ^{60}Co sources. Middle right: AmBe source shielded with paraffin. These sources produce γ peaks at 0.662, 1.173, 1.332, and 4.440 MeV, along with an additional 2.2 MeV peak from neutron capture on hydrogen in the paraffin. Four side insets: BaF_2 detector calibration peaks, each fitted with a Gaussian function.

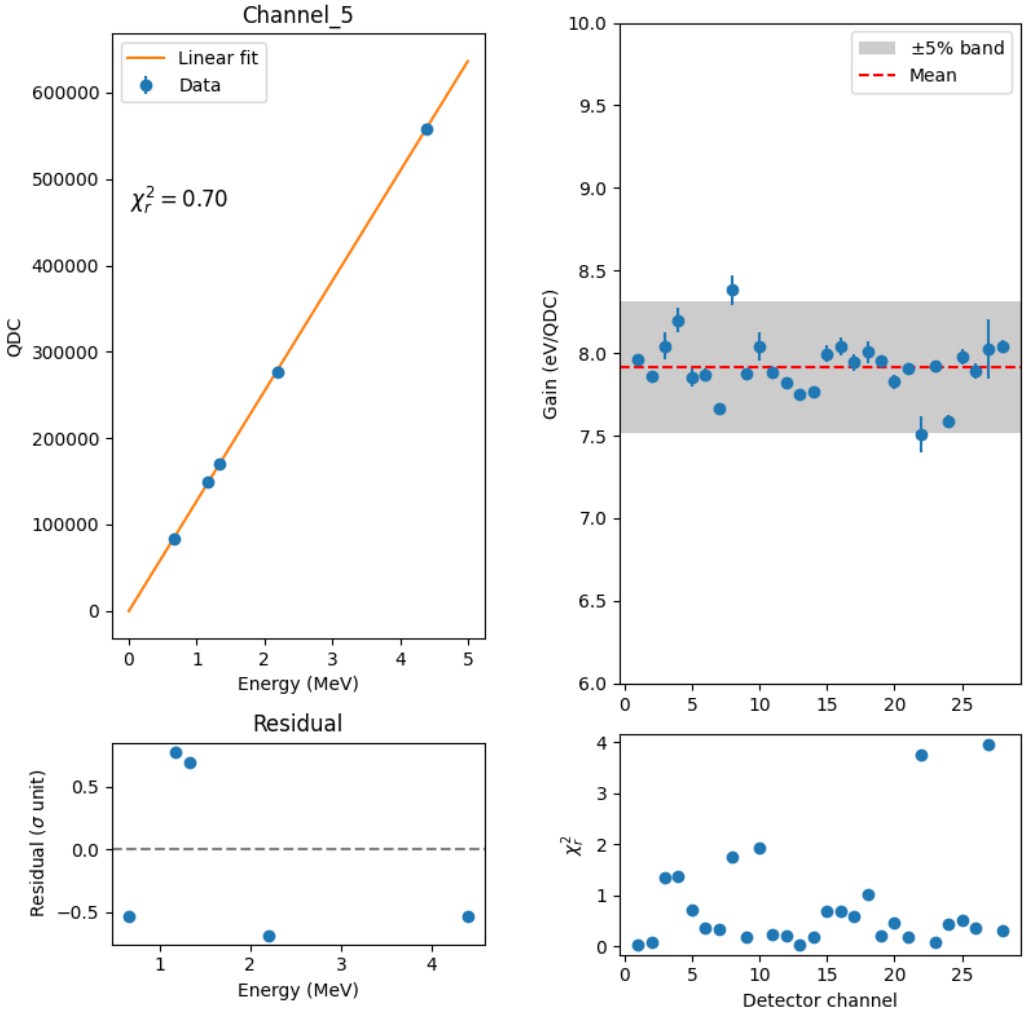

Figure 8.8. Left: Linear calibration of the detector response based on fitted peak positions. The lower panel shows residuals in units of σ. Right: Measured gain values for all BaF_2 detectors in eV/QDC, preliminarily aligned within ±5% by tuning the PMT high voltage.

The standard deviation of the calibration peaks are used to characterize the energy resolution of the detectors. For all detectors, the energy resolution depends on the incident energy and is well described by the function [226]:

$$\frac{\sigma^2(E)}{E^2} = \frac{A}{E} + \frac{B}{E^2} + C \tag{8.2}$$

where $\frac{A}{E}$ accounts for statistical fluctuations in the number of electron-hole pairs created by an incident energy E, $\frac{B}{E^2}$ represents the electronic noise of the signal readout chain, and the constant term C accounts for inefficiencies in scintillation light collection.

The fit result for one detector is shown in the left panel of Figure 8.9. On the right, the relative energy resolution for all detectors at 6 MeV is about 2.5 ± 0.6%. Specifications of linearity within a few percent and a resolution better than 5% in the ROI are achieved.

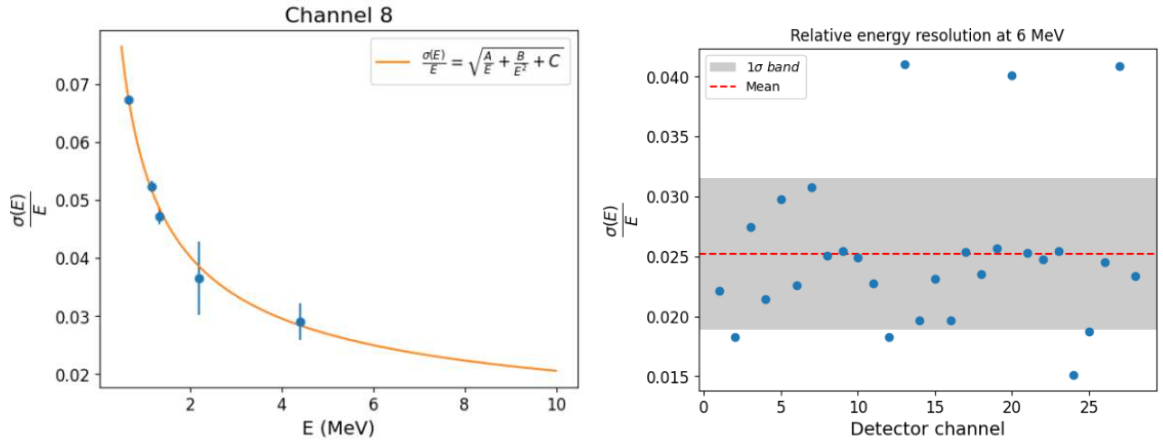

Figure 8.9. Left: Relative detector energy resolution fitted by the Equation 8.2. Right: Relative energy resolution of all detectors at 6 MeV, the relevant energy for γ-NR coincidences. The mean value of 2.5% is sufficient to proceed with the coincidence analysis.

The detectors also exhibited excellent time stability, monitored via the position of the fourth α peak over time. This peak can be measured with percent-level statistical precision within just a few minutes, and a stability of 0.5% was observed over a continuous 9-day period. Gain drifts are primarily attributed to electronic temperature fluctuations of the PMT electronics. For this reason, the PMTs are powered on well in advance of each measurement. To correct for any residual gain drift, an online calibration is performed for each data acquisition segment (typically corresponding to one day of reactor operation, i.e., approximately 7 hours), using the position of this α peak.

The full-peak detection efficiency was determined using a ^{60}Co source with a known activity, positioned at a well-defined distance from a BaF_2 crystal. The measured full-peak efficiency was found to be 23±3% lower than predicted by GEANT4 simulations. This discrepancy has also been reported in previous studies [233, 234], and is attributed to aging effects in the 40+ year-old detectors. A regeneration procedure for BaF_2 crystals via annealing [235, 236] is being considered to improve coincidence event statistics in future measurements. The total efficiency, including both geometrical and intrinsic detector contributions, is estimated at 3.2%.

8.4.2 Final characterisation of the external background

After the installation of the BaF_2 detectors, the background under various shielding configurations and reactor operating conditions was measured and can be seen in the left panel of Figure 8.10. Under reactor-OFF conditions (green spectrum), the background rate in the CRAB ROI ([4.7, 7.6] MeV) is very low. As discussed in Section 8.1.1, reactor operation induces high-energy background—primarily from γ-rays and neutrons—explaining the elevated background level seen in the red spectrum. To mitigate this, shielding was implemented during installation, leading to a 20-fold reduction in background (blue spectrum). During standard operation, a detection threshold just below 2 MeV is applied to reduce the total counting rate per detector while preserving the highest-energy α peak at 2.86 MeV. This peak is essential for accurate monitoring of detector response. The individual background rates within the CRAB ROI for each detector are shown in Figure 8.11. With an average rate of 2.3 Hz per detector, the system meets the initial design requirement of remaining below 3 Hz, thereby ensuring an acceptable level of accidental coincidence probability.

When the reactor is operational, a peak at 1.29 MeV appears in the energy spectrum, indicating neutron activation of ^{41}Ar in the air. This peak is notably intense and thus constitutes a non-negligible source of

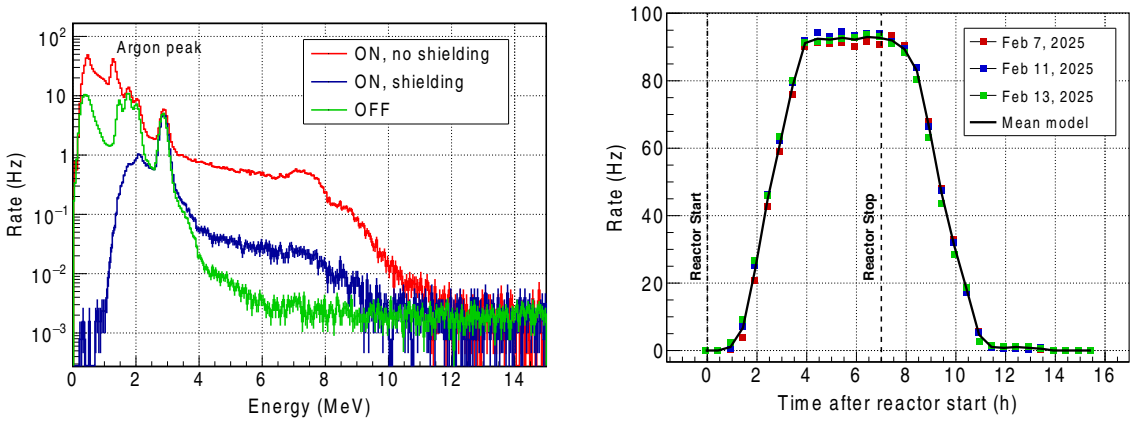

Figure 8.10. Left: Background energy spectra recorded with a BaF_2 detector under three conditions: reactor off (green), reactor at full power without shielding (red), and with shielding (blue). Under standard operation, the detection threshold visible in the blue spectrum is set just below the last α peak. A peak at 1.29 MeV, attributed to ^{41}Ar activity, is clearly observed in the spectrum where no threshold is employed. Right: Time evolution of ^{41}Ar activity measured in an external BaF_2 detector over three different days of reactor operation (colored points). The black curve represents a model of the ^{41}Ar activity, obtained by averaging the three datasets. Figures from [193].

high-energy background in the cryogenic detectors. To monitor this contribution, an additional BaF_2 detector was placed outside the lead crown, near the cryostat, to track the time evolution of the ^{41}Ar activity and construct an accurate background model. The rate in the ^{41}Ar peak was recorded every 30 minutes over several days during nominal reactor operation (seven hours per day at full power). Its temporal evolution, plotted on the right panel of Figure 8.10 for a three-day period, exhibits a highly reproducible pattern. The average daily profiles are used to define a model employed in the cryodetector high-energy rate analysis presented in Section 8.5.1. Interestingly, both the activation and decay phases of the observed time profile are inconsistent with the expected behavior for ^{41}Ar, which has a half-life of approximately 110 minutes. It was found that the dominant contribution originates from the volume of air within a "pneumatic rabbit system" located near the CRAB setup. This system circulates irradiated samples in a pipe passing through the reactor core, where the air becomes activated by the intense neutron flux. The activated argon then slowly diffuses through the tubing into the reactor hall. As a result, both the rise and decay of the ^{41}Ar background are delayed by roughly one hour relative to the reactor's start and stop times. Consequently, the time evolution of this background differs significantly from a simple exponential activation and decay governed solely by the radioactive half-life of ^{41}Ar.

8.4.3 Data processing

The 28 detectors are read out using the FASTER acquisition system, whose operation was briefly described in Section 7.4.4.3. This system produces ROOT files containing, for each event, the list of triggered channels, the trigger times, and the charges deposited in each channel. These files are then processed using an online calibration based on the reference γ calibration and on the monitoring of the fourth α peak to reconstruct the deposited energy for each event. The results of this processing are stored in an HDF5 file, which serves as input for the coincidence analysis between the γ-detectors and the cryogenic detectors. For all events within a large region of interest ([3,8] MeV), this file contains the reconstructed γ energy, the triggering channel, the raw event timestamp, and the event time converted to the cryogenic detector time frame (see next section).

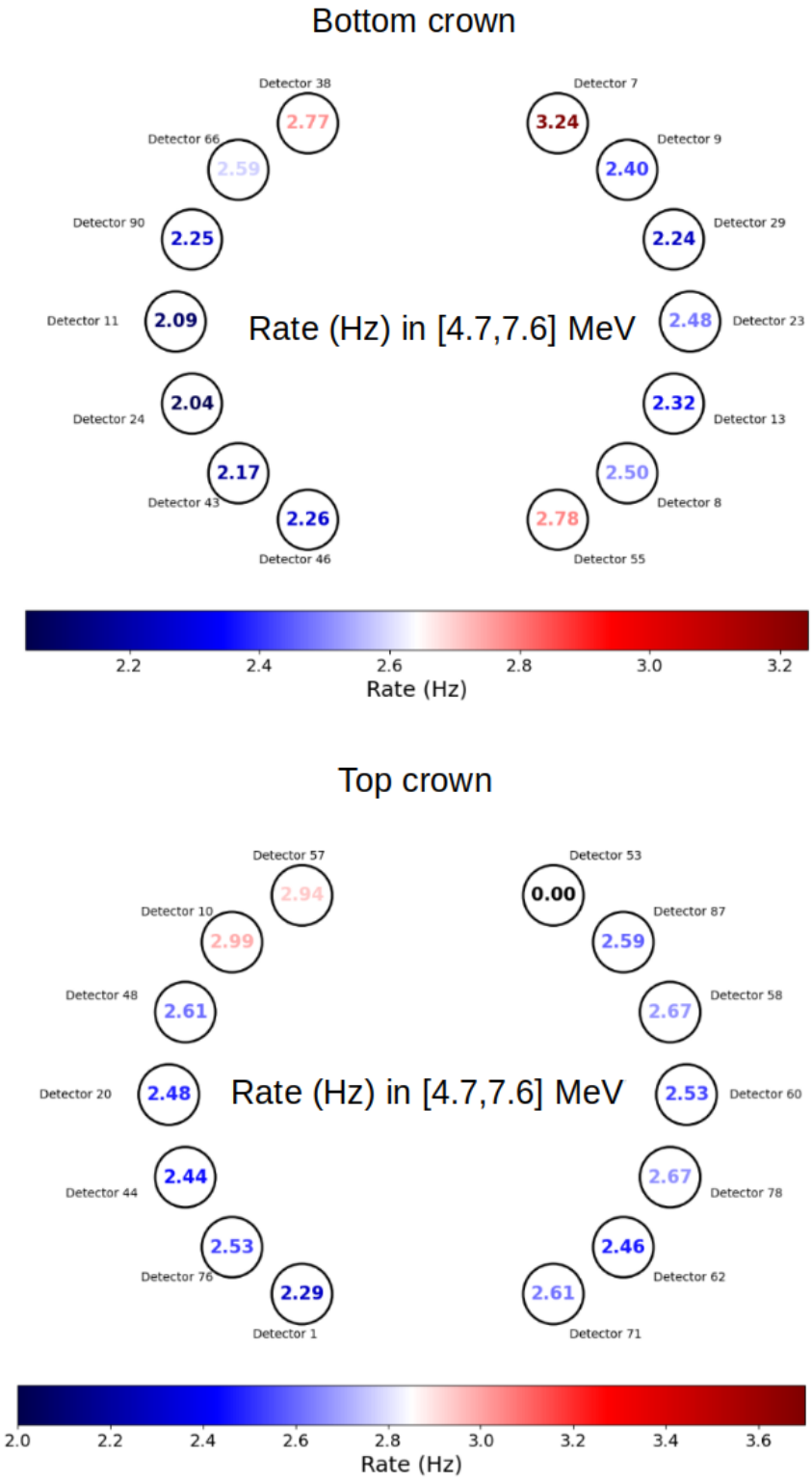

Figure 8.11. Background rate within the CRAB ROI ([4.7–7.8] MeV) for all BaF_2 modules in the crown. The last channel (detector 53 of the top crown) is used by an external pulser for clock synchronization and therefore does not record background events.

8.4.4 DAQ synchronization

The γ-NR coincidence requires synchronization between the clocks of the two acquisition systems: VDAQ for the cryodetector and FASTER for the γ-detectors. In the case of NUCLEUS experiment, the VDAQ clock was used as a common reference clock and distributed to the veto acquisition system (see Section 4.1.3). However, FASTER does not support external clock input from VDAQ, making hardware-level synchronization unfeasible. Instead, synchronization is performed offline on the software side. For this purpose, an external pulse generator sends a square signal (5 V amplitude, 10 Hz frequency, 500 μs width) to both acquisition systems. Channel 2 in VDAQ and channel 28 in FASTER are dedicated to receive this pulser signal. The relative time drift between the two clocks is then determined using the time difference between the pulses recorded in both acquisitions: $T_{\mathrm{VDAQ}} - T_{\mathrm{FASTER}}$ (see Figure 8.12).

We observe a global clock drift of approximately 63 μs/s. This drift is composed of a slope of 2.3 μs/s superimposed with periodic jumps of 100 μs, which originate from the time resolution limitation of VDAQ. These slopes are simply estimated using two consecutive pulser points.

We arbitrarily chose to correct the FASTER timestamps in order to express them in the VDAQ clock reference frame. The correction procedure, illustrated in Figure 8.12, proceeds as follows:

- A γ-detector event triggers the FASTER DAQ, with an associated timestamp T_{old} in the FASTER clock reference frame.
- The most recent synchronization pulse time $T_{\mathrm{last\ pulse}}$ is identified, along with the measured time offset between the two acquisition systems at that point, $T_{\mathrm{diff,pulser}}$.
- The corrected event time in the VDAQ clock reference frame, T_{corr}, is then computed according to the formula:

$$T_{\mathrm{corr}} = T_{\mathrm{old}} + T_{\mathrm{diff,pulser}} + \mathrm{slope} \times (T_{\mathrm{old}} - T_{\mathrm{last\ pulse}}) \tag{8.3}$$

To validate the synchronization procedure, a second pulser was connected with a different frequency of 0.74 Hz and operated for 3 hours. After applying the clock correction to the second pulser signals recorded by FASTER, we compare their timestamps with those recorded by the VDAQ system. The resulting time difference distribution plotted in Figure 8.13 shows that the pulses are successfully reconstructed in coincidence even after several hours of data acquisition, with a time jitter of approximately 65 μs. This is within the rise time of the cryogenic detectors, which is on the order of 100 μs, and thus confirms the validity of the synchronization method. The first synchronized coincidence data are presented in Section 8.5.3.

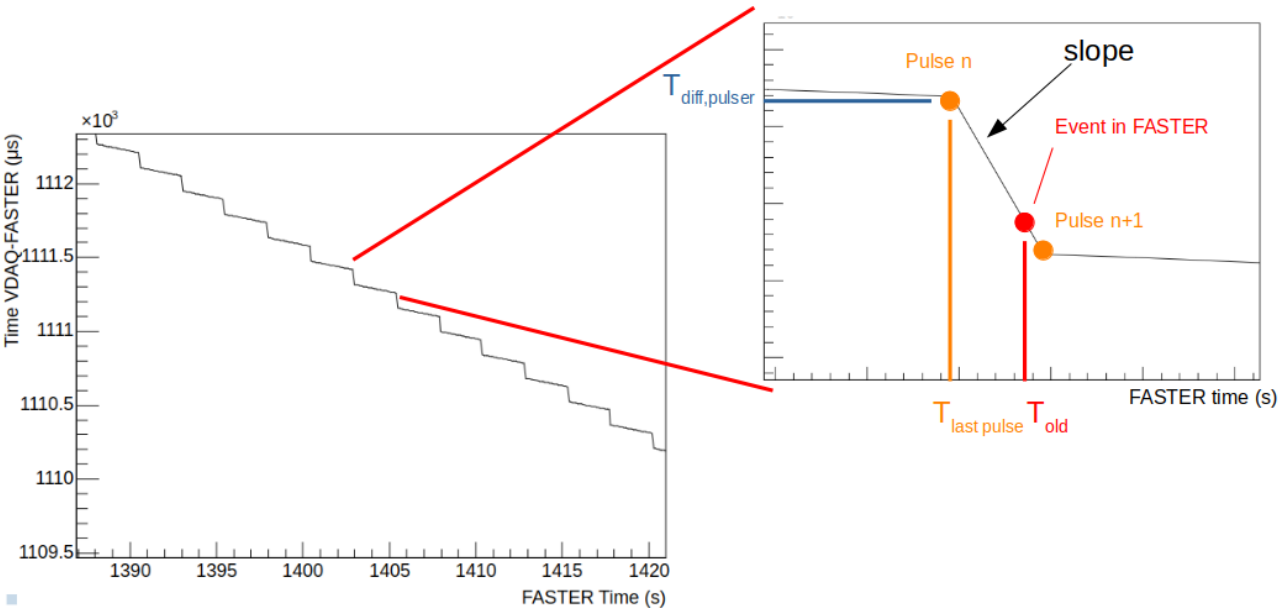

Figure 8.12. Time difference between the pulse timestamps recorded by the VDAQ and FASTER acquisition systems, showing a global clock drift of 63 μs/s. Several discrete jumps of 100 μs are also observed, attributed to the VDAQ sampling frequency. The correction method for the clock drift is described in the text, and the applied correction formula (Equation 8.3) is illustrated in the inset.

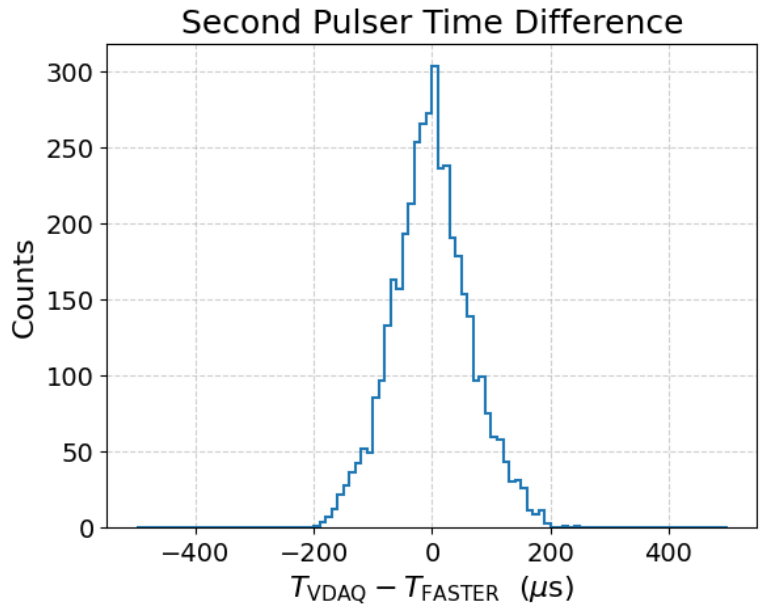

Figure 8.13. Time difference of the second pulser signal after applying clock drift correction using the first pulser as reference. The synchronization is validated by the resulting distribution, which has a time jitter of 65 μs on the order of the rise time of the cryodetector signals.

8.5 Commissioning of the cryodetectors

In this section, I present a summary of the commissioning of the two $CaWO_4$ detectors listed in Table 8.2, carried out in Vienna.

- **Small wafer $CaWO_4$ crystal:** During the commissioning of this detector, a baseline energy resolution of 7 eV was achieved. However, due to a leak in the helium circulation system, it was difficult to maintain stable operating conditions, and this performance could not be sustained over time. Most of the time, a degraded resolution of around 20 eV was observed. Nevertheless, this demonstrated that achieving the target baseline energy resolution is technically feasible. Additionally, the detector exhibited unexpectedly slow response times, which became problematic given the high event rate induced by neutron captures, leading to stream saturation. We suspect a poor thermal coupling between the Transition Edge Sensor (TES) and the thermal bath, which would explain the slow decay time. This also interfered with the proper functioning of the PID loop, making it difficult to stabilize the detector at a fixed working point. Under these conditions, the detection of CRAB peaks was severely compromised. As such, I will not present data from this cryodetector.

- **$CaWO_4$ cube:** This cube detector operated under rather unusual conditions. Indeed, an unexpected serial resistance in the readout circuit resulted in a very low gain, such that the detector's dynamic range was limited to energy depositions between 10 and 200 keV. Under these conditions, the CRAB peaks are of course not detectable. However, this surprising feature offered a unique opportunity to study high-energy events induced by neutron capture. Following neutron captures, the subsequent de-excitation cascades can produce low-energy γ rays or conversion electrons, typically in the energy range of a few keV up to 100 keV. These particles have a high probability of depositing their full energy in the cryodetector. The study of such events allowed us to validate our understanding of the signal components—first by comparing the predicted and measured event rates (see Section 8.5.1), and then by comparing the measured energy spectrum shape to the simulation prediction (see Section 8.5.2). Finally, coincidences with the γ-detectors could also be validated using these events (see Section 8.5.3). This detector features a decay time of a few tens of milliseconds, keeping the pile-up rate at an acceptable level, although pile-up was still accounted for in the analyses presented in the following sections.

8.5.1 Rate analysis

The study of the high-energy event rate in the $CaWO_4$ cube would offer a valuable validation of the simulations. To obtain the event rate in the cryodetector, I used the CAIT framework introduced in Section 4.3, with necessary adaptations to the stream trigger procedure. Indeed, the neutron beam induces a high event rate, leading to more frequent pile-up. The standard triggering procedure suffers from poor baseline estimation for subtraction in the case of pile-up events, which can result in missed pulses. To address this issue, a so-called "bin-to-bin" method is used for triggering. This method involves differentiating the stream sample by sample. Since the pulse rise time spans several samples, a downsampling factor of 10 is first applied. The differentiated stream is then computed as the difference between two consecutive samples after downsampling. The differentiated stream (shown in red in Figure 8.14) exhibits sharp transitions that are clearly identifiable even in the presence of pile-up. A high-energy event is tagged when the difference between two consecutive samples exceeds +4 mV. This method, already employed for the COV detector in NUCLEUS [90], ensures 100% trigger efficiency for the pulses of interest in this analysis. The amplitude in millivolts of all events triggered by the bin-to-bin analysis is then extracted using the Optimum Filter (OF) amplitude. A software threshold of 15 mV is then applied, corresponding to an energy of 20 keV based on the calibration curve shown on left of the Figure 8.17 (see Section 8.5.2).

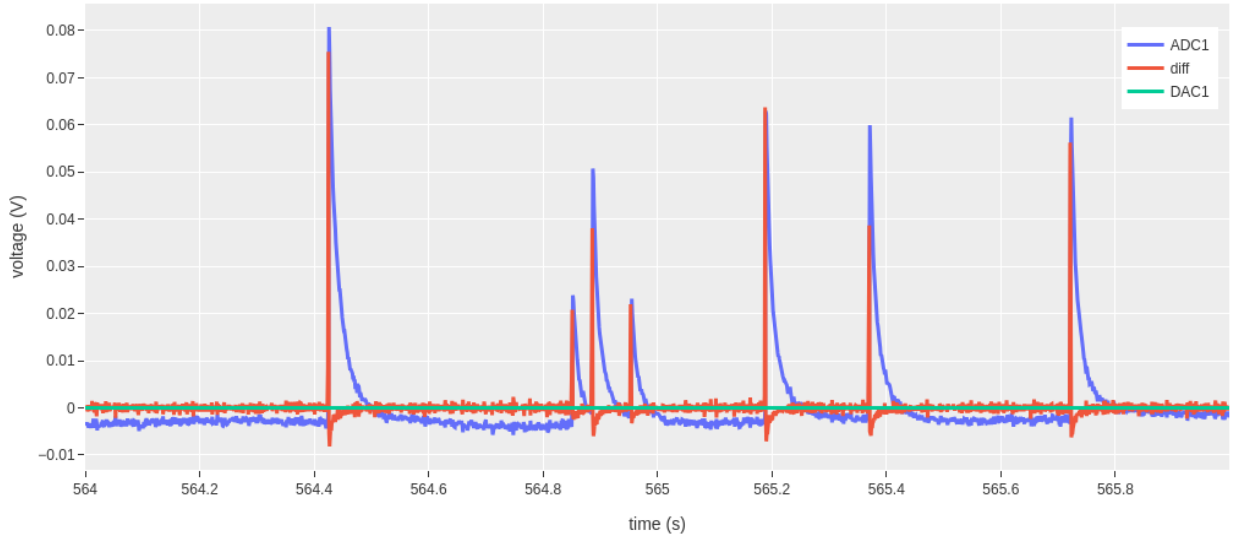

Figure 8.14. $CaWO_4$ stream sampled at 10 kHz showing pulses and pile-up events. The red curve corresponds to the differentiated blue stream, after downsampling to 1 kHz. Sharp transitions in the red signal clearly indicate the occurrence of pulses, even in the presence of pile-up.

Figure 8.15 shows the time evolution of the event rate recorded during one full day of reactor operation at full power (7 hours), followed by three days with the reactor turned off. The data (black points) are binned in 30-minute intervals. A clear rise in the event rate is observed during the reactor ON period, followed by an exponential-like decay once the reactor is shut down.

The data are fitted with a model consisting of four main contributions and three free parameters. The first contribution corresponds to the beam-induced event rate from neutron captures in the $CaWO_4$ crystal and surrounding materials, as predicted by the TOUCANS simulation (blue curve) [194]. This component scales with the neutron flux ϕ_n, which is the first fit parameter. The second contribution arises from the production of unstable ^{187}W isotopes within the crystal, created by neutron capture on ^{186}W. These isotopes undergo β-decay with a half-life of 23.8 hours, leading to an activation-deactivation curve (orange). This contribution is modeled using the FISPACT code [237], based on the recorded reactor power history, and also scales with ϕ_n. In addition to these beam-related components, two background sources are included in the model. First the ^{41}Ar activation (pink curve), whose time evolution was extracted from dedicated measurements in a BaF_2 detector (see right panel of Figure 8.10) and rescaled by a second fit parameter K_{Ar}. Finally a constant background rate R_{off} (green curve), accounts for ambient radioactivity unrelated to reactor operation. This constitutes the third parameter of the model.

The complete model, shown in red in Figure 8.15, demonstrates excellent agreement with the data. The best-fit yields a χ^2 value of 150.4 for 137 degrees of freedom (p-value = 0.20), indicating a statistically acceptable fit. The extracted parameter values are: $\phi_n = (441.8 \pm 1.7)$ cm^{-2}s^{-1}, consistent with the direct neutron flux measurement of $\phi_{exp} \approx (469 \pm 47)$ cm$^{-2} \cdot$ s^{-1}; $K_{Ar} = (1.25 \pm 0.06) \times 10^{-3}$, which is on the same order as the surface area ratio between the BaF_2 and cryogenic detectors; and $R_{off} = (72.6 \pm 0.8) \times 10^{-3}$s^{-1}, representing the ambient background level. This excellent agreement between data and simulation confirms our understanding of both the signal and background components. Additionally, I performed a rate scan by varying the neutron beam intensity using boron attenuators placed in the primary beam. The measured event rate exhibited an affine dependence on the beam intensity. The extrapolated event rate at zero beam intensity matches the expected contributions from ^{41}Ar activation and the constant background R_{off}, further validating the robustness of the model.

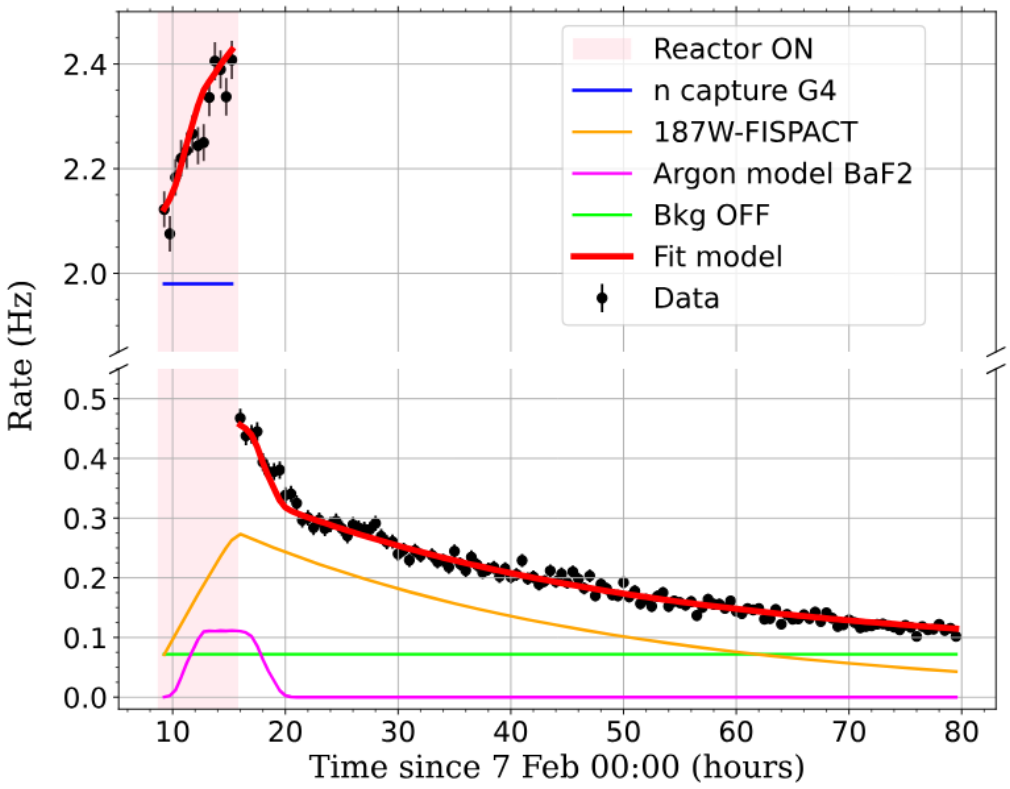

Figure 8.15. The black points represent the measured event rate above 20 keV over time, recorded during a 7-hour period of reactor operation at full power (red shaded area), followed by a 3-day reactor-off phase. A model with only three free parameters provides an excellent fit to the data (red curve). The colored lines indicate the four individual contributions to the model: the prompt beam-induced rate at full reactor power (blue), the delayed component from the activation and subsequent decay of ^{187}W (orange), the ^{41}Ar activation model (magenta), and a constant background from ambient γ-radiation during reactor-off periods (green). See the main text for details on the fit parameters and modeling. Figure from [193].

8.5.2 Spectrum analysis

From the traces recorded for each trigger identified in the differentiated stream, a standard analysis as described in Section 4.3 is performed, yielding the raw spectrum displayed on the left of Figure 8.16. Several peaks are observed, resulting from low-energy γ or conversion electrons produced by the de-excitation of low-lying states in tungsten isotopes interacting within the crystal. While conversion electrons always deposit all their energy in the crystal, γ can either fully deposit their energy through the photoelectric effect or escape the crystal. In addition, X-rays may be emitted following internal conversion, when vacancies in inner atomic shells are filled. The resulting spectrum is a combination of all these contributions, as simulated with GEANT4.

Each peak exhibits a noticeable left-sided tail. Further investigation revealed that these tail events correspond to pulses occurring on a slowly decaying baseline caused by preceding pulses. This leads to an underestimation of the optimum filter amplitude due to improper baseline subtraction. Simulations of such pulses on the data stream confirmed that mild pile-up produces this left tail. To address this, a data cleaning procedure is applied to remove these misreconstructed pulses. First, a cut requires a single pulse per trace and a flat baseline prior to the trigger to eliminate pile-up events. Second, a cut based on the RMS of the optimum filter is applied. The resulting cleaned spectrum is shown in orange on the left of Figure 8.16. This cleaning leads to a non-negligible

loss of events, leading to a cut inefficiency. A procedure implemented in CAIT [157] allows for the simulation of physical pulses with known amplitudes directly on the stream, on which the same cuts are then applied. This yields the survival probability as a function of pulse amplitude (see right of Figure 8.16). The estimated cut efficiency is constant at 0.58 ± 0.02 and shows no dependence on the pulse amplitude (i.e energy). The energy spectrum is corrected for this cut efficiency.
A background spectrum is estimated from reactor-OFF data taken during a period in which the decay rate of ^{187}W is similar to the mean decay rate observed during the reactor-ON period. This reference period corresponds to the time interval between 28 h and 32 h in Figure 8.15. This spectrum, shown in grey in the left panel of Figure 8.16, is subtracted from the data spectrum. It originates from interactions of ambiant γ-rays and β electrons from ^{187}W.

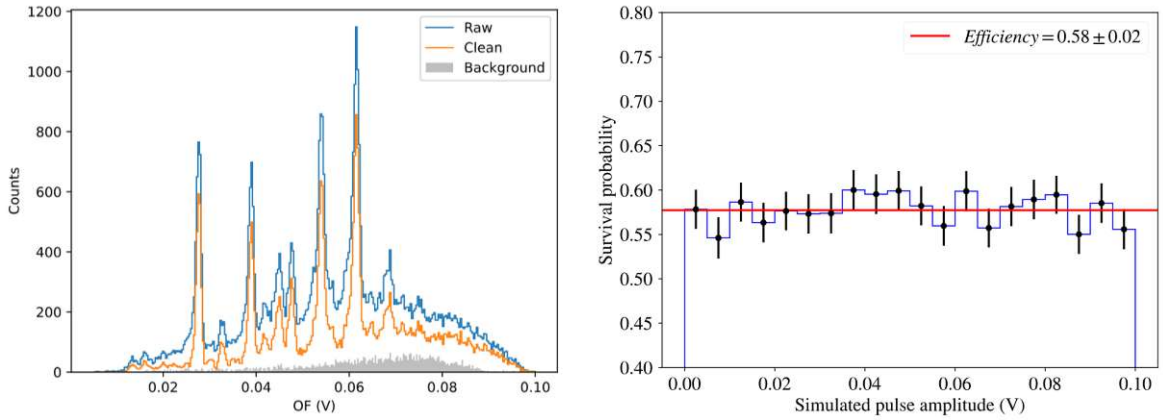

Figure 8.16. Left: Raw (blue) and cleaned (orange) deposited energy spectra in the $CaWO_4$ cube showing several electron conversion lines. Also shown is the background spectrum (grey). Right: Cut efficiency versus pulse amplitude.

The final step is to calibrate the spectrum. The observed peak structure closely matches the predicted simulated spectrum in both the number of peaks and their relative intensities. An ad hoc alignment between the predicted and measured peak positions yields the energy scale in the left panel of Figure 8.17. The calibration deviates from linearity due to the high operating point in the TES transition curve between the superconducting and normal phases. To confirm this calibration curve, an independent calibration was performed using an intense 3 GBq ^{241}Am source placed outside the cryostat, providing a reference point at 59.5 keV. The corresponding peak position in millivolts is obtained by fitting the measured ^{241}Am spectrum (see right panel of Figure 8.17). Two peaks are visible in the spectrum; the first was confirmed to correspond to the 59.5 keV line by conducting an attenuation measurement through a 5 cm polyethylene (PE) block. The observed attenuation factor was consistent with that expected for 59.5 keV rays, confirming the peak's origin. Additionally, complementary measurements were carried out using a NaI crystal. The first measurement, taken with the source placed away from the cryostat and its dewar, detected the 59.5 keV peak. A second measurement, with the NaI crystal placed inside the dewar, reproduced the second, higher-energy peak. This confirmed its origin as gamma interactions in the surrounding materials. The position of this point was found in good agreement with the calibration curve. This calibration curve is then applied to the dataset to convert reconstructed amplitudes from volts to energy in keV. The simulated spectrum is then convolved with a Gaussian resolution function, with the resolution width fitted to the experimental peak widths. The resulting comparison shows excellent agreement between the measured and predicted spectra as observed on left of the Figure 8.18, thereby validating our simulation of the de-excitation cascades.

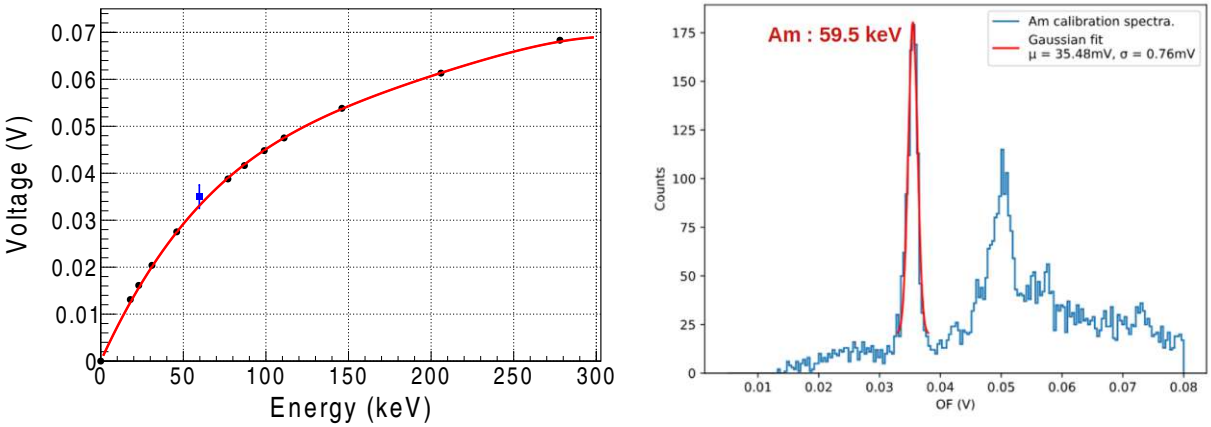

Figure 8.17. Left: Correspondance between the measured positions (in volts) of the 11 most intense peaks and their corresponding energies as predicted by the simulation (black points). A 4th-degree polynomial, constrained to pass through the origin, is used as an effective calibration curve (red line), achieving percent-level precision across all points. The blue point represents an independent calibration using a 59.5 keV γ-ray from a ^{241}Am source. Figure from [193]. Right: Independent calibration using the 59.5 keV γ-ray line from a ^{241}Am source. The peak position is extracted via a Gaussian fit and shows excellent agreement with the calibration curve derived from the simulated peaks (left panel).

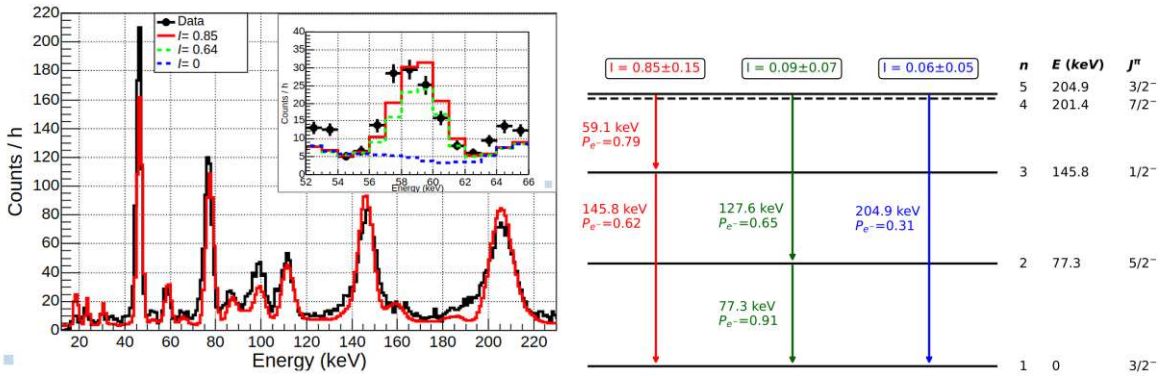

Figure 8.18. Left: Background-subtracted energy spectrum measured with the $CaWO_4$ detector (black points), compared to the simulation prediction (red curve). The inset shows a zoom on the 59.1 keV peak, which was initially absent from the simulation (dashed blue curve). Incorporating the updated decay scheme of ^{187}W (right panel) resolves this discrepancy, resulting in improved agreement (red curve). Right: Updated decay scheme of the fifth excited state of ^{187}W, derived from comparison between the experimental spectrum and the simulated one. Spin, parity, and energy values are provided for each nuclear level. Three decay branches are shown, each with a relative intensity I. The internal conversion probabilities P_{e^-} (i.e., emitting a conversion electron instead of a γ) are also provided. Figures from [193].

Initially, the peak observed around 60 keV in the measured data was not reproduced in the simulated spectrum (blue spectrum in the inset of Figure 8.18). After reviewing the nuclear database RIPL-3 [177], which was used as input for FIFRELIN, we identified the origin of the discrepancy. One de-excitation of the fifth excited state of ^{187}W (204.9 keV, $3/2^-$) to the ground state consists of a cascade of two γ: one at 59.1 keV and another at 145.8 keV. The right panel of Figure 8.18 shows the decay scheme of the fifth excited state of ^{187}W. The additional peak at 59.1 keV in the measured data can be interpreted as events where the 145.8 keV γ escapes the cryogenic detector while the 59.1 keV γ is fully absorbed. However, due to a lack of experimental data, the

branching ratio for this decay path was set to zero in the nuclear database. We propose the following updated transition probabilities from the fifth excited state of ^{187}W which provide the best agreement between the measured and simulated spectra:

$$I^{5\to3}_{59\text{ keV}} = 0.85 \pm 0.15$$
$$I^{5\to2}_{127\text{ keV}} = 0.09 \pm 0.07$$
$$I^{5\to1}_{205\text{ keV}} = 0.06 \pm 0.05$$

8.5.3 First coincidence data

The 10-100 keV events discussed in the previous sections originate from neutron captures whose de-excitation also involves the emission of a primary γ with energy in the MeV range, escaping the cryodetector. It is therefore possible to detect this high-energy γ in the surrounding BaF_2 detector array. We used this configuration to test the coincidence detection between low-energy particles depositing energy in the cryodetector (electrons or γ rays from the de-excitation cascades) and the primary high-energy γ rays detected by the BaF_2 array. These coincidence events are analogous to the ones ultimately targeted in the experiment between a low-energy pure nuclear recoil and a high-energy γ. As such, they serve as a key validation of both the synchronization between the two data acquisition systems and the overall detection efficiency of the BaF_2 array using physical coincidence signals. According to simulations, an energy window of 3.5 to 6.0 MeV in the BaF_2 detectors was found to be optimal for this study. This choice balances the expected rate of γ from signal events and the rate of accidental coincidences, the latter being dominated by ambient background and estimable from the BaF_2 single-event spectrum.

Figure 8.19 shows the distribution of time differences between cryodetector events in the 10–300 keV range and BaF_2 events in the 3.5–6.0 MeV range. A clear coincidence peak is observed above a flat background of accidental coincidences, the level of which agrees with the expected accidental rate calculated from the product of the individual event rates in BaF_2 and the coincidence time window. The coincidence peak is well described by a Gaussian fit with a standard deviation of 80 μs, consistent with the time jitter measured with the second pulser generator (see Section 8.4.4). The peak appears shifted by 582 μs relative to the synchronization established by the pulser signal. This time offset is attributed to delays introduced by the SQUID readout electronics, which the pulser signal does not pass through during synchronization procedure.

The excess of true coincidences over accidentals has a high statistical significance, exceeding 20 σ. The ability to detect such coincidences constitutes a major validation of the experimental setup and paves the way for high-precision measurements using γ-tagging. The measured coincidence rate is (1300 ± 61) events over 7 hours. After correcting for the aging-related drop in BaF_2 detection efficiency described in Section 8.4.1, and normalizing to the neutron flux as inferred from the rate analysis, the predicted rate is 1455 events over 7 hours. The 2.6 σ discrepancy between measurement and prediction may indicate an energy-dependent aging effect in the BaF_2 detectors efficiencies, which will be further investigated through dedicated measurements. Nevertheless, the selection based on coincidence with the emitted γ introduces a non-negligible contribution from accidental coincidences. This can bias the coincidence spectrum measured in the cryodetector. In Appendix C, I propose a simple analytical method to correct the coincidence spectrum by subtracting the contribution from accidental coincidences.

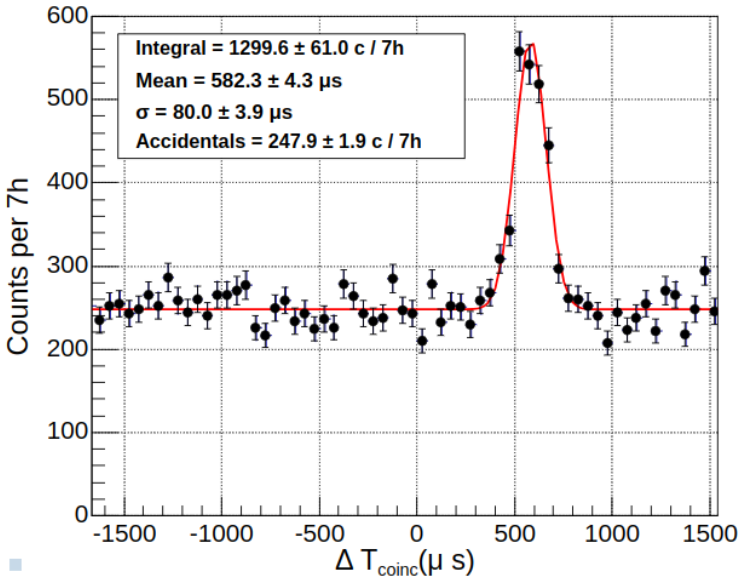

Figure 8.19. Distribution of the time difference between events in the cryogenic detector in the 10–300 keV range and events in the BaF_2 detectors in the 3.5–6.0 MeV range. Figure from [193].

8.6 Future of CRAB

Although the CRAB peak was not observed during the Vienna measurements, the results presented in this chapter are encouraging and point to a promising future for the CRAB project. Hardware upgrades carried out in 2025 aim to enable high-precision measurements on various target materials, including $CaWO_4$, Al_2O_3, and Ge.

8.6.1 Hardware improvements

Several hardware improvements have recently been implemented, with the main goal of achieving low energy resolution, which is essential for observing the CRAB peaks. Simulations have shown that an energy resolution in the range of 5–10 eV (or even below) is required to perform high-precision measurements in $CaWO_4$. To reach this resolution, efforts are focused on reducing electronic noise, notably by working on the grounding scheme and shortening the cable length between the cryostat and the acquisition rack, which will be relocated closer to the cryostat. As shown in the left panel of Figure 8.20, a μ-metal magnetic shield has been installed around the cryostat to mitigate ambient magnetic fields, which can interfere with the detector readout system, particularly the TES stabilization and SQUID readout. Additionally, a LED system—similar to the one used in the NUCLEUS experiment and described in Section 4.4.1 has been installed. The right panel of Figure 8.20 shows a picture of the optical fiber through which the LED delivers light pulses containing several photons toward the cryodetector. This system enables electronic recoil calibration of the detector [153]. Since the detector response differs between electronic (ER) and nuclear recoils (NR), performing CRAB calibration in parallel with LED calibration allows for an ER-NR inter-calibration. This inter-calibration is of major importance, as we aim to calibrate cryodetectors that will be deployed at various experimental sites for physics measurements. The LED system is portable, making it suitable for consistent ER calibration across different setups. Thanks to the ER-NR inter-calibration performed in Vienna, it becomes possible to translate the ER calibration into the NR energy scale, even at sites where only LED calibration is possible.

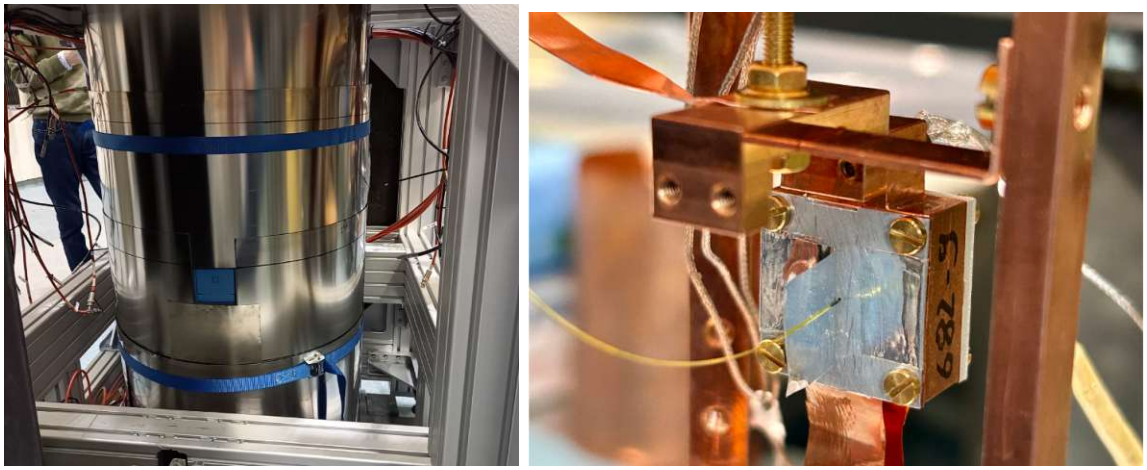

Figure 8.20. Left: μ-metal shielding installed around the cryostat dewar to mitigate ambient magnetic fields (Credits: S.Dorer). Right: Installation of an optical fiber connecting the cryodetector to an LED source for electronic recoil calibration (Credits: C.Doutre).

8.6.2 Perspectives: High precision measurement

The next cooldown is scheduled for Autumn 2025, during which we plan to carry out high-precision measurements with both $CaWO_4$ and Al_2O_3 detectors. As discussed in Section 5.6, the $CaWO_4$ crystal is particularly suited for studying defect formation induced by nuclear recoils. A linearity study based on the three calibration peaks could help probe the underlying mechanisms of defect creation and provide experimental validation for molecular dynamics simulations reported in [175]. Understanding this aspect of the detector response is essential, as it can lead to distortions in CEνNS or dark matter recoil energy spectra [197, 198].
As for the Al_2O_3 detector, a more precise measurement of the spectrum is expected to highlight, in addition to the CRAB single-γ peak, the structure observed around 570 eV (see Figure 5.9). This feature arises from a timing effect in slow 2-γ nuclear transitions. Its amplitude results from the interplay between the time it takes for the nuclear recoil to stops in the material and the emission time of the second gamma. As such, it offers a valuable probe of nuclear recoil stopping times in matter.
We also aim to apply the CRAB method to a germanium detector. Germanium, as a semiconductor material, offers the distinct advantage of enabling simultaneous heat and ionization readout. Such detectors are widely used in cryogenic experiments, leveraging the ionization signal to discriminate between ER and NR. However, in the sub-keV energy range, the ionization yield of nuclear recoils drops significantly. There is currently no consensus on whether this ionization yield vanishes entirely or not. The ratio of ionization energy for a nuclear recoil to that of an electronic recoil of same energy is known as the quenching factor. Figure 8.21 summarizes the current status of quenching factor measurements. While the Lindhard model provides a good description of data above a few keV, experimental results in the sub-keV range show discrepancies: some datasets remain consistent with the model, while others suggest a significant deviation. As a result, the ionization yield remains uncertain in this energy regime. Since the ionization signal is critical for particle identification and background rejection, this uncertainty has a significant impact on the sensitivity of germanium-based experiments searching for sub-keV nuclear recoils induced by CEνNS or low-mass dark matter interactions. Recently, the RICOCHET and TESSERACT experiments—both experts in germanium detector technology—joined the CRAB collaboration. They are currently preparing a germanium detector with dual heat and ionization readout, which is planned to be deployed within the CRAB setup in 2026. The CRAB method provides several monoenergetic nuclear recoil lines in the sub-keV range. Combined with γ-tagging, this allows the extraction of up to four nuclear recoil calibration peaks, enabling the measurement of the ionization yield and the determination of the quenching factor (see Section 7.3).

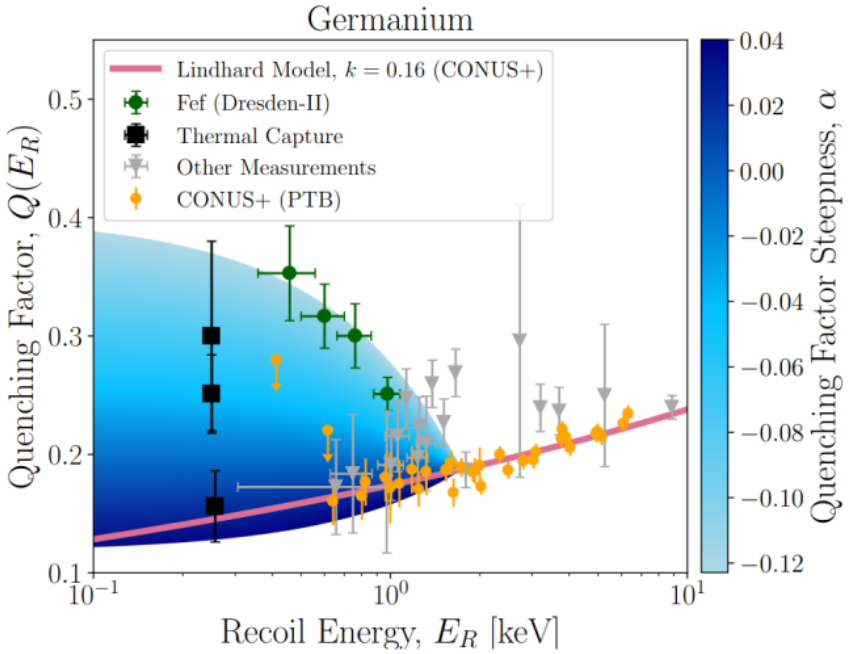

Figure 8.21. Parametrization of the germanium quenching factor between 100 eV and 10 keV. The Lindhard model prediction is shown as the solid pink curve. Measurements based on neutron capture reactions are represented by black points [188]. Results from neutron scattering experiments conducted by the CONUS+ collaboration are shown in orange [66], and exhibit good agreement with the Lindhard model. Finally, data obtained using an iron filter (FeF) technique are shown in green and suggest a higher quenching factor in the sub-keV range [173]. This compilation illustrates the current uncertainties in the quenching factor below 1 keV, where experimental results diverge significantly and no consensus has yet been reached. Figure from [238].

Conclusion

Following the hypothesis of a new neutrino–matter coupling via neutral current interactions — namely, coherent elastic neutrino–nucleus scattering (CEνNS) — proposed by Freedman, and its first observation by the COHERENT collaboration in 2018, significant efforts have been made to measure this process near nuclear reactors. Reactors provide an intense flux of low-energy neutrinos (below 10 MeV), ensuring the conditions for a coherent scattering. Measuring the reactor neutrinos offers a way to test the Standard Model at low energies and potentially probe new physics.

NUCLEUS is one of the experiments aiming to detect CEνNS from reactor neutrinos. It will be installed at the Chooz nuclear power plant this year and benefits from cryogenic detectors that can achieve extremely low energy thresholds. This enables the detection of very low-energy nuclear recoils (NR) induced by CEνNS. In addition to the challenge of detecting such low-energy nuclear recoils, NUCLEUS must also overcome the difficulty of suppressing backgrounds at the shallow overburden of the VNS, down to just a few events per week, in order to observe the rare CEνNS process. A blank setup was assembled in Munich to conduct a First Commissioning Run (FCR), with the goal of validating the simultaneous operation of all NUCLEUS components and demonstrating part of the background rejection.

The first part of this thesis focuses on validating the background mitigation strategy of the NUCLEUS experiment, which relies on both passive and active shielding systems, such as the Muon Veto and the Cryogenic Outer Veto (COV). My work involved the development and commissioning of the Muon Veto, including its hardware implementation and the analysis of its performance. During the First Commissioning Run (FCR), the measured muon rate exhibited excellent time stability and showed good agreement with simulation predictions. By exploiting coincidences with the COV during the FCR, the muon rejection power of the Muon Veto was quantified, yielding a detection efficiency of 98.6% , meeting specifications and ensuring efficient suppression of muon-induced background. This result contributed to reducing the background rate in a $CaWO_4$ cryodetector to below 1000 d.r.u. in the keV energy range, close with the expected values for the FCR setup. As part of this effort, I conducted the background analysis in the $CaWO_4$ cryodetector. These results provided a green light for relocating the NUCLEUS experiment to the VNS site.

The Muon Veto modules were the first components to be installed at the VNS, where they measured an on-site muon rate of 312 Hz, corresponding to a dead time of 7.2%. A technical run is scheduled including a minimal detector configuration to characterize the VNS background with 4 $CaWO_4$ target crystals instrumented by double TES (totaling 7 g of active mass).

Once CEνNS has been measured, the next step will be to search for deviations in the shape of the recoil spectrum that could hint at new physics. To conduct such a study, a precise understanding of the detector response to low-energy nuclear recoils is essential, which requires dedicated calibration. Standard calibration methods using LEDs or X-ray sources primarily induce electronic recoils and therefore do not accurately reproduce the cryodetector's response to nuclear recoils. It would lead to significant biases in the energy scale, strongly impacting the sensitivity to new physics. A low-energy nuclear recoil calibration is thus required — and this is exactly what the CRAB method addresses.

The second part of this thesis focuses on the CRAB method, which aims to precisely calibrate the response of cryodetectors to low-energy nuclear recoils. The principle relies on radiative neutron capture in the target crystal: the emission of a gamma ray by an excited nucleus is associated with a nuclear recoil of approximately 100 eV. Simulations of gamma-ray cascades in materials commonly used in cryogenic detectors — namely $CaWO_4$, Al_2O_3, Si, and Ge — were performed using the FIFRELIN code. Combined with simulations of displacement cascades resulting from the nuclear recoil, this allowed the determination of the resulting recoil energy spectra in these materials. These results were promising, as they revealed the presence of several nuclear recoil calibration

lines in the sub-keV energy range for all those materials.

The CRAB method has been validated twice using a portable neutron source thermalized with polyethylene: first with a $CaWO_4$ target in 2022, and then with an Al_2O_3 target in 2024, each showing a calibration peak at 112 eV and 1.14 keV, respectively. However, a significant background originating from fast neutron scattering limited the precision of the measurements.

To overcome this limitation, a dedicated CRAB facility has been deployed at the Atominstitut in Vienna, near the TRIGA Mark-II research reactor, which provides a pure thermal neutron beam. The goal is to conduct a phase II of the CRAB project under low-background conditions. This thesis presented the design of this phase II setup, with particular emphasis on the use of gamma detectors to exploit gamma–nuclear recoil coincidences. Simulations presented in this work show that such coincidence techniques improve the signal-to-noise ratio and enable the extraction of calibration peaks in materials such as $CaWO_4$ and Ge.

The preparation, installation, and commissioning of this second phase have yielded promising results. Although the energy resolution achieved in Vienna has not yet been sufficient to resolve the CRAB peaks, we were able to validate our understanding of signal and background components, as well as provide an additional validation of our gamma cascade simulations. Notably, this included an update to the decay scheme of ^{187}W. First coincidences between gamma emissions and nuclear cascades in the cryodetector have also been observed, providing experimental validation of my preliminary simulation work that demonstrated the feasibility of detecting such coincidences, thereby confirming the potential of this powerful technique. These results are promising for a high-precision measurement program in the coming months using $CaWO_4$, Al_2O_3, and Ge targets. Each material is expected to exhibit one or more nuclear recoil calibration peaks, allowing sensitivity to different physical effects. The single heat-channel readout of $CaWO_4$ and Al_2O_3 enables distinct studies: in $CaWO_4$, it allows probing the physics of crystal defect creation and the resulting non-linearity in the detector response; in Al_2O_3, it provides access to timing effects associated with specific nuclear transitions. Finally, the dual readout (heat and ionization) of the Ge detector paves the way for a measurement of the quenching factor in the highly debated sub-keV energy range.

A

Working principle of cryostats

This appendix aims to explain the basic operating principles of the cryostats used by the NUCLEUS and CRAB experiments. NUCLEUS employs dry cryostats, while CRAB uses a wet cryostat. These systems mainly differ in how they reach a temperature of around 1 K. However, both are dilution refrigerators to further cool down to the base temperature of approximately 10 mK. I will first describe the principle of wet cryostats and how they reach 1 K using cryogenic liquids. Then, I will explain how dry cryostats achieve similar cooling using a pulse tube instead of liquid cryogens. After that, I will provide a brief overview of the dilution refrigeration system common to both setups.

A.1 Wet cryostat pre-cooling

As the name suggests, a wet cryostat uses cryogenic liquids to achieve cooling. The cryostat is placed inside a dewar, which contains Liquid Helium (LHe). LHe has a boiling point of approximately 4 K, and can therefore cool the cryostat down to this temperature. Since helium is expensive and evaporates quickly during filling, a pre-cooling step is typically performed using liquid nitrogen, which has a boiling point of 77 K. This significantly reduces helium consumption by lowering the temperature of the system beforehand. During the filling process with LHe, the dewar is connected to a helium recovery system, which collects the evaporated helium gas for recycling and reuse. This step is essential to minimize losses. The dewar is filled by inserting a filling tube connected to the Helium can (see left side of Figure A.1).

The cryostat contains a **1 K pot** connected to the dewar through a narrow tube, allowing it to draw liquid helium. This 1 K pot is a small reservoir (see right side of Figure A.1). Using a vacuum pump, one evacuates the gas above the liquid helium in the pot. From thermodynamics, in a closed system, a liquid is in equilibrium with its gas phase at a pressure equal to the saturation vapor pressure $P_{sat}(T)$. Pumping reduces the pressure above the liquid helium, breaking the equilibrium and causing additional helium to evaporate in order to re-establish balance. Since evaporation is an endothermic process, with an enthalpy of vaporization of about $\Delta H_{vap} \approx 0,08$ kJ/mol, the required energy is drawn from the surrounding environment. This cools the system down to approximately 1 K — hence the name 1 K pot. This cooling method has a fundamental limit: as the temperature decreases, the vapor pressure of helium drops exponentially, approaching zero around 1 K. Below this point, helium evaporation becomes negligible, and further cooling through pumping is no longer effective.

This use of cryogenic liquid is constraining because it requires regular refilling. But still, wet cryostats have proven to be able to reach low noise levels and good time stability.

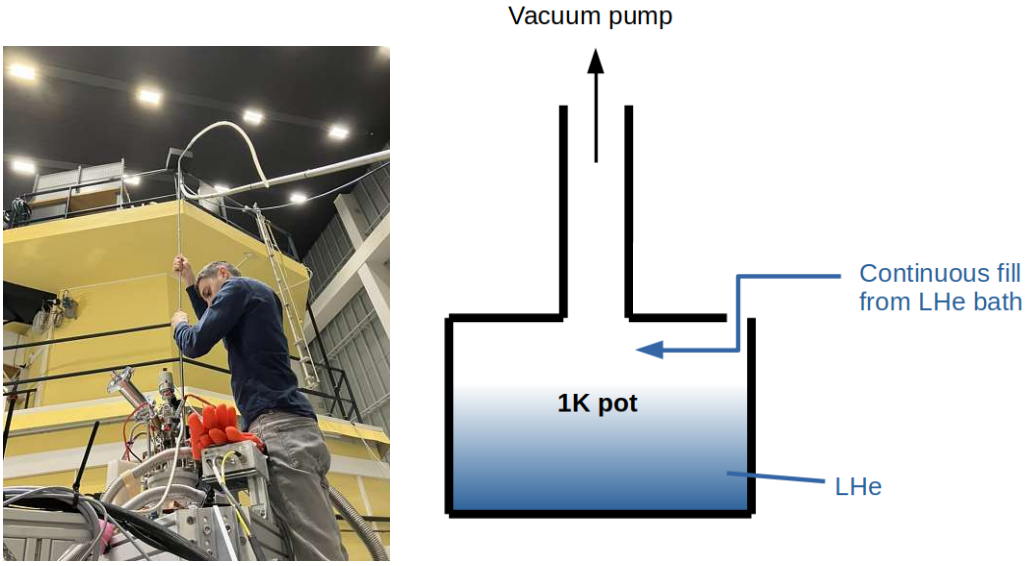

Figure A.1. Left: Picture taken in Vienna during the dewar filling operation with liquid helium. Right: Schematic diagram of a 1 K pot setup showing the helium evaporation forced by a vacuum pump for achieving 1 K.

A.2 Dry cryostat pre-cooling

Dry cryostats don't rely on the use of cryogenic liquid and instead use a pulse tube. A pulse tube is a type of cryocooler used to cool the cryostat down to a few Kelvin (3–5 K). It operates by creating pressure oscillations in a gas, usually helium, using a compressor. These pressure waves travel through the pulse tube, causing the gas inside to undergo successive thermodynamic cycles of compression and expansion. When the gas expands, it absorbs heat from the cold end; when it compresses, it releases heat at the warm end. A regenerator, which is a porous material, is placed before the pulse tube to store and release heat during the pressure changes, improving efficiency. The gas flow and heat exchange are carefully timed so the cold end remains cool while heat is pumped away to the warm end. However, the mechanical vibrations generated by the compressor and the pulse tube can affect the performance of sensitive cryogenic detectors. Thus, to achieve low vibration levels, a vibration decoupling system must be employed. More details can be found in [239, 240].

A.3 Dilution refrigerator

Wet and dry cryostats use different methods to reach temperatures in the Kelvin range. To go even lower, dilution refrigerators rely on the circulation of a mixture of helium-3 (^{3}He) and helium-4 (^{4}He). By pumping on ^{3}He at the still stage, the system can be cooled to significantly lower temperatures than when pumping on ^{4}He, due to the higher enthalpy of vaporization of ^{3}He. This process enables temperatures as low as 0.7 K to be reached.

When the system is cooled below 0.86 K, a thermodynamic phenomenon occurs: the ^{3}He/^{4}He mixture spontaneously separates into two phases — a ^{3}He-rich (concentrated) phase and a dilute phase, as illustrated in the phase diagram in figure A.2. To avoid reviving any potentially painful memories of thermodynamic chemistry, I'll explain the diagram simply: the vertical axis represents temperature, and the horizontal axis shows the concentration of ^{3}He. Below 0.86 K, the diagram clearly shows phase separation, forming the dilute and concentrated branches.

At a fixed temperature T_1, the intersections of a horizontal line with the two branches give the mole fractions of ^{3}He in each phase. For example, at T_1, the dilute phase contains a fraction y_1 of ^{3}He, while the concentrated phase contains x_1. If the temperature is increased to T_2, the fraction in the dilute phase becomes $y_2 > y_1$, and in the concentrated phase $x_2 < x_1$. This indicates that ^{3}He has transferred from the concentrated phase to the dilute phase. We then deduce that the dilution of ^{3}He into ^{4}He is an endothermic process. This is the fundamental mechanism that provides cooling in dilution refrigerators. In fact, the system's cooling power depends on the slope of the branches, which become steeper at lower temperatures, thus improving performance. It is also worth noting that the mole fraction of ^{3}He in the dilute phase never vanishes — even at absolute zero, it remains around 6.4%, a critical aspect of dilution refrigerator operation. A schematic of the circulation circuit is shown in Figure A.3. At the bottom lies the mixing chamber, which contains the two phases: the lighter, ^{3}He-rich concentrated phase at the top, and the denser dilute phase below. The dilute phase is connected to the still, where a pump selectively evaporates ^{3}He (rather than ^{4}He, which becomes superfluid and does not evaporate easily at these temperatures). As ^{3}He is extracted from the dilute phase, its concentration decreases. However, since it cannot fall below 6.4% due to thermodynamic constraints, ^{3}He flows from the concentrated phase into the dilute phase to restore the balance. This flow is driven by an osmotic pressure gradient at the phase boundary, resulting from the ^{3}He concentration difference. This forced dilution of ^{3}He into ^{4}He is what enables the system to reach temperatures as low as 10 mK. In figure 6.2.1.1, we also see that the extracted ^{3}He is returned to the concentrated phase through a series of heat exchangers. The incoming ^{3}He is warm, while the extracted ^{3}He is cold. These thermal couplings between the outgoing and returning flows are crucial, as they pre-cool the incoming ^{3}He before it reaches the cold mixing chamber, increasing the overall efficiency of the cooling process.

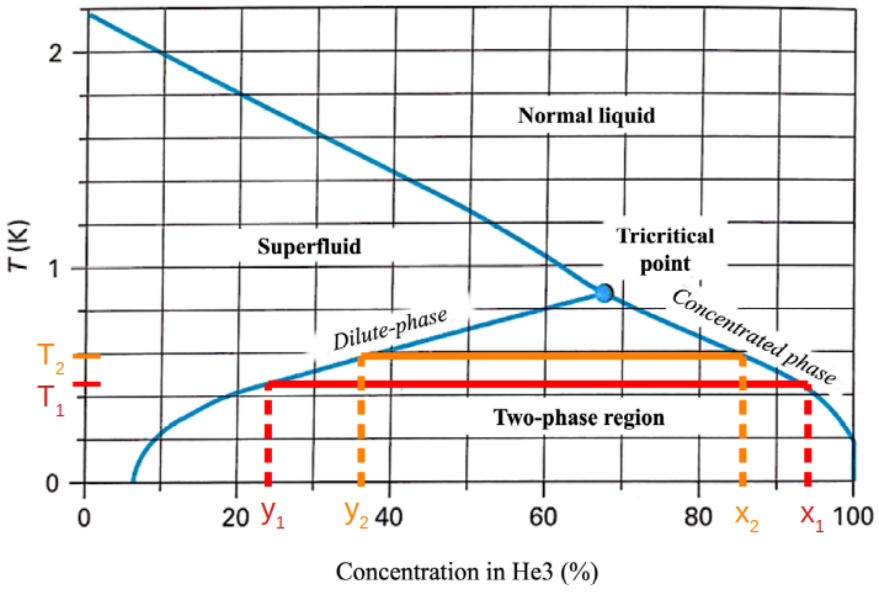

Figure A.2. Phase diagram of ^{3}He/^{4}He mixture. Adapted from [241].

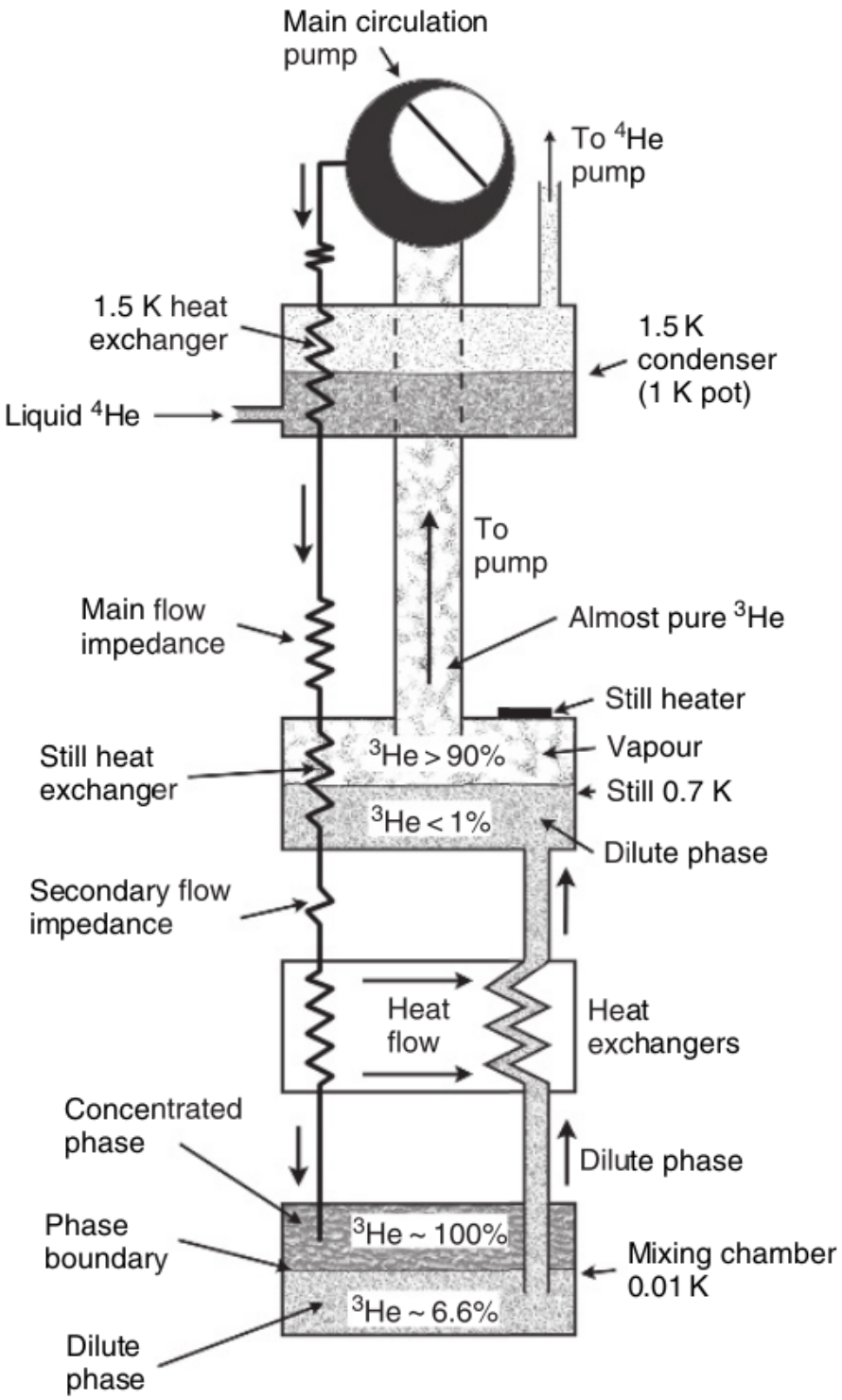

Figure A.3. Scheme of a dilution refrigerator. Figure from [239].

B

Correction for accidental coincidences contribution

As explained in this thesis, when analyzing coincidences between a cryodetector and an external detector, it is possible to look at the coincidence and anticoincidence spectra. The anticoincidence spectrum simply corresponds to the complement of the coincidence spectrum with respect to the single spectrum. The coincidence spectrum includes a contribution from accidental coincidences — that is, events occurring independently in both detectors within the same coincidence time window, without being physically correlated. This appendix aims to provide an estimation of the accidental coincidence spectrum, which can then be subtracted from the measured coincidence spectrum in order to isolate the spectrum of true coincidences, corresponding to physically correlated events detected simultaneously by both systems.

The probability for such an accidental coincidence is given by:

$$P_{\text{acc}} = 1 - \exp(-R \cdot \Delta t) \approx R \cdot \Delta t, \tag{B.1}$$

where R is the background rate in the external detector and Δt is the width of the time coincidence window. The approximation holds for $R \cdot \Delta t \ll 1$.

At first glance, one might think that correcting for accidentals simply consists of subtracting the single spectrum weighted by P_{acc} from the coincidence spectrum. However, this approach overestimates the accidental contribution, since the single spectrum contains some true coincidences — which, by definition, cannot contribute to accidental coincidences. In fact, only events in anticoincidence have a probability P_{acc} of being misclassified as coincidences. Therefore, a more accurate estimation would involve weighting the anticoincidence spectrum by P_{acc}. However, the anticoincidence spectrum we observe in the data is biased, as it is defined as the complement of the coincidence spectrum with respect to the singles. As a result, it underestimates the true number of anticoincidence events, leading again to an inaccurate estimation of accidentals.

To properly estimate the accidental contribution based on the available (biased) coincidence and anticoincidence spectra, Figure B.1 formalizes the problem providing a graphical representation of the situation.

Let us define:

- $N_{\text{CC,true}}$: the number of true (physical) coincidences
- $N_{\text{AC,true}}$: the number of true anticoincidence events
- $N_{\text{CC,data}}$: the number of events reconstructed as coincidences in the data
- $N_{\text{AC,data}}$: the number of events reconstructed as anticoincidences in the data

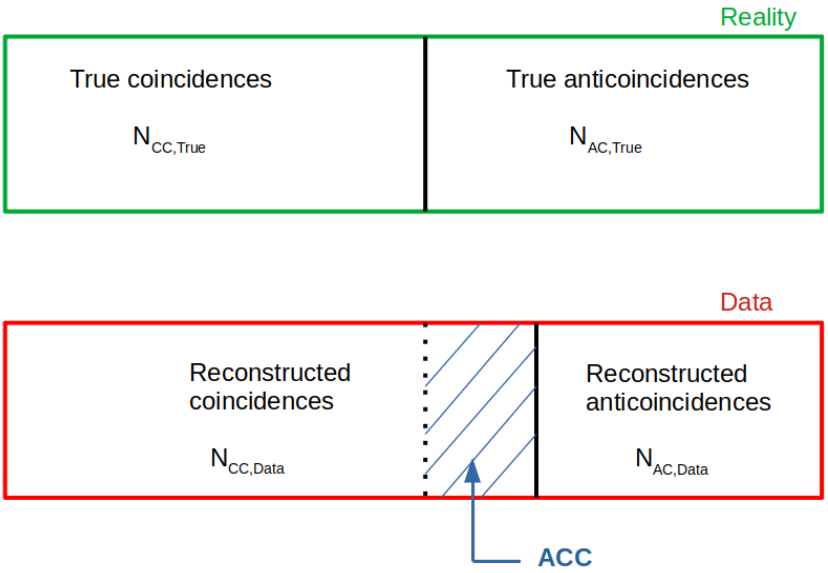

Figure B.1. Illustrative diagram showing, at the top, the true distribution of coincidence and anticoincidence events, and at the bottom, the data as observed — where coincidences encroach on the anticoincidence region due to the contribution from accidentals.

The reconstructed number of coincidences includes both true coincidences and a contribution from accidental coincidences, denoted as *Acc*:

$$N_{\mathrm{CC,data}} = N_{\mathrm{CC,true}} + Acc \tag{B.2}$$

This accidental contribution is given by:

$$Acc = P_{\mathrm{acc}} \cdot N_{\mathrm{AC,true}} \tag{B.3}$$

The total number of events being fixed, we have:

$$N_{\mathrm{CC,true}} + N_{\mathrm{AC,true}} = N_{\mathrm{CC,data}} + N_{\mathrm{AC,data}} \tag{B.4}$$

Substituting $N_{\mathrm{CC,data}}$:

$$N_{\mathrm{CC,true}} + N_{\mathrm{AC,true}} = N_{\mathrm{CC,true}} + Acc + N_{\mathrm{AC,data}} \tag{B.5}$$

$$\Rightarrow N_{\mathrm{AC,true}} = Acc + N_{\mathrm{AC,data}} \tag{B.6}$$

Plugging this into Equation B.3:

$$Acc = P_{\text{acc}} \cdot (Acc + N_{\text{AC,data}}) \tag{B.7}$$

$$\Rightarrow Acc \cdot (1 - P_{\text{acc}}) = P_{\text{acc}} \cdot N_{\text{AC,data}} \tag{B.8}$$

$$\Rightarrow Acc = \frac{P_{\text{acc}}}{1 - P_{\text{acc}}} \cdot N_{\text{AC,data}} \tag{B.9}$$

This final expression provides a reliable estimate of the number of accidental coincidences using only known quantities: the measured number of anticoincidence and the accidental probability P_{acc}. Generalizing this result to the entire energy spectrum, the accidental spectrum can be obtained by weighting the anticoincidence spectrum observed in the data by a factor of $\frac{P_{\text{acc}}}{1-P_{\text{acc}}}$. One can consider the limiting case where $P_{\text{acc}} \to 1$. In this regime, the accidental contribution does not diverge, because simultaneously $N_{\text{AC,data}} \to 0$. In this case, the accidental contribution becomes unresolvable, which is consistent with intuition: when the probability of accidental coincidence approaches 1, the coincidence condition loses its discriminating power, and no meaningful information can be extracted from the coincidence analysis.

C

Résumé en Français

Dans cette thèse, je présente les travaux que j'ai réalisés dans le cadre des collaborations NUCLEUS et CRAB. Ces travaux s'inscrivent dans le contexte de la détection de neutrinos et du développement de détecteurs cryogéniques, notamment en ce qui concerne leur calibration.

Depuis leur première détection en 1956, les neutrinos suscitent un grand intérêt en physique, car ils ont permis de révéler des phénomènes fondamentaux en physique des particules, tels que les oscillations de neutrinos ou la mesure de paramètres du Modèle standard. Le processus de désintégration bêta inverse est historiquement celui utilisé pour détecter les neutrinos. Il nécessite cependant une énergie supérieure à 1,8 MeV et présente une très faible section efficace. Les neutrinos sont en effet réputés pour interagir très faiblement avec la matière.

Une autre interaction, la diffusion cohérente neutrino-noyau (CEνNS), prédite en 1974, n'a été détectée pour la première fois qu'en 2018 par l'expérience COHERENT. La section efficace de ce processus est proportionnelle au carré du nombre de neutrons de la cible, ce qui rend l'utilisation de matériaux lourds très avantageuse pour augmenter le taux d'interaction — de plus d'un ordre de grandeur par rapport à la désintégration bêta inverse. De plus, cette interaction ne possède pas de seuil énergétique, ce qui permet d'explorer la physique du Modèle standard à très basse énergie.

Pour garantir que la diffusion se produise bien dans le régime cohérent — c'est-à-dire que le neutrino interagisse avec l'ensemble du noyau —, il faut des neutrinos de basse énergie (inférieure à 10 MeV). Les neutrinos de réacteur, abondants dans ce régime, sont donc des candidats idéaux. Lors d'une interaction CEνNS, le neutrino transfère une partie de son énergie au noyau, produisant un recul nucléaire d'énergie très faible, signature expérimentale de l'interaction. L'utilisation de cibles lourdes maximise la section efficace, mais réduit d'autant plus l'énergie du recul. Deux défis majeurs en découlent : atteindre un seuil en énergie ultra-bas avec une bonne résolution, et assurer une réjection efficace du bruit de fond pour obtenir un rapport signal/bruit proche de l'unité. Les enjeux sous-jacents à la détection de CEνNS sont détaillés dans le chapitre 1.

Le chapitre 2 est consacré à la collaboration NUCLEUS, qui utilise des détecteurs cryogéniques de très petit volume, capables d'atteindre des seuils de détection extrêmement bas. La cible choisie est le tungstène, un élément riche en neutrons, afin de maximiser la section efficace du processus CEνNS. Ces détecteurs, de quelques millimètres cubes, fonctionnent comme des calorimètres : l'énergie déposée par un recul nucléaire se traduit par un échauffement. Refroidis à une température d'environ 10 mK, leur capacité calorifique devient quasi nulle, ce qui amplifie la variation de température pour un dépôt d'énergie donné.

À la surface de ces cryodétecteurs se trouve un capteur à transition supraconductrice (TES) qui mesure ces élévations de température. Ce capteur, maintenu à sa température critique, voit sa résistance varier fortement (de quelques mΩ) pour une élévation de température de l'ordre du μK. Cette variation est mesurée à l'aide de SQUIDs (Superconducting Quantum Interference Devices).

Appendix C. Résumé en Français

NUCLEUS sera installé à proximité des réacteurs de la centrale nucléaire de Chooz, dans les Ardennes (France). Ce site, situé en surface, est exposé à de nombreuses sources de bruit de fond. Les neutrons atmosphériques, par exemple, peuvent produire des reculs nucléaires indiscernables de ceux induits par les neutrinos. Des blindages passifs, tels que des couches de polyéthylène et de plomb, sont utilisés pour atténuer respectivement les neutrons et les rayonnements gamma. Les muons cosmiques représentent une autre source de bruit : ils peuvent induire des réactions de spallation dans les blindages, produisant des neutrons rapides susceptibles d'interagir avec les détecteurs. Pour limiter tous ces événements, des système de veto actifs sont utilisés : le Muon Veto et le Cryogenic Outer Veto (COV). J'ai été particulièrement impliqué dans le développement du Muon Veto, dont les détails sont présentés au chapitre 3.

Ce système est constitué de 28 panneaux de scintillateurs formant un cube entourant le détecteur. Lorsqu'un muon traverse un panneau, il produit de la lumière acheminée vers des SiPMs via des fibres optiques. Ce signal lumineux permet de déclencher un veto : tout événement détecté dans les cryodétecteurs dans une fenêtre inférieure à 240 μs autour du passage du muon est rejeté.

Cette thèse présente les tests de réponse de chaque panneau et la calibration des SiPMs. Nous avons notamment vérifié que les distributions d'énergie déposée par les muons se distinguaient nettement de celles des γ ambiants, condition nécessaire pour bien définir un seuil de détection. En décembre 2022, le Muon Veto a été installé au laboratoire souterrain (UGL) de l'Université technique de Munich, dans le cadre d'un montage à blanc de l'expérience. Son fonctionnement a montré une grande stabilité sur plusieurs semaines, en accord avec les variations de pression atmosphérique. Les données collectées se sont révélées cohérentes avec les prédictions des simulations, tant sur le taux d'événements que sur la forme des spectres. Ces mesures ont permis d'estimer l'atténuation du rayonnement cosmique par la UGL, donnée cruciale pour les simulations de bruit de fond.

Le montage à blanc visait à tester l'intégralité du dispositif expérimental (détecteurs, acquisition, synchronisation, etc.) dans des conditions réalistes de fonctionnement prolongé. Le First Commissioning Run (FCR), mené durant l'été 2024 et présenté dans le chapitre 4, avait plusieurs objectifs : valider individuellement chaque composant de l'expérience NUCLEUS, mais aussi tester leur fonctionnement en coïncidence, notamment entre les détecteurs cryogéniques et les systèmes de veto. Ce test était indispensable pour s'assurer d'une bonne réjection du bruit de fond, condition préalable à l'installation de l'expérience sur le site de Chooz.

La région d'intérêt en énergie (<200 eV) est dominée par un bruit de fond appelé low energy excess, dont l'origine semble liée à des contraintes mécaniques interfaciales. Ainsi, pour le FCR, l'étude de la réjection du bruit de fond a porté sur la région 1–10 keV, permettant de valider l'efficacité des systèmes de veto et de fournir une référence fiable pour les simulations. J'y présente notamment mon travail sur la synchronisation des horloges des différents systèmes d'acquisition et sur les premières études de coïncidence entre le Muon Veto et le COV. Ce dernier, placé au centre du dispositif, est également capable de détecter les muons, ce qui permet de quantifier l'efficacité du veto. En sélectionnant les événements pour lesquels la différence de temps ΔT_{COV-MV} est comprise entre -23.7 μs et -0.3 μs, on obtient une efficacité de coïncidence de 98.6 %, en excellent accord avec la prédiction de 99.0 % issue des simulations. Cette efficacité légèrement inférieure à 100 % s'explique par la présence d'interstices entre les panneaux scintillants du Muon Veto.

Pour évaluer le bruit de fond dans les cryodétecteurs, l'analyse présentée dans cette thèse utilise le logiciel d'analyse CAIT, développé à l'HEPHY (Vienne) pour l'expérience CRESST. L'analyse consiste à trigger les pulses dans le stream et estimer leur amplitude qui constitue une observable de l'énergie déposée. Puis on applique une transformée de Fourier pour extraire les composantes fréquentielles du signal et du bruit. Un filtrage fréquentiel, par la méthode de l'Optimum Filter (OF), permet d'améliorer le rapport signal/bruit, rendant possible la détection de pulses de très faible amplitude, et donc d'atteindre des seuils énergétiques suffisamment bas pour observer les reculs nucléaires induits par les neutrinos (typiquement < 200 eV). L'amplitude des pulses, mesurée en volt, doit ensuite être convertie en énergie. Pour cela, une calibration des détecteurs est nécessaire.

Plusieurs méthodes existent. L'approche standard consiste à utiliser une source de rayons X, par exemple du fer, qui produit un pic de calibration à 5.9 keV. Cependant, cette méthode remplit une région en énergie dans laquelle on souhaite précisément mesurer le bruit de fond ; elle n'a donc pas été utilisée pour le FCR. À la place, nous avons utilisé des LED capables de générer des pics de calibration dans une large gamme d'énergie (quelques centaines d'eV à 10 keV). Cette méthode présente l'avantage de pouvoir être mise en œuvre lors de courtes sessions de calibration intégrées au planning de l'expérience. Lors du FCR, deux cryodétecteurs ont été testés : un en $CaWO_4$ et un en Al_2O_3. L'analyse présentée dans cette thèse se concentre exclusivement sur la cible en $CaWO_4$. Le taux de bruit de fond mesuré dans ce détecteur était de 2951 ± 202 événements/kg/keV/jour. Après application de l'anticoincidence avec les systèmes de veto (COV et Muon Veto), ce taux est descendu à 868 ± 88 événements/kg/keV/jour. Si l'efficacité de réjection par les systèmes de veto est en bon accord avec les simulations, le taux global mesuré reste supérieur d'un facteur 1.7 par rapport à celui prédit. Cette différence, bien que significative, reste acceptable, et suggère la présence d'effets non pris en compte dans la simulation. Elle constitue en cela une information précieuse pour affiner et ajuster les simulations. Malgré tout le FCR a été une réussite et a validé en partie la rejection de bruit fond et a donné le feu vert pour le déménagement de NUCLEUS à CHOOZ. Le Veto Muon et les blindages ont été les premiers éléments déplacés à Chooz pour un commissioning.

Le deuxième volet de ma thèse porte sur la calibration des cryodétecteurs à l'aide de la méthode CRAB. Alors que les méthodes standards, telles que l'utilisation de sources X ou de LED, permettent de calibrer les reculs électroniques (ER), le signal recherché dans notre cas est un faible recul nucléaire (NR). La réponse des détecteurs diffère fortement entre ER et NR, en raison des mécanismes de dépôt d'énergie très distincts pour ces deux types d'interactions. Il est donc essentiel de calibrer spécifiquement les reculs nucléaires. Toutefois, la calibration des NR à basse énergie constitue un véritable défi, que la méthode CRAB vise précisément à relever.

Le chapitre 5 présente la méthode CRAB, qui repose sur la capture radiative de neutrons. Un isotope constituant la cible du détecteur peut capturer un neutron thermique, ce qui le conduit dans un état excité. Lors de sa désexcitation, il émet un γ d'une énergie de quelques MeV. Par conservation de la quantité de mouvement, le noyau subit un recul dont l'énergie est fixée par la cinématique à deux corps. Ce processus génère ainsi un pic de calibration bien défini dans la région sub-keV.

Dans ce chapitre, je présente plusieurs simulations de la méthode CRAB, dans lesquelles un faisceau de neutrons thermiques est dirigé vers différents matériaux cibles couramment utilisés en détection cryogénique : $CaWO_4$, Al_2O_3, Ge et Si. L'objectif est d'étudier l'intensité des pics de calibration par rapport au continuum des reculs nucléaires induits par des cascades de désexcitation multi-γ, qui constituent une source majeure de bruit de fond. Il est donc crucial de simuler correctement ces cascades. Pour cela, le code FIFRELIN est utilisé : il reconstruit le schéma de niveaux de chaque isotope à partir de données nucléaires expérimentales et de modèles théoriques, détermine les rapports d'embranchement des transitions ainsi que leur durée de vie, et reproduit fidèlement les cascades de désexcitation.

L'énergie du recul nucléaire associée à une transition multi-γ dépend du timing de la cascade. Elle résulte d'une relation subtile entre le temps de ralentissement du noyau dans la matière et le temps d'émission des γ secondaires, tertiaires, etc. Le code IRADINA permet d'estimer l'énergie des reculs nucléaires correspondant à chaque cascade prédite par FIFRELIN. Les simulations révèlent que certaines transitions dites « lentes », pour lesquelles la durée de vie des niveaux intermédiaires est plus longue que le temps d'arrêt du recul nucléaire, génèrent des pics de calibration additionnels, notamment dans les cibles en Al_2O_3 et Ge.

Le $CaWO_4$ se révèle être un matériau particulièrement favorable, ses trois isotopes fournissant des pics de calibration à 81 eV, 112 eV et 160 eV. Bien que le pic à 81 eV soit rapidement noyé dans le continuum des reculs nucléaires induits par les cascades multi-γ (notamment en raison des limites de résolution énergétique du détecteu), le pic à 112 eV est très intense et relativement facile à identifier. L'Al_2O_3 quant à lui fournit un pic

intense à 1145 eV. Enfin, dans le germanium, les transitions lentes induisent plusieurs pics de calibration situés entre 300 et 600 eV.

Le chapitre 6 porte sur les validations expérimentales de la méthode CRAB à l'aide d'une source portable de neutrons thermalisés dans du polyéthylène. Ce chapitre se concentre sur la validation de la méthode CRAB sur des cibles en $CaWO_4$ et Al_2O_3, qui ont révélé la présence des pics CRAB attendus. Cette campagne de mesures a également permis de valider la performance des cryodétecteurs avant le déménagement du cryostat pour la phase II de CRAB.

Les validations présentées au chapitre 6 souffraient toutefois d'un fort bruit de fond causé par les neutrons rapides non thermalisés dans le polyéthylène. Ce bruit de fond empêchait d'effectuer une calibration de haute précision et limitait la sensibilité à des effets physiques subtils, tels que les effets de timing ou la création de défauts cristallins pouvant affecter la réponse du détecteur. Pour remédier à cela, il a été décidé d'installer un dispositif expérimental à l'Atominstitut de Vienne, en Autriche, dans le cadre de la phase II du projet CRAB. Le réacteur de recherche sur place fournit un flux de neutrons purement thermiques, ce qui permet de supprimer le bruit induit par les neutrons rapides. Le chapitre 7 présente cette phase II, ses intérêts et ses motivations.

En particulier, les simulations réalisées démontrent l'intérêt de détecter le recul nucléaire en coïncidence avec le γ émis, détecté par des détecteurs PARIS. Cette coïncidence permet d'éliminer le continuum induit par les transitions multi-γ et de relâcher la contrainte sur la résolution énergétique des cryodétecteurs pour la détection des pics de calibration. En particulier, cette méthode permet de récupérer le pic à 81 eV pour le $CaWO_4$ et de détecter jusqu'à quatre pics dans le germanium. Ces résultats ont fait l'objet d'un proposal soumis à la collaboration PARIS afin d'obtenir des détecteurs. Cependant, en raison d'une forte demande, nous nous sommes finalement orientés vers des cristaux de fluorure de baryum (BaF_2) issus de l'expérience Château de Cristal. Le dispositif de la phase II consiste donc en un faisceau de neutrons réfléchi vers le cryodétecteur placé dans le cryostat humide. Autour du cryostat sont disposés 28 détecteurs BaF_2 pour assurer la détection en coïncidence des gammas.

Dans le cadre de ma cotutelle avec l'Université technique de Vienne, j'ai passé ma deuxième année à l'Atominstitut pour préparer la phase II de CRAB. La préparation, l'installation et les premières données de commissioning sont détaillés au chapitre 8. Celui-çi commence par la campagne de mesure et de caractérisation du bruit de fond neutronique et gamma sur site. Ce bruit de fond externe, s'il est trop élevé dans les détecteurs BaF_2, peut compromettre la coïncidence γ–recul nucléaire. Cette situation a justifié l'installation de blindages passifs autour du cryostat, composés de briques de plomb et de tapis de bore carboré (B_4C).

Ce chapitre présente également la caractérisation de la réponse des détecteurs BaF_2, incluant leur calibration en énergie et leur efficacité de détection. La calibration a été réalisée en ligne grâce à un pic produit par une contamination interne du baryum par du radium, générant quatre désintégrations alpha. Toutefois, la réponse des détecteurs aux particules alpha étant affectée par le phénomène de quenching, une calibration absolue préalable a été effectuée à l'aide de sources γ telles que le césium, le cobalt et l'AmBe.

Côté cryogénie, après avoir validé le fonctionnement des cryodétecteurs à Munich avec une résolution énergétique inférieure à 5 eV, le cryostat a été transféré à Vienne. Lors du commissioning, deux détecteurs en $CaWO_4$ ont été testés. Malheureusement, la résolution énergétique atteinte n'était pas encore suffisante pour observer le pic CRAB. Cependant, un des cryodétecteurs a fonctionné avec un gain très faible, le rendant sensible à des dépôts d'énergie de plusieurs keV. Cette particularité ouvre la voie à l'étude des cascades de désexcitation multi-γ, notamment celles impliquant un γ de faible énergie ou un électron de conversion de quelques dizaines de keV. À ces énergies, ces événements peuvent déposer l'intégralité de leur énergie dans le cryodétecteur. Les simulations prédisent des lignes de conversion électronique comprises entre 10 et 200 keV.

Cette thèse présente l'analyse d'un run avec faisceau, au cours duquel ces lignes de conversion étaient clairement

visibles. Nous avons même observé un excellent accord en forme entre le spectre d'énergie déposée simulé et celui obtenu expérimentalement. En réalité, un pic de conversion électronique était présent dans les données mais absent du spectre simulé. Ce pic provient d'une branche de désintégration du cinquième niveau excité du ^{187}W, dont le rapport d'embranchement était inconnu dans les bases de données nucléaires et donc non simulé. Nous avons déterminé le rapport d'embranchement correspondant au meilleur accord avec l'intensité observée dans les données. Ce résultat constitue en soi une mesure de ce rapport d'embranchement, susceptible d'être utilisée pour mettre à jour les données nucléaires.

Par ailleurs, j'ai étudié l'évolution du taux d'événements déposant plus de 20 keV dans le cryodétecteur au cours d'une journée de faisceau suivie de trois jours sans faisceau. Le taux, naturellement plus élevé avec le faisceau, montre une légère augmentation jusqu'à l'arrêt du réacteur, puis chute drastiquement et décroît de façon exponentielle durant les trois jours suivants. À partir des simulations, nous avons identifié plusieurs contributions à ces événements de haute énergie et construit un modèle reposant sur trois paramètres de normalisation : la contribution liée au faisceau (gammas de faible énergie et électrons de conversion), l'activation du ^{187}W (émetteur bêta) et le bruit de fond ambiant dû à la radioactivité naturelle et à l'argon de l'air, qui s'active au cours d'une journée de fonctionnement du réacteur. Le modèle dépend notamment du flux neutronique, et nous avons obtenu un excellent accord entre les données et le modèle pour un flux compatible avec une mesure indépendante réalisée à l'aide d'un tube ^{3}He. Ces concordances en taux de comptage et en forme de spectre valident notre compréhension du signal et du bruit de fond, ainsi que la qualité de nos prédictions des cascades réalisées par FIFRELIN.

Enfin, ces événements à haute énergie, résultant de cascades comportant un γ primaire de plusieurs MeV suivi d'un γ secondaire de faible énergie, offrent la possibilité d'effectuer une coïncidence entre le dépôt d'énergie dans le cryodétecteur (dû au γ secondaire) et celui dans les détecteurs BaF_2 (provoqué par le γ primaire). L'étude des temps d'événements dans les deux acquisitions a révélé un pic de coïncidence, validant la synchronisation entre les systèmes.

À la fin de ma thèse, un travail a été initié afin de réduire le bruit électronique et d'améliorer la résolution énergétique, ce qui devrait permettre de détecter le ou les pics CRAB lors des prochaines campagnes expérimentales.

Bibliography

[1] W. Pauli, **Pauli letter collection, https://cds.cern.ch/record/83282**, Typed copy.

[2] J. Chadwick, **Intensitätsverteilung im magnetischen Spectrum der β-Strahlen von radium B + C**, Verhandl. Dtsc. Phys. Ges. **16** (1914) 383.

[3] C.L. Cowan, F. Reines, F.B. Harrison, H.W. Kruse and A.D. McGuire, **Detection of the Free Neutrino: a Confirmation**, Science **124** (1956) 103.

[4] D.Z. Freedman, **Coherent effects of a weak neutral current**, Phys. Rev. D **9** (1974) 1389.

[5] D. Akimov and Albert, **Observation of coherent elastic neutrino-nucleus scattering**, Science **357** (2017) 1123–1126.

[6] D. Akimov and J.B. Albert, **COHERENT 2018 at the Spallation Neutron Source**, 2018, .

[7] N. Ackermann, H. Bonet, A. Bonhomme, C. Buck, K. Fülber, J. Hakenmüller, J. Hempfling, G. Heusser, M. Lindner, W. Maneschg, K. Ni, M. Rank, T. Rink, E. Sánchez García, I. Stalder et al., **Direct observation of coherent elastic antineutrino–nucleus scattering**, Nature **643** .

[8] NUCLEUS Collaboration, **Exploring CEνNS with NUCLEUS at the Chooz nuclear power plant**, The European Physical Journal C **79** (2019) 1018.

[9] L. Thulliez, D. Lhuillier, F. Cappella, N. Casali, R. Cerulli, A. Chalil, A. Chebboubi, E. Dumonteil, A. Erhart, A. Giuliani, F. Gunsing, E. Jericha, M. Kaznacheeva, A. Kinast, A. Langenkämper et al., **Calibration of nuclear recoils at the 100 eV scale using neutron capture**, Journal of Instrumentation **16** (2021) P07032.

[10] E. Rutherford, **VIII. Uranium radiation and the electrical conduction produced by it**, The London, Edinburgh, and Dublin Philosophical Magazine & Journal of Science **47** (1899) 109.

[11] M.M. Villard, **Sur la reflexion et la refraction des rayons cathodiques et des rayons deviables du radium**, C. R. Acad. Sci. Paris **130** (1900) 1010.

[12] H.A. Bethe and R.F. Bacher, **Nuclear Physics A. Stationary States of Nuclei**, Rev. Mod. Phys. **8** (1936) 82.

[13] T.D. Lee and C.N. Yang, **Question of Parity Conservation in Weak Interactions**, Phys. Rev. **104** (1956) 254.

[14] C.S. Wu, E. Ambler, R.W. Hayward, D.D. Hoppes and R.P. Hudson, **Experimental Test of Parity Conservation in Beta Decay**, Phys. Rev. **105** (1957) 1413.

[15] M. Goldhaber, L. Grodzins and A.W. Sunyar, **Helicity of Neutrinos**, Phys. Rev. **109** (1958) 1015.

[16] J.C. Palathingal, **Helicity of Antineutrinos Emitted by Nuclei**, Phys. Rev. Lett. **24** (1970) 524.

[17] G. Danby, J.-M. Gaillard, K. Goulianos, L.M. Lederman, N. Mistry, M. Schwartz and J. Steinberger, **Observation of High-Energy Neutrino Reactions and the Existence of Two Kinds of Neutrinos**, Phys. Rev. Lett. **9** (1962) 36.

[18] K. Kodama, N. Ushida and C. Andreopoulos, **Observation of tau neutrino interactions**, Physics Letters B **504** (2001) 218.

[19] **Precision electroweak measurements on the Z resonance**, Physics Reports **427** (2006) 257.

[20] D. Vignaud, **The GALLEX solar neutrino experiment**, Nuclear Physics B - Proceedings Supplements **60** (1998) 20.

[21] V.N. Gavrin, **The Russian-American gallium experiment SAGE**, Phys. Usp. **54** (2011) 941.

[22] Kamiokande-II Collaboration, **Observation of B-8 Solar Neutrinos in the Kamiokande-II Detector**, Phys. Rev. Lett. **63** (1989) 16.

[23] Kamiokande-II Collaboration, **Experimental Study of the Atmospheric Neutrino Flux**, Phys. Lett. B **205** (1988) 416.

[24] B. Pontecorvo, **Inverse Beta Processes and Nonconservation of Lepton Charge**, Sov. Phys. JETP **7** (1958) 172.

[25] SNO Collaboration, **Direct evidence for neutrino flavor transformation from neutral current interactions in the Sudbury Neutrino Observatory**, Phys. Rev. Lett. **89** (2002) 011301.

[26] The Super-Kamiokande Collaboration Collaboration, **Measurement of the Flux and Zenith-Angle Distribution of Upward Throughgoing Muons by Super-Kamiokande**, Phys. Rev. Lett. **82** (1999) 2644.

[27] Planck Collaboration, **Planck 2018 results. VI. Cosmological parameters**, Astron. Astrophys. **641** (2020) A6.

[28] KATRIN Collaboration, **Direct neutrino-mass measurement based on 259 days of KATRIN data**, Science **388** (2025) adq9592.

[29] C. Arnaboldi, F. Avignone and J. Beeman, **Physics potential and prospects for the CUORICINO and CUORE experiments**, Astroparticle Physics **20** (2003) 91.

[30] GERDA Collaboration, **Probing Majorana neutrinos with double-β decay**, Science **365** (2019) 1445.

[31] E. Armengaud et al., **The CUPID-Mo experiment for neutrinoless double-beta decay: performance and prospects**, Eur. Phys. J. C **80** (2020) 44.

[32] J. Barranco, O.G. Miranda and T.I. Rashba, **Probing new physics with coherent neutrino scattering off nuclei**, Journal of High Energy Physics **2005** (2005) 021–021.

[33] Particle Data Group Collaboration, **Review of Particle Physics**, Phys. Rev. D **98** (2018) 030001.

[34] P. Paganini, **An introduction to the standard model of particle physics**, 2019.

[35] J. Papavassiliou, J. Bernabeu, D. Binosi and J. Vidal, **The effective neutrino charge radius**, European Physical Journal C - EUR PHYS J C **33** (2003) .

[36] G. Degrassi, A. Sirlin and W.J. Marciano, **Effective electromagnetic form factor of the neutrino**, Phys. Rev. D **39** (1989) 287.

[37] P. Vogel and J. Engel, **Neutrino electromagnetic form factors**, Phys. Rev. D **39** (1989) 3378.

[38] K. Fujikawa and R.E. Shrock, **Magnetic Moment of a Massive Neutrino and Neutrino-Spin Rotation**, Phys. Rev. Lett. **45** (1980) 963.

[39] W. Xiong et al., **A small proton charge radius from an electron–proton scattering experiment**, Nature **575** (2019) 147.

[40] PREX Collaboration Collaboration, **Accurate Determination of the Neutron Skin Thickness of ^{208}Pb through Parity-Violation in Electron Scattering**, Phys. Rev. Lett. **126** (2021) 172502.

[41] D. Adhikari and Albataineh, **Precision Determination of the Neutral Weak Form Factor of**, Physical Review Letters **129** (2022) .

[42] J. Lewin and P. Smith, **Review of mathematics, numerical factors, and corrections for dark matter experiments based on elastic nuclear recoil**, Astroparticle Physics **6** (1996) 87.

[43] R.H. Helm, **Inelastic and Elastic Scattering of 187-Mev Electrons from Selected Even-Even Nuclei**, Phys. Rev. **104** (1956) 1466.

[44] M. Cadeddu, C. Giunti, Y.F. Li and Y.Y. Zhang, **Average CsI Neutron Density Distribution from COHERENT Data**, Phys. Rev. Lett. **120** (2018) 072501.

[45] B.T. Reed, F.J. Fattoyev, C.J. Horowitz and J. Piekarewicz, **Implications of PREX-2 on the Equation of State of Neutron-Rich Matter**, Phys. Rev. Lett. **126** (2021) 172503.

[46] J. Liao, D. Marfatia and K. Whisnant, **Degeneracies in long-baseline neutrino experiments from nonstandard interactions**, Phys. Rev. D **93** (2016) 093016.

[47] O.G. Miranda, M.A. Tórtola and J.W.F. Valle, **Are solar neutrino oscillations robust?**, Journal of High Energy Physics **2006** (2006) 008.

[48] S. Davidson, C.P. na Garay, N. Rius and A. Santamaria, **Present and future bounds on non-standard neutrino interactions**, Journal of High Energy Physics **2003** (2003) 011.

[49] V. De Romeri, O.G. Miranda, D.K. Papoulias, G. Sanchez Garcia, M. Tórtola and J.W.F. Valle, **Physics implications of a combined analysis of COHERENT CsI and LAr data**, JHEP **04** (2023) 035 [ttfamily arXiv:2211.11905[hep-ph]].

[50] J. Billard, M. Boulay, S. Cebrián, L. Covi, G. Fiorillo, A. Green, J. Kopp, B. Majorovits, K. Palladino, F. Petricca, L. Roszkowski (chair) and M. Schumann, **Direct detection of dark matter—APPEC committee report***, Reports on Progress in Physics **85** (2022) 056201.

[51] J.Billard, **Bolometric detection of CENNS: concept, status and prospects**, 2022, .

[52] D. Baxter, J.I. Collar, P. Coloma, C.E. Dahl, I. Esteban, P. Ferrario, J.J. Gomez-Cadenas, M. Gonzalez-Garcia, A.R.L. Kavner, C.M. Lewis, F. Monrabal, J.M. Vidal, P. Privitera, K. Ramanathan and J. Renner, **Coherent Elastic Neutrino-Nucleus Scattering at the European Spallation Source**, 2020 [ttfamily arXiv:1911.00762].

[53] K. Scholberg, **Prospects for measuring coherent neutrino-nucleus elastic scattering at a stopped-pion neutrino source**, 2006.

[54] T. Lasserre, **Neutrinos Sources for CEvNS", Lecture given at the Mona School, Magnificent CEvNS 2023**, .

[55] B.R. Davis, P. Vogel, F.M. Mann and R.E. Schenter, **Reactor antineutrino spectra and their application to antineutrino-induced reactions**, Phys. Rev. C **19** (1979) 2259.

[56] P. Vogel, G.K. Schenter, F.M. Mann and R.E. Schenter, **Reactor antineutrino spectra and their application to antineutrino-induced reactions. II**, Phys. Rev. C **24** (1981) 1543.

[57] F. von Feilitzsch, A. Hahn and K. Schreckenbach, **Experimental beta-spectra from 239Pu and 235U thermal neutron fission products and their correlated antineutrino spectra**, Physics Letters B **118** (1982) 162.

[58] P. Huber, **Determination of antineutrino spectra from nuclear reactors**, Phys. Rev. C **84** (2011) 024617.

[59] T.A. Mueller, D. Lhuillier, M. Fallot, A. Letourneau, S. Cormon, M. Fechner, L. Giot, T. Lasserre, J. Martino, G. Mention, A. Porta and F. Yermia, **Improved predictions of reactor antineutrino spectra**, Phys. Rev. C **83** (2011) 054615.

[60] G. Mention, M. Fechner, T. Lasserre, T.A. Mueller, D. Lhuillier, M. Cribier and A. Letourneau, **Reactor antineutrino anomaly**, Phys. Rev. D **83** (2011) 073006.

[61] L. Périssé, A. Onillon, X. Mougeot, M. Vivier, T. Lasserre, A. Letourneau, D. Lhuillier and G. Mention, **Comprehensive revision of the summation method for the prediction of reactor $\overline{\nu}_e$ fluxes and spectra**, Phys. Rev. C **108** (2023) 055501.

[62] R. Rogly, **Measurement of the 235U fission antineutrino spectrum by the STEREO experiment and preparation of the NUCLEUS coherent neutrino scattering experiment**, theses, Université Paris-Saclay, Oct., 2022.

[63] L. Wen, J. Cao and Y. Wang, **Reactor Neutrino Experiments: Present and Future**, Annual Review of Nuclear and Particle Science **67** (2017) 183–211.

[64] W.E. Ang, S. Prasad and S.S. Chirayath, **Antineutrino detection for temporal monitoring of fuel burnup in a large nuclear reactor**, Nuclear Instruments and Methods in Physics Research Section A: Accelerators, Spectrometers, Detectors and Associated Equipment **1028** (2022) 166353.

[65] C. Buck, K. Fülber, J. Hakenmüller, G. Heusser, M. Lindner, W. Maneschg, T. Rink, H. Strecker, T. Schierhuber, V. Wagner and R. Wink, **A novel experiment for coherent elastic neutrino nucleus scattering: CONUS**, Journal of Physics: Conference Series **1342** (2020) 012094.

[66] A. Bonhomme and al., **Direct measurement of the ionization quenching factor of nuclear recoils in germanium in the keV energy range**, The European Physical Journal C **82** (2022) .

[67] H. Bonet and al., **Full background decomposition of the CONUS experiment**, The European Physical Journal C **83** (2023) .

[68] CONUS Collaboration Collaboration, **Constraints on Elastic Neutrino Nucleus Scattering in the Fully Coherent Regime from the CONUS Experiment**, Phys. Rev. Lett. **126** (2021) 041804.

[69] T.C. Collaboration, **The CONUS+ experiment**, 2024,.

[70] V. Belov and Brudanin, **The nuGeN experiment at the Kalinin Nuclear Power Plant**, Journal of Instrumentation **10** (2015) P12011.

[71] νGeN collaboration Collaboration, **First results of the νGeN experiment on coherent elastic neutrino-nucleus scattering**, Phys. Rev. D **106** (2022) L051101.

[72] H.T.-K. Wong, **Taiwan EXperiment On NeutrinO — History and Prospects**, The Universe **3** (2015) 22.

[73] C. Collaboration, **The CONNIE experiment**, 2016,.

[74] A.E. Chavarria, J.I. Collar, J.R. Peña, P. Privitera, A.E. Robinson, B. Scholz, C. Sengul, J. Zhou, J. Estrada, F. Izraelevitch, J. Tiffenberg, J.R.T. de Mello Neto and D. Torres Machado, **Measurement of the ionization produced by sub-keV silicon nuclear recoils in a CCD dark matter detector**, Phys. Rev. D **94** (2016) 082007.

[75] CONNIE Collaboration Collaboration, **Exploring low-energy neutrino physics with the Coherent Neutrino Nucleus Interaction Experiment**, Phys. Rev. D **100** (2019) 092005.

[76] B. Cervantes-Vergara, S. Perez, J. D'Olivo, J. Estrada, D. Grimm, S. Holland, M. Sofo-Haro and W. Wong, **Skipper-CCDs: Current applications and future**, Nuclear Instruments and Methods in Physics Research Section A: Accelerators, Spectrometers, Detectors and Associated Equipment **1046** (2023) 167681.

[77] J.J. Choi and Jeon, **Exploring coherent elastic neutrino-nucleus scattering using reactor electron antineutrinos in the NEON experiment**, The European Physical Journal C **83** (2023) .

[78] J. Choi and B. Park, **Improving the light collection using a new NaI(Tl) crystal encapsulation**, Nuclear Instruments and Methods in Physics Research Section A: Accelerators, Spectrometers, Detectors and Associated Equipment **981** (2020) 164556.

[79] E. Alfonso-Pita et al., **Scintillating Bubble Chambers for Rare Event Searches**, Universe **9** (2023) 346.

[80] P. Giampa, **The Scintillating Bubble Chamber (SBC) Experiment for Dark Matter and Reactor CEvNS**, PoS **ICHEP2020** (2021) 632.

[81] M. Chaudhuri, **The Mitchell Institute Neutrino Experiment at Reactor (MINER)**, in *Proceedings of the XXIV DAE-BRNS High Energy Physics Symposium, Jatni, India*, B. Mohanty, S.K. Swain, R. Singh and V.K.S. Kashyap, eds., (Singapore), pp. 589–593, Springer Nature Singapore, 2022.

[82] R. Collaboration, **Ricochet Progress and Status**, 2021, .

[83] D. Misiak, **Development of new cryogenic low-threshold detectors for the search of light dark matter and low-energy neutrino physics**, Ph.D. thesis, 2021. .

[84] CRESST Collaboration, **Results on light dark matter particles with a low-threshold CRESST-II detector**, Eur. Phys. J. C **76** (2016) 25.

[85] R. Strauss, J. Rothe and al., **The Nucleus experiment: a gram-scale fiducial-volume cryogenic detector for the first detection of coherent neutrino–nucleus scattering**, The European Physical Journal C **77** (2017) .

[86] R. Strauss, J. Rothe, G. Angloher, A. Bento, A. Gütlein, D. Hauff, H. Kluck, M. Mancuso, L. Oberauer, F. Petricca, F. Pröbst, J. Schieck, S. Schönert, W. Seidel and L. Stodolsky, **Gram-scale cryogenic calorimeters for rare-event searches**, Physical Review D **96** (2017) .

[87] G. Angloher, P. Bauer and Bento, **Results on MeV-scale dark matter from a gram-scale cryogenic calorimeter operated above ground: CRESST Collaboration**, The European Physical Journal C **77** (2017) .

[88] M. Apollonio, A. Baldini, C. Bemporad and Caffau, **Search for neutrino oscillations on a long base-line at the CHOOZ nuclear power station**, The European Physical Journal C **27** (2003) 331–374.

[89] H. de Kerret, Y. Abe and Aberle, **The Double Chooz antineutrino detectors**, The European Physical Journal C **82** (2022) .

[90] C. Goupy, **Stratégie de réduction des bruits de fond pour détecter la diffusion cohérente des anti-neutrinos de reacteurs sur noyaux avec l'expérience NUCLEUS**, Ph.D. thesis, 2024.

[91] M. Gordon, P. Goldhagen, K. Rodbell, T. Zabel, H. Tang, J. Clem and P. Bailey, **Measurement of the flux and energy spectrum of cosmic-ray induced neutrons on the ground**, IEEE Transactions on Nuclear Science **51** (2004) 3427.

[92] A. Tang, G. Horton-Smith, V.A. Kudryavtsev and A. Tonazzo, **Muon simulations for Super-Kamiokande, KamLAND, and CHOOZ**, Phys. Rev. D **74** (2006) 053007.

[93] **Sciences 'a l'´Ecole. http://www.sciencesalecole.org/ plan-cosmos-a-lecole-materiel/**, .

[94] P. Theodórsson, **Measurement of Weak Radioactivity**, WORLD SCIENTIFIC (1996), .

[95] **Saint-Gobain Crystal BC-408**, `https://seltokphotonics.com/upload/iblock/f8b/f8bffb8aa2e48a4535524d7f8d50284a.pdf` (2021).

[96] **KETEK. SiPM TIA Module**, `https://www.ketek.net/wp-content/uploads/KETEK-SiPM-Module-PE33xx-WB-TIA-xP.pdf` (2022).

[97] V. Wagner, R. Rogly, A. Erhart, V. Savu, C. Goupy, D. Lhuillier, Vivier and for the NUCLEUS collaboration, **Development of a compact muon veto for the Nucleus experiment**, Journal of Instrumentation **17** (2022) T05020.

[98] BlueFors, **LD, Dilution Refrigerator Measurement System**, `https://bluefors.com/products/dilution-refrigerator-measurement-systems/ld-dilution-refrigerator-measurement-system/` (2024).

[99] A. Wex, **Creation of a Vibration Free Environment in a Dry Dilution Refrigerator at Millikelvin Temperatures**, 2023.

[100] A. Wex, J. Rothe and L. Peters, **Decoupling pulse tube vibrations from a dry dilution refrigerator at milli-Kelvin temperatures**, Journal of Instrumentation **20** (2025) P05022.

[101] A. Erhart, V. Wagner and A. Wex, **A Plastic Scintillation Muon Veto for Sub-Kelvin Temperatures**, 2023, .

[102] T.N. collaboration and C. Goupy, **Exploring coherent elastic neutrino-nucleus scattering of reactor neutrinos with the NUCLEUS experiment**, 2022, .

[103] C. Goupy, **First estimate of backgrounds at sub-keV energies for the NUCLEUS CEvNS experiment**, https://doi.org/10.5281/zenodo.6767550 (June, 2022).

[104] X.-F. Navick, D. L'Hôte and R. Tourbot, **Ionization measurement at very low temperature for nuclear and electron recoils discrimination by ionization-heat simultaneous measurement for dark matter research**, Nuclear Instruments and Methods in Physics Research Section A: Accelerators, Spectrometers, Detectors and Associated Equipment **442** (2000) 267.

[105] C. Goupy, S. Marnieros, B. Mauri, C. Nones and M. Vivier, **Prototyping a High Purity Germanium cryogenic veto system for a bolometric detection experiment**, 2024, .

[106] N. Ashcroft and N. Mermin, **Solid State Physics**, HRW international editions, Holt, Rinehart and Winston (1976), .

[107] J.F.M. Rothe, **Low-Threshold Cryogenic Detectors for Low-Mass Dark Matter Search and Coherent Neutrino Scattering**, 2021.

[108] B. Mauri, **Prototyping of innovative cryogenic detectors for the detection of coherent elastic neutrino-nucleus scattering**, Ph.D. thesis, 2022.

[109] F. Pröbst, M. Frank, S. Cooper, P. Colling, D. Dummer, P. Ferger, G. Forster, A. Nucciotti, W. Seidel and L. Stodolsky, **Model for cryogenic particle detectors with superconducting phase transition thermometers**, J. Low Temp. Phys. **100** (1995) 69.

[110] A. Senyshyn, H. Kraus, V.B. Mikhailik and V. Yakovyna, **Lattice dynamics and thermal properties of** $CaWO_4$, Phys. Rev. B **70** (2004) 214306.

[111] S.H. Moseley, J.C. Mather and D. McCammon, **Thermal detectors as x-ray spectrometers**, Journal of Applied Physics **56** (1984) 1257.

[112] D. Mccammon, **Thermal Equilibrium Calorimeters – An Introduction**, vol. 99, pp. 1–34 (2005),

[113] K. Irwin and G. Hilton, **Transition-Edge Sensors**, in *Cryogenic Particle Detection*, C. Enss, ed., (Berlin, Heidelberg), pp. 63–150, Springer Berlin Heidelberg (2005),

[114] M. Gonzalez, **Introduction to low temperature detectors**, 2024.

[115] P. Mangin and R. Kahn, **SUPERCONDUCTING QUANTUM INTERFERENCE DEVICE "SQUID"**, in *Superconductivity: An introduction*, (Cham), pp. 289–311, Springer International Publishing (2017),

[116] É. Du Trémolet de Lacheisserie and M. Cyrot, **Magnétisme: Matériaux et applications. II**, Collection Grenoble sciences, EDP Sciences (2000),

[117] J. Rothe, **Internal Note: SQUID resets and Flux Quantum Losses**, 2024.

[118] K.T. Mpofu and P. Mthunzi-Kufa, **Recent Advances in Quantum Biosensing Technologies**, in *Current Developments in Biosensors and Emerging Smart Technologies*, S. Karakuş, ed., (Rijeka), IntechOpen (2024),

[119] H. Abele, G. Angloher, B. Arnold, M. Atzori Corona, A. Bento, E. Bossio, J. Burkhart, F. Cappella, M. Cappelli, N. Casali, R. Cerulli, A. Cruciani, G. Del Castello, M. del Gallo Roccagiovine, S. Dorer et al., **Sub-keV Electron Recoil Calibration for Cryogenic Detectors using a Novel X-ray Fluorescence Source**, 2025,

[120] L. Peters, **A new data analysis tool for NUCLEUS and first results from the commissioning phase**, 2024.

[121] CRAB Collaboration and NUCLEUS Collaboration Collaboration, **Observation of a Nuclear Recoil Peak at the 100 eV Scale Induced by Neutron Capture**, Phys. Rev. Lett. **130** (2023) 211802.

[122] J. Allison, K. Amako and J. Apostolakis, **Recent developments in Geant4**, Nuclear Instruments and Methods in Physics Research Section A: Accelerators, Spectrometers, Detectors and Associated Equipment **835** (2016) 186.

[123] J. Allison, K. Amako and Apostolakis, **Geant4 developments and applications**, IEEE Transactions on Nuclear Science **53** (2006) 270.

[124] S. Agostinelli, J. Allison and K. Amako, **Geant4—a simulation toolkit**, Nuclear Instruments and Methods in Physics Research Section A: Accelerators, Spectrometers, Detectors and Associated Equipment **506** (2003) 250.

[125] **ROOT. Data Analysis Framework.**, .

[126] tba., **A first background prediction at sub-keV energies for the NUCLEUS CEvNS experiment at the Chooz nuclear power plant. tba**, 2025.

[127] P. Adari, A.A. Aguilar-Arevalo and D. Amidei, **EXCESS workshop: Descriptions of rising low-energy spectra**, SciPost Physics Proceedings (2022) .

[128] G. Angloher, S. Banik and G. Benato, **Latest observations on the low energy excess in CRESST-III**, SciPost Phys. Proc. (2023) 013.

[129] R. Romani, **Observations of the LEE in a Two Channel SPICE Athermal Phonon Detector**, 2023.

[130] F. Pucci, **Results of doubleTES detectors**, 2023.

[131] J. Gascon, **Heat-Only background discrimination in EDELWEISS and RICOCHET cryogenic germanium detectors**, 2023.

[132] M.Kaznacheeva, **New excess measurements from NUCLEUS**, 2024.

[133] Angloher, G., Banik, S., Benato, G. and CRESST Collaboration, **DoubleTES detectors to investigate the CRESST low energy background: results from above-ground prototypes**, Eur. Phys. J. C **84** (2024) 1001.

[134] R. Anthony-Petersen, C.L. Chang and Chang, **Low energy backgrounds and excess noise in a two-channel low-threshold calorimeter**, Applied Physics Letters **126** (2025) 102601 [ttfamily arXiv:https://pubs.aip.org/aip/apl/article-pdf/doi/10.1063/5.0247343/20436183/102601_1_5.0247343.pdf].

[135] N. Schermer, **Development of the NUCLEUS 10g Cryogenic Detector for Exploring Coherent Elastic Neutrino Nucleus Scattering**, 2021.

[136] Langenkämper and A. al., **A Cryogenic Detector Characterization Facility in the Shallow Underground Laboratory at the Technical University of Munich**, 2018.

[137] H. Bethe, **Zur Theorie des Durchgangs schneller Korpuskularstrahlen durch Materie**, Annalen der Physik **397** (1930) 325.

[138] **ON THE ENERGY LOSS OF FAST PARTICLES BY IONISATION**, in *Collected Papers of L.D. Landau*, D. TER HAAR, ed., pp. 417–424, Pergamon (1965), .

[139] P.V. Vavilov, **Ionization Losses of High-Energy Heavy Particles**, Sov. Phys. JETP **5** (1957) 749.

[140] H. Bichsel, **Straggling in thin silicon detectors**, Rev. Mod. Phys. **60** (1988) 663.

[141] S. Pethuraj, V. Datar, G. Majumder, N. Mondal, K. Ravindran and B. Satyanarayana, **Measurement of cosmic muon angular distribution and vertical integrated flux by 2 m × 2 m RPC stack at IICHEP-Madurai**, Journal of Cosmology and Astroparticle Physics **2017** (2017) 021.

[142] I. Briki, M. Mazouz and L. Ghedira, **Angular distribution of low momentum atmospheric muons at ground level**, Journal of Cosmology and Astroparticle Physics **2023** (2023) 025.

[143] B. Olmos Yáñez and A.A. Aguilar-Arevalo, **A method to measure the integral vertical intensity and angular distribution of atmospheric muons with a stationary plastic scintillator bar detector**, Nuclear Instruments and Methods in Physics Research Section A: Accelerators, Spectrometers, Detectors and Associated Equipment **987** (2021) 164870.

[144] **Saint Gobain Crystals. BC-91A**, https://seltokphotonics.com/upload/iblock/f8b/f8bffb8aa2e48a4535524d7f8d50284a.pdf (2021).

[145] D.E. GROOM, N.V. MOKHOV and S.I. STRIGANOV, **MUON STOPPING POWER AND RANGE TABLES 10 MeV–100 TeV**, Atomic Data and Nuclear Data Tables **78** (2001) 183.

[146] T. Eggert and al., **Latest developments in ketek's silicon photomultiplier solutions.**, https://indico.cern.ch/event/774201/contributions/3429249/attachments/1878071/3093392/C04_190618_-_KETEK_SiPM_-_TEG_-_iWorid_Tobias.pdf (2019).

[147] V.-G. Savu, **Reactor neutrino studies : STEREO and NUCLEUS experiments**, Ph.D. thesis, 2021.

[148] S. Baker and R.D. Cousins, **Clarification of the use of CHI-square and likelihood functions in fits to histograms**, Nuclear Instruments and Methods in Physics Research **221** (1984) 437.

[149] P. Theodórsson, **Measurement of Weak Radioactivity**, WORLD SCIENTIFIC (1996).

[150] p. Module meteostat, **https://dev.meteostat.net/python/installation**, .

[151] D. Collaboration, **Observation of the temperature and barometric effects on the cosmic muon flux by the DANSS detector**, 2022.

[152] K. Jourde, D. Gibert, J. Marteau, J. de Bremond d'Ars, S. Gardien, C. Girerd and J.-C. Ianigro, **Monitoring temporal opacity fluctuations of large structures with muon radiography: a calibration experiment using a water tower**, Scientific Reports **6** (2016) .

[153] G. Del Castello, **LANTERN: A multichannel light calibration system for cryogenic detectors**, Nuclear Instruments and Methods in Physics Research Section A: Accelerators, Spectrometers, Detectors and Associated Equipment **1068** (2024) 169728.

[154] T. Ullrich and Z. Xu, **Treatment of Errors in Efficiency Calculations**, 2012.

[155] F. Wagner, **Machine learning methods for the raw data analysis of cryogenic dark matter experiments [Diploma Thesis, Technische Universität Wien]**, 2022.

[156] F. Wagner, **Towards next-generation cryogenic dark matter searches with superconducting thermometers [Dissertation, Technische Universität Wien; Österreichische Akademie der Wissenschaften]**, 2023.

[157] F. Wagner, D. Bartolot, D. Rizvanovic, F. Reindl, J. Schieck and W. Waltenberger, **Cait: Analysis Toolkit for Cryogenic Particle Detectors in Python**, Computing and Software for Big Science **6** (2022) .

[158] p. CAIT module, **https://cait.readthedocs.io/en/latest/**, .

[159] S.R. Golwala, **Exclusion limits on the WIMP nucleon elastic scattering cross-section from the Cryogenic Dark Matter Search**, Ph.D. thesis, UC, Berkeley, 2000. 10.2172/1421437.

[160] **Wikipedia, Spectral density**.

[161] E. Gatti and P.F. Manfredi, **Processing the Signals From Solid State Detectors in Elementary Particle Physics**, Riv. Nuovo Cim. **9N1** (1986) 1.

[162] S.D. Domizio, F. Orio and M. Vignati, **Lowering the energy threshold of large-mass bolometric detectors**, Journal of Instrumentation **6** (2011) P02007.

[163] V. Radeka and N. Karlovac, **Least-square-error amplitude measurement of pulse signals in presence of noise**, Nuclear Instruments and Methods **52** (1967) 86.

[164] E. Casnati, A. Tartari, C. Baraldi and G. Napoli, **Measurement of the Kbeta/Kalpha yield ratios of Cu, Mo and Cd stimulated by 59.54 keV photons**, Journal of Physics B: Atomic and Molecular Physics **18** (1985) 2843.

[165] H. Abele, G. Angloher, B. Arnold, M.A. Corona, A. Bento, E. Bossio, F. Buchsteiner, J. Burkhart, F. Cappella, M. Cappelli, N. Casali, R. Cerulli, A. Cruciani, G.D. Castello, M. del Gallo Roccagiovine et al., **Commissioning of the NUCLEUS Experiment at the Technical University of Munich**, 2025, .

[166] C. Alduino, K. Alfonso and Artusa, **Analysis Techniques for the Evaluation of the Neutrinoless Double-Beta Decay Lifetime in 130Te with CUORE-0**, Physical Review C **93** (2016) .

[167] O. Azzolini, M.T. Barrera and Beeman, **Analysis of cryogenic calorimeters with light and heat read-out for double beta decay searches**, The European Physical Journal C **78** (2018) .

[168] M. Abdullah et al., **Coherent elastic neutrino-nucleus scattering: Terrestrial and astrophysical applications**, .

[169] J.L. Feng and J. Kumar, **Dark-Matter Particles without Weak-Scale Masses or Weak Interactions**, Phys. Rev. Lett. **101** (2008) 231301.

[170] R. Essig, A. Manalaysay, J. Mardon, P. Sorensen and T. Volansky, **First Direct Detection Limits on Sub-GeV Dark Matter from XENON10**, Phys. Rev. Lett. **109** (2012) 021301.

[171] D. Baxter et al., **Snowmass2021 Cosmic Frontier White Paper: Calibrations and backgrounds for dark matter direct detection**, 2022.

[172] J. Lindhard and M. Scharff, **Energy Dissipation by Ions in the kev Region**, Phys. Rev. **124** (1961) 128.

[173] J.I. Collar, A.R.L. Kavner and C.M. Lewis, **Germanium response to sub-keV nuclear recoils: A multipronged experimental characterization**, Phys. Rev. D **103** (2021) 122003.

[174] Albakry, **First Measurement of the Nuclear-Recoil Ionization Yield in Silicon at 100eV**, Physical Review Letters **131** (2023) .

[175] G. Soum, **The CRAB project : precise detection and simulation of nuclear recoils for the calibration of cryogenic detectors in the 100eV energy range**, theses, Université Paris-Saclay, May, 2025. .

[176] R. Firestone, K. Abusaleem, M. Basunia, F. Bečvář, T. Belgya, L. Bernstein, H. Choi, J. Escher, C. Genreith, A. Hurst, M. Krtička, P. Renne, Z. Révay, A. Rogers, M. Rossbach et al., **EGAF: Measurement and Analysis of Gamma-ray Cross Sections**, Nuclear Data Sheets **119** (2014) 79.

[177] R. Capote, M. Herman, P. Obložinský, P. Young, S. Goriely, T. Belgya, A. Ignatyuk, A. Koning, S. Hilaire, V. Plujko, M. Avrigeanu, O. Bersillon, M. Chadwick, T. Fukahori, Z. Ge et al., **RIPL – Reference Input Parameter Library for Calculation of Nuclear Reactions and Nuclear Data Evaluations**, Nuclear Data Sheets 110 3107. 22, 24, 25 (2009) .

[178] O. Litaize, O. Serot and L. Berge, **Fission modelling with FIFRELIN**, Eur. Phys. J. A **51** (2015) 177.

[179] H. Almazán and al., **Improved STEREO simulation with a new gamma ray spectrum of excited gadolinium isotopes using FIFRELIN**, The European Physical Journal A 55 (2019) 183. 24 (2019) .

[180] L. Thulliez, **Caractérisation des fragments de fission et développement du dispositif expérimental FALSTAFF**, theses, Université Paris-Saclay, Sept., 2017.

[181] A. Gilbert and A.G.W. Cameron, **A COMPOSITE NUCLEAR-LEVEL DENSITY FORMULA WITH SHELL CORRECTIONS**, Canadian Journal of Physics **43** (1965) 1446 [ttfamily arXiv:https://doi.org/10.1139/p65-139].

[182] S. Goriely, S. Hilaire and A.J. Koning, **Improved microscopic nuclear level densities within the Hartree-Fock-Bogoliubov plus combinatorial method**, Phys. Rev. C **78** (2008) 064307.

[183] J. Kopecky and M. Uhl, **Test of gamma-ray strength functions in nuclear reaction model calculations**, Phys. Rev. C **41** (1990) 1941.

[184] D. Brink, **Individual particle and collective aspects of the nuclear photoeffect**, Nuclear Physics **4** (1957) 215.

[185] S. Goriely and E. Khan, **Large-scale QRPA calculation of E1-strength and its impact on the neutron capture cross section**, Nuclear Physics A **706** (2002) 217.

[186] C.E. Porter and R.G. Thomas, **Fluctuations of Nuclear Reaction Widths**, Phys. Rev. **104** (1956) 483.

[187] T. Kibédi, T. Burrows, M. Trzhaskovskaya, P. Davidson and C. Nestor, **Evaluation of theoretical conversion coefficients using BrIcc**, Nuclear Instruments and Methods in Physics Research Section A: Accelerators, Spectrometers, Detectors and Associated Equipment **589** (2008) 202.

[188] K.W. Jones and H.W. Kraner, **Energy lost to ionization by 254-eV ^{73}Ge atoms stopping in** Ge, Phys. Rev. A **11** (1975) 1347.

[189] C. Borschel and C. Ronning, **Ion beam irradiation of nanostructures – A 3D Monte Carlo simulation code**, Nuclear Instruments and Methods in Physics Research Section B: Beam Interactions with Materials and Atoms **269** (2011) 2133.

[190] R.M. Thaler, **Nuclear Physics: Physics of the Nucleus. M. A. Preston. Addison-Wesley, Reading, Mass., 1962.**, Science **137** (1962) 848.

[191] CRAB COLLABORATION Collaboration, **Study of collision and γ-cascade times following neutron-capture processes in cryogenic detectors**, Phys. Rev. D **108** (2023) 072009.

[192] J.-P. Crocombette, **Cascade Modeling**, in *Handbook of Materials Modeling: Methods*, S. Yip, ed., (Dordrecht), pp. 987–997, Springer Netherlands (2005),

[193] C. Collaboration, **The CRAB facility at the TU Wien TRIGA reactor: status and related physics program**, 2025,

[194] L. Thulliez, B. Mom and E. Dumonteil, **TOUCANS: a versatile Monte Carlo neutron transport code based on Geant4**, 2023,

[195] M. Chadwick, P. Obložinský and M. Herman, **ENDF/B-VII.0: Next Generation Evaluated Nuclear Data Library for Nuclear Science and Technology**, Nuclear Data Sheets **107** (2006) 2931.

[196] Cai and T. Kittelmann, **NCrystal: A library for thermal neutron transport**, Computer Physics Communications **246** (2020) 106851.

[197] G. Soum-Sidikov, J.P. Crocombette, M.C. Marinica, C. Doutre, D. Lhuillier and L. Thulliez, **Calculation of crystal defects induced in $CaWO_4$ cryogenic detector by 100 eV displacement cascades using a data driven force field**, Phys. Rev. D **111** (2025) 085021.

[198] S. Sassi, M. Heikinheimo, K. Tuominen, A. Kuronen, J. Byggmästar, K. Nordlund and N. Mirabolfathi, **Energy loss in low energy nuclear recoils in dark matter detector materials**, Phys. Rev. D **106** (2022) 063012.

[199] A.N. Villano, M. Fritts, N. Mast, S. Brown, P. Cushman, K. Harris and V. Mandic, **First observation of isolated nuclear recoils following neutron capture for dark matter calibration**, Phys. Rev. D **105** (2022) 083014.

[200] K. Harris, A. Gevorgian, A. Biffl and A. Villano, **Neutron capture-induced silicon nuclear recoils for dark matter and CEvNS**, Physical Review D **107** (2023) .

[201] M. Martin, **Nuclear Data Sheets for A = 248**, Nuclear Data Sheets **122** (2014) 377.

[202] G.D. Castello, **Development of energy calibration and data analysis systems for the NUCLEUS experiment**, 2023, .

[203] M. Stahlberg, **Probing Low-Mass DarkMatter with CRESST-III - Data Analysis and First Results**, Ph.D. thesis, Vienna, Tech. U., 2021. 10.34726/hss.2021.45935.

[204] CRESST Collaboration Collaboration, **Observation of a low energy nuclear recoil peak in the neutron calibration data of the CRESST-III experiment**, Phys. Rev. D **108** (2023) 022005.

[205] F. James, **Statistical Methods in Experimental Physics**, WORLD SCIENTIFIC, 2nd ed. (2006), .

[206] **History, Development and Future of TRIGA Research Reactors**, no. 482 in Technical Reports Series, INTERNATIONAL ATOMIC ENERGY AGENCY, Vienna (2016), .

[207] **The PARIS project**, Acta Phys. Pol. B 40, 565 (2009) .

[208] D. R.Martin, **Proposal to use PARIS clusters for accurate studies of sub-keV nuclear recoils in cryo-detectors**, 2023.

[209] C. Ghosh, V. Nanal, R. Pillay, K. Anoop, N. Dokania, S. Pal, M. Pose, G. Mishra, P. Rout, S. Kumar, D. Pandit, D. Mondal, S. Pal, S. Banerjee, P. Napiorkowski et al., **Characterization of PARIS LaBr3(Ce)-NaI(Tl) phoswich detectors up to E $\sim$ 22 MeV**, Journal of Instrumentation **11** (2016) P05023–P05023.

[210] Adam Maj, **The PARIS calorimeter project: status, first experiments and perspectives**, 2024, .

[211] J. Billard, J. Gascon, S. Marnieros and S. Scorza, **Transition Edge Sensors with Sub-eV Resolution And Cryogenic Targets (TESSERACT) at the underground laboratory of Modane (LSM)**, Nucl. Phys. B **1003** (2024) 116465.

[212] TRIGA Center, **The TRIGA Mark-II Reactor**, .

[213] Physik Instrumente, **PI M-037 Rotary Table. https://www.pi-usa.us/en/products/motorized-rotary-stages-goniometers/rotary-tables-7-38**, .

[214] Physik Instrumente, **PI Hexapod H820. https://www.physikinstrumente.de/de/produkte/hexapoden-parallelkinematiken/h-820-6-achsen-hexapod-700825**, .

[215] **Details zum System drylin SLW. https://www.igus.at/info/linear-guides-drylin-slw**, 2022, .

[216] W.H. Bragg and W.L. Bragg, **The reflection of X-rays by crystals**, Proceedings of the Royal Society of London. Series A, Containing Papers of a Mathematical and Physical Character **88** (1913) 428 [ttfamily arXiv:https://royalsocietypublishing.org/doi/pdf/10.1098/rspa.1913.0040].

[217] VacuTec GmbH, **VacuTec Zählrohre. https://www.vacutec-gmbh.de/de/produkte/umwelt/zaehlrohre-gm-p-n/neutronen-zaehlrohre.html**, .

[218] DENEX GmbH, **DENEX 200-TN. http://www.denex-gmbh.de/200.php?sprache=de**, .

[219] D. Sebastian, **Towards the experimental realization of a novel approach for the low energy calibration of cryogenic particle detectors using nuclear recoils via neutron capture induced gamma emission**, Ph.D. thesis, TUWien, to be published.

[220] **Alváris - Rack construction technology. https://alvaris.com/en/gestellbautechnik/**, .

[221] **Newport S-2000A Stabilizer^{TM} Top Performance Pneumatic Vibration Isolators with Automatic Re-Leveling**, .

[222] J.P. Vivien, **Boules et Châteaux de Cristal. Détecteurs multicompteurs γ 4π**, in *Ecole Internationale Joliot-Curie de Physique Nucléaire*, Septembre, 1983.

[223] B. Bastin, **Étude de la structure des noyaux riches en neutrons autour de la fermeture de couches N=28 par spectroscopie gamma en ligne.**, theses, Université de Caen, Oct., 2007. .

[224] Belli and al., **Investigation of rare nuclear decays with BaF2 crystal scintillator contaminated by radium**, The European Physical Journal A **50** (2014) .

[225] B.N.L. National Nuclear Data Center, **NuDat (Nuclear Structure and Decay Data)**, March 18,, 2008.

[226] F.Knoll, **Radiation Detection and Measurement.**, 1999.

[227] M. Hamada, Y. Nunoya, S. Sakuragui and S. Kubota, **Suppression of the slow component of BaF2 crystal by introduction of SrF2 and MgF2 crystals**, Nuclear Instruments and Methods in Physics Research Section A: Accelerators, Spectrometers, Detectors and Associated Equipment **353** (1994) 33.

[228] D. Etasse and al., **Fast Acquisition System for Nuclear Research**, .

[229] S. Marrone, E. Berthomieux, F. Becvar, D. Cano-Ott, N. Colonna, C. Domingo-Pardo, F. Gunsing, R. Haight, M. Heil, F. Käppeler, M. Krtička, P. Mastinu, A. Mengoni, P. Milazzo, J. O'Donnell et al., **Pulse shape analysis of signals from BaF2 and CeF3 scintillators for neutron capture experiments**, Nuclear Instruments and Methods in Physics Research Section A: Accelerators, Spectrometers, Detectors and Associated Equipment **568** (2006) 904.

[230] L. Dinca, P. Dorenbos, J. de Haas, V. Bom and C. Van Eijk, **Alpha–gamma pulse shape discrimination in CsI:Tl, CsI:Na and BaF2 scintillators**, Nuclear Instruments and Methods in Physics Research Section A: Accelerators, Spectrometers, Detectors and Associated Equipment **486** (2002) 141.

[231] h. CLYC, .

[232] E. Andreas, **Background Mitigation and Calibration for NUCLEUS**, Ph.D. thesis, TUM, to be published.

[233] M. Lopez-Jimenez, **On-line γ spectroscopy of ^{32}Mg produced by projectile fragmentation and study of ^{36}Ca and ^{35}Ca radioactivity**, theses, Université de Caen, Feb., 2000. .

[234] V. Lima, **Etude de la réaction de cassure du ^{11}Be sur cible de ^{48}Ti ; le towing mode, un outil spectroscopique pour l'étude des noyaux.**, theses, Université Paris Sud - Paris XI, Oct., 2004.

[235] Z. Wei, R.-Y. Zhu, H. Newman and Z. Yin, **Light yield and surface treatment of barium fluoride crystals**, Nuclear Instruments and Methods in Physics Research Section B: Beam Interactions With Materials and Atoms **61** (1991) 61.

[236] D.-A. Ma and R.-Y. Zhu, **On optical bleaching of barium fluoride crystals**, Nuclear Instruments and Methods in Physics Research Section A: Accelerators, Spectrometers, Detectors and Associated Equipment **332** (1993) 113.

[237] J.-C. Sublet, J. Eastwood, J. Morgan, M. Gilbert, M. Fleming and W. Arter, **FISPACT-II: An Advanced Simulation System for Activation, Transmutation and Material Modelling**, Nucl. Data Sheets **139** (2017) 77.

[238] Y. Li, G. Herrera and P. Huber, **New Physics versus Quenching Factors in Coherent Neutrino Scattering**, 2025,

[239] **Chap.6 - Dilution Refrigerators**, in *The Art of Cryogenics*, G. Ventura and L. Risegari, eds., (Oxford), pp. 143–161, Elsevier (2008),

[240] J.-M. Duval, **Study of a pulse tube cooler providing 5 W of cooling power at 80 Kelvin**, theses, INP Grenoble, Jan., 2002.

[241] L. Duband and P. Camus, **Réfrigération aux températures inférieures à 1 K**, Techniques de l'Ingénieur (2021) .